Electrochemical impedance spectroscopy as a probe of cement hydration and microstructure

270   340

$Z'(\Omega)$

Aldo Fernando Sosa Gallardo

Ph.D. Thesis

August 2020

Electrochemical impedance spectroscopy as a probe of cement hydration and microstructure

by

Aldo Fernando Sosa Gallardo

Academic Supervisors:

Professor John L. Provis and Professor Derek C. Sinclair

A thesis submitted in partial fulfilment of the requirement for the degree of Doctor of Philosophy

Department of Materials Science and Engineering

The University of Sheffield

August 2020

In loving memory of my sister Desiree

who has been the inspiration of my life.

To my grandparents Antonio and Ramona

who always looked after my brothers, my sisters and me, and to whom I will be

eternally grateful.

To my mother Adriana

who made me the person that I am today and that without her support, I could not

have reached my dreams.

To my beloved brothers Jorge, Eibar and my beloved sister Fernanda

who have been my role models and have supported me in my life.

To my beloved wife Lucy

who was always by my side throughout this path.

To Fabiola, Fred, Michael and Dalia

who made sure I started on the right foot and have been avid supporters in my

journey

To Ramona (the dog)

Whose loyal companionship kept me sane during the long nights of writing.

Abstract

Understanding the hydration and microstructural evolution of cement has been a controversial subject for many decades. As a result of this, different techniques have been used to assess cement hydration. One of the techniques which has demonstrated to be a sensitive and useful technique is Alternating Current Impedance Spectroscopy (ACIS). However, this technique is not yet fully accepted by the cement research community and industry. This has been particularly evident in many cement studies at early hydration ages (>24hrs) in which the ACIS information available at this time is very limited due to instrument and data interpretation limitations, and the complex chemical composition, and continuous pore solution and microstructural development of cement paste. In this project, a custom-cell design is proposed to perform ACIS measurements in cement paste at early ages (>24hrs). The selection of the custom-cell is systematically assessed through a rigorous selection process of the cell components and experimental protocol. To evaluate the performance of the custom-cell design and demonstrate the capabilities of ACIS as a probe of cement hydration and microstructural development at early ages, three techniques (i.e. isothermal calorimetry, Vicat needle test, and scanning electron microscopy) are used as a benchmark to support and complement ACIS data interpretation. The results show that ACIS measurement can be performed at early cement hydration ages by using the proposed custom-cell design (decreases parasitic effects at high frequencies). The benchmark techniques demonstrated that ACIS is a promising and capable characterisation technique to assess the characteristics of the pore solution, thermochemical and microstructural changes during cement hydration. However, further experimental work is required to take further the potential of ACIS.

Keywords: Cement hydration, Alternating current impedance spectroscopy, Experimental protocol, Custom-cell design.

I

Acknowledgments

After an enjoyable but challenging 5-year period, I have finally completed my research project and I would like to express my deepest gratitude to those who made it possible. Their guidance and expertise enabled me to complete this chapter of my life.

II

Contents

Figures and Tables

Nomenclature

Cement chemistry notations		
Compound	**Chemical formula**	**Abbreviation**
Calcium oxide	CaO	C
Silica	SiO_2	S
Aluminium oxide	Al_2O_3	A
Ferric oxide	Fe_2O_3	F
Water	H_2O	H
Sulphur trioxide	SO_3	$\bar{S}$
Sodium oxide	Na_2O	N
Potassium oxide	K_2O	K
Carbon dioxide	CO_2	c
Magnesium oxide	MgO	M
Titanium dioxide	TiO_2	T
Major clinker phases		
Tricalcium silicate (alite)	$3CaO \cdot SiO_2$	C_3S
Dicalcium silicate (belite)	$2CaO \cdot SiO_2$	C_2S
Tricalcium aluminate (aluminate)	$3CaO \cdot Al_2O_3$	C_3A
Tetracalcium aluminoferrite (ferrite)	$4CaO \cdot Al_2O_3 \cdot Fe_2O_3$	C_4AF
Calcium sulphate sources		
Gypsum	$CaSO_4 \cdot 2H_2O$	$C\bar{S}H_2$
Hemihydrate	$CaSO_4 \cdot 0.5H_2O$	$C\bar{S}H_{0.5}$
Anhydrite (A)	$CaSO_4$	$C\bar{S}$
Hydrate phases		
Calcium silicate hydrate	$CaO\text{-}SiO_2\text{-}H_2O$	C-S-H
Calcium hydroxide (portlandite)	$Ca(OH)_2$	CH
Ettringite	$C_3A \cdot 3C\bar{S} \cdot 32H$	AFt
Monosulphate	$C_3A \cdot C\bar{S} \cdot nH$	AFm

Section	Name	Abbreviation
Portland cement & Blends (Ch.4-7)	White Portland cement	wPc
	Grey Portland cement	gPc
	Ground granulated blast furnace slag	GGBFS
	Fly ash	FA
	Silica fume	SF
Characterisation methods	Alternating current impedance spectroscopy	ACIS
	Isothermal calorimetry	IC
	Scanning electron microscopy	SEM
	Finite element model	FEM
Model and simulation (Ch.8)	Conductivity	σ
	Permittivity	ε
	Degree of hydration	DoH

Chapter 1:

INTRODUCTION

1.1 Background
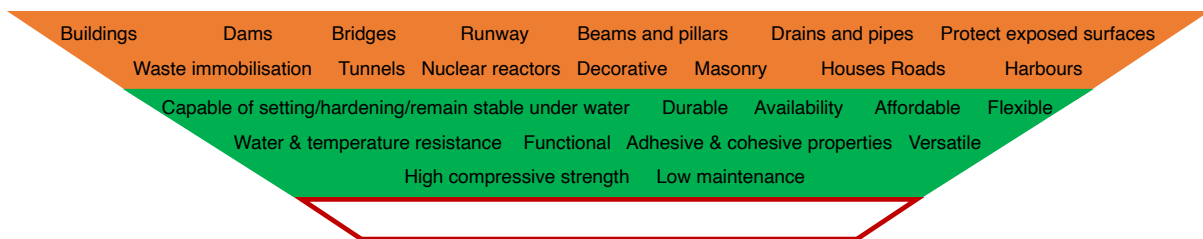
Fig. 1-1. Portland cement applications and properties.

All the applications and properties shown in Fig. 1-1 have something in common, Portland cement; not only the second most used material in the world, but also one of the most complex. Portland cement is a multi-phase material mainly composed of calcium silicates, aluminates and other minor constituents. Despite the widespread use of Portland cement as a construction material and the advances in cement research, the hydration process and microstructural development of cement are not well understood. Furthermore, the desire to improve the mechanical properties of Portland cement and reduce the carbon emissions from its industrial production has led practitioners to partially replace Portland cement with different supplementary cementitious materials (SCMs) and other mineral admixtures (e.g. metakaolin, rice husk ash and natural pozzolans), which yields a more complex cementitious system [1]–[5].

1

Immediately after Portland cement is mixed with water, a series of simultaneous and consecutive reactions take place, leading to different physical and chemical changes [6]–[10]:

- Dissolution of constituents
- Aqueous solution formation
- Release of heat
- Hydrated product formation
- Water consumption
- Setting and hardening of the cement paste
- Densification of the hardened microstructure

The final physical and mechanical properties of the resulting hardened cement paste are determined by the hydration process, curing conditions, chemical composition and fineness of cement constituents, mineral admixtures, and any contamination present.

1.1.1 Cement characterisation techniques

Understanding the hydration process at early ages and the influence of different parameters on the early and final properties, the kinetics and mechanism(s) of hydration, and microstructural development of cements and blends, has long been a subject of interest for cement researchers and the industry [11]–[16]. This has been done with the objective of improving the durability, properties, performance and cost-effectiveness of cement, whilst reducing the environmental impact of the industry and contributing to the development of new cementitious materials [3], [12], [17]–[19].

Over the years, numerous techniques and interpretation methods have been proposed and designed to assess cement properties. Some of these include:

- Isothermal calorimetry: measures the heat release during cement hydration [20].

- Vicat needle test: determines the initial and final setting times (EN 196-3, [21]).
- Electron microscopy techniques: assessment of microstructural features [22].
- Mathematical models and simulations: study cement properties [23].
- X-ray diffraction techniques: assessment of cement chemical composition.
- Mercury intrusion porosimetry: assessment of porosity features in the microstructure [7]–[9].
- Ion chromatography and inductively coupled plasma optical emission spectroscopy (ICP-OES): assessment of the pore solution [7]–[9].
- Nuclear magnetic resonance spectroscopy: assessment of chemical composition, microstructure and state of water [7]–[9].
- Among other techniques (see Fig. 2-9)

Although a lot has been learned about Portland cement properties from these techniques, there is still a knowledge gap about cement complexity, attributed to the difficulty of time-resolved analysis as it requires a technique which is suitable to analyse different states of Portland cement paste (i.e. liquid and hardened). Therefore, the number of characterisation techniques that can analyse the material in both states is limited.

Another technique that has been used in cement research is alternating current impedance spectroscopy (ACIS). This technique is able to acquire and identify changes in the chemical, electrical and microstructural features of a system by evaluating the electrical response as a function of frequency, including during the process of setting and hardening. ACIS has demonstrated to be an effective and powerful technique, and has been used in studies in the cement research field due to the possibility to obtain electrical, chemical, and microstructural information for different materials [24]–[30]. Although ACIS is a powerful and sensitive technique, it has not been fully accepted by the cement research community due to certain limitations such as current dispersion, electrode and parasitic effects and complex data interpretation because of the high conductivity of Portland cement paste at early hydration stages [31]–[36].

1.2 Aim of the project

The main aim of this research project is to assess and demonstrate the true value of alternating current impedance spectroscopy (ACIS), in parallel with other supporting techniques, to determine its capabilities as a characterisation tool to assess the early hydration process of Portland cements. To achieve this aim, the research project was structured into four sections:

1) Systematic assessment and design of a customised electrochemical cell design to perform impedance measurements on Portland cement paste at early hydration stages (Ch. 4).
2) Assessment of the electrical response of Portland cement during early hydration at different admixture replacement levels and water to cement ratios (Ch. 5-6).
3) Assessment of the microstructural development of Portland cement by ACIS (Ch. 7).
4) To model and simulate cement microstructure and the impedance response at different hydration stages (Ch. 8).

1.3 Thesis outline

The chapters in this thesis are an adaptation of five unpublished articles (currently in process of submission). Although these articles may be considered as separate scientific contributions, they are related to each other [37]–[40].

The thesis is divided into nine chapters, as shown in Fig. 1-2. Chapter 3 consists of a combination of the "materials and methods" components of each unpublished article section. Chapters 4-8 each contain a brief introduction, results and discussion, and a conclusion section. Chapter 9 (conclusions) consists of an overall reflection and recommendations for further research based on this project.

Chapter 1
Introduction

•Portland cement
•Cement classification
•Hydration & microstructural development
•Characterisation techniques

Chapter 2
Literature review

•Sample preparation
•Experimental methodology
•Techniques:
  - ACIS   - IC
  - Vicat test   - SEM
  - FEM

Chapter 3
Material & methods

Section I

Evaluating parameters that could produce parasitic effects in the ACIS measurements and providing guidance for appropriate experimental protocols.

Chapter 4
Electrochemical cell design

Section II

Assessing the parameters that influence ACIS measurements of cement and blends, at early hydration ages, based on the electrochemical, thermochemical, setting behaviour, and pore solution development.

Chapter 5-6
Portland cement
Portland cement and blends

Section III

Evaluating the microstructural development of cement and blends at early hydration ages by assessing the electrochemical response and other properties.

Chapter 7
Microstructural assessment

Section IV

Highlighting the use of FEM, by using an impedance FEM package (previously used to analyse dielectric materials for microstructural effects) and integrating basic cement microstructural and intrinsic properties to model and simulate the impedance response of cement microstructure at different hydration stages.

Chapter 8
Modelling and simulation

Overall project reflection and future research.

Chapter 9
Conclusion

*ACIS: Alternating current impedance spectroscopy; IC: Isothermal calorimetry; SEM: Scanning electron microscopy; FEM: Finite element model.

Fig. 1-2. Thesis outline.

5

Chapter 2:

LITERATURE REVIEW

2.1 Portland cement

Portland cement is defined as "*A hydraulic cement capable of setting, hardening and remaining stable under water. It consists essentially of hydraulic calcium silicates usually containing small amounts of calcium sulphate* [41]".

Portland cement is produced by crushing, grinding and blending of raw materials that can provide a source of calcium (e.g. limestone, chalk and sea-sells) and silica (e.g. clays, shales and sand), followed by heat treatment at about 1420-1450°C.

The clinker obtained through this process is then ground together with a small amount (≈ 4-5%) of a calcium sulphate source, which helps to control the reaction of aluminate upon final mixing of the cement with water. This prevents undesirable effects that could affect the hydrated product formation, setting of Portland cement, and mechanical properties of the hydrated cement.

The oxide composition of Portland cement is made up of CaO (67%), SiO_2 (22%), Al_2O_3 (5%), Fe_2O_3 (3%) and other minor components such as MgO (3%), sulphates and alkalies (i.e. Na_2O and K_2O). Cement chemists often abbreviate these oxides into a set of notation that is specific to describing cement chemistry: CaO is represented as C, SiO_2 as S, Al_2O_3 as A, FeO_3 as F (list in the Nomenclature section).

The major clinker phases present in Portland cement are C_3S (alite), $\beta\text{-}C_2S$ (belite), C_3A (aluminate), and C_4AF (ferrite). These phases present different polymorphs and may contain significant amounts of guest or substituent oxides in their crystal structure depending on the clinker composition and manufacturing process, e.g. MgO, Al_2O_3, Fe_2O_3, K_2O, Na_2O, TiO_2. The overall chemical composition and physical properties of Portland cement are shown in Table 2-1.

C_3S is the main constituent and reactive phase, and the most important in Portland cement, due to its essential contribution to the early and long-term strength development. The presence of C_3S in high quantities defines a material as a true Portland cement.

C_2S reactivity is slower than C_3S and mainly contributes to the long-term strength development. The differences between the reactivity of these two phases is attributed to the variances in their crystal structural arrangement. C_3S presents a crystal structure more defective than C_2S (i.e. O^{2-} ions are concentrated in one side of each Ca^{2+} ion, leading to unfilled sites), and contains a more ionic oxide site, which makes C_3S more prone to reaction [6]–[9], [42], [43].

C_3A reacts with water faster than other clinker phases, leading to the formation of hydrated products and rapid release of heat. This is regulated by the inclusion of calcium sulphate. Inadequate addition of calcium sulphate can affect the C_3A reaction, leading to a potential quick/flash setting of the cement [6], [7], [44].

C_4AF reaction with water is variable but slower than C_3A due to differences in its composition which range from CF to C_6AF. However, $C_2(A,F)$ or C_4AF are more common in Portland cements [9], [44].

Table 2-1. Chemical composition and physical properties of Portland cement. Information compiled from [6]–[9], [42].

Chemical composition					
Compound	C= CaO	S= SIO$_2$	A= Al$_2$O$_3$	F= Fe$_2$O$_3$	Others
Content (%)	~ 67	~ 22	~ 5	~ 3	~ 3
Major clinker phases					
Compound	**Content (%)**	**Contribution to**		**Degree of reactivity**	
		Strength development	**Heat of hydration**		
C$_3$S	50-70	High*	Moderate	Rapid	
β-C$_2$S	15-30	Low (*) High (**)	Low	Slow	
C$_3$A	5-10	High*	High	Rapid	
C$_4$AF	5-15	Very low	Moderate	Slow and moderate	
Physical properties of ordinary Portland cement (ASTM C150, [41])					
Fineness (m^2/kg) Air permeability test	≥ 260		**Soundness (mm)**	≤ 10	
Setting time (minutes)			**Compressive strength (MPa)**		
Initial Final	≥ 45 ≤ 375		3 days 7 days 28 days	≥ 12 ≥ 19 ≥ 28	

* Early ages, ** Later ages.

2.2 Cement classification

The types of cements more commonly used in construction are classified by different standard specifications (i.e. main constituents, performance and properties).

According to ASTM International (C150/C150M, [45]), Portland cement is classified into eight types. Conversely, the European Standard (BS EN 197-1, [46]) classifies twenty-seven subcategories arranged into five main cement types: CEM I (Portland

cement with up to 5% of minor additional constituents), CEM II (Portland cement and up to 35% of certain supplementary cementitious materials), CEM III (Portland cement and higher proportions of blast furnace slag), CEM IV (Portland cement and higher proportions pozzolana), and CEM V (Portland cement and combinations of pozzolana or fly ash and blast furnace slag).

The selection of a cement for a particular application (e.g. nuclear waste immobilisation, or as a building material) requires a correct evaluation based on its specifications; performance; environment exposure; and certain mechanical, physical, chemical requirements [9].

Fig. 2-1 shows the general composition and characteristics of the main five cement types, according BS EN 197-1, with an approximate percentage composition of their components [47].
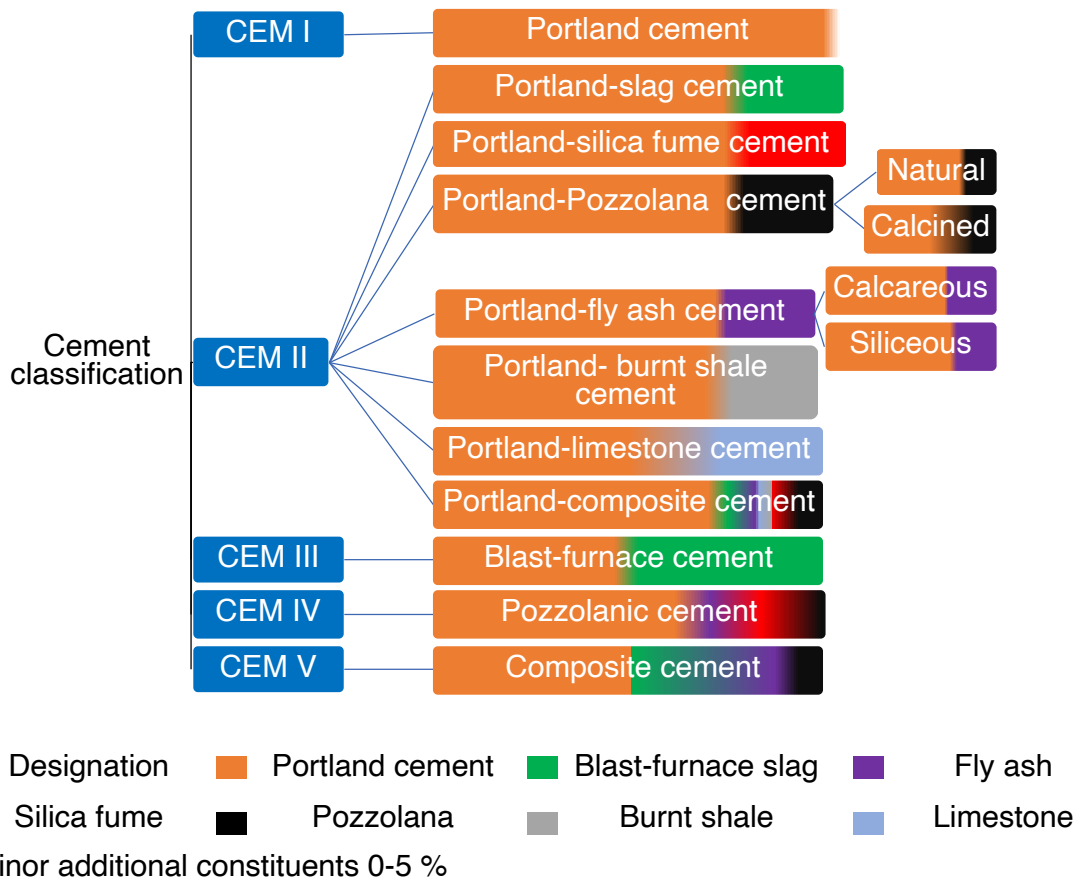
Fig. 2-1. Portland cement classification. Information compiled from [47].

2.2.1 Supplementary cementitious materials

The desire to improve the mechanical and durability properties of cement, and to reduce the environmental impact generated by its industrial production (around 8% of the global CO_2 emission), has led practitioners to push forward new pro-environment policies and partially replace Portland cement with different supplementary cementitious materials (SCMs) which yield more complex cementitious systems. For example, Portland cement may be blended with ground granulated blast furnace slag (GGBFS), fly ash (FA), and silica fume (SF), and other mineral admixtures (e.g. metakaolin, rice husk ash and natural pozzolans).

SCMs are classified as inert (materials that do not react with water); latent hydraulic (materials that react directly with water to produce C-S-H in an alkaline environment); and pozzolanic (materials that react with lime or CH product to produce additional C-S-H and other products). SCMs characteristics are shown in Table 2-2.

The addition of these admixtures influences the kinetics and mechanism(s) of hydration, microstructural development, and final physical properties of Portland cement [1]–[5], [48].

Previous investigations have demonstrated that partial replacement of Portland cement by SCMs can reduce the environmental impact of cement production, life-cycle cost; and improve the long-term performance of cement. However, further research is required to understand the effect of SCMs on the hydration process and properties of cementitious materials [11]–[15], [19], [49], [50].

Table 2-2. SCMs characteristics. Information compiled from [7], [9], [17], [51]–[54].

SCMs*		Derived from	Major chemical components (approx. %)				Type of reaction
			SIO_2	Al_2O_3	Fe_2O_3	CaO	
GGBFS (Ground-granulated blast-furnace slag)		Ironmaking by-product	**28- 38**	**8-24**	~ 0	30-50	Latent hydraulic & Pozzolanic
FA[1] (Fly ash)	W	coal-fired furnaces by-product	**35-42**	18-26	6-8	**18-20**	
	V		**49-67**	**16-29**	4-10	1-4	Pozzolanic
SF (Silica fume)		silicon alloys production by-product	**92-95**	0.6-0.9	0.6-0.9	0.30-0.39	
NP[2] (Natural pozzolans)	P	Volcanic or sedimentary	**70-71**	**12-13**	1-2	0.8- 1	
	VA		**43-72**	**9-20**	1-12	1-15	
MK (Metakaolin)		thermal treatment of kaolin	51-53	**42-44**	< 2	< 0.2	

FA[1]: calcareous (W) and siliceous (V); NP[2]: pumice (P) and volcanic ashes (VA).

2.3 Hydration and microstructural development of Portland cement

For over 100 years, there has been growing interest in the industry and academia to understand the complexity of the hydration process, microstructural development and properties of Portland cement; and the influence on these of different parameters, e.g. physicochemical properties, addition of admixtures/aggregates, and mixing and curing conditions [1], [11]–[16], [55].

Immediately after cement powder is mixed with water, different simultaneous and consecutive chemical reactions are triggered, leading to the dissolution of the clinker

phases [7], [44]; formation of a pore solution (containing different ionic species, e.g. K^+, Na^+, Ca^{2+}, SO_4^{2-} and OH^-) [56]; nucleation, precipitation and crystallisation of different hydration products (i.e. C-S-H, CH, AFt and AFm); release of heat; consumption of water; and the setting and hardening of Portland cement paste [57].

The hydration of Portland cement can be described by exploring its mechanisms, kinetics and heat of hydration; changes in the pore solution; and microstructural development.

2.3.1 Mechanism(s) and kinetics of Portland cement hydration

For many decades, numerous researchers have contributed to the knowledge of cement with several investigations, theoretical models and simulations. Nevertheless, the hydration process of Portland cement and its individual phases are still not completely understood. However, a deeper understanding of the mechanisms and kinetics of cement hydration processes at early age is required to improve the intrinsic properties of cement, reduce the environmental impact of its manufacturing, and develop new sustainable cementitious materials [1], [4], [58], [59].

Researchers have considered the hydration process to be characterised by a through-solution hydration process consisting of the dissolution of the clinker phases into their ionic constituents and the formation of hydrate products (dominant at early hydration stages); and a solid-state process taking place at the surface of the clinker phases (dominant at later hydration stages) [6]–[9]. However, up to now, the solid-state process is very difficult to analyse from a crystallographic or microstructural perspective due to restricted ion mobility in the solution and the participation of different factors [60]–[62].

The kinetics and mechanisms of hydration are related to the progress of the reaction and the changes in the cement with time [7], [44], including:
- Reaction rate of cement constituents ($C_3A > C_3S > C_4AF > C_2S$)

- Degree of hydration (Fig. 2-2)

- Hydrate product formation

- Pore solution (dissolution rate and ionic concentration)

- Heat release
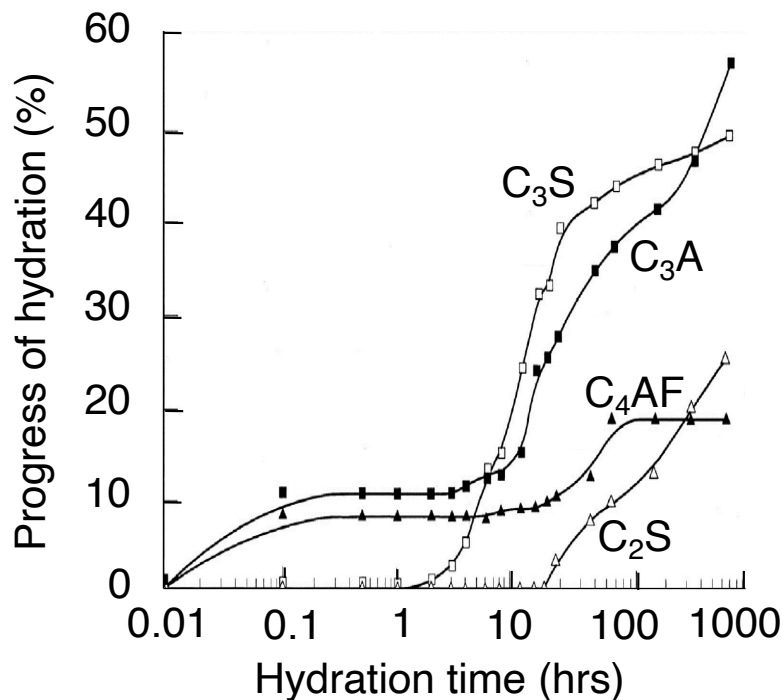
Fig. 2-2. Clinker phases consumption of ordinary Portland cement paste. Adapted from [7].

As mentioned before, C_3A is the most reactive clinker phase; however, its reaction is influenced by the $CaSO_4$ content in the cement system. In the absence of $CaSO_4$, the hydration of C_3A may potentially produce quick/flash setting of cement leading to the formation of C_4AH_{19} and C_2AH_8 as initial hydrate products, which may then transformed to a more stable hydrated phase, i.e. C_3AH_6. In the presence of $CaSO_4$, the rate of hydration of C_3A is decreased, avoiding undesirable setting behaviour of cement and leading mainly to the formation of AFt (i.e. $C_3A \cdot 3C\bar{S} \cdot 32H$) and other minor hydrated products (i.e. $C_4A\bar{S}H_{12}$ or C_4AH_{19}) [9], [44].

The hydration of C_4AF leads to the formation of hydrated products (i.e. $C_6(A,F)\bar{S}_3H_{32}$ and $C_4(A,F)\bar{S}H_{18}$) with a similar structure to that of the AFt and AFm formed by C_3A reaction but with a different chemical composition also including some iron [63], [64]. The reactivity of C_4AF depends on the amount of alumina content in the cement and the formation temperature during the clinkering process; however, the rate of reaction is usually lower than that of C_3A [6], [7], [9].

The hydration of C_3S and β-C_2S leads to the formation of similarly structured CH and C-S-H hydrated products. The chemical composition of the hydrated C-S-H phases depends on the water to cement ratio, temperature and stage of hydration. The difficulty of isolating C-S-H phases from the CH also produced during C_3S and C_2S hydration has generated uncertainties about its precise structure due to the broad diffraction signal of C-S-H and its variable chemical composition (e.g. C/S ratios). However, studies have demonstrated that the structure of C-S-H is similar to the mineral tobermorite [65], [66].

The CH formed participates in different reactions that affect the durability of cement, e.g. leaching and chemical resistance, particularly buffering the high pH inside the cement pore fluid. At the same time, the morphology of CH is influenced by the available space required for hydrated product formation; heat evolution, rate of hydration, and the presence of foreign ions in the cement system [7].

The hydration of Portland cement is commonly divided into five stages: initial, dormant, acceleration, deceleration and long-term periods. A brief description of the behaviour of each clinker phase and the pore solution during the five hydration stages is shown in Table 2-3.

Table 2-3. Hydration stages of Portland cement. Compiled from [6], [44], [67].

I: initial period (<1 hrs)	
General	Consists of rapid dissolution of ionic species into the pore solution and the initial formation of hydrated products.
C_3S β-C_2S	Dissolution of phases and yielding of a C-S-H layer at the cement particle surface. The β-C_2S reaction is slower than C_3S.
C_3A	Dissolves and reacts with Ca^{2+} and SO_4^{2-}, produces AFt and other minor product layers at the cement particle surface. The reaction rate and formation of hydrated products is affected by the sulphate dissolution rate and $CaSO_4$ content in the cement.
C_4AF	Reactivity depends on its A/F ratio, generally similar and slower than C_3A reaction.
Pore solution	K^+, Na^+ and SO_4^{2-}, OH^-, SiO_4^{4-} and Ca^{2+} ions are released. The Al and Si ion concentrations are lower during all stages. The pore solution becomes saturated with respect to calcium hydroxide.
II: Dormant period (1-3 hrs)	
General	Overall hydration rate decreases, and the hydration of the clinker phases is slower. Calcium hydroxide concentration in the pore solution reaches its highest level and begins to decrease. CH hydrate products precipitate at the end of the period.
C_3S	Dissolution rate and its contribution to the overall heat release rate decreases.
C_3A	The reaction rate decreases at this stage. Numerous theories have been proposed about this process: the formation of AFt around C_3A surface; adsorption of SO_4^{2-} at the C_3A surface, decrease of active dissolution sites due to Ca^{2+} ion intake by Al-rich layer; formation of an osmotic membrane at the C_3A surface.
Pore solution	The concentration of calcium hydroxide in the pore solution decreases and the SO_4^{2-} concentration remains constant. SO_4^{2-} and Ca^{2+} concentrations are limited by the presence of $CaSO_4$.

III: Acceleration period (3-12 hrs)	
General	The hydration rate and the release of heat increase again due to the nucleation and formation of large amounts of hydrated products, particularly C-S-H.
C_3S	The hydration rate accelerates rapidly, reaching a maximum rate of hydration between 5-10 hrs.
C_3A	Faster hydration continues, due to $CaSO_4$ consumption.
Pore solution	Ca^{2+} and SO_4^{2-} concentrations decrease with time, whereas OH^- concentration increases.
IV: Deceleration period (12-24 hrs)	
General	Hydration rate decreases at a gradual rate and becomes diffusion controlled. C-S-H formation and CH content decrease. Transformation of AFt to AFm takes place.
C_3S	The hydration rate decreases steadily.
β-C_2S	The relative contribution of β-C_2S to C-S-H formation increases with time.
C_3A	Phases react with AFt to form AFm.
C_4AF	
Pore solution	After calcium sulphate depletion, the concentration of SO_4^{2-} decreases and aluminate and silicate ion concentrations slightly increase.
V: Long-term period (>1 day)	
General	C-S-H formation continues, and hardening and refinement of the microstructure take place. During this process the long-term properties of cement are developed, such as strength, durability and permeability. A significant fraction of C_3S and C_3A are hydrated.
Pore solution	K^+ and Na^+ concentrations undergo minimal changes and SO_4^{2} concentration is lower.

2.3.2 Heat of hydration

During the hydration of Portland cement, heat is liberated by different reactions. A better comprehension of the reactivity of cement constituents, and the influence of different parameters, e.g. impurities, admixture addition, and mixing conditions, is possible through the evaluation of the heat of hydration. The heat released depends on the content, composition, and fineness of cement, water to cement ratio, and the curing temperature.

Fig. 2-3 shows the heat of hydration curve of white Portland cement. Hydration stages and exothermic maximum peaks are highlighted.

During the initial period, a rapid and intense liberation of heat is generated after the initial hydration of C_3S and C_3A (I, Fig. 2-3). During the dormant period, the heat release rate decreases (II, Fig. 2-3).

During the acceleration period, the heat of hydration increases due to the hydration of C_3S and the formation of C-S-H and CH, reaching a second peak at the end of this period (about 6-10 hours) (III, Fig. 2-3).

This process is followed by a gradual decrease of the heat liberated during the deceleration period. Small third and fourth peaks (IV, respectively, in Fig. 2-3) may be observed and are possibly due to the renewed AFt formation and AFt to AFm transformation depending on the type of cement.

Finally, the heat of hydration reaches an equilibrium state during the long-term period, V, Fig. 2-3 [6], [7], [10].
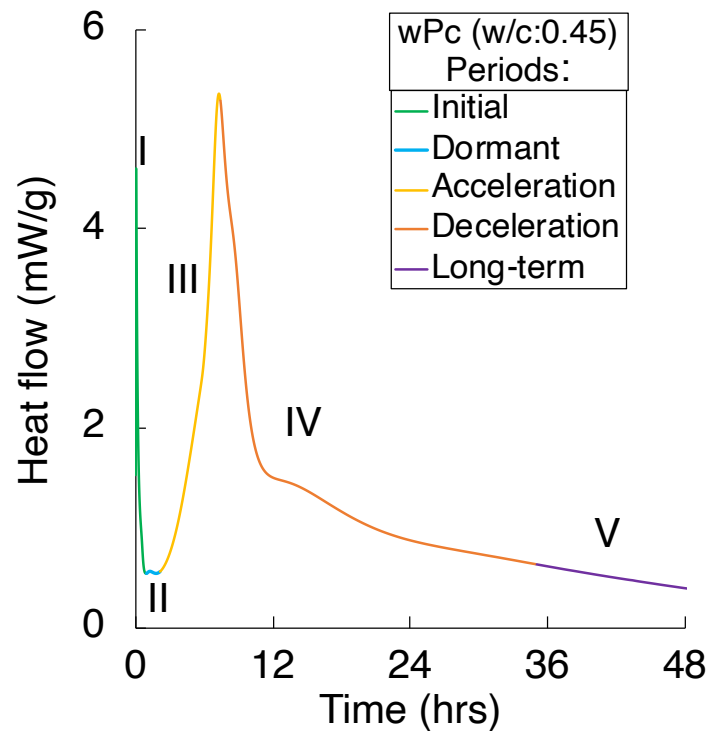
Fig. 2-3. Heat of hydration curve of white Portland cement: I) initial hydration II) C_3S reaction, and C-S-H and CH formation, III) AFt formation, and IV) AFt to AFm transformation.

2.3.3 Pore solution

The pore solution composition (e.g. Ca^{2+}, K^+, Na^+, SO_4^{2-}, and OH^-) reflects the liquid phase of cement paste and determines the formation of hydrated products by precipitation reactions. The ionic concentrations of these species vary over time (Fig. 2-4). The assessment of the pore solution supports the understanding of the kinetics and mechanisms of hydration, hydrated product formation, electrical response, and the interactions between solid and liquid phases of cement paste [68]–[71].

There exist different methods and techniques to extract the liquid phase from cement, e.g. filtration, centrifugation and high pressure extraction, whose application depends on the hydration stage and water to cement ratio of the cement paste.

However, a complete qualitative analysis of the pore solution over time is difficult to obtain due to the convoluted reaction mechanisms, certain instrument limitations, and the difficulty to extract the liquid phase when the cement paste has hardened and gained considerable strength [72]–[74].
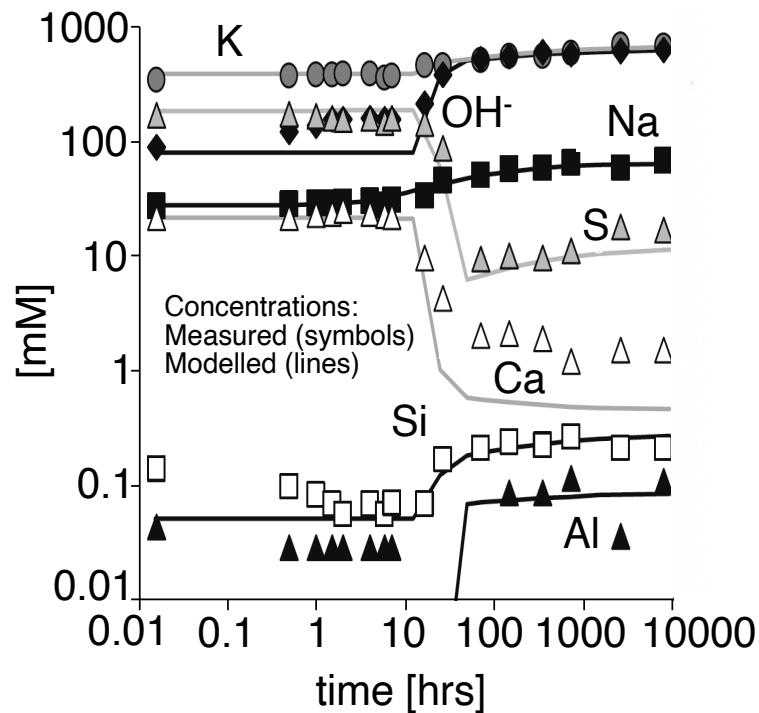
Fig. 2-4. Pore solution development during the hydration of ordinary Portland cement hydration. Adapted from [75].

Immediately after cement is mixed with water, a high concentration of ionic species is released into the pore solution, producing a series of changes in its composition and degree of oversaturation as a result of the dissolution of cement constituents (6 to 24 hrs). This leads to the precipitation of hydrated products whose formation also depends on other factors, e.g. clinker composition, temperature and surface defects.

19

At longer hydration ages (>1 day), the concentrations of K^+, Na^+ and OH^- increase and Ca^+ decreases, reaching their ultimate value after 28-90 days [56], [68], [75]–[77]. Further details of the ionic species in the pore solution are shown in Table 2-4.

Table 2-4. Pore solution composition: early and middle hydration stages (I-IV). Information compiled from [7], [56], [75].

Ion	Hydration stage		Concentration dependence
	Early (I-II)	**Middle (III-IV)**	
K^+/ Na^+	Ions released into the pore solution in the form of sulphate as a result of the high solubility of alkali sulphates and then $CaSO_4$.	Additional ions from the clinker phases enter the pore solution.	Alkali sulphate content and water to cement ratio.
SO_4^{2-}		The concentration changes slightly and slowly. After the formation of AFt and SO_4^{2-} adsorption by C-S-H, the concentration decreases.	Water-soluble sulphates, water to cement ratio, and source of $CaSO_4$.
Ca^{2+}	The dissolution of free lime, C_3S and C_2S disperses the ions into the pore solution. The pore solution is saturated with respect to $Ca(OH)_2$.	The concentration declines due to CH precipitation and AFt formation.	pH, alkali and OH^- content. e.g. $Ca^{2+}\downarrow$ with $K^+/Na^+\uparrow$ $Ca^{2+}\uparrow$ with pH/$OH^-\downarrow$
OH^-	Hydration of C_3S and dissolution of alkalis releases ions into the pore solution	Concentration rises.	Alkali content.
Si & Al	Concentrations are low during all the stages.		

* Higher pH values increase SO_4^{2-}, Si, Al and Fe concentrations.

2.3.4 Microstructural development

Over the past decades, understanding the microstructural development of cement has been of great importance to predict and improve the physical and mechanical properties of cement. However, up to now, the formation, distribution and interactions between the microstructural components (e.g. hydrated products, pore structure, unreacted cement particles, and remaining water) are not completely understood as a result of the complexity of cement hydration [78], [79].

Cement paste, where the properties depend on the physical and chemical properties of cement and the water to cement ratio, is formed after Portland cement is mixed with water. As the hydration process continues, the cement paste goes through different changes and stages (dissolution of clinker grains, nucleation of hydrates, and growth of bulk solid phases) that lead to paste setting, i.e. conversion of the cement paste from a plastic state to a solid state.

2.3.4.1 Setting of Portland cement

The time required for the stiffening of cement paste (loss of consistency) is known as setting time. It is divided into the initial setting (the elapsed time paste takes to start losing its plasticity) and the final setting (the elapsed time paste takes to completely lose its plasticity and starts to gain a certain structural strength). The setting time varies depending on the cement type and the specification standard used [6], [7], [80]–[82]. Fig. 2-5 shows the setting times of white Portland cement determined by the Vicat needle penetration displacement test (according to EN 196-3 standard procedure).

At the end of the setting, the beginning of the hardening process starts (strength and hardness development). A partial fraction of cement reacts and the hydration of cement constituents continues, filling much of the water-filled pore space with hydrated products and connecting the solid phases of the system [7].
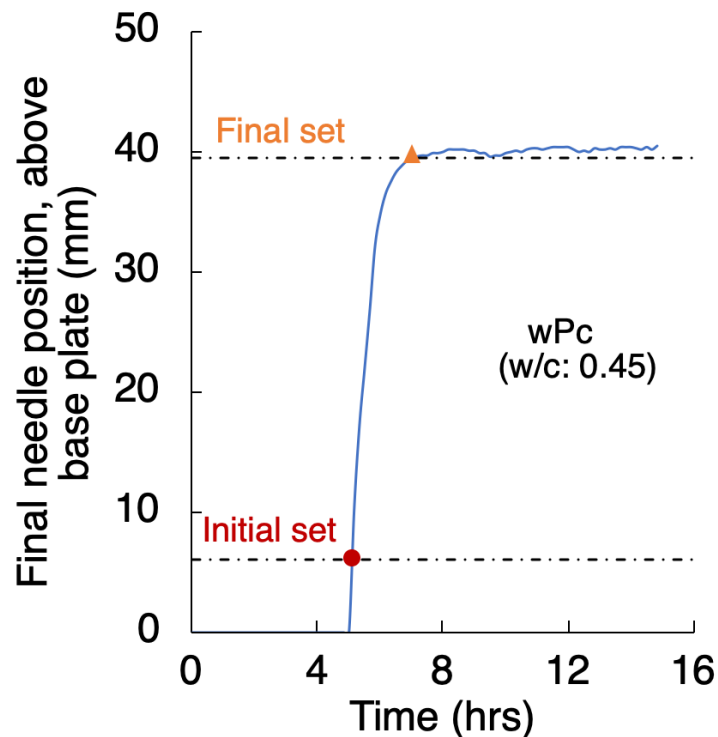
Fig. 2-5. Setting times of white Portland cement as defined by the Vicat test.

Generally, the setting of Portland cement is mainly attributed to C_3S and C_3A hydration and the related hydrated product formation (i.e. C-S-H and AFt). The volume of C_3S and C_3A hydrated products varies according the clinker composition and water to cement ratio affecting cement setting times.

To control the reaction of C_3A and setting of cement, a source of $CaSO_4$ is added to the clinker. The amount of $CaSO_4$ required depends on the content and fineness of C_3A in the cement clinker. The resulting $A/\bar{S}$ ratio will determine the aluminate and sulphate ion concentrations in the pore solution, the type of precipitation products formed (AFt or AFm), and the setting behaviour of cement (Fig. 2-6) [6], [7], [9], [44].
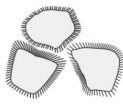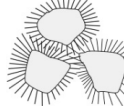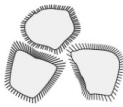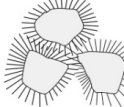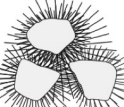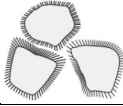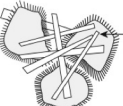
Reactivity of C$_3$A in clinker	Availability of sulphate in solution	Hydration time			
		<10 min	**10-45 min**	**1-2 h**	**2-4 h**
Low	Low	Workable	Workable	Less workable	Normal set
High	High	Workable	Less workable	Normal set	Ettringite in pores
High	Low	Workable	Quick set		
High	None/ Very low	False set	C$_4$AH$_{19}$ and C$_4$A $\overline{\text{S}}$ H$_{18}$ in pores		
Low	High	False set	Crystallisation of gypsum needles in pores		

Fig. 2-6. Aluminium/sulphate ratio effect on setting behaviour of Portland cement. Adapted from [6].

2.3.4.2 Hydrated cement phases

Hydrated phases are formed at different rates and amounts as cement reacts with water (Fig. 2-7). These hydrated phases have different characteristics, e.g. chemical composition, crystalline structure, morphology and volumetric properties. Therefore, the contribution of each hydrated phase to the physical and mechanical properties of cement paste varies [59], [79], [80].

The main hydration product of C$_3$S and C$_2$S is C-S-H, which is a term used to denote crystallographically disordered calcium silicate hydrate products. The C-S-H composition varies (e.g. C/S ratio) depending on the cement composition, water to cement ratio and curing temperature. Even though the structure of C-S-H is not fully

understood, C-S-H has an important role in determining the final mechanical and physical properties of Portland cement [83], [84].

Portlandite (CH), a by-product of C_3S and C_2S hydration, is the second most abundant hydrated product in the hydration of Portland cement. CH contributes to different reactions that affect the durability of Portland cement, e.g. chemical resistance, leaching and alkali-aggregate reactions [85].

Ettringite, a member of the AFt group (i.e. A: Al_2O_3, F: Fe_2O_3 and t: trisulphate), is formed during the hydration of Portland cement by the reaction of C_3A and C_4AF with $CaSO_4$ and OH^- ions. The AFt phase cannot be formed if there is an absence or a low amount of $CaSO_4$ available, leading to an undesirable setting behaviour of the cement paste (Fig. 2-6). The AFm (m: monosulphate) phase is formed by the dissolution of AFt phases after the sulphate content is exhausted, depending on the $A/\bar{S}$ ratio [6], [7], [42], [86]. More detailed information on the hydrated phases is provided in Table 2-5.
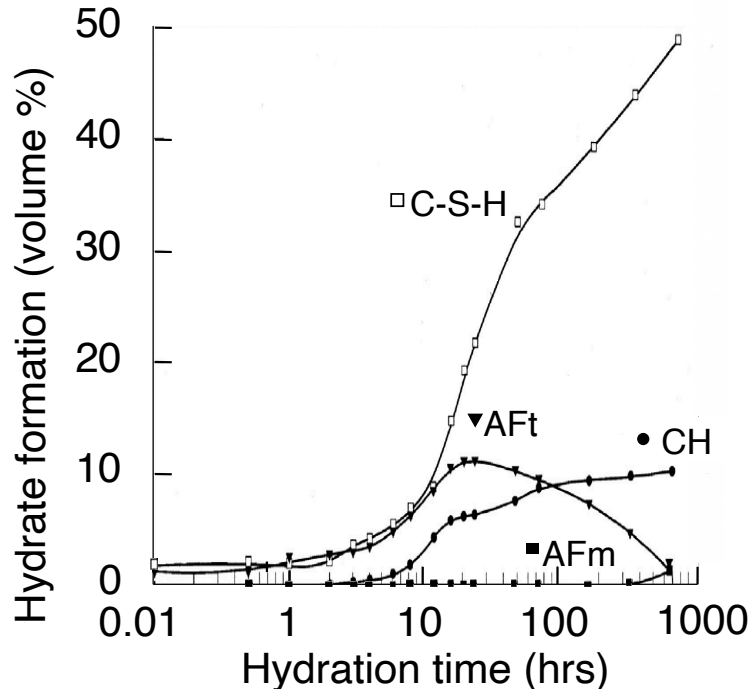
Fig. 2-7. Hydrate phase formation by hydration of ordinary Portland cement paste. Adapted from [7].

Table 2-5. Microstructural composition and characteristics of Portland cement hydration products. Information compiled from [6], [7], [42], [87]–[90].

Category	Hydrated products		
	C-S-H	**CH**	**AFt and AFm**
Volume (Hydrates)	50-60%	20-30%	15-20%
Structure	Amorphous/disordered or nearly amorphous. Varies from poorly crystalline fibres to reticular network.	Large crystals with a hexagonal structure (7-15 μm). Varies from non-descript to stack of large plates.	AFt: Needle-shaped. AFm: hexagonal-plate.
General	Formation mechanism and structure are not well understood.	Contribution to PC strength is limited due to small surface area.	The proportions of A and F vary, and depend on the clinker composition. AFm ↑ as AFt ↓.
Unhydrated Portland cement			
Unhydrated clinker grains can be found in the microstructure depending on the particle size distribution of anhydrous cement and the degree of hydration.			

2.3.4.3 Pore structure of Portland cement

Portland cement pore structure, developed during the hydration process, contains different types of pores (empty or water-filled spaces within cement microstructure) such as micro-, meso-, and macropores. These can be divided into three categories: gel pores, capillary pores and air voids (Table 2-6) [6], [7], [9].

The gel pores, located in the interlayer space of C-S-H, do not have a major influence on the strength development of Portland cement paste. However, this type

of pores has a strong influence on the drying shrinkage and creep behaviour of cement [87], [91]–[94].

The capillary pores are divided into three subcategories (small, medium and large pores). These types of pores have significant influence on Portland cement properties, e.g. strength, permeability and durability [6], [7], [89], [90].

Air voids usually have a spherical shape and are divided into two subcategories: (i) entrapped pores, formed during the mixing and curing of cement; and (ii) entrained pores, formed by the addition of admixtures or aggregates. These types of pores strongly influence the strength of Portland cement [6], [42], [87], [88]. Also, entrained air voids can be intentionally incorporated in cementitious mixtures to decrease the damage caused by freezing and thawing or to produce foaming for lightweight concretes [95], [96].

The water contained in the microstructure of hydrated Portland cement is classified in three categories: gel water, capillary water, and chemically combined water (bound to hydrated products), Table 2-6 [97]–[99].

Gel water is divided into two subcategories: (i) interlayer water, held between the layer of C-S-H and whose loss generates shrinkage in the C-S-H structure; and (ii) the absorbed water, absorbed on hydrated product surfaces and responsible for cement shrinkage [92].

Capillary water is divided into two subcategories: (i) free water whose removal does not affect the microstructure; and (ii) water under capillary tension whose removal contributes to shrinkage of the paste [87], [90].

Table 2-6. Microstructural composition: Pores and water. Information compiled from [6], [7], [42], [87]–[90].

Pore structure composition						
Level	Micro-	Meso-		Micro-pores		
Category	Gel pores	Capillary pores		Air voids		
Subcat.		Small	Medium	Large	Entrained	Entrapped
Size (µm)	≤ 0.004	0.004-0.01	0.01-0.05	0.05-10	50-200	>3000
Water						
Category	Gel water		Combined	Capillary water		
Subcat.	Interlayer	Absorbed		Under cap. tension		Free
Contained in	C-S-H layers	Hydrated products Surface		Pores (µm)		
				0.005-0.05		>0.05

2.3.5 Influencing factors

The properties of Portland cement are determined by its manufacturing process (burning temperature, heating and cooling rate, comminution); chemical composition (clinker composition, presence of impurities and foreign ions, and $CaSO_4$ source and content); and fineness.

On the other hand, the properties of hydrated Portland cement paste are determined by the hydration and microstructural development process. Both of these processes are determined by Portland cement properties, water to cement ratio, curing conditions, heat of hydration and the presence of admixtures in the cement paste (Fig. 2-8) [6], [19], [100]–[102].

The analysis of these parameters is essential to develop a better comprehension of the hydration and microstructural development processes; to predict and improve the properties and experimental data analysis; and to develop new approaches to assess cementitious materials.
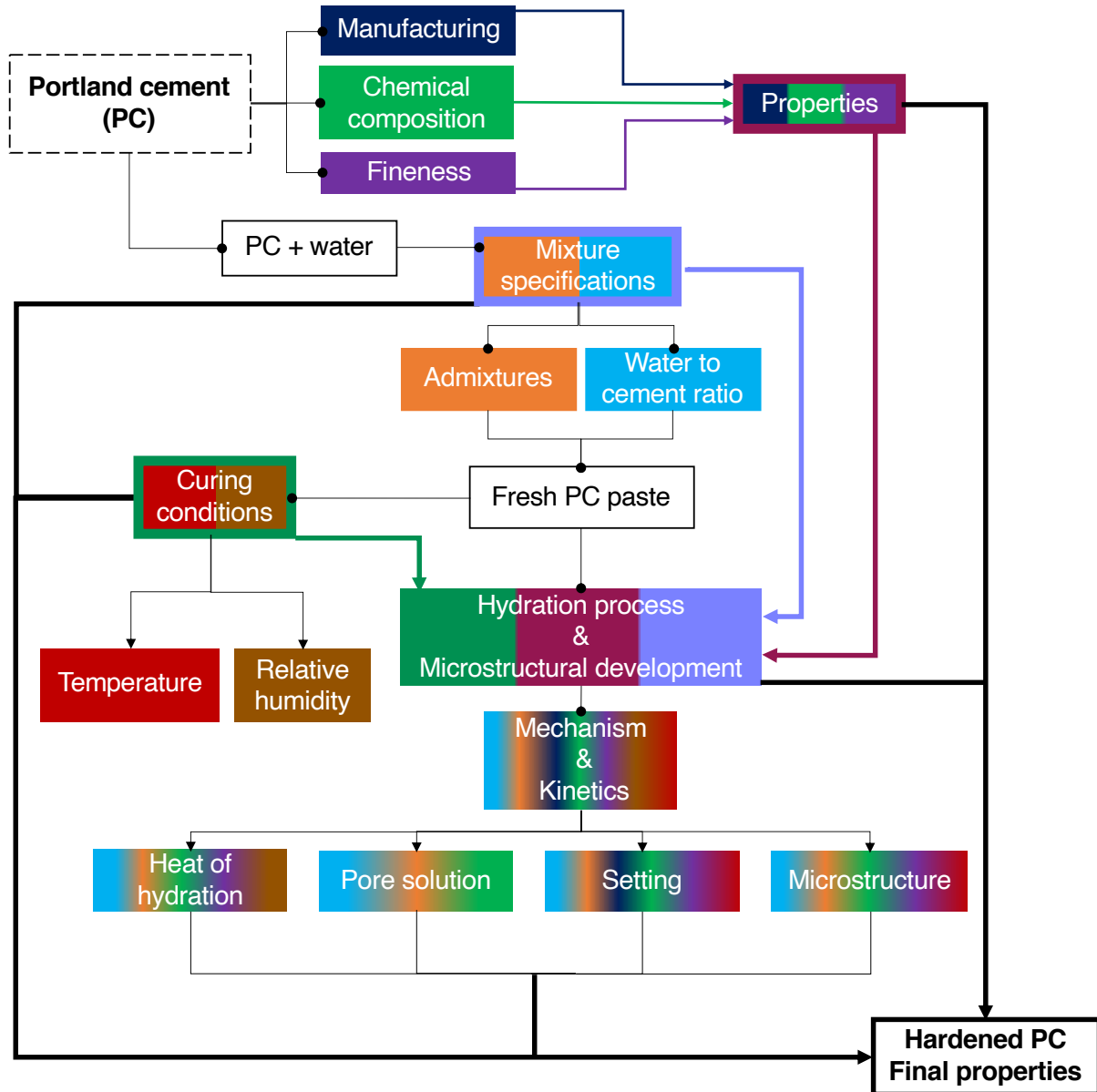
Fig. 2-8. Factors influencing the hydration process, microstructural development and final properties of Portland cement paste [7], [9], [59], [70], [103]–[106].

Numerous investigations have focused on evaluating and identifying the influential factors that may affect the hydration and properties of Portland cement. From these investigations it can be highlighted that the chemical composition and fineness; mixing and curing conditions; and presence of chemical admixtures are fundamental

parameters to evaluate the hydration process of Portland cement. These parameters may affect:

- The dissolution rate of cement phases and spacing between particles.
- The diffusion rate of water.
- Hydration process (e.g. degree of hydration, heat of hydration, reaction rate,).
- Pore solution (e.g. development, ionic strength, dissolution and content of alkali, Ca^{2+}, SO_4^{2-} and OH^-).
- Setting behaviour.
- Hydrated product formation (e.g. crystal structure, composition and content).
- Microstructural development (e.g. porosity, solid-space ratio, water content in pores, percolation degree).
- Properties (e.g. workability, pH, creep resistance, permeability, electrochemical, compressive strength and durability).

As an example, the fineness of Portland cement (i.e. particle size and surface area) may affect the workability, percolation degree, rate of hydration, heat of hydration and compressive strength development, i.e. workability decreases whilst the other parameters generally increase with a higher particle surface area [103], [107], [108].

The water-cement ratio determines the available free water to react with cement particles and their interparticle spacing [106]. Ideally, to complete the hydration of Portland cement, a minimum w/c ratio of about 0.42 is needed to ensure sufficient spacing between cement particles allowing all particles to come into contact with water (i.e. w/c ratio of 0.42 ensures the minimum amount of water to hydrate and fill the space between cement particles). However, complete hydration of Portland cement is possible at lower w/c ratios by using certain curing conditions (e.g. relative humidity, temperature and sealing) and/or water reducer agents. At low w/c ratios, the free water available to react with cement is limited, decreasing the degree of hydration, porosity, setting times and workability, and increasing the heat of hydration. Nevertheless, full hydration of cement particles is theoretically possible with a w/c ratio of 0.20-0.24

(based solely on the amount of water required to convert the clinker phases to hydrates, without consideration of wetting or flow characteristics), depending on the clinker composition and curing conditions [56], [100], [103], [109]–[111].

The curing temperature affects the degree of hydration, heat of hydration, bonding processes of some phases, and the final properties. High curing temperatures increase the permeation of free water through the hydration products and, at early and late hydration stages, decreases the final degree of hydration [7], [100].

Finally, the presence of admixtures in Portland cement may be designed to influence many binder characteristics including the flow, hydration rate, heat of hydration, setting times, hydrated product formation, porosity and final properties of Portland paste. The effects of these admixtures can differ depending on the physicochemical properties and quantity of the admixture used, w/c ratio, curing conditions, and physico-chemical properties of the cement clinker and admixture [2], [3], [12], [51], [112].

Despite advances in research, the effects of the partial replacement of Portland cement with SCMs on the hydration kinetics and mechanism(s), microstructural development and final properties need further investigation. The presence of admixtures in Portland cement leads to a more complex system to analyse, as a result of their individual reactions and interactions with cement constituents [1]–[5]. For instance, a decrease in the Ca/Si ratio of C-S-H, a total depletion of portlandite and a low pH have been observed when Portland cement is partially replaced by ≥24 weight percent of silica fume [12].

2.4   Characterisation techniques

Over the past decades, progress in science and technology has allowed researchers to develop and improve different characterisation techniques and methods. As a

result, cement science has made considerable progress in understanding the complexity of the cement hydration process and products [113].

These characterisation techniques and methods (Fig. 2-9) have diverse scopes and limitations according to their field of study and can be used for specific or multiple purposes of analysis. For example, X-ray diffraction is used for phase identification of crystalline structures and to follow the hydration kinetics of cement to identify, analyse and estimate different chemical reactions and processes.

The use of a single technique or data interpretation method is not enough to disclose a complete evaluation of a parameter. Different techniques and methods are needed as a benchmark to build a more complete picture of a certain parameter under different perspectives; and to evaluate, compare and support the performance, data analysis and interpretation derived from these techniques [6], [9], [44].
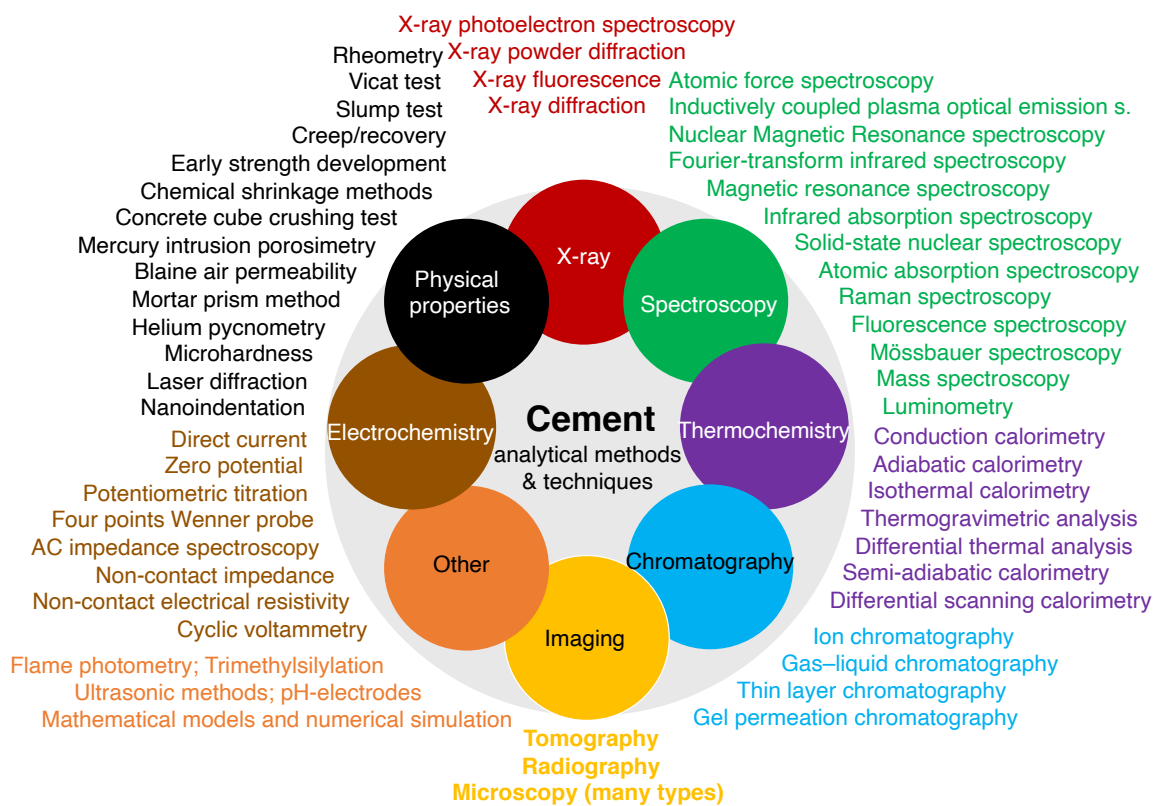
Fig. 2-9. Cement research characterisation techniques [6], [7], [9], [44].

Most of these techniques have crucial instrument specifications, and calibration and experimental procedures that help establish the compatibility and reproducibility of the measurements and subsequent data interpretation [44].

The use of these characterisation techniques and methods has significantly contributed to cement research , with the application of different experimental and data analysis approaches.

However, despite the advances in cement research and its numerous characterisation techniques, there are still gaps of knowledge and instrument and experimental limitations to assess cement hydration, Fig. 2-10.

In comparison to these limitations (Fig. 2-10), ACIS can provide constant analysis of the microstructural development of cement, from early age hydration stages, through the analysis of the electrical response, allowing researchers to understand, monitor and establish a relationship among different parameters such as:

- Microstructural (e.g. setting and hardening process, porosity and spatial local defects)
- Mixing conditions (e.g. curing conditions and water content)
- Pore solution: (e.g. ionic strength and ion mobility)
- Chemical composition (e.g. addition of admixtures and contaminations)
- Mechanical properties (e.g. durability)
- Hydrated product formation rate
- Hydration kinetics
- Influence of admixtures and contaminants
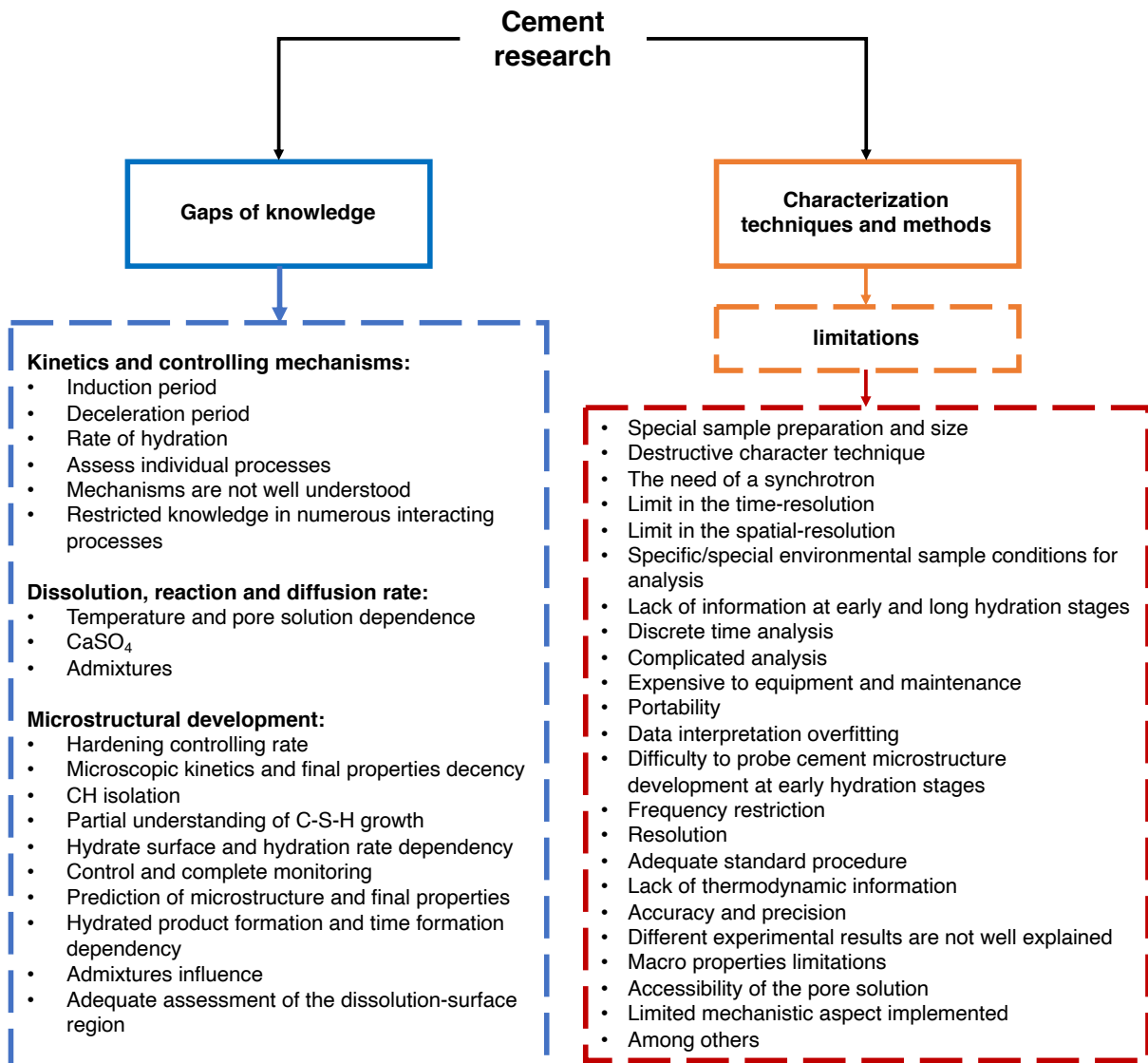
Fig. 2-10. Gaps of knowledge and technique and method limitations summary [6], [7], [9], [44].

In this research, alternating current impedance spectroscopy (ACIS) was used as a probe of cement hydration and microstructural development. Isothermal calorimetry (IC), Vicat testing, and scanning electron microscopy (SEM) were used to support ACIS data interpretation. In addition, the finite element method was used to generate a microstructural model of cement paste, at different hydration stages, to simulate and

compare the simulated impedance response against the experimental values obtained.

2.4.1 Alternating current impedance spectroscopy (ACIS)

Alternating current impedance spectroscopy (ACIS) is a widely used experimental technique; it is able to assess the electrochemical response of a system as a function of frequency by applying a sinusoidal voltage perturbation. The ACIS response is commonly studied as a function of time and/or temperature, and allows the analysis of different electrochemical and microstructural processes and their [114].

2.4.1.1 ACIS background

The foundations of ACIS date back to around the 19th century. Oliver Heaviside introduced circuit analysis terms (e.g. impedance, admittance, conductance and inductance) and developed complex problem operational methods that provided the basis for the Linear Systems Theory [115]. In 1894, Nernst and Finkelstein applied impedance spectroscopy to aqueous electrolytes, different organic fluids and oxides to determine the dielectric properties [116], [117]. Not long after that, in 1920, Warburg's work spread the theory of impedance applied to electrochemical systems [117]–[120]. The invention of the potentiostat (Archie Hickling, 1940) and different investigations also contributed to the ACIS field [114], [121], [122], including:

- A diffusion model for homogeneous chemical reactions by Levart & Schuhmann [123], [124].
- Non-uniform current and potential distribution in disc electrodes by Newman [125], [126].
- Frequency-dependent complex dielectric constant by brothers Cole & Cole [127].
- Equivalent circuit for kinetics applications by Dolin & Ershler, and Randles [128], [129].
- Transmission line models for porous and rough electrodes by Levie [130].

- Low-frequency inductive loops by Epelboin & Loric [131].
- Double-layer structure by Frumkin [132].

In the 1970s, Macdonald et al. and Boukamp applied nonlinear complex regression techniques to impedance measurements as an ACIS data interpretation method [133]–[135]. In the same period, the frequency response analyser was invented and a simplified concept of transfer function for ACIS was presented by Gabrielli et al. [136]–[138]. Since then, ACIS has been used in several research fields [139]–[141], including:

- Biology (e.g. micro-organism detection).
- Biomedical science (e.g. pathology, environmental pollution, food decomposition and toxicology).
- Solid/liquid-state electrochemistry (e.g. electroceramics and cementitious material microstructure, corrosion analysis of metals, batteries and photovoltaic system).
- ACIS introspective testing (e.g. data interpretation, electrochemical-cell design, and technique capabilities, limitations and measurement influencing factors).

In the 1920s, cement researchers started to apply electrical analysis on hydrating cement paste to determine setting time helped through resistivity and conductivity measurements [142]–[144]. Since this work, different investigations have been focused on the relationship between the properties of cement and its electrical response during hydration. The implementation of ACIS has emerged as a cement characterisation technique to assess cement properties [31], [145]–[147].

From the 20th century to the present day, researchers have used ACIS to continue the study of the relationship between the electrochemical response and the chemical and microstructural properties of cement [14], [101], [156], [148]–[155]. During this time ACIS has been used in different investigations to assess cement hydration, to acquire and identify changes in the chemical, electrical and microstructural features of a system by evaluating the electrical response of cement paste as a function of

frequency [24]–[30]. ACIS measurements are often represented as a Nyquist plot of the complex impedance, in which Z' and -Z'' represent the real and imaginary components, respectively.

The ACIS spectra for cementitious materials have been found to be composed of high and low frequency semicircle arcs, which are attributed to the cement bulk response and the cement-electrode response, respectively. At the same time, the cement bulk response arc at high frequency has been attributed to the aqueous solution (i.e. pore solution) and the solid phases and interfaces [114], [121], [122].

In order to assess the ACIS response of cementitious materials, it is necessary to consider the cement system as a circuit whereby the electrical response depends on the reactance and resistance behaviour, which can be represented by an equivalent circuit model.

2.4.1.2 ACIS data interpretation methods

ACIS measurements can be analysed using an equivalent circuit model (ECM, Fig. 2-11), based on a combination of resistors, capacitors and other components (e.g. Warburg elements) that are used to represent a sample material and the material-electrode interface, to simplify the analysis of a complex system. However, due to the existence of numerous ECMs that can be used to analyse data, an accurate relationship between the microstructural features and electrical components is difficult to obtain due to various factors: [27], [114], [121], [122], [157]–[160]

- An accurate ECM is difficult to obtain due to the microstructural inhomogeneity of cement paste, chemical composition, and mechanism and kinetics of cement hydration.
- Numerous equivalent circuit models can have identical impedance response and provide an outstanding fit with the impedance data. However, the

description and interpretation of these ECMs have different perspectives, parameters, and processes taken into account.

- The choice of the electrical components and its arrangement depends on the physical intuition of the author and the data (collected different conditions) used to support the selection of the ECM.
- The significance of the electrical components and its arrangement in large or complex ECMs is challenging to determine, potentially leading to misinterpretation of the system behaviour which affects the validity and accuracy of the ECM.
- Lack of mathematical rigour (e.g. empirical values and components).

Up to now, numerous researchers have proposed different ECMs for cements, using different electrical components and arrangements, to simplify the equivalent circuit and simulate an impedance response similar to that obtained by experiments [24], [102], [141].

Cement bulk response   Cement-Electrode response

R_0: solid + liquid phase resistance R_2: charge-transfer resistance
R_1: solid-liquid interface resistance C_2: cement-electrode interface
C_1: solid-liquid interface capacitance
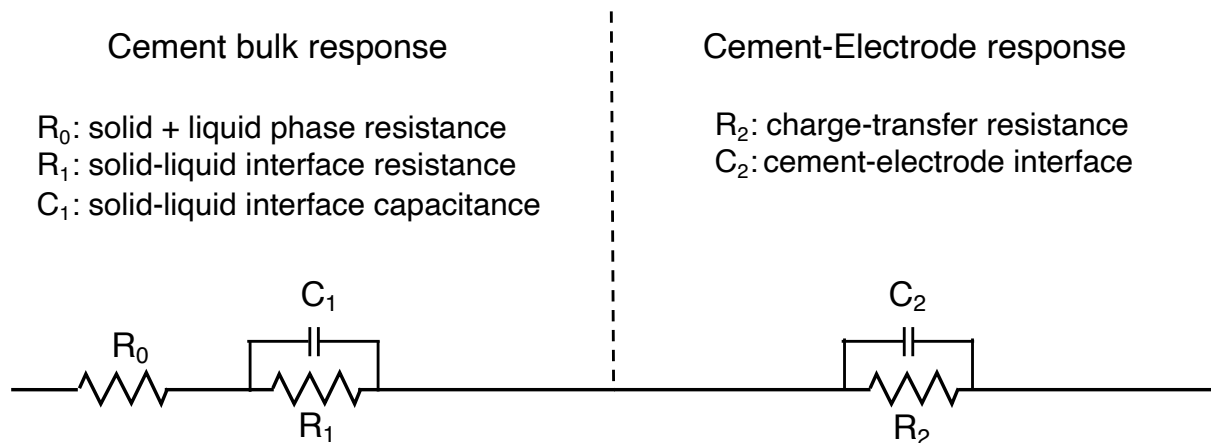
Fig. 2-11. Cement paste equivalent circuit model. Adapted from [160].

The correct implementation of ECMs is of great importance for the assessment of the ACIS data, allowing a broader number of ways to analyse and verify the data, and obtain electrical, microstructural and interfacial information of cementitious systems. In the last decades, several ECMs have been established to characterize cementitious materials by implementing different perspectives, relationships and parameters to generate these models and study cement properties, such as: [14], [27], [161]–[167]

- ACIS analysis based on:
    - The solid-solution phase and interphase relationships.
    - The microstructural properties (e.g. continuous matrix, pore properties, hydrated products, unreacted clinker, pore solution within pores, conductive and discontinuous paths, etc).
    - Conductive materials (e.g. electrical double layer, ionic species within the pores, pore size and connectivity, ion diffusion, solid-liquid resistance, mass transport properties etc).
    - Ion migration (e.g. pore solution capacitance and resistance, electrode properties, reaction kinetics, ion diffusion, ion mobility, percolation, pore properties, solid-liquid interface relationship, etc).
    - Simulation approaches.

- ACIS to assess:
    - Electrical properties.
    - Durability of cementitious materials.
    - The degree of hydration.
    - Microstructural development relationship.
    - Clinker chemical compositions, admixtures, contaminations and ternary systems.
    - Steel corrosion resistance.

Through these investigations, ACIS has been demonstrated to be a powerful, sensitive and promising technique. However, the use of a single of an ECM or approach, to analyse ACIS data and represent cement hydration microstructural development, is difficult to obtain and evaluate. This is attributed to the complex chemical composition and continuous microstructural and pore solution development of cementitious materials [31]–[36].

A method to present and analyse ACIS measurements consists of using a complex impedance, Z^*, plots ($Z^* = Z' - jZ''$ where Z' and Z'' are the real and imaginary components of impedance respectively, and j: $\sqrt{-1}$). The impedance measurements obtained are divided into the high-frequency region (i.e. material bulk response), the low-frequency region (i.e. material-electrode response), and the intersection point between the high and low-frequency responses represents the material resistivity, Fig. 2-12. [114], [121], [122].

Fig. 2-12 shows a schematic representation of a high frequency arc in the impedance response of cement paste systems (R_0: solid + liquid phase resistance; R_1: solid-liquid interface resistance; $R_0 + R_1$: Bulk resistance; interception point on the real axis of the Z^* plot: value in which the impedance response is purely resistive; and ω: applied angular frequency).
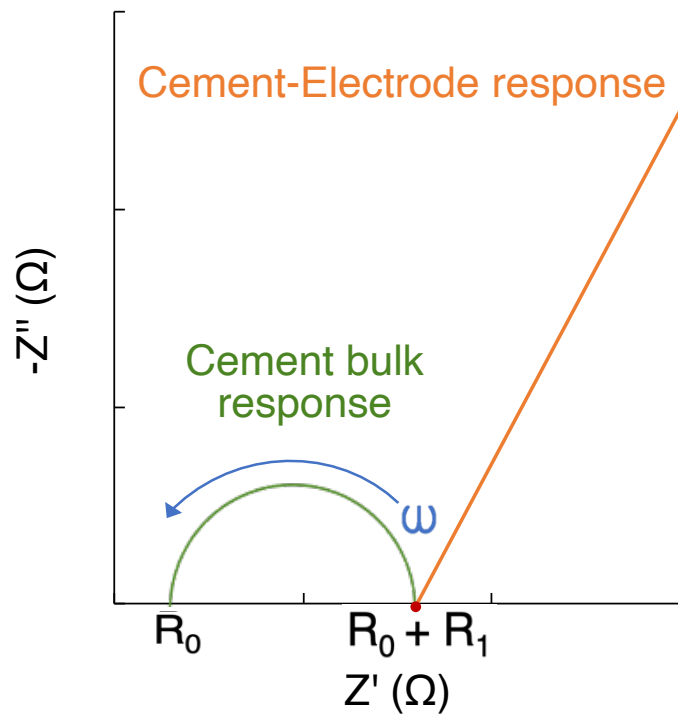
Fig. 2-12. Schematic complex impedance spectrum of cement paste. Adapted from [155], [159], [168].

ACIS analysis methods can provide a better understanding of several phenomena that take place during hydration and microstructural development of Portland cement. For example, insight can be gained into kinetics and mechanisms, ionic strength of the pore fluid and resistive property changes, and the influence of different parameters (e.g. fineness, chemical composition, water content, curing temperature and admixtures content) on electrical response [13], [114], [155], [169], [170]. However, since ACIS is a highly sensitive technique, its measurements can be affected by parasitic effects which are often overlooked leading to data misinterpretation, Fig. 2-13. For example, stray inductance and capacitance effects which arise from instrument components (e.g. connections, calibration, leads quality and positioning), electrochemical cell designs (i.e. geometry, electrode properties and their configuration), experimental procedures (i.e. amplitude of perturbation, frequency and current range), and the properties of the system under analysis.

As a result of these difficulties, ACIS experimentation for in-situ analysis of cements requires significant caution in experimentation. For example, a small cable in combination with a low impedance cell can exhibit stray inductance as the frequency increases. In addition, effects such as magnetic coupling, produced by the current flowing in leads, can produce a perturbation (false inductance) in the impedance measurements [27], [31], [34], [158], [159], [171].
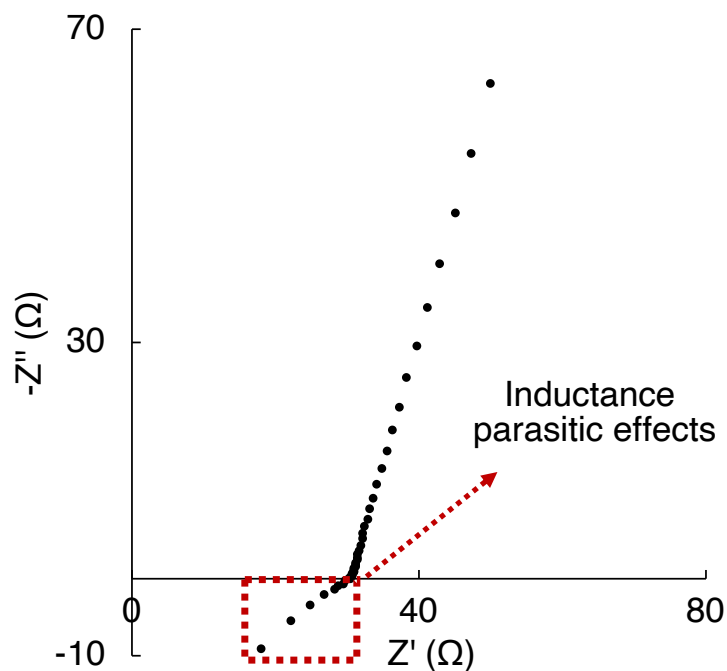
Fig. 2-13. Inductance effects in the ACIS spectrum of white Portland cement attributed to the highly conductive cement state, electrochemical cell design, and instrument drawbacks.

In the early hydration stages of Portland cement, ACIS measurements show certain limitations which have restricted the more widespread application of this technique to the study cement hydration, e.g. current dispersion, data interpretation, electrode and parasitic effects [31]–[34]. Therefore, recent work has focused on the development of strategies to minimise the interferences of parasitic effects in ACIS data at early ages,

and the improvement of ACIS studies to obtain meaningful data to understand cement properties [37], [158], [172]–[175].

Although ACIS has demonstrated to be a powerful technique used in cement research, it is not yet fully accepted by the research community due to the limitations mentioned above (Fig. 2-14) [31]–[34]. Because of this fact, supporting characterisation techniques are needed to complement the assessment and interpretation of ACIS data in the analysis of Portland cement paste hydration and microstructural development.

Disadvantages

Advantages

-Different data analysis methods
-Accuracy may be affected by instrument drawbacks and data interpretation.
-Complex data interpretation
-Mechanistic uncertainty in porous materials.
-Lack of mathematical rigour in data analysis.
-Each frequency response analyser has its own limitations
-Bulk response suffers from geometrical limitations.
-Difficulty to analyse highly conductive materials.

ACIS

- Sensitive, non-invasive & non-destructive method.
-Measurement rapid and easy to perform.
-Samples do not require special preparation.
-Experimentation can be carried out at normal room temperature and pressure conditions.
-Enables analysis at a wide frequency range.
-Analysis of reaction mechanism(s) and chemical and microstructural changes
-Different data analysis methods
-Capable to measure time constant over many order of magnitudes.

Fig. 2-14. Disadvantages and advantages of ACIS [31], [114], [121], [176]–[179].

2.4.2 Isothermal calorimetry (IC)

Since the hydration of Portland cement is an exothermic process (section 2.3.2), isothermal calorimetry (IC), a high precision and accurate technique capable of measuring the heat released from samples, can be used to determine the heat of hydration of cementitious system, study hydration kinetics and the influence of admixtures and contaminants.

To measure the heat flow from cementitious pastes at early hydration stages, a twin calorimeter (an instrument with one sample channel and one reference sample channel) can be used to decrease noise and increase measurement sensitivity. In this technique different sample preparation procedures can be used:

Internal mixing:
- Dry cement is added to a glass ampoule attached to an admix ampoule.
- Syringes attached to the admix ampoule are then filled with the required volume of water.
- The glass and admix ampoule are then loaded either into or outside the calorimeter channels to reach thermal equilibrium. This will depend on the mixing setup and the type of calorimeter.
- The water is injected into the sample (dry cement) under stirring. This process can be performed automatically or manually.

External mixing:
- Dry cement is mixed with water outside the calorimeter.
- Cement paste is then transferred into a glass/polyethylene ampoule (sample).
- A second ampoule (reference) is then filled with the required volume of water.
- The reference and sample ampoule are loaded into the calorimeter channels to reach thermal equilibrium.

After the thermal equilibrium of the system is reached, the heat flow of the sample is obtained by recording the heat exchange and accumulation rates. The information

recorded is transformed into a voltage signal proportional to the heat flow that is then measured. Finally, the measurements obtained are represented by a calorimetric curve, i.e. a plot of the heat evolution rate over time, Fig. 2-15 [180]–[185].

Isothermal calorimetry has been widely used in cement research to assess the heat and rate of hydration; premature stiffening; and the effect of admixtures and contaminations, among other parameters (e.g. fineness, w/c ratio, $CaSO_4$ content), Fig. 2-15. As a result of these investigations, a better understanding of Portland cement thermochemical properties and hydration kinetics has been possible [5], [81], [185]–[189].

Nevertheless, the information obtained by IC is limited during the dormant and long-term hydration stages, since these chemical and physical changes are not always accompanied by marked heat flow events [180], [182], [190], [191].
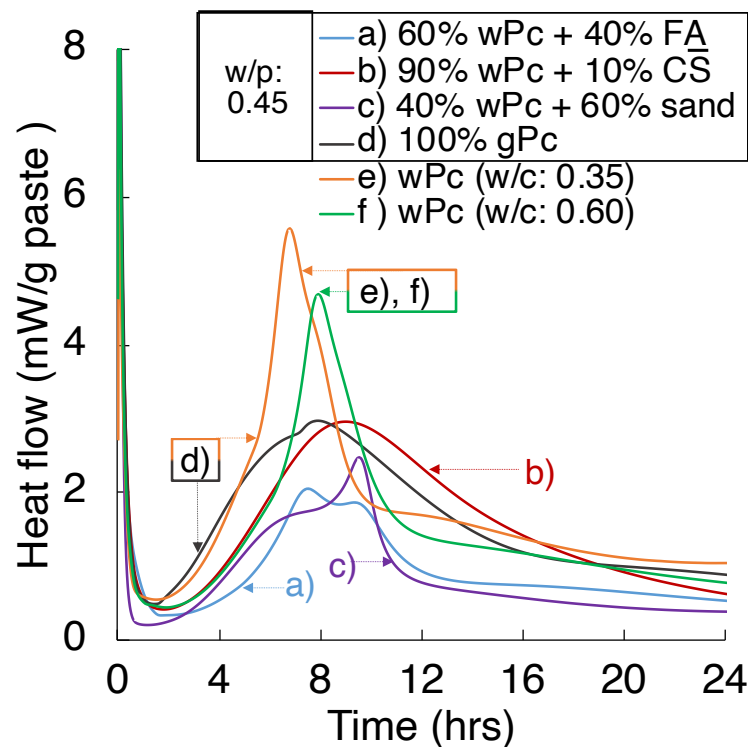
Fig. 2-15. Calorimetric curves of cement pastes, highlighting the influence of a) mineral admixtures, b) calcium sulphate, c) aggregates, d) fineness and chemical composition, and e,f) water to cement ratio, on the hydration heat.

2.4.3 Vicat test

The Vicat needle test assesses the initial and final setting times based on physical changes in the material which lead to increased yield stress, measured via the displacement of a weighted needle which is dropped into the cement paste [192], [193]. This is essentially a two-point measurement determining initial and final setting times.

The information obtained by this test is limited by physical changes and macroscopic properties of the cement paste; allowing researchers not only to understand the setting behaviour of cement and its influencing factors (Fig. 2-16) but also to complement different areas of study (e.g. electro-, thermo- and physico-chemical properties) [66], [80], [200], [81], [191], [194]–[199].

There exist different standard procedures to determine the setting of cement paste by using the Vicat needle test. According to the standard procedure EN 196-3 [21], the initial setting time is recorded when the distance between the needle and the surface of the plate is 6 ± 3 mm. The final setting time is recorded when the needle penetrates only 0.5 mm into the paste, Fig. 2-16.
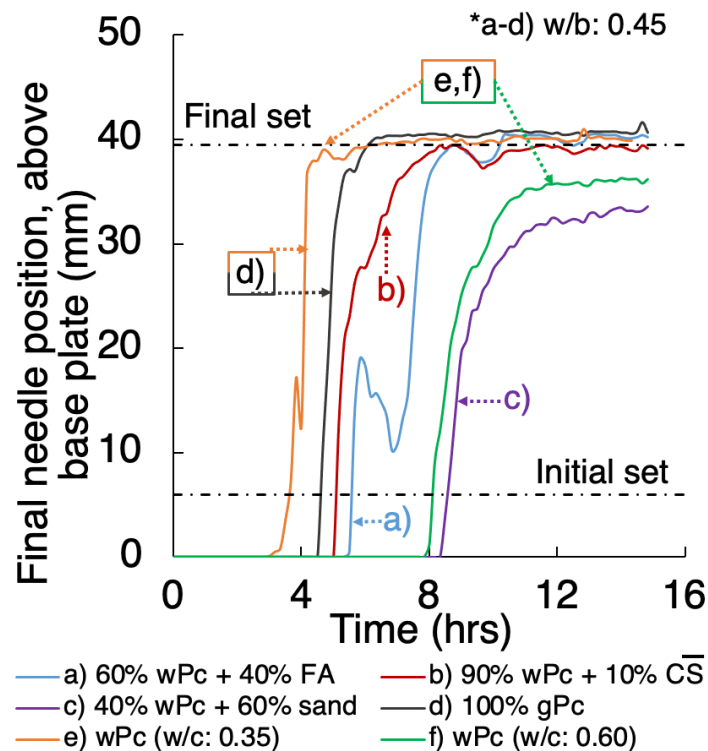
Fig. 2-16. Setting of cement pastes, highlighting the influence of a) admixtures, b) calcium sulphate, c) aggregates, d) particle size, e) water to cement ratio particle size, on the setting times. *w/b: water to binder ratio: 0.45 for gPc, and wPc + FA/C$\bar{S}$/sand pastes.

2.4.4 Scanning electron microscopy (SEM)

Scanning electron microscopy (SEM) is a microscopic technique that allows relatively high-magnification imaging and compositional analysis of a material. It is widely used in cement research as a result of the wide qualitative and quantitative information that it can provide, e.g. surface topography, and chemical composition and its spatial variation.

This technique uses an electron beam that is accelerated and focused across a sample. The surface topography of a sample can be reconstructed by scanning the electron beam and collecting the different signals emitted from the sample (i.e. SE:

secondary and BSE: backscattered electrons) which are then detected. The number of detected electrons depend on the variations of the sample surface.

Other type of interactions between the surface and the beam allow the user to perform various complementary analyses. For example, the chemical composition of a material and its spatial variation can be analysed by combining the scanning electron microscope with an energy-dispersive spectrometer. The focused electron beam generates an emission of X-ray photons, whose energy depends on the elemental composition of the sample, that is converted to an electrical signal and then detected and quantified [201], [202].

This technique has been used in numerous investigations to determine the microstructural features of hydrated cementitious materials (e.g. porosity, particle morphology, percolation, and phases identification), follow the hydrated product formation, and evaluation of different parameters that cause cement damage or deterioration. However, this technique presents certain drawbacks in the sample preparation (i.e. grinding and coating) which can limit the resolution of the image, damage the surface morphology of the sample, and create artefacts leading to a risk of misinterpretation of data [60], [93], [202]–[207].

2.4.5 Finite element modelling

The Finite Element Method (FEM), a discretisation technique, is one of the most widely numerical methods used among the science and engineering communities. It is a powerful tool for solving complex mathematical problems, developing models and simulations [208], [209].

Numerous investigations have used FEM to model and simulate microstructural features, the transport properties of different materials, and changes in material characteristics under specific conditions, e.g. temperature, pressure and mechanical force. These investigations are based on a diverse number of approaches (e.g.

differential, inverse and stochastic), parameters and methods that are used to generate a model at certain conditions [210]–[214].

FEM has also been employed to assess the relationship between microstructural features and the electrical response of different electroceramics. The results obtained from these investigations show a series of numerical methods that overcome significant limitations of previous methods that were used to simulate the electrical response of heterogeneous core-shell microstructures. This has demonstrated the capabilities of FEM in combination with different mathematical approaches to model and simulate physicochemical properties of these materials [212], [215]–[219].

The objective of FEM is to generate a discrete model that subdivides a system (i.e. a complex mathematical problem) into small geometrical components called finite elements (i.e. simpler equations). These finite element equations are solved and assembled back into a discrete model to generate an approximation to the initial mathematical model (Fig. 2-17). The finite elements, connected by nodal displacement and force nodes, can be represented as one-, two- or three-dimensional with a variation of geometries that depend on the approach and specific application used for the model [208], [220], [221].

Recently FEM has been used in cement research to evaluate and estimate the mechanical properties, kinetic mechanisms and microstructural development of cementitious materials, overcoming certain experimental limitations and supporting experimental data interpretation. FEM has also been used to assess the transport properties, chloride diffusivity, the fracture in tension and pore-scale properties. The studies showed FEM to be a promising approach to gain a better understanding of the relationship between microstructural features and intrinsic properties of cement systems, allowing the study of different physicochemical phenomena within cement paste [67], [222]–[225]. However, as a result of the complexity associated with the physicochemical properties and hydration processes of cement, and computational and FEM limitations; an accurate and precise model of cement hydration has not yet

been established [67], [208], [225]–[227]. Therefore, further investigation is needed to develop models capable of solving more complex systems, and to simulate cement properties by using an accurate and precise approach.
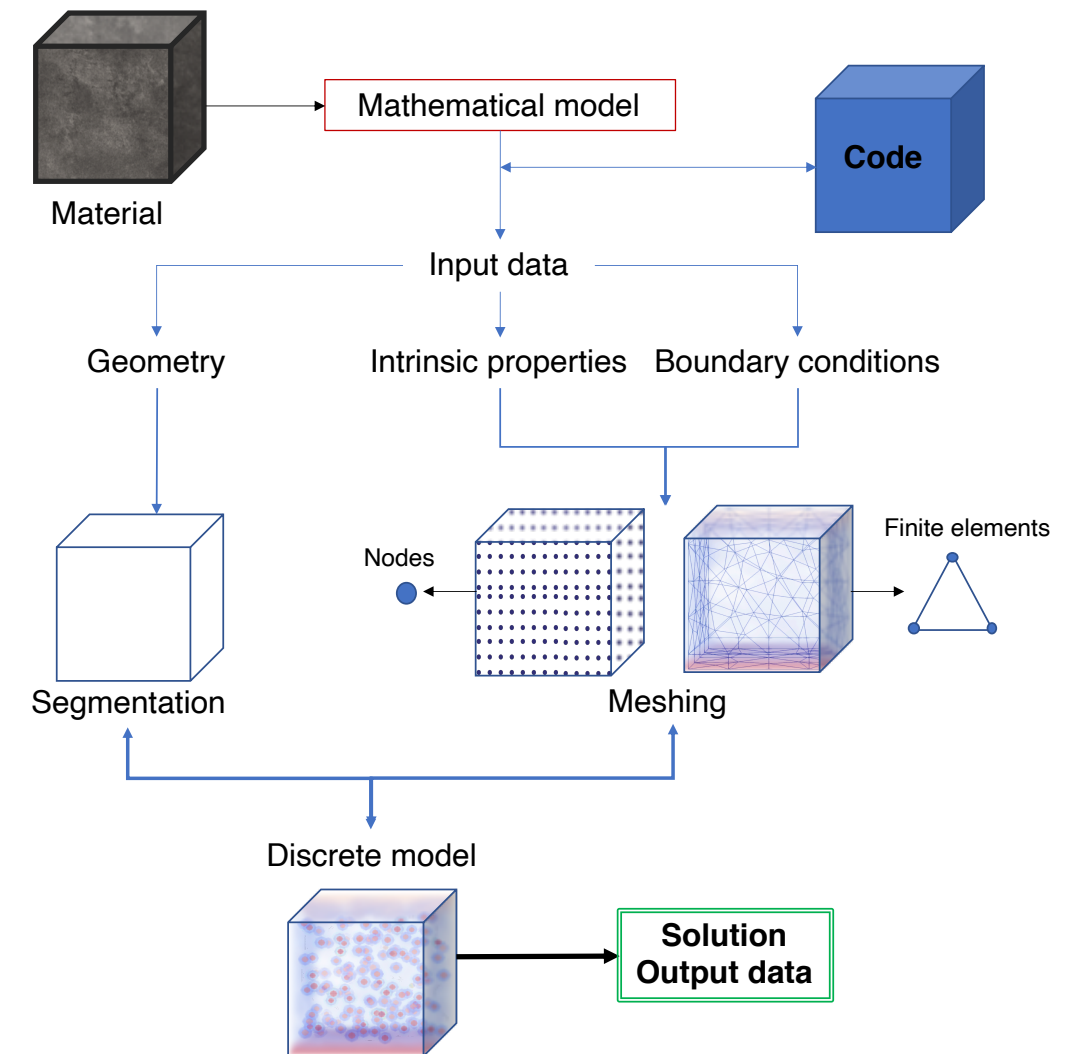
Fig. 2-17. Finite element method process [208], [220], [221].

2.5 Overview diagram

In this chapter, a synthesised description of Portland cement properties and characterisation techniques has been presented. The aim of the literature review is to explore the complexity of cement and build a solid background that supports the

experimental methodology and the assessment of cement hydration at early ages by alternating current impedance spectroscopy and other supporting techniques (Fig. 2-18).
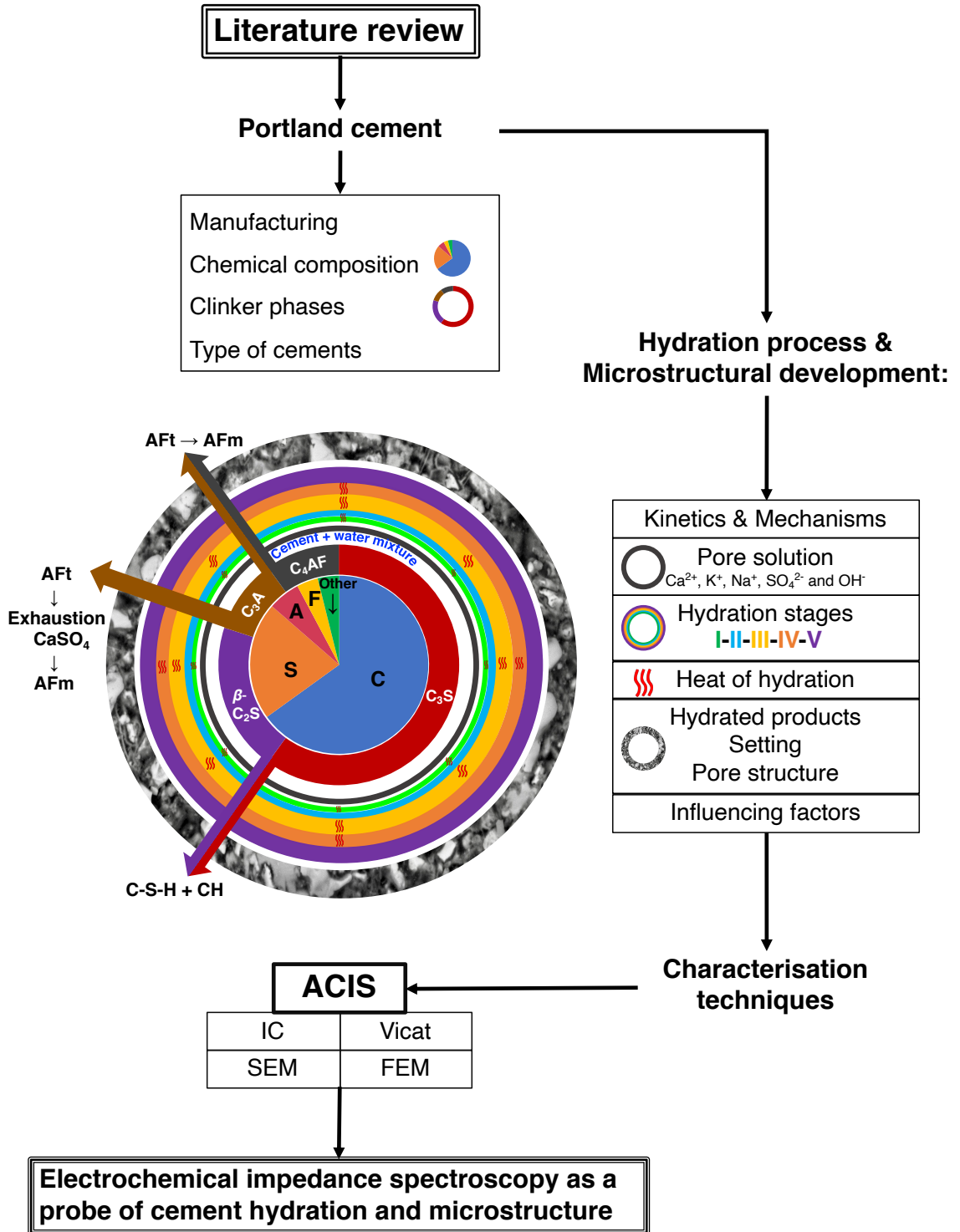
Fig. 2-18. Literature review overview diagram.

Chapter 3:
MATERIALS & METHODS

3.1 Sample preparation

Samples were prepared at room temperature (20 $\pm$ 3 °C and 50 $\pm$ 15% relative humidity) by mixing water with grey Portland cement (Cemex; gPc) or white Portland cement (wPc; Lafarge Blue Circle Snowcrete), both classified as CEM I 52.5R under BS EN 197-1, at different water to cement ratios (w/c). Samples were also produced with different replacement levels of standard silica sand under EN 196-1; or anhydrite (A; Fisher C/2440/60, >95%); or ground-granulated blast-furnace slag under EN 15167-1 (GGBFS; Ecocem); or fly ash under EN 450-1 (FA; Cemex, [228]); or silica fume under EN 1326-1 (SF; ELKEM silicon materials, MS grade 940-U, [229]). Table 3-1 shows the chemical compositions and physical properties of the wPc, gPc and mineral admixtures used. The specific mixtures tested are outlined at the beginning of each chapter.

Each sample was hand mixed by combining the components for 3 min to form a homogeneous paste, and then transferred into analysis vessels: 300 g into a custom-designed cell as described below (for ACIS measurements), or 20 g into a plastic (HDPE) ampule (for thermochemistry measurement), or 300 g into a plastic mould (for the Vicat setting test), or 50 g into a plastic vial (for SEM analysis). Prior to the start of the analysis, all samples were vibrated for 2 min to reduce the level of entrapped air bubbles.

Table 3-1. Chemical composition of cementitious materials as determined by X-ray fluorescence analysis, and average particle size d_{50} from laser particle sizing.

Compound (wt.%)	wPc	gPc	GGBFS	FA	SF
SiO_2	23.7	19.8	36.0	50.2	95.8
Al_2O_3	3.9	4.9	11.3	25.2	0.31
CaO	66.5	62.5	41.8	2.3	0.4
Fe_2O_3	0.2	3.1	0.3	9.3	0.1
MgO	0.9	1.6	6.5	1.7	0.1
Na_2O	0.2	0.4	-	1.1	-
K_2O	0.5	0.9	0.4	3.6	1.3
SO_3	2.6	3.7	0.7	2.4	0.5
TiO_2	-	0.2	0.5	-	-
Others	1.0	-	0.2	2.5	0.2
LOI	1.2	2.4	2.0	3.6	3.9
d_{50} (μm)	11.0	13.0	11.2	12.8	0.7

*LOI: Loss on ignition at 950°C

3.2 Instrumental analysis

The samples were subjected to ACIS measurements using an impedance analyser with a single channel (Metrohm AutoLab, PGSTAT204) connected to a custom two-electrode cell design, Fig. 3-1, filled to a depth of 7.5 cm with cement paste for each experiment [230]. To avoid sample leakage, the electrodes were inserted in the bottom face of the container and attached with a hard-plastic adhesive.
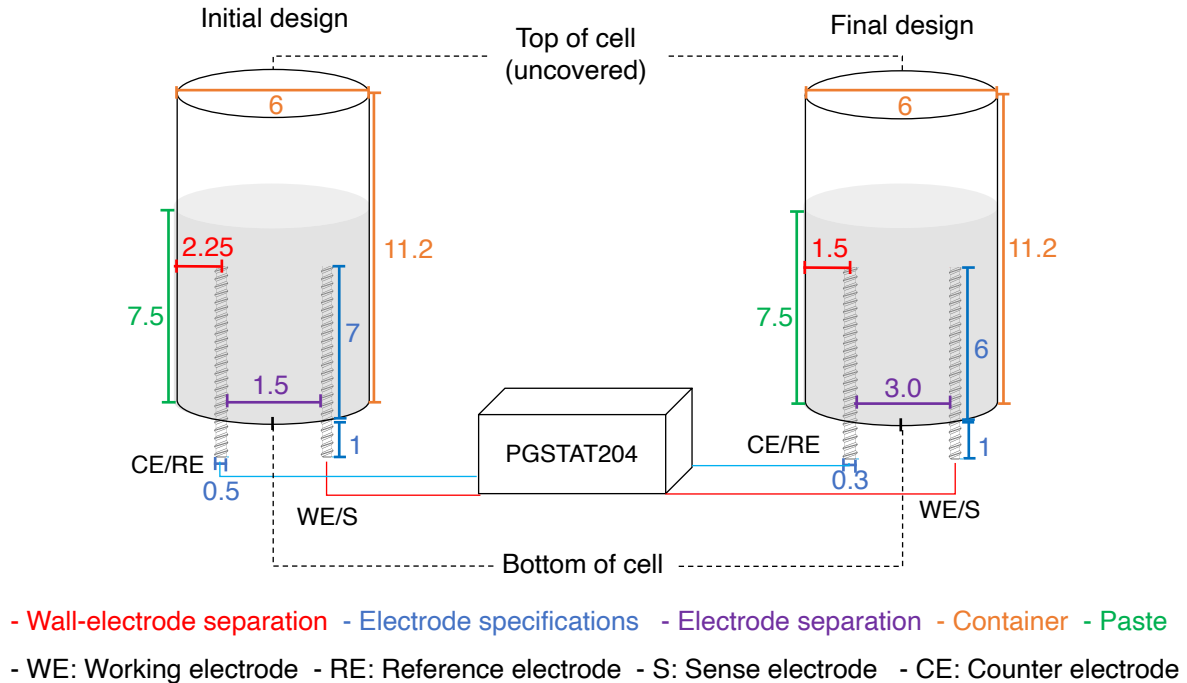
Fig. 3-1. ACIS initial and final custom-cell design diagrams (scale in cm).

Table 3-2 shows the initial and final custom cell specifications, and the acquisition measurement details used in each chapter.

The initial custom cell used in chapter 4 (Electrochemical cell design and impedance spectroscopy of cement hydration), was designed using a cylindrical plastic (PP) container (ϕ 6 × 11.2 cm) and two threaded stainless-steel electrodes (ϕ 0.5 × 8 cm) to evaluate different instrument and cell design parameters.

After the assessment of different cell designs, a final custom cell was selected for ACIS measurements in the following chapters (Chapter 5-8), using the same container dimensions with two threaded stainless-steel electrodes of different dimensions (ϕ 0.3 × 7 cm).

Table 3-2. Initial and final custom cell specifications and acquisition measurement details.

Cell design name	Initial custom cell	Final custom cell		
Applied in chapter	4	5 to 6	7	8
Container dimensions	$\phi\, 6 \times 11.2$ cm			
Electrode dimensions	$\phi\, 0.5 \times 8$ cm	$\phi\, 0.3 \times 7$ cm		
Electrode separation	1.5 cm	3.0 cm		
Acquisition measurement (hrs)	0-24 / 24-48 every 5 min; 48-72 every 15 min; 72-92 every 20 min	4 & 24	4, 8, 12 & 24	5 min., 4, 8, 12, 24 & 627

ACIS measurements (50 data points per cycle) were collected at room temperature over a frequency range of 100 Hz to 1 MHz, an applied perturbation amplitude of 10 mV and current range up to 1 mA. Measurements were obtained at different times directly after cement was mixed with water.

After data acquisition, ACIS measurement data were calibrated and corrected following the procedure in section 3.2.1. The data obtained from this technique are conveniently represented as a Nyquist plot, where the imaginary plane is conventionally plotted as -Z'' and the real plane is Z' of the complex impedance formalism, Z* [121].

3.2.1 ACIS calibration and measurement correction procedure

The impedance response of the cell in a short circuit arrangement (without sample) was measured before the samples were tested, to enable minimisation of the parasitic effects associated with the cell components and leads. The measurement correction

was made at each frequency, considering the ACIS response of the cement sample and the parasitic effects as additional quantities in the final ACIS measurements (Chapter 4: Fig. 4-10 and Fig. 4-14) [171], [231], [232].

3.2.2 Supporting characterisation techniques

SEM characterisation was carried out with a Hitachi TM3030 instrument equipped with an energy dispersive X-ray analyser (EDX) for elemental analysis. The modes used in the analysis were backscattered electron imaging (BSE) and EDX elemental mapping with an accelerating voltage of 15 kV. More detailed information related to the SEM sample preparation is provided in Fig. 3-2.

Isothermal calorimetry tests were conducted during the first 24 hrs after mixing according to the standard procedures [233] using an 8-channel TAM Air isothermal calorimeter (TA Instruments).

Initial and final setting measurements, according to EN 196-3, were determined by applying 90 penetrations during the first 15 hrs after mixing, using a Vicatronic apparatus (Matest, E044N).

SEM sample preparation

Mixing		
wPc + water	w/c: 0.35 & 0.45	Curing temperature: ≈ 20 °C
gPc + water wPc + anhydrite + water wPc + admixture + water	w/c: 0.45	

- Transfer each paste into a plastic vial (50 g).
- Cut samples at different hydration stages (2 cm slices).

Stop cement hydration at 4/8/12/24 hrs after mixing by:
- Solvent exchange method
    (2x): 1:5 to solvent volume ratio of isopropanol (1 day).
- Vacuum drying (2 hrs)

4 hrs sample:
Mount the sample into a metal stub using a sticky carbon disc

8-24 hrs samples:
- Cut slices into small pieces
- Clean residual dust (compressed air)
- Spread petroleum jelly into the internal walls and base of a cylindrical plastic mould
- Place 3 pieces into the mould
- Cover the pieces with an epoxy resin*
- Cure samples for 6-24 hrs

Sample grinding and polishing (process by hand):	
Sandpaper grade	
• 120	Remove a thin layer of resin until the surface of the cement sample is exposed
• 400	**I.** ○ x 10, **II.** ↥ x 10, **III.** turn the sample 180°, **IV.** ↥ x 10, **V.** turn the sample 90° and change the sandpaper grade.
• 800	Repeat the process above
• 1200	Repeat the process above six times (change step **V:** turn the sample 180°).
Diamond paste	
• 18/6/4/1 µm	○ x 100 each grade
• 0.25 µm	○ x 300

- Clean the sample with an ultrasonic bath with isopropanol
- Dry the sample in a desiccator for 24 hours.
- Coat the surface of the sample with a layer of carbon (sputter coater)
- Mount the sample into a metal stub using a sticky carbon disc.

*Epoxycure 2; Buehler; 4:1 resin to hardener; ↥: linear motion; ○ : circular motion.

Fig. 3-2. SEM sample preparation.

3.3 Experimental methodology

3.3.1 Electrochemical cell design (Ch.4)

To assess the hydration process of cement by ACIS, the experimentation was divided into two stages.

The first stage objective is, by evaluating different cell designs (changing just one parameter at a time), to select a custom cell design and procedure which could be capable of providing reliable impedance measurements with the minimum noise and external interference (parasitic effects), for wPc at early hydration periods.

Likewise, the first stage of experimentation was divided into two segments: the initial cell set-up (Table 3-3) consisted of the selection of an electrode attachment method capable of maintaining the electrodes at a fixed position in the container, avoiding sample leakage and unwanted contributions to the ACIS measurements.

To verify linearity of the ACIS response, and the sensitivity of the cement system at early ages, evaluation of the amplitude of perturbation was carried out, followed by an analysis of the leads (identified as the main source of parasitic effects). Finally, the sample/cell geometry was evaluated.

Table 3-3. Initial cell design and experimental specifications (**baseline setting**).

Parameter	Specifications
Electrode attachment	Method: hard-plastic adhesive and **SS nuts**
System linearity	Amplitude (mV): 1 and **10**
Leads effects	Height in relation to the ground (**10 cm**), twisted leads, position: **vertical** and horizontal, (Fig. 4-7)
	Length (cm): **150**, 200, and 250

After selecting the initial cell set-up parameters, the second segment (Table 3-4), electrode effects, was focused on comparing the impedance response of wPc to different electrode specifications such as the surface area, material, and electrode position.

Table 3-4. Electrode effects specifications (**baseline setting**).

Parameter	Specifications
Surface area (cm)	Diameter: 1, **0.5**, and 0.3
	Length:1, 2, 4, 6, and **7**
	Texture: **threaded** and flat
Material	**SS** and mild steel
Position	Electrode separation (cm): **1.5**, 3, and 6
	Electrode position: **bottom**, top, vertical, and horizontal

After evaluation of the first stage, the second experimental stage was carried out by the custom cell calibration and the ACIS measurements correction procedure shown in section 3.2.1 (Chapter 4: Fig. 4-10 and Fig. 4-14). The purpose of the procedure was to establish the high-frequency parasitic response of the leads in combination with the cell components.

3.3.2 ACIS data interpretation (Ch. 5-8)

To support ACIS data interpretation, different groups of Portland cement at different w/c ratios; or replacement levels of sand; or anhydrite, or GGBFS; or FA; or SF, were assessed by ACIS measurements and supported by calorimetry, setting tests and microstructural imaging analysis (SEM). The sample specifications of each group are shown at the beginning of each chapter.

The Nyquist plot format was used to display and analyse ACIS measurements. Inductance effects were identified via ACIS values falling below the real axis. The real and imaginary components of the signal measured (100 Hz-1 MHz) were plotted as a function of time. This enabled observation of a distinctive perspective of the

impedance data obtained, separating the time dependence of the high-frequency and low-frequency responses to separate the cement-bulk and cement-electrode response and observe their behaviour.

An equivalent circuit model (ECM), adapted from Fig. 2-11, was used to represent the electrical behaviour of cement paste at early hydration stages ($\leq$ 24 hrs) as observed in Fig. 3-3.

The cement bulk response is represented by an inductor (L_0: used just when there is an inductance behaviour in the ACIS measurement, attributed to a high conductive state of the solution-solid), two resistors (R_0: resistance behaviour of the solution-solid interface, and R_1: resistance behaviour of the solution-solid phase) and a capacitor (C_1: capacitance behaviour of the solution-solid phase).

As the cement-electrode interface is not ideal, and the electrical double layer resistance behaviour is significantly large and the capacitance behaviour is imperfect; the cement-electrode response is best represented by a constant phase element: CPE (electrical double layer with imperfect capacitance behaviour), rather than by an ideal capacitor in parallel with a resistor (Fig. 2-11).

Cement bulk response

L_0 : solid + liquid phase inductance
R_0: solid + liquid phase resistance

R_1: solid-liquid interface resistance
C_1: solid-liquid interface capacitance

Cement-Electrode response

CPE*: Electrical double layer non-ideal capacitance
*CPE: Constant phase element

C_1

R_0

R_1

L_0

CPE
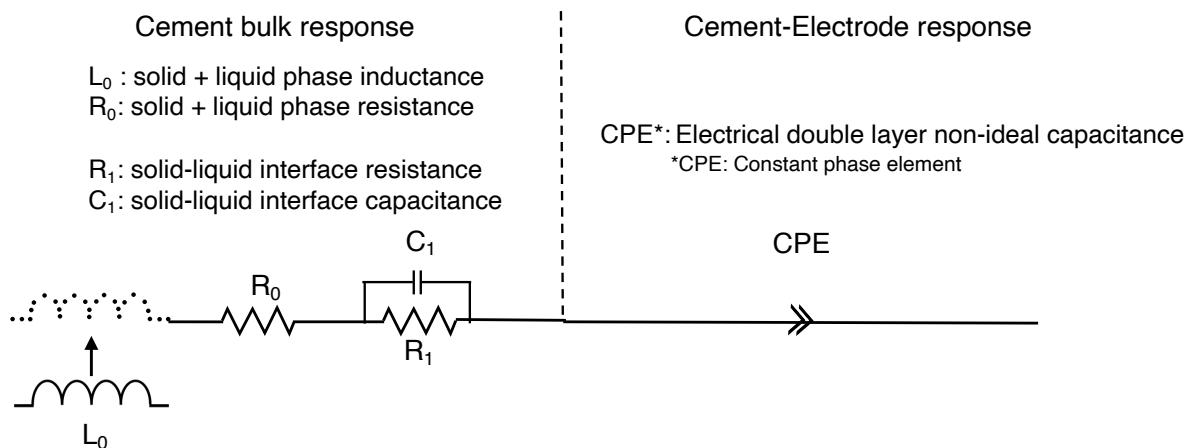
Fig. 3-3. Equivalent circuit model for fitting ACIS data.

Conductivity measurements were obtained from the resistivity of each cementitious paste by dividing the intercept point ($R_0 + R_1$) on the real axis of the Z* plots into a cell constant. The cell constant was obtained, by regression analysis (Fig. 3-4), measuring the conductance of an NaOH solution of known conductivity at different concentrations, Table 3-5. The cell constant was calculated as the slope of a plot of the NaOH conductivity against the measured conductance.

Prior to the start of the calibration measurement, the NaOH solution was placed into the custom cell design for 30 min. The measurements were collected at room temperature over a frequency range of 100 Hz to 1 MHz, an applied perturbation amplitude of 10 mV and current range up to 1 mA [153], [218], [234]–[236].

Table 3-5. Conductivity and measured conductivity of NaOH solution at different concentrations.

Label	Mass percent (%)	NaOH conductivity (S/cm)	Measured conductance (S)
a)	0.25	0.0123	0.3108
b)	0.5	0.0248	0.5784
c)	1	0.0486	0.9921
d)	2	0.0931	1.7456

Cell constant = Slope: 17.6526726
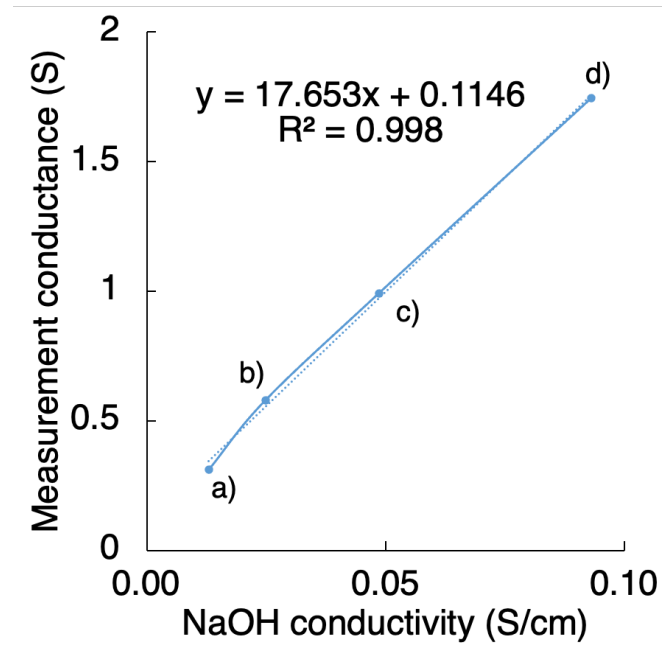
Fig. 3-4. Conductivity calibration curve.

3.4. Model description (Ch. 8)

The FEM package used, developed in-house at the University of Sheffield [216], [217], has the capabilities to simulate and analyse the impedance response of various core-shell microstructured materials, e.g. electroceramics. However, the influence of chemical processes on the impedance response is not directly taken into account.

The FEM approach here was established via previous impedance response simulations for a ceramic microstructure, as detailed in [216]. The key assumptions are that the material properties are linear, isotropic, and that the inductive effects are negligible when compared with capacitive behaviour in the Hz-MHz frequency range. External surfaces are either assigned as insulating, or a defined voltage can be applied to them. This is typically done on the top and bottom surfaces of a sample allowing an impedance response to be generated through the sample [212].

Even though these assumptions are not completely valid for cement systems due to time-dependence of material properties, and the complex chemical composition and hydration process of cement, these assumptions are taken into consideration to generate all the components of the microstructure (shell, core-shell), and approximate and simplify the analysis of the impedance behaviour of the system [31], [35], [216], [226], [237], [238]. More detailed information related to the model description is provided in section 8.1.

The microstructure of the cement model is simplified to be based on the hydration of spherical C3S particles of 20 μm diameter and considering C-S-H as the hydrate product formed. As a starting point, particles are confined into a cube with lateral dimension of 200 μm and meshed using a combination of 7188 tetrahedron prism elements. In previous investigations lower domain sizes (e.g. 50 μm and 100 μm) have been implemented, using a broader particle size distribution range, to simulate cement hydration and properties [239]–[243]. Therefore, the representative volume element within this domain size is large enough to simulate and characterise the hydration of C3S particles, however, the time and computer resources required to generate the solution increases.

An algorithm previously developed for predicting the capacitance and dielectric breakdown strength (i.e. failure of a dielectric material to resist an applied electric field) in a composite material [211], and based on creating a random dispersed array of seed points (each representing an C_3S particle centre in the model here) within a cube, was used to define a three-dimensional structure, which was meshed.

To decrease the computational time and maintain the simplicity of the model, the C_3S particle size was defined according to previous investigations in which it was determined that an average particle size ranging from 10-30 μm is generally representative of Portland cement and C_3S, and this was then further simplified by taking the value of 20 μm for all the spheres [241], [244]–[246]. The C_3S particles were assumed to be spherical, to simplify the algorithm formulation, minimize the

computational time and compliance of the matrix with a volume constraint, providing the minimum surface area to volume ratio to represent a dense packed microstructure. However, this shape is not representing the true cement particle shape (i.e. irregular) [67], [237], [247], [248].

To simulate the C_3S consumption and C-S-H growth, the volumes of all C_3S core particles were shrunk towards their centroid, generating the volume ratio chosen and representing C_3S hydration. The shrunken volume is filled with prism elements to generate the shell volume with its own intrinsic properties and then filled with the C-S-H phase.

To simulate the frequency response of the system, the initial frequency range was 1 Hz to 1 MHz, using a potential of 10 mV applied on a contact material with conductivity of 10 kS/m. More detailed information related to the model is provided in Fig. 3-5.

Randomly distribution of seed points in a cube (Centre of C$_3$S grains core).

Generation of the three-dimensional structure by a Voronoi tessellation (subdivision of the space into cells).

- Structure defined by the arrangement of the seed points.
- Generation of grain and subgrain (shell) shape and characteristics.
- The volume of the core (C$_3$S grain) shrunk towards their centre, depending the degree of hydration. The volume shrunken is replaced by the shell (C-S-H).

Regions of tetrahedral element are meshed using Gmsh.

Fills the volume of the cube

Voronoi tessellation postprocessing.

- Discretise the structure with tetrahedron elements by to eliminating extremely small surfaces.
- Tetrahedron elements are filled with prism element.

Assignation of material intrinsic properties (conductivity & permittivity) of the structure (water-pore solution / C$_3$S core & shell).

Simulate the impedance response of the structure generated at the designated frequency range by the FEM package.

- Solving Maxwell's equations (time & space) in combination with Ohms and Gauss's laws, and time-domain finite element method:

$$\nabla \circ \vec{\jmath}\,(r,t) = -\nabla \circ \left(\sigma(r)\nabla\varphi(r,t) + \varepsilon(r)\frac{\partial}{\partial t}\nabla\phi(r,t) \right) = 0$$

∇: Del operator
$\circ$: Dot operator
$\vec{\jmath}$: Current density
r: Position
$\frac{\partial}{\partial t}$: Rate of change with time

σ: Conductivity
φ: Electric potential
ε: Permittivity
t: Time
ϕ: Magnetic flux

Assumptions:

Material properties are linear and isotropic.

Inductive effects are negligible.

Permittivity as function of position.

Fig. 3-5. FEM model procedure [213], [216]–[218].

3.5. Overview diagram
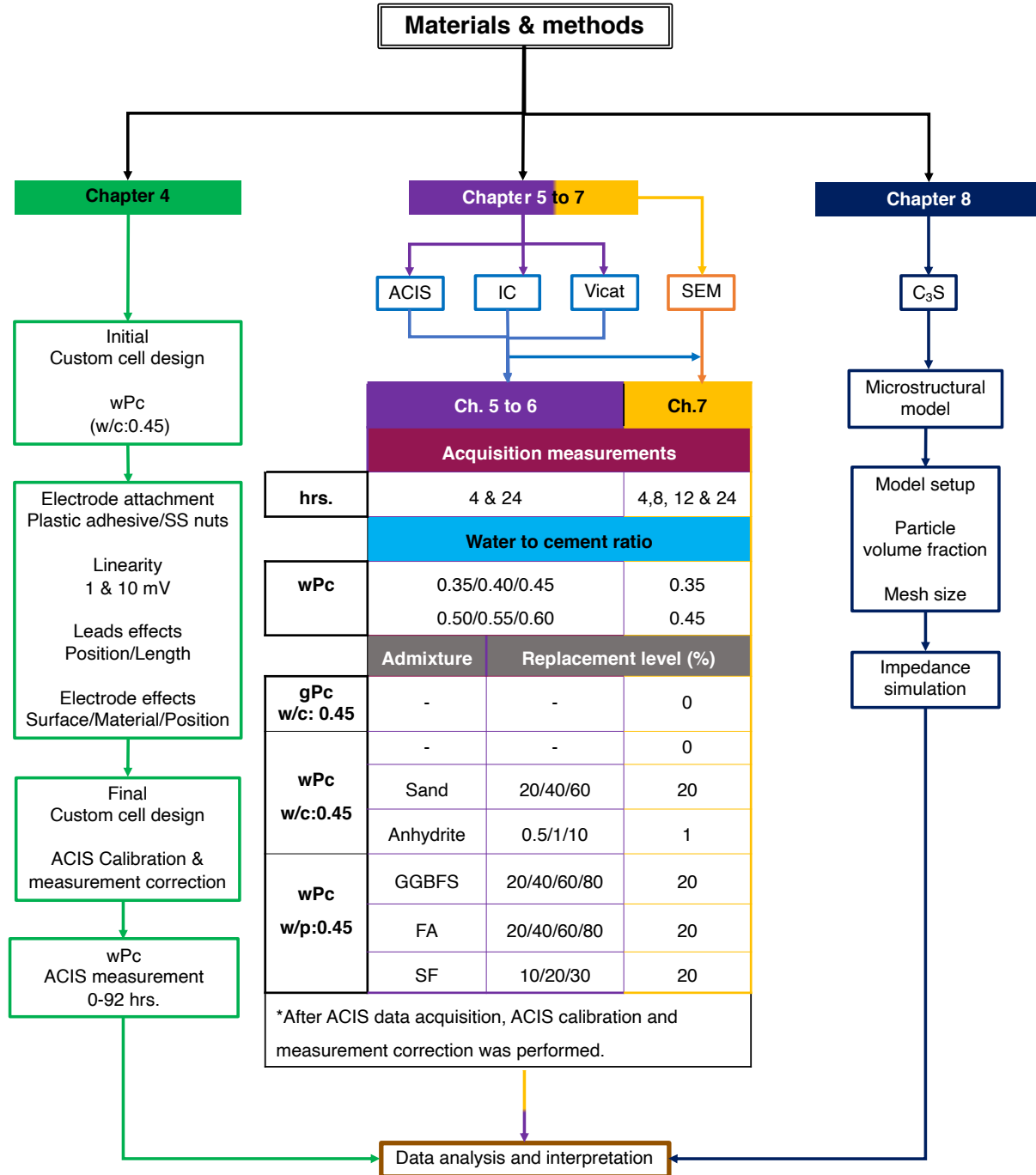
Fig. 3-6. Materials and methods overview diagram [37]–[40], [249].

Chapter 4:

ELECTROCHEMICAL CELL DESIGN

Note: This chapter is based on the paper *"Electrochemical cell design and characterisation of cement hydration by impedance spectroscopy"* by A. F. Sosa Gallardo and J. L. Provis, Journal of Materials Science, 2020, vol. 56 pp.1203-1220 [37].

4.1 Introduction

This chapter assesses electrochemical cell design and the impedance response during cement hydration. The results show that a significant decrease of the parasitic effects at high frequencies (caused mainly by leads and electrode effects) can be achieved through an optimal cell design and impedance measurements correction, enabling correlation of impedance measurements to particular aspects of the cement hydration process. However, due the limited solid phase microstructural development and the high conductivity of cement paste at low degrees of hydration, the parasitic effects could not be fully eliminated for fresh or early-age cement pastes.

To enable more accurate assessment of the hydration of cement by ACIS, the aim of this chapter is to investigate and evaluate the parameters that could produce parasitic effects in the ACIS measurements, and to provide guidance for appropriate experimental protocols. Understanding these parameters and their influence on the ACIS measurements is crucial in obtaining reliable data and thus correct data interpretation.

4.2 Sample specifications

To evaluate the initial cell design, the experimental procedure and to assess the hydration process of cement by ACIS, wPc paste samples were prepared at a water to cement ratio (w/c) of 0.45.

4.3 Results and discussion

In previous investigations the hydration of white Portland cement (wPc) was studied by ACIS during the first 72 hours after mixing [250]. The impedance measurements obtained were affected by parasitic inductance effects at high frequencies (that appear below the Z' axis intercept), potentially leading to unreliable data interpretation.

Fig. 4-1 shows the impedance spectra of wPc during the first 72 hrs. During all experimentation it can be noticed that the high frequency data (below the Z' axis, red line) show parasitic inductive effects mainly related to the effects of the leads, and influenced by factors including the high conductivity and low microstructural development of the cement paste, magnetic coupling and electrode effects, cell design, potentiostat response, and working frequency range [27], [231], [232].

With an increase in frequency the inductance increases, and as a result, the capacitive-resistive arc at high-frequencies disappears. This indicates that the information in that frequency range is altered by the inductance effects and cannot be analysed or considered reliable data for characterisation of the cement.

Even though the parasitic inductance effects were only visibly affecting the high frequency data, it was possible that all frequency ranges (high, medium and low) were affected by the same parasitic effects since they can influence potential-working electrode response and the measured capacitance at different frequencies.
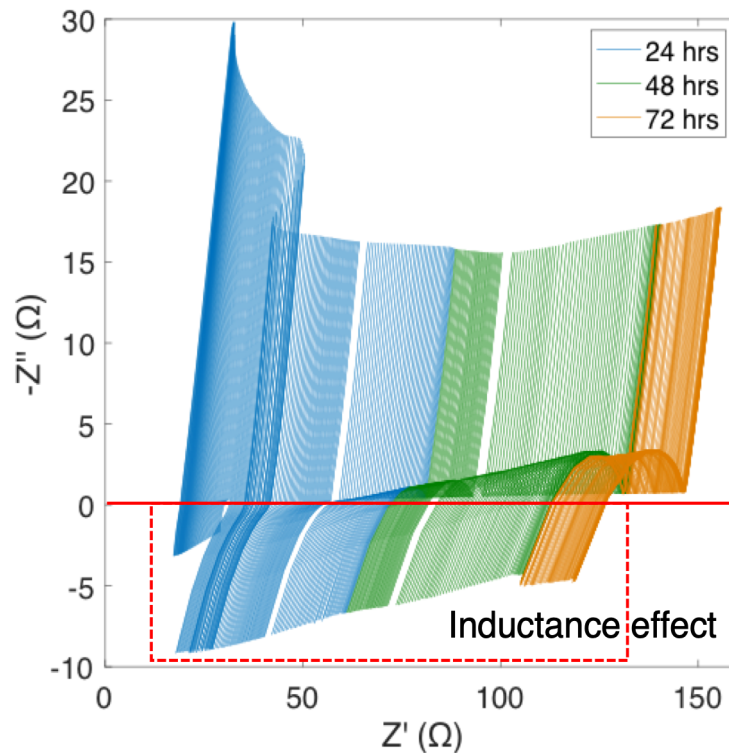
Fig. 4-1. ACIS data during the first 72 hours of wPc hydration. Dashed line indicates the part of the data showing a strong influence of inductance, falling below the Z' axis.

The ACIS measurements obtained were evaluated by examination of Lissajous and resolution plots, and Nyquist plots. The information obtained regarding the cement material response at early age was limited because of the high conductivity of the cement paste produced by the water content, the high ionic strength of the pore solution, the hydration kinetics, and the continuous and open pore structure [100], [169], [185].

4.3.1 Initial cell set-up

4.3.1.1 System linearity

ACIS relies on the use of an amplitude small enough to obtain a linear response which can be expressed analytically. The linearity of the system is directly related to the amplitude that is applied to the system. To find the optimal amplitude permutation and verify the linear response for cement systems, raw impedance data were used to generate Lissajous and resolution plots. The amplitude must be small enough to minimise perturbation of the material behaviour during cement hydration, but large enough that a high-fidelity signal can be recorded.

The Lissajous plots, e.g. Fig. 4-2, show the AC potential (x-axis) and the AC current (y-axis). The information obtained allows the verification of the linearity of the ACIS response in which the AC amplitude should be small enough so that the response of the electrochemical cell can be considered to be linear, but large enough to measure the system response [122], [251]–[253]. The resolution plots, e.g. Fig. 4-3, show the AC current and the AC potential (y-axis) as a function of time (x-axis). The information obtained allows measurement of the sensitivity of the system and the noise significance in the processed data. Two different amplitude perturbations (10 mV and 1 mV) were used to verify the sensitivity and linear response of the experimental procedure for cement systems, in the frequency range 1 MHz to 100 Hz and at a fixed current of 1 mA.

At an amplitude of 10 mV (Fig. 4-2), the Lissajous plots show that the linearity of the ACIS response is maintained, with central symmetry of a straight line with respect to the origin of the plots at each frequency. In the same way, the resolution plots (Fig. 4-3) show a high resolution of both signals at each frequency.

Conversely, at an amplitude of 1 mV (Fig. 4-4), the Lissajous plots show a strongly non-linear response, as that the central symmetry of the plot is not maintained and the shape is disturbed by noise. Likewise, the resolution plots (Fig. 4-5) show a high resolution for the current signal, but a low resolution for the potential signal.
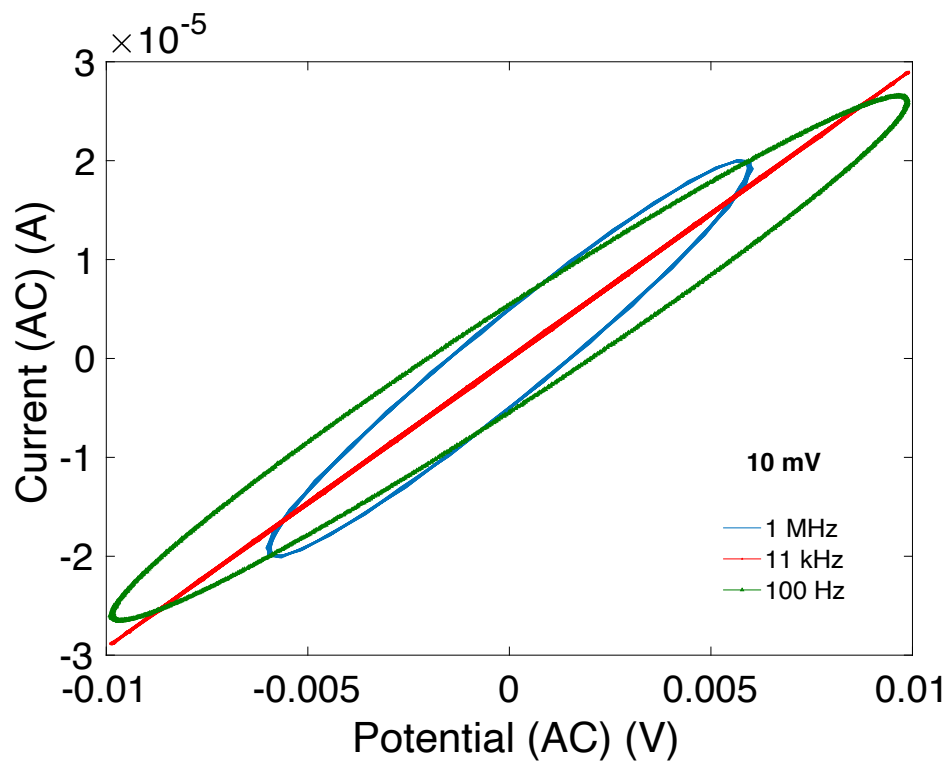
Fig. 4-2. Lissajous plot of wPc paste at 5 min after mixing, amplitude of 10 mV.
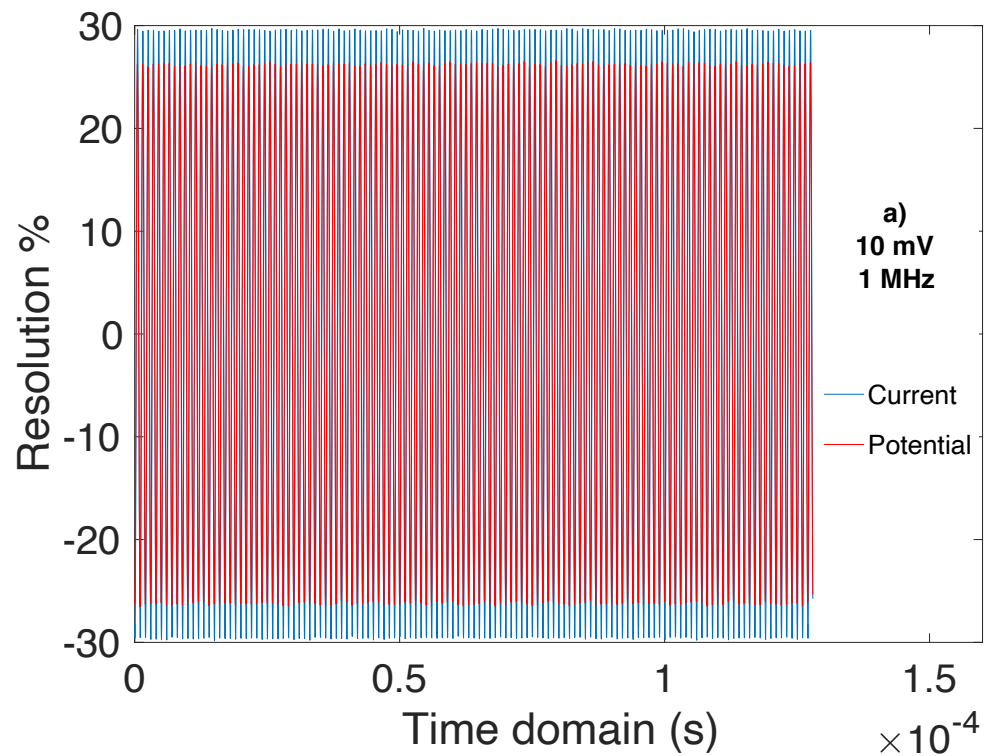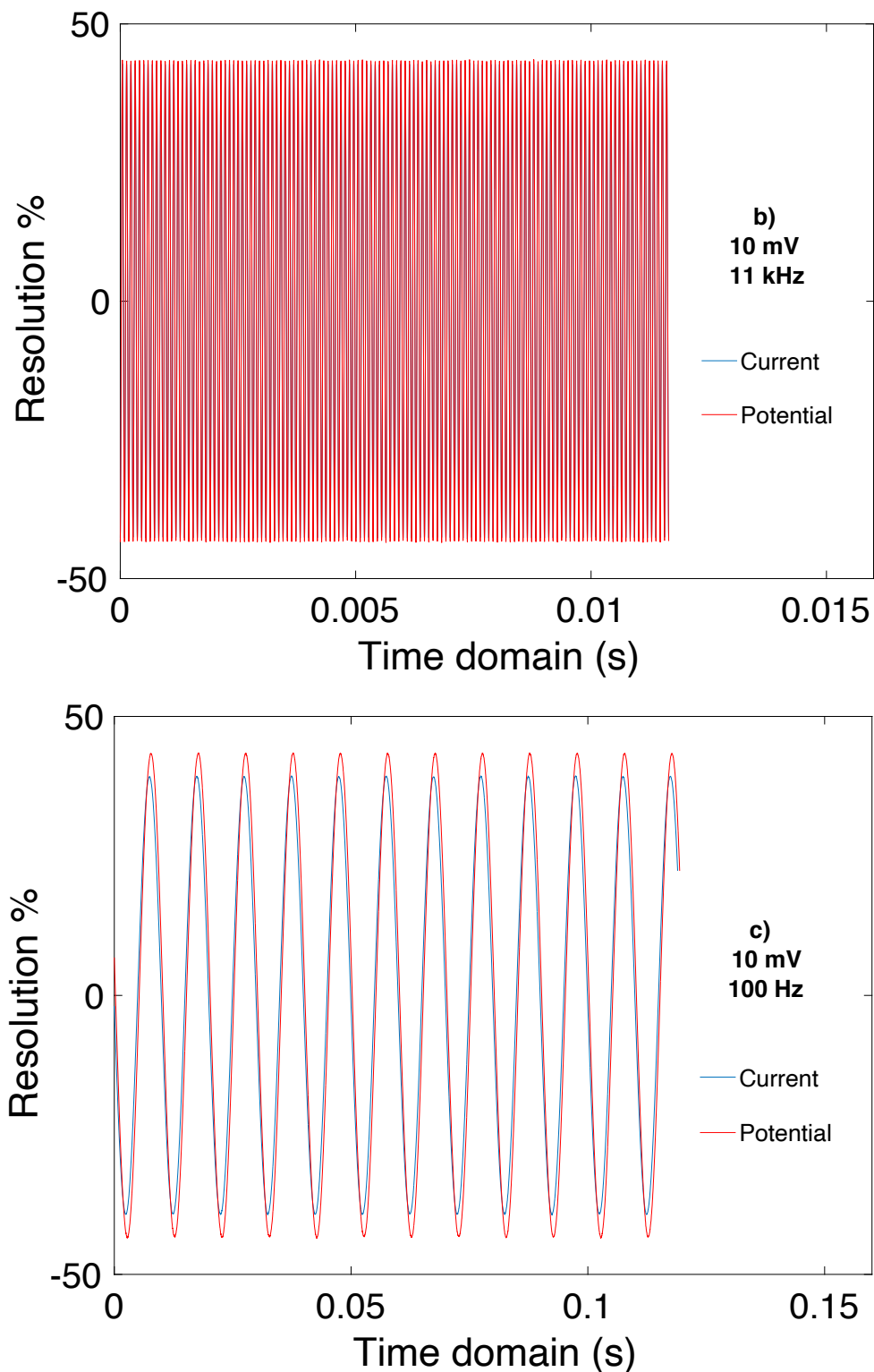
Fig. 4-3. Resolution plots of wPc at 5 min after mixing and using a perturbation amplitude of 10 mV: frequency a) 1 MHz, b) 11 kHz, and 100 Hz.
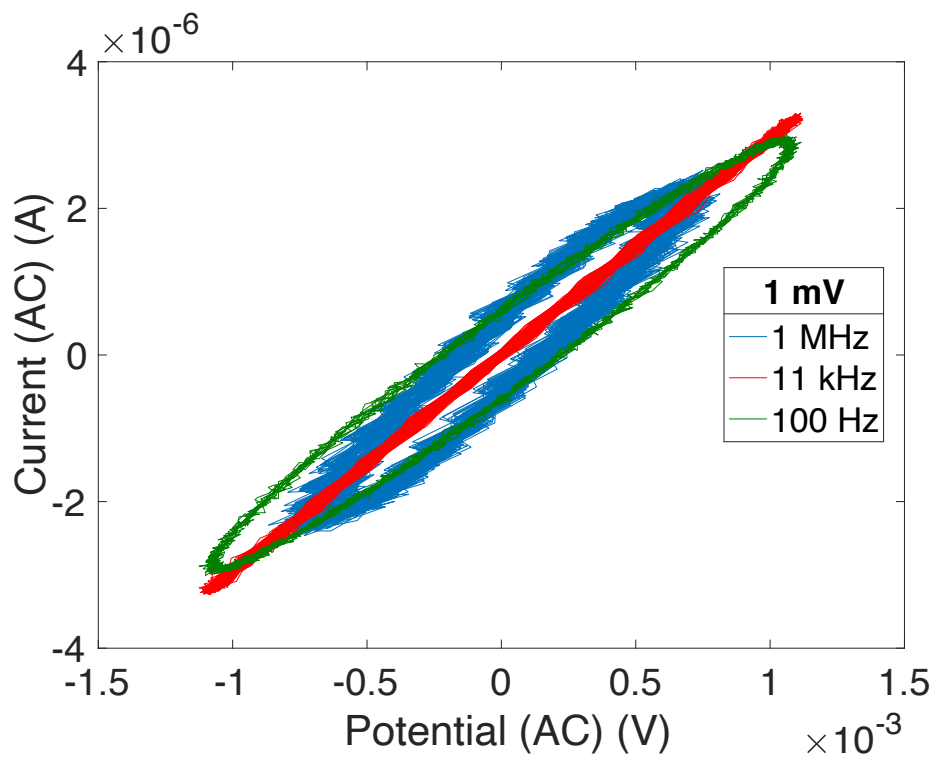
Fig. 4-4. Lissajous plot of wPc paste at 5 min after mixing, amplitude 1 mV.
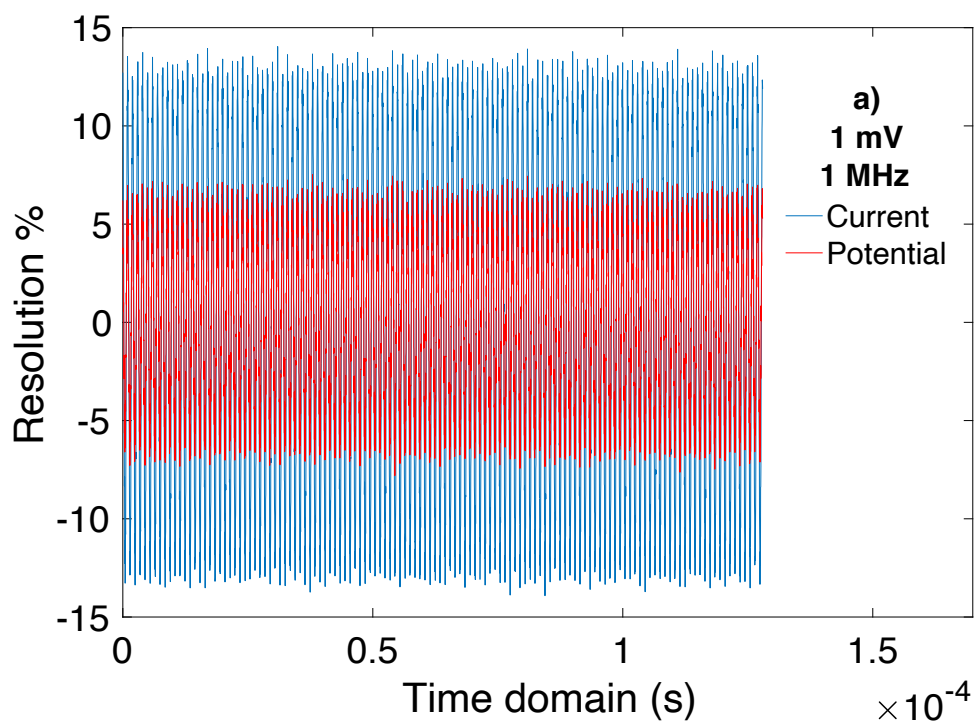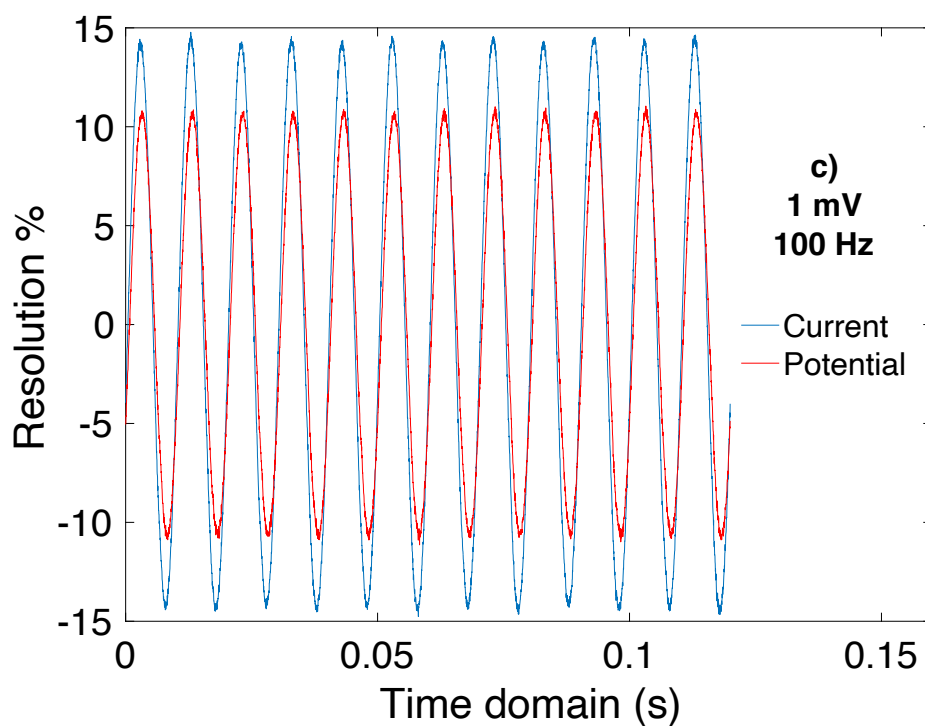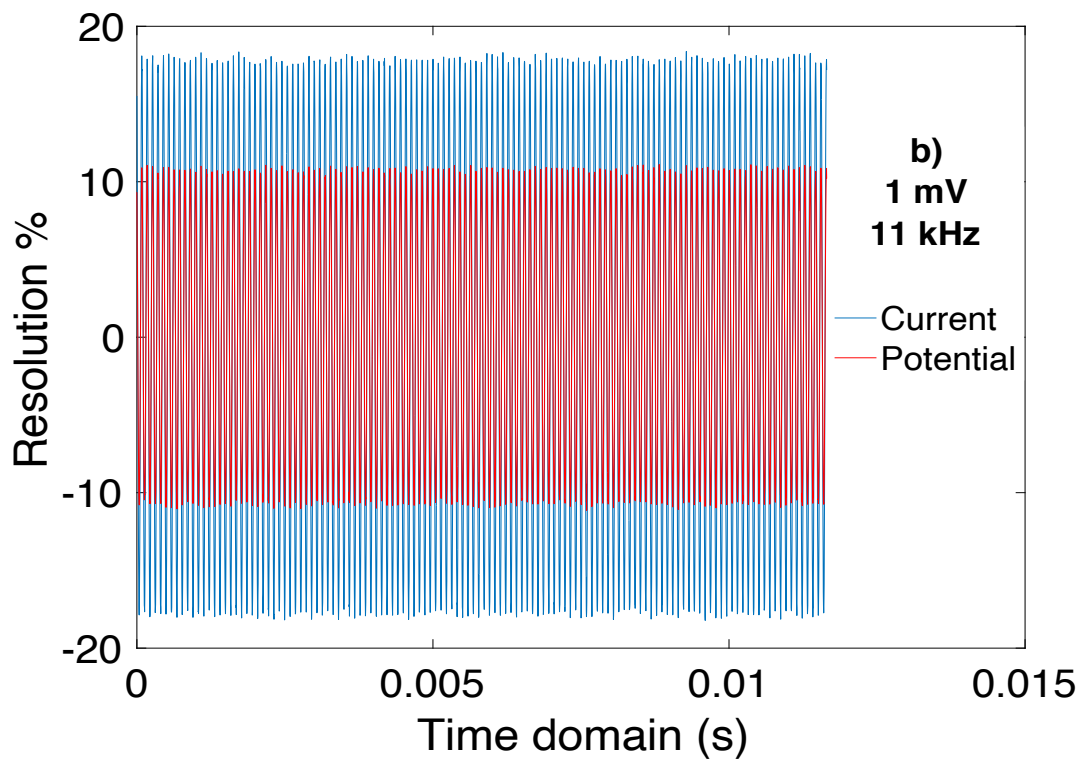
Fig. 4-5. Resolution plots of wPc at 5 min after mixing and using a perturbation amplitude of 1 mV: frequency a) 1 MHz, b) 11 kHz, and 100 Hz.

To avoid nonlinear effects and based on the evaluation between both amplitudes, a linear response and accurate data can be obtained using 10 mV as the preferred amplitude for analysis of cement systems in the apparatus described here. This amplitude is selected due to the reduction of the errors that could be produced by charge-transfer resistance, noise, and polarisation during the impedance measurements. Smaller amplitudes will degrade and distort the impedance measurements, leading to inaccurate measurements and non-linear response [254]–[257].

4.3.1.2 Electrode attachment

The electrode-cell attachment was assessed by comparison of the ACIS responses measured during wPc hydration using the SS electrodes attached with SS nuts, and with hard-plastic adhesive. Fig. 4-6 shows the ACIS response of wPc as a function of the electrode attachment method, at hydration times of 5 min and 24 h. The electrodes that were attached with hard-plastic adhesive show fewer inductance effects at high frequency (likely to impact the impedance measurements) for both ages.

The electrodes attached with SS nuts show higher inductance effects due to the decrease in resistance as a result of the increase of the number of flux lines and amount of energy stored in the electrodes. Also, the changes in the ACIS values at both ages, as a result of an increase in the electrode surface area and a decrease of the electrode separation at the bottom of the cell produced by the attachment of the SS nuts to the SS electrodes, mean that an uneven current is flowing through the SS electrodes and nuts (which are acting as both working and counter-electrodes, Fig. 3-1) [258]–[260].

For the cement at an early stage of hydration, with both attachment methods, it is not possible to identify a high-frequency semicircular arc, as the measured values fall below the Z' axis. As mentioned before, this is probably due to the high conductivity of

the fluid cement paste with a highly-connected aqueous phase of relatively high ionic strength, and the parasitic effects of the leads and cell. At longer ages cement hydration proceeds, inductance decreases, and an increasing tendency in the resistance is observed, progressively yielding a more noticeable high frequency semicircular arc. This can be attributed to the microstructural development, water consumption and reduction of the connectivity of the pores [27], [169]. These trends are discussed in section 4.3.3.
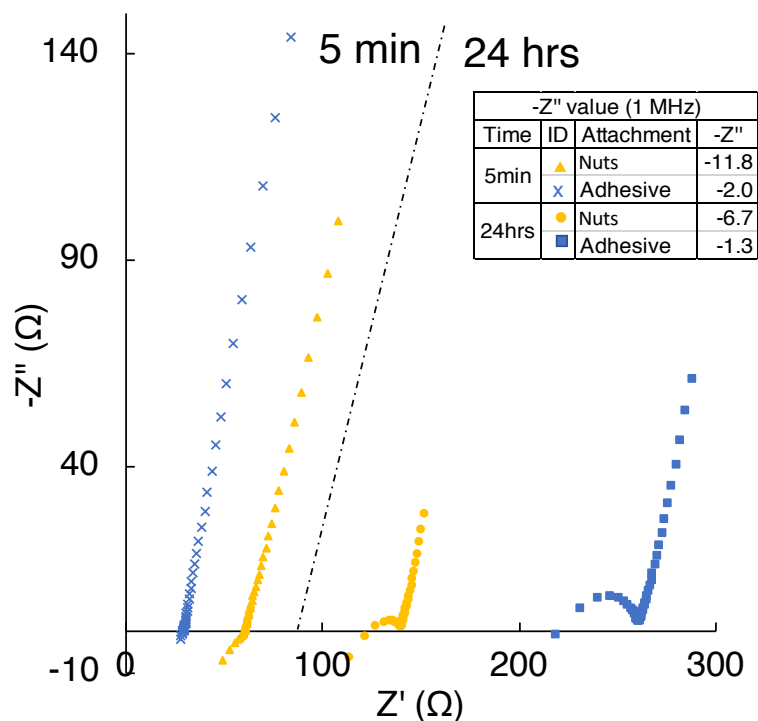
Fig. 4-6. ACIS measurements of wPc at different ages, testing electrode attachment methods as indicated.

4.3.1.3 Lead effects

Parameters related to the leads, such as length and diameter, degree of grounding and shielding, weak end contacts, and positioning, are some of the main sources of noise and error in ACIS measurements. Parasitic perturbations produced due to the

leads have been found in both high and low impedance cells in the form of stray capacitance or stray inductance, respectively [261], [262]. These measurement perturbations are difficult to evaluate due to the interconnecting wiring, the external environment, and the parameters previously mentioned. For example, the AC current that passes through the current-transporting leads produces a magnetic field which couples to the leads from which the potential is measured, leading to unwanted AC voltages which could lead to mutual inductance errors in the ACIS measurements. Previous studies have proposed different solutions to minimise these parasitic perturbations [171], [263], [264].

To evaluate the lead effects on ACIS measurements for cement pastes at early age, different lead positions and lengths were analysed using the initial cell design. Fig. 4-7 shows a schematic representation of the parameters evaluated; (a) distance of the leads between the working surface and the electrochemical cell, (b) twisting of leads, (c) alignment of connections between the leads and the SS electrodes, and (d) lead length.
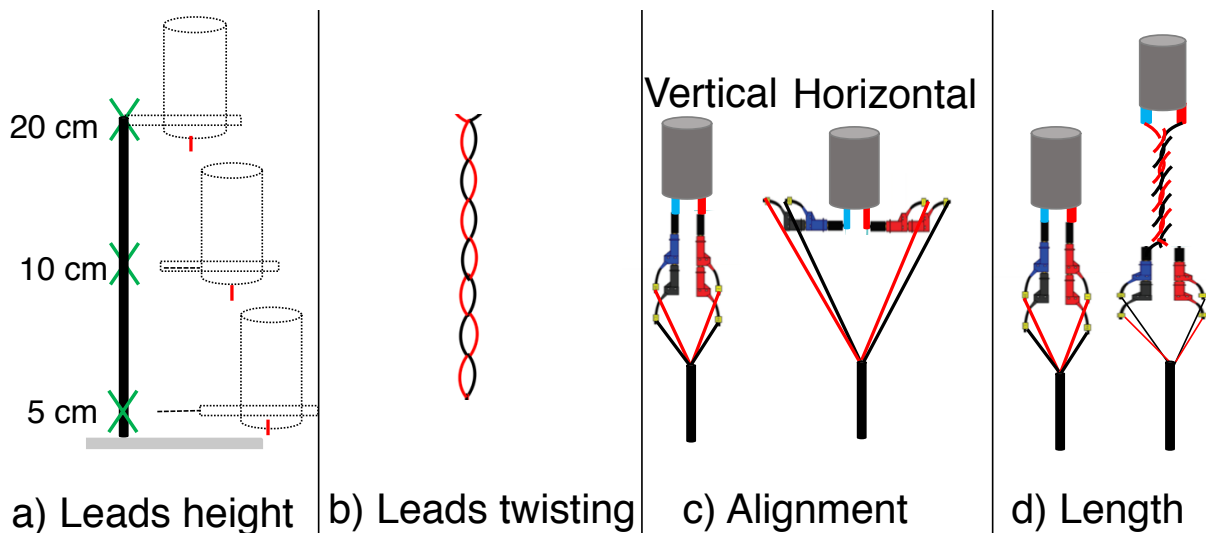
Fig. 4-7. Illustration of the lead parameters evaluated.

Fig. 4-8a-b shows that there is not a significant change in the impedance spectra as a result of changing the distance of the leads between the working surface and the electrochemical cell, or by twisting the leads. These results confirm that these lead arrangements (i.e. conductor, insulation, binder, braid, jacket, and connectors) are suitable for the following experiments.

Similarly, there are no meaningful changes in the ACIS measurements when changing the alignment of the connections between the leads and the SS electrodes (Fig. 4-8c), since the SS electrode position (3 cm separation distance) is restricted and does not allow the leads to separate further from each other. Also, the results are an indication that the impedance measurements are not affected by the magnetic coupling or the pickup effects produced by the low-intensity magnetic field of the leads.

However, it can be observed that an increase in the lead length has a meaningful impact on the ACIS measurements. Fig. 4-8d shows the changes in parasitic effects and Z' values as the length of the leads increases. The lead length increase raises the resistance, leading to a negative impact on the measured signal amplitude as a result of the wave deterioration as the leads move away from the energy source. Also, when AC is applied, a phase shift between the applied amplitude and the current can occur [259], [263], [265].

The following experiments were therefore conducted using the standard cables (150 cm); it was not possible to further reduce the length of the leads due to the limitations of the equipment available.
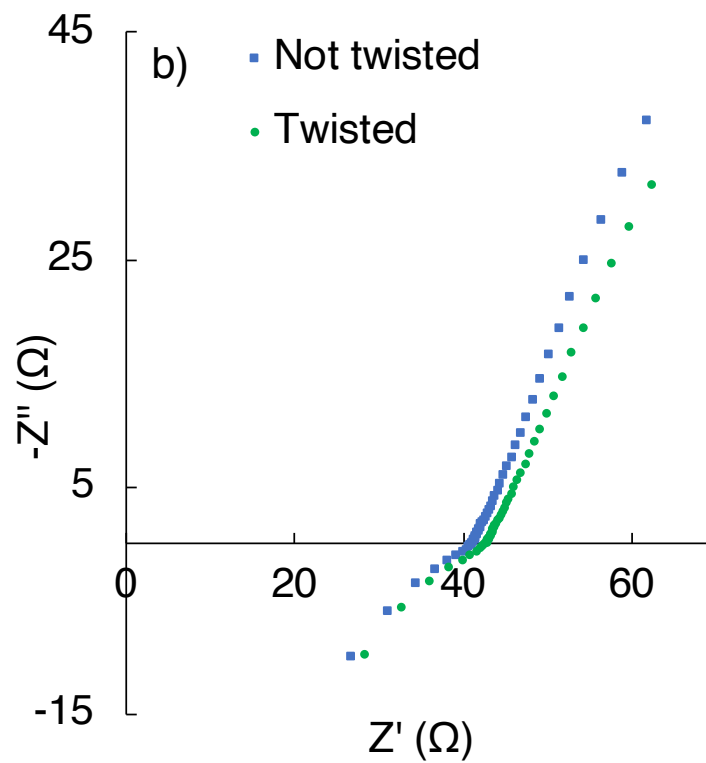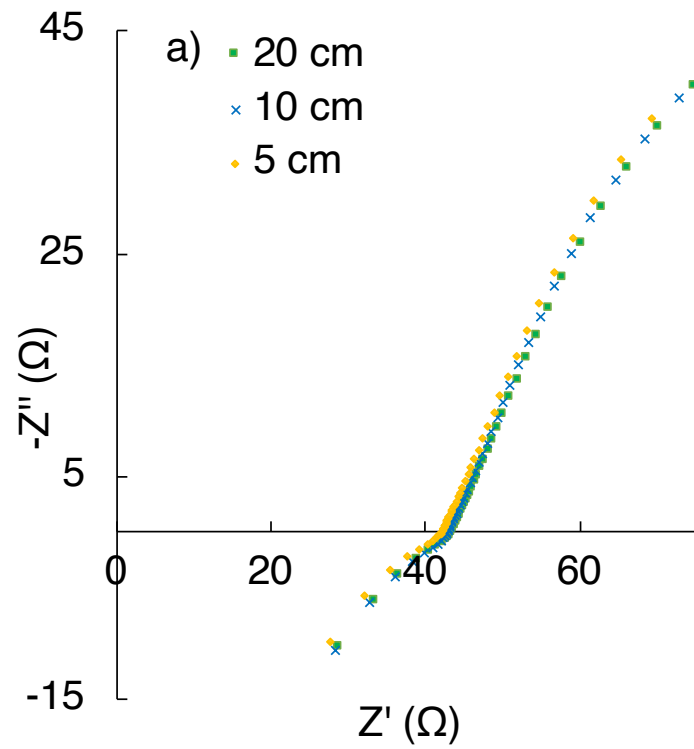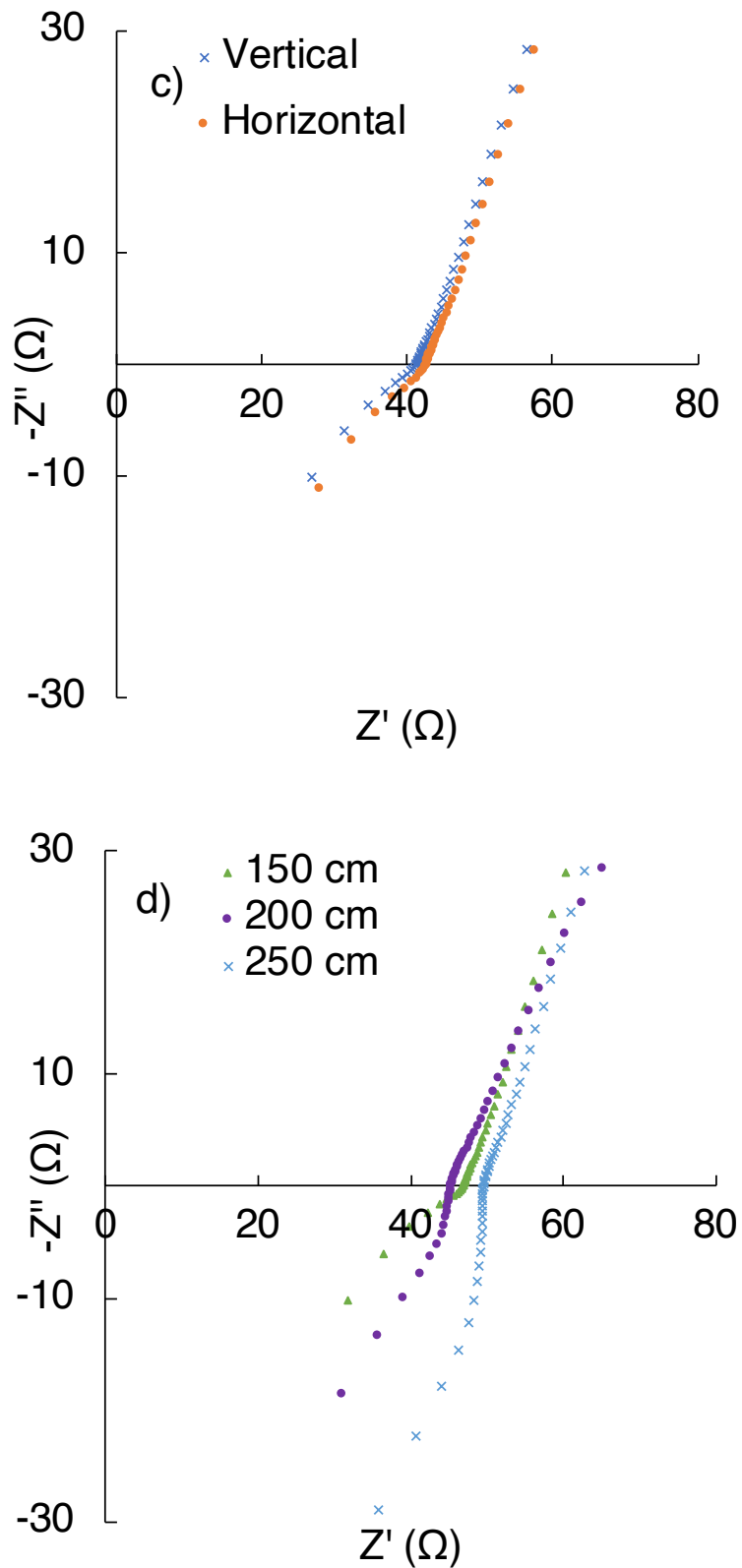
Fig. 4-8. ACIS measurements with different lead parameters: a) height above working surface, b) twisting, c) alignment, and d) length.

4.3.2 Electrode effects

The cement paste parameters measured by ACIS can be divided into two categories: the first set corresponds to the properties and behaviour of the cement itself (e.g. conductivity, kinetics, pore solution), and the second relates to the electrode-cement interaction (e.g. diffusion, adsorption, capacitance, electrical double layer capacitance). ACIS measurements can be affected by the electrode performance which depends on the system under analysis, the electrode specifications (e.g. surface area and material), and the electrode position. A significant change in any of these parameters will have a significant impact on the electrode performance and stability, which may lead to collection of erroneous data or misinterpretation of ACIS measurements [266].

An ideal electrode design should have a surface area which is able to deliver a uniform current density to ensure a uniform potential distribution over the electrodes and the sample [267]. The electrode alignment needs to be symmetrical not only to avoid uneven current distribution, but also to decrease errors produced by differences in potential distribution. In addition, the study of the electrode material should be performed considering the sample material under investigation, since interactions with the sample can affect the electrode surface (e.g. corrosion and/or passivation layers), leading to an unwanted contribution to the measured impedance, and erroneous data interpretation. Cement paste and its pore solution have a highly alkaline environment (pH around 12 to 14) which can in turn influence the passivation properties of the electrode material [7], [9], [171], [268]. The electrode material needs to have good electrical properties and performance to obtain good electric field distribution and reduce unwanted impedance responses. It is fundamental to understand the electrode effects to obtain a better cell configuration which could retrieve more information about the cement system.

This section presents discussion of the influence of the electrode effects on cement ACIS measurements, intending to obtain insight into the relationship between the electrode effects and the ACIS response. To enable comparison of the results obtained using electrodes of differing surface areas, the results were normalised by multiplying the impedance obtained by the electrode surface area under investigation.

4.3.2.1 Electrode surface area

Fig. 4-9a-c shows the electrode surface area effects in the cement ACIS measurements of wPc pastes. At early age (5 min after mixing the cement pastes), the impedance values are slightly affected by the changes in the electrode surface area when either length (Fig. 4-9a) or diameter (Fig. 4-9b) are varied. As the electrode surface area increases, the parasitic inductance effects are seen at high frequencies, and the values on the Z' axis increase, showing a correlation between the electrode surface area and the impedance values. The information at high frequency is obscured due to parasitic inductance effects which arise from the lead effects (as discussed in the preceding section) and the state of the cement paste (low developed microstructure and highly conductive). At longer ages (24 h), the results show a higher influence of the electrode surface area on the ACIS measurements, following the same tendency as at early ages. The increase in the resistance and the reduction of the inductance effects are produced by the microstructural development of the cement paste. These changes can be observed through the appearance of a high frequency semicircular arc at longer ages.

It is important to notice that changes in the ACIS measurements produced by changing the electrode texture from threaded to flat (Fig. 4-9c) are small at early age, and almost null for a more mature cement paste. These changes will not influence the effective surface area drastically (in terms of the distribution of electrical flux lines), but they will have an impact on the contact between the electrodes and the cement paste.

81

Parameters measured by ACIS such as electrical double layer capacitance (EDLC), electron transfer resistance (ETR), and the uncompensated electrolyte resistance will depend on the ionic concentration and the ion types in the aqueous phase, the temperature, the reaction kinetics, the electrode surface area, and the current distribution [121], [269]–[272]. As the electrode surface area increases, the electrode-sample reaction kinetics, the parameters previously mentioned, and the current distribution will rise, leading to differences in the ACIS response as observed in the results (Fig. 4-9a-c). Considering the experimental system as a circuit, as the electrode surface area is changed, the magnetic flux through the circuit, the amplitude, and current dispersion through the cement paste also change, affecting the parasitic effects and the impedance values.

Time	ID	Length (cm)	-Z"
	●	1.0	-28.83
	─	2.0	-32.19
5min	✳	4.0	-35.8
	◆	6.0	-41.6
	▲	7.0	-44.4
	◆	1.0	-5.4
	▲	2.0	-6.3
24hrs	■	4.0	-65.8
	+	6.0	-115
	✳	7.0	-114
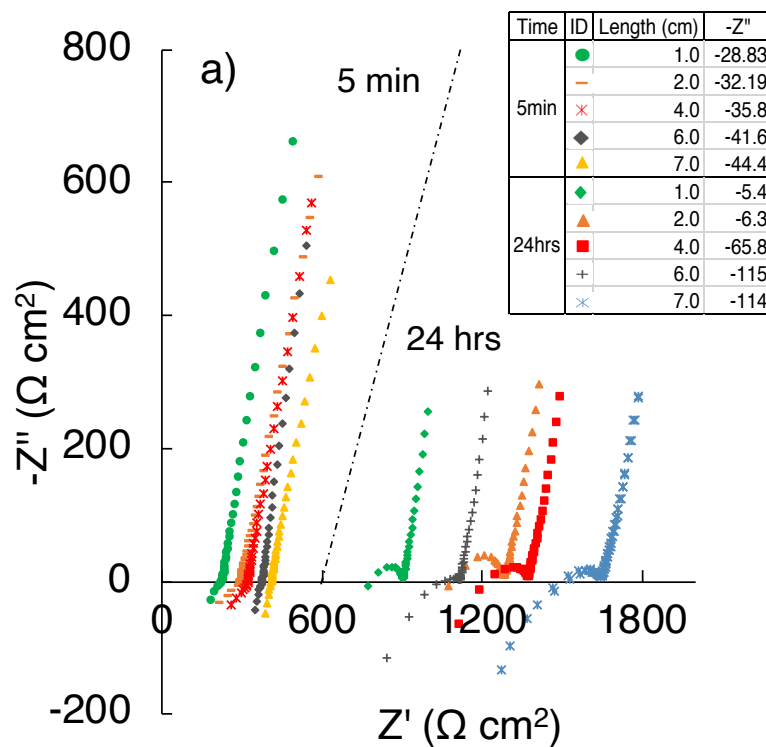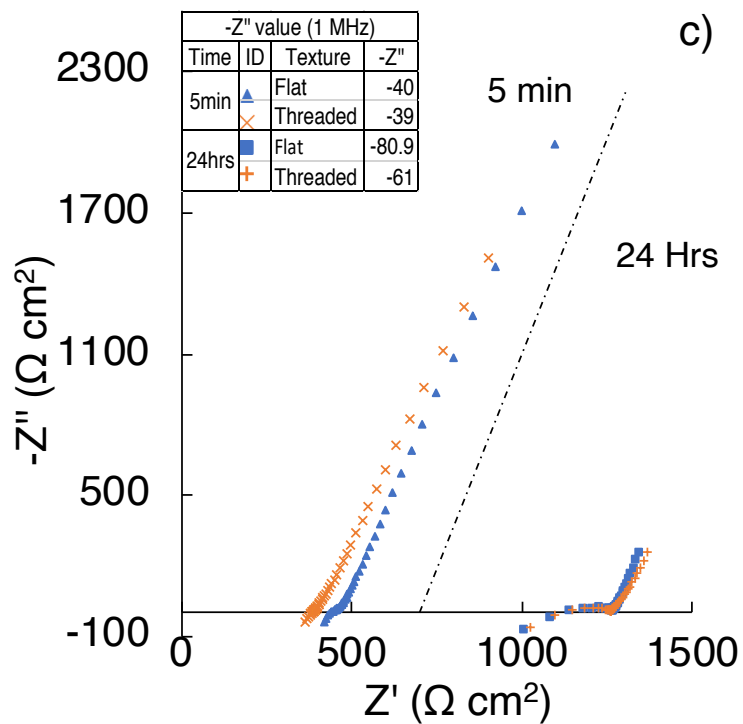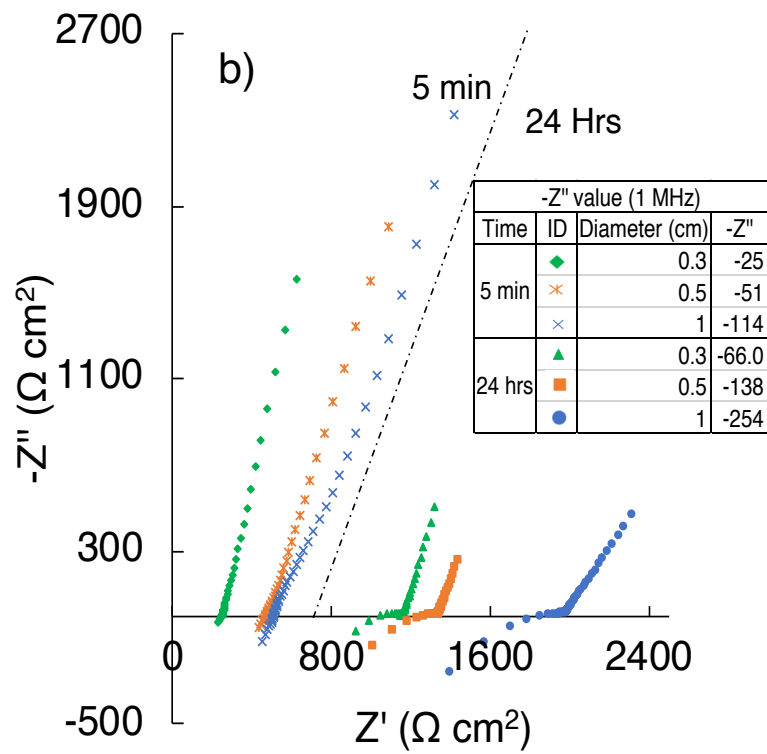
Fig. 4-9. ACIS response of wPc and gPc pastes at 5 min and 24 h after mixing, varying electrode parameters as indicated in the legend: a) electrode length, b) electrode diameter and c) texture.

Fig. 4-10 shows the short circuit cell ACIS measurements obtained from two different SS electrode diameters. ACIS measurements show -Z" negative values in which inductance effects (-Z") and the resistance values (Z' axis), produced by the leads, the cell, and the frequency dependence of both parasitic components, are observed [36], [231], [232]. The reason for a lower impedance value is explained by Eq. 1 (based on the comparison between both diameters).

$$R = \rho \frac{l}{A}$$

(1)

Here R is the electrical resistance of the electrode, ρ is the specific resistivity, l is the length and A is the cross-sectional area [231], [234]. Therefore, the electrical resistance of the electrode is expected to be reduced as the cross-sectional area decreases while the inductance effects maintain the same values because they are caused by the leads, and not by the cell specifications.
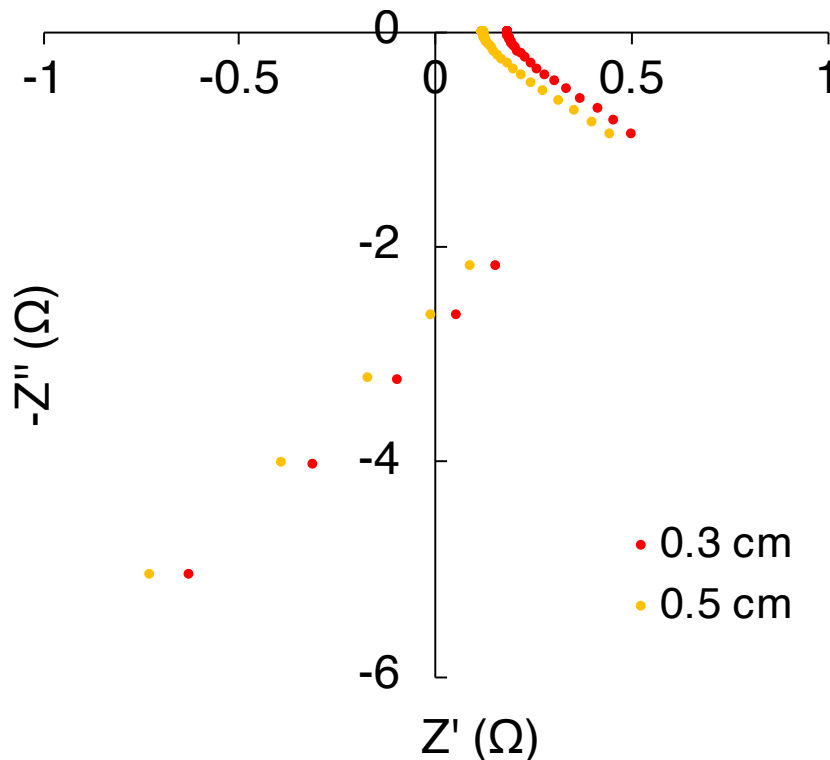
Fig. 4-10. ACIS data for short circuit calibration measurement.

Regarding the final custom cell design as a result of this parametric study, it was decided to use threaded electrodes with 3 mm diameter and 7 cm length, of which 6 cm would be in contact with the cement paste and 1 cm would be outside the cell for connection of the WE and the RE.

The decision to use this electrode specification was made considering that the threaded texture did not have a significant effect on the effective surface area for the ACIS measurements but did significantly increase the electrode-sample contact to reduce the likelihood of debonding at that interface. The electrode length (7 cm) was selected to ensure a uniform current distribution, larger values of the EDLC, and effective surface area through the cement paste [269], [273], [274]. Finally, it was observed in Fig. 10b that a decrease in the electrode diameter was able to reduce the parasitic effects, and it is expected that the lower total internal resistance of the cell would increase the fractional contribution of the cement bulk to the overall impedance measurements.

4.3.2.2 Electrode material

Fig. 4-11 shows the influence of the electrode material on the measured ACIS spectra of wPc pastes. At early age, the ACIS measurements in the high frequency range and the inductance effects are not considerably affected by the choice of electrode materials among those tested here. However, at low frequencies it is possible to observe a difference in the part of the response that is attributed to diffusional processes, due to the variation in the electrode material having an impact on the reaction rates between the cement paste and the electrode [272], [275], [276]. At longer ages, there is a greater impact on the ACIS measurements due to the choice of electrode material.

The increase in resistance, the disappearance of the inductance effects, and the emergence of a high frequency semicircular arc when using mild steel electrodes can

all be related to the combination of the response of the cement microstructure development and the formation of a protective iron oxide film on the steel surface generated by the alkaline environment of the cement paste [178], [277], [278]. The electrode surface film has a strong influence on the ACIS measurements obtained using mild steel electrodes.

Conversely, the ACIS measurements obtained with SS electrodes are determined mainly by the cement bulk and the electrode-cement interface [275], [278]–[280]. This fact is attributed to the action exerted by the chromium-rich oxide film (passive film) on the SS electrode surface giving as a result a more stable electrode response. The reaction between the cement paste and the SS electrodes is slower than the reaction involving mild steel electrodes.
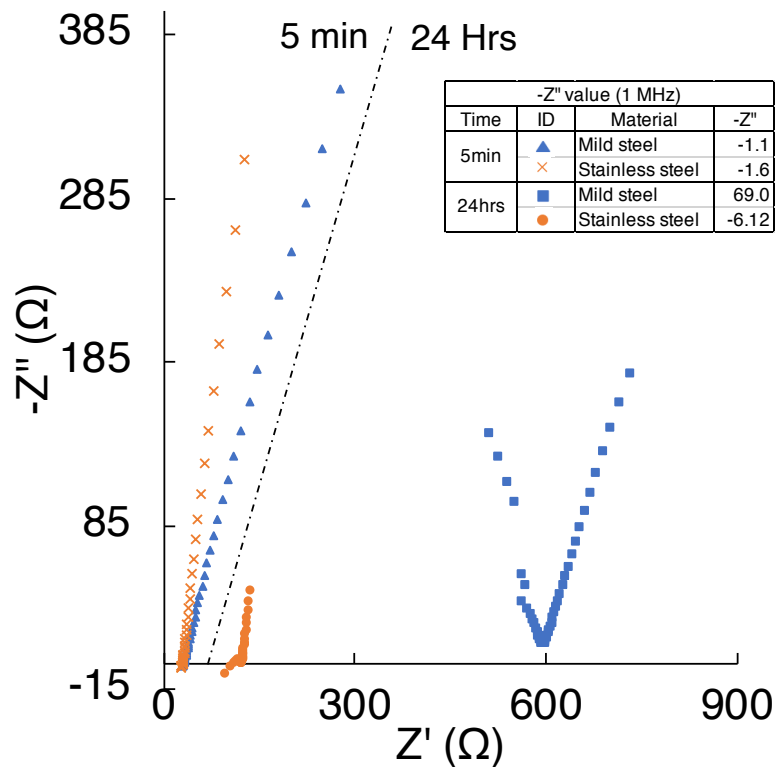
Fig. 4-11. ACIS data for wPc pastes, for different electrode materials as noted.

It is evident that the correct electrode material selection can enhance the ACIS measurements in terms of specific capacitance, diffusion rates, EDLC, accuracy, and performance [122], [280], [281]. Comparison of the ACIS results showed that SS electrodes are suitable in a highly alkaline environment, without affecting the impedance measurements and ensuring a stable electrode-cement interface and interaction, uniform current distribution, and better performance than mild steel electrodes.

Stainless steel and mild steel were considered suitable materials in this investigation. Other electrode materials, such as graphite or platinum, were not considered because of the single-use application and the higher cost.

4.3.2.3 Electrode position

Fig. 4-12 shows the effects of electrode separation effects on the ACIS spectra of wPc pastes. Taking the electrode separation distance of the initial cell (3 cm) as a reference, the results at both ages show an increase in the impedance values of Z' axis (ohmic resistance) when the electrode separation is either increased or decreased. The low-frequency response, dominated by diffusional behaviour, appears significantly less sensitive to the electrode separation.

At 1.5 cm electrode separation, inductance increases slightly because of mutual inductance effects as the separation between the electrodes is insufficient, whereas at 6.0 cm electrode separation, inductance increases considerably as the mutual inductance decreases and the self-inductance of the leads increases.
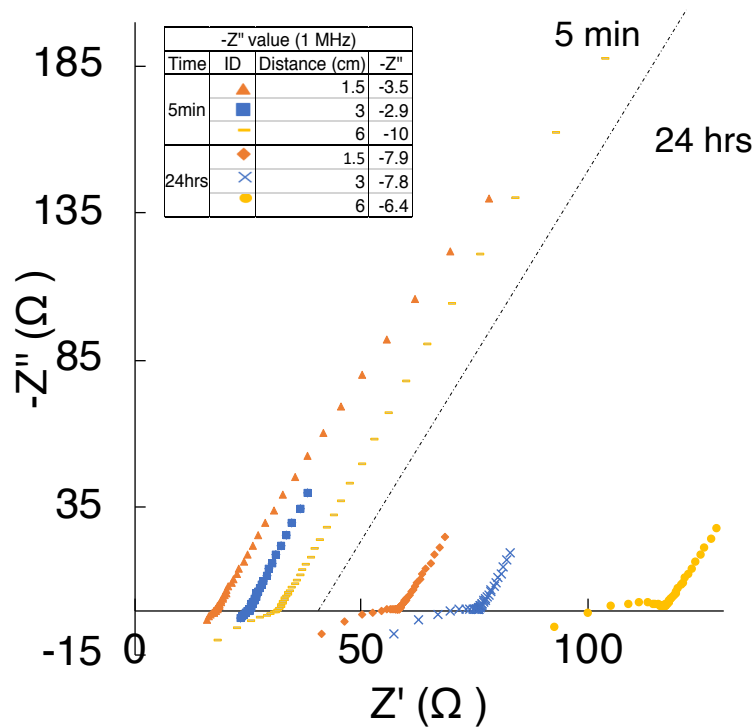
Fig. 4-12. ACIS data for wPc pastes as a function of the separation between the electrodes.

Fig. 4-13 shows the effects of the electrode positions on the impedance spectra of wPc pastes. The electrode positions studied were to have the electrodes located at the bottom (Fig. 3-1), top, and lateral faces of the polypropylene cell, without changing the distance between the SS electrodes.

At early age, the impedance measurements are not affected by the majority of the electrode positions. The only position which influences the impedance measurements is at the top of the cell, where the ohmic resistance and inductance effects increase. This tendency is probably due to cement bleeding and air entrapment produced by electrode insertion from the top of the cell filled with cement paste.

At later age (24 h), the ACIS measurements and spectra are more notably affected by the electrode positions. The vertical, horizontal and top electrode positions show an increase in the ohmic resistance values (Z' axis) and the inductance effects at high

frequencies are reduced, giving as a result the emergence of a semicircular arc. These ACIS measurements are the result of the combined response of the cement microstructural development and the ohmic resistance produced by the differential shrinkage and the potential cracking of cement generated by the thermal restrains and the stress/load of the electrodes position [169], [282].

The influence of the position of the electrodes in the ACIS measurements at later age is due to the sample geometry and the electrode direction changing the restraint of shrinkage of cement, leading to cracks that induce an increase in the ohmic resistance values [271], [283]–[287].

-Z" value (1 MHz)			
Time	ID	Position	-Z"
5min	●	Vertical	-2.2
	×	Horizontal	-2
	■	Bottom	-2.9
	▲	Top	-6.7
24hrs	×	Vertical	-2.4
	■	Horizontal	0.4
	◆	Bottom	-7.8
	●	Top	-3.3
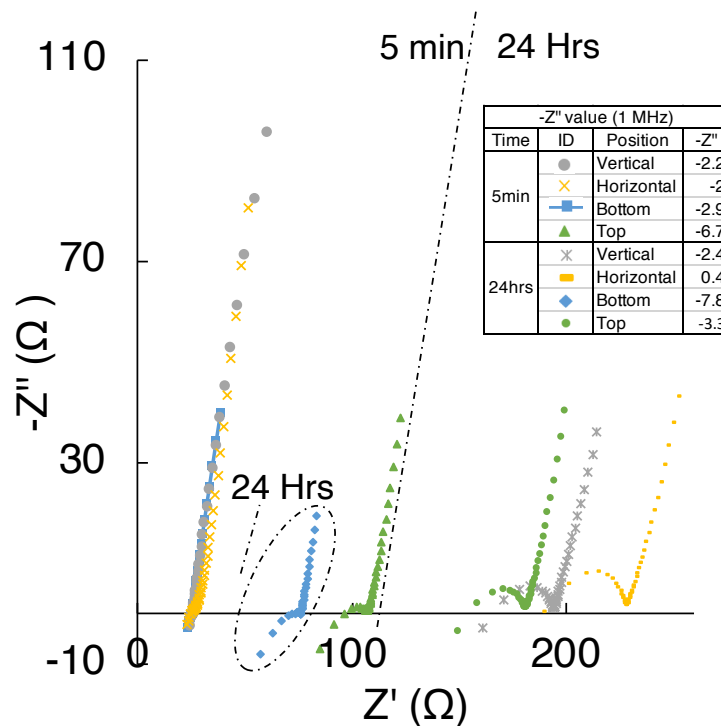
Fig. 4-13. ACIS data for wPc pastes, as a function of the electrode position.

Based on these results and considering the practicalities of cell construction and loading, it was decided to position the electrodes at the bottom face of the custom cell since this location showed a better performance on the ACIS measurements, without cracks appearing in the hardened cement, and ensuring consistent measurement of the cement paste.

4.3.3 Calibration and measurements correction

Calibration experiments followed the same experimental procedure and the set-up used in the previous cell design test, as any change in the configuration affects the ACIS measurements and therefore the calibration values (Fig. 4-8d). The ACIS measurement corrections were carried out after verifying the reproducibility of the short circuited custom cell design measurement, and considering the calibration measurements as an additive correction to the ACIS measurements [37], [171], [231], [232].

Fig. 4-14 shows the impedance spectra before and after application of these corrections, for wPc at early age. After the correction, the impedance spectra show high frequency data above the Z' axis, with a high frequency semicircular arc, while the measurements at low frequencies do not change. For correct data interpretation, it is necessary to apply this correction to the raw ACIS measurements.
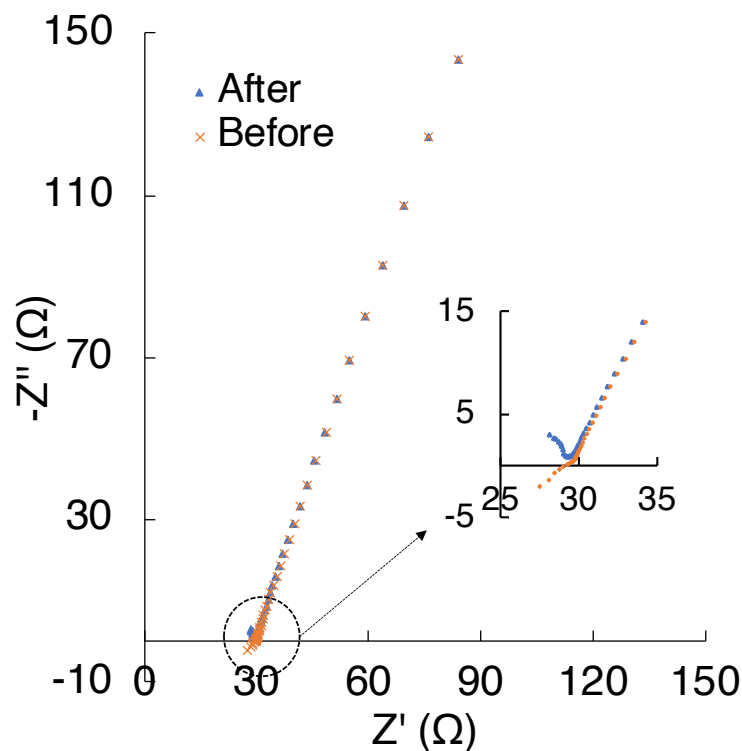
Fig. 4-14. ACIS data for measurement correction of wPc system.

4.3.4 ACIS of white Portland cement

To select a cell design, the evaluation of ACIS measurements for different cell parameters was presented in the preceding sections. Fig. 4-15 shows the custom cell design specification involved the use of threaded SS electrodes ($\phi\,0.3 \times 7$ cm) and the cylindrical polypropylene container ($\phi\,6 \times 11.2$ cm) used for the following experiments. The time between measurement acquisitions was every 5 min (0-24 hrs), 10 min (24-48 hrs), 15 min (48-72 hrs) and 20 min (72-92 hrs). Subsequently, the impedance data were calibrated and corrected.
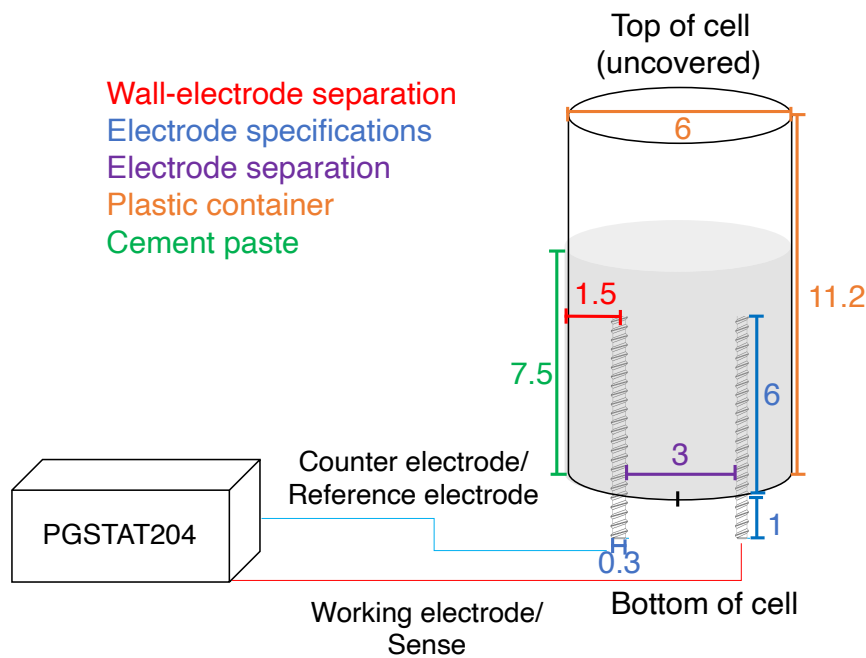
Fig. 4-15. Final cell design diagram (scale cm).

Fig. 4-16a shows the ACIS spectra of wPc during the first 92 hours after mixing. Before the first 3.5 hrs, the inductance effects are removed from the ACIS spectra by application of the calibration and correction as described above. However, after 3.5 hrs, inductance effects suddenly appear (followed by an increase in Z' values), showing a decreasing trend which disappears after 30 hrs. At longer ages and as the

hydration proceeds, the emergence of semicircular arcs at high frequency is more developed, while the increase of Z' axis values becomes slower due to the thickness of the hydrated products increases and the hydration process slows [14], [170], [226].

The conductivity was obtained from the resistivity of the wPc paste by dividing the Z' axis intercept point of the impedance spectra into a cell constant. The cell constant was obtained by measuring the ACIS response of different concentrations of NaOH solutions of known conductivity [153], [218], [234]–[236], using the cell shown in Fig. 4-15. Fig. 4-16b shows the conductivity and resistivity as a function of time for wPc. On the first day of the hydration reaction, three perturbations are observed as the resistivity increases slightly and the conductivity drops quickly. At longer ages, the resistance increases rapidly, showing an increase in the amplitude and number of perturbations, while the conductivity decreases reaching a point where the changes in conductivity are minor.

Fig. 4-16c shows a second perspective of the impedance spectra of wPc, by plotting the real component (Z') against time for two different frequencies. At early ages, between 3.5-10 hrs, the Z' values at high frequencies decrease as inductance emerges (highlighted), while the Z' values at low frequencies change slightly. At longer ages, Z' values at both frequencies show an increasing resistance behaviour.

Fig. 4-16d shows a different perspective of the impedance spectra of wPc by plotting the imaginary component (-Z'') against time. The results show small changes at high and low frequencies. To illustrate the inductance behaviour between 3.5-30 hrs, -Z'' values at 100 Hz and 1 MHz are highlighted. At early ages, the -Z'' values at 1 MHz rapidly decrease and become negative due to the emergence of inductance effects, while -Z'' values at 100 Hz decrease slowly, reaching a minimum value at 10 hrs and followed by a short increase period between 10-14 hrs. At longer ages, an increasing tendency of -Z'' values is observed at 1 MHz, in which the -Z'' values once more become positive at 30 hours due to the disappearance of inductance effects. The -Z'' values at 100 Hz decrease until 50 hrs, reaching a period with low activity.

a)

b)
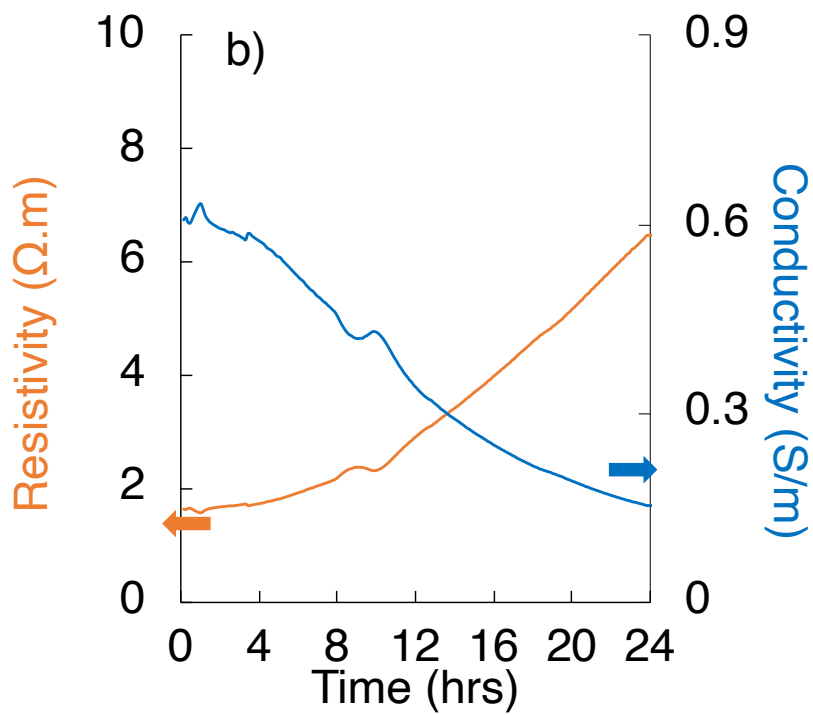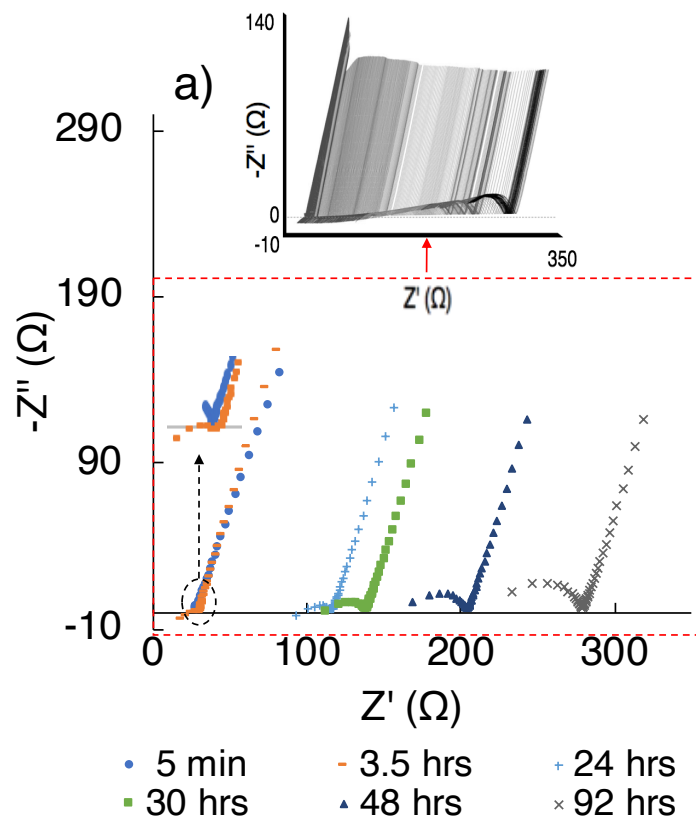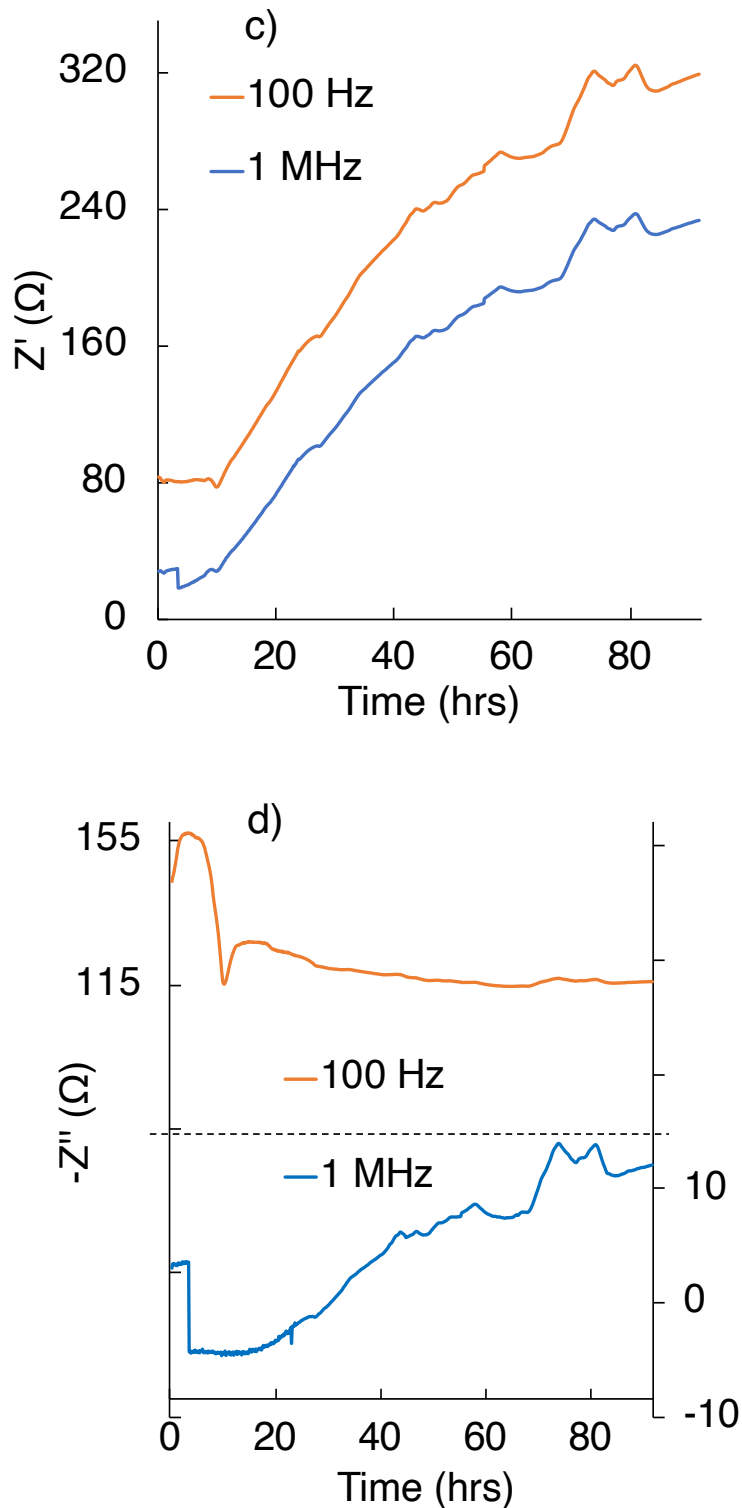
Fig. 4-16. ACIS response of wPc paste as indicated in the legend: a) Nyquist plots; b) conductivity and resistivity; and for frequencies of at 100 Hz and 1 MHz, c) the real component, and d) the imaginary component.

Cement hydration is divided (usually on the basis of calorimetric results) into five stages: dissolution, induction/dormant, acceleration, deceleration/diffusion, and long-term reaction [4], [6], [44]. The chemical and microstructural processes taking place during these stages are also identifiable in the ACIS data. At early ages (dissolution and induction stages), the results show small impedance and resistivity values due to the high conductivity of the cement paste (with ions in the aqueous phase supplied by the rapid dissolution of soluble alkali and calcium sulphates), and limited solid phase microstructural development. At 3.5 hrs after mixing, the ACIS values at high frequencies are affected by the sudden emergence of inductance effects. Between the end of the induction period and the beginning of the acceleration period, the dissolution of C_3S and C_2S increases the ionic strength of the cement paste pore fluid, followed by the nucleation of C-S-H and initial crystallisation of CH. At this point the resistivity starts to decrease.

During the deceleration period, the heat flow and reaction rate of silicates decreases, and the microstructure is affected by water consumption, pore reduction, and space limitation. At this point, the results show increasing Z' values (Fig. 4-16c), and the inductance effects (-Z") remain unchanged. At approximately 10 hrs, the low frequency values in Fig. 4-16b decrease, while the Z' values in Fig. 4-16c show a perturbation at both high and low frequencies.

At the end of the deceleration period and during the long-term reaction period (~15 hrs), the inductance effects (-Z") start to decrease, until they disappear at 30 hrs. The Z' values keep increasing at both frequencies, probably because of the microstructural development, reduced water content, and the partial closure and eventual depercolation of the pore structure.

At longer ages (>30 hrs), a high-frequency arc starts to emerge, and while the microstructure continues developing slowly, the diameter of the high frequency arc increases, as can be observed in

Fig. 4-16a. The conductivity decreases to reach a certain point where no further significant changes can be appreciated, while the resistivity keeps increasing due to the slow microstructural development [4], [34], [67].

4.4 Conclusions

This chapter has assessed the electrochemical cell design and ACIS measurements during cement hydration in the early stages of hydration, in both the fresh (fluid) and . The results demonstrate the importance of the correct assessment of the parameters (e.g. electrode, lead and parasitic effects, and procedure) in the cell design to reduce the parasitic effects that appear in ACIS data.

A good correlation between the ACIS measurements and the cement hydration stages was obtained. However, due to the limited solid phase microstructural development and the high conductive condition of cement at early hydration periods, the parasitic effects could not be fully corrected until the cement had hydrated sufficiently to yield a microstructure that was able to raise the resistivity of the paste.

It is therefore possible to highlight the following conclusions:

1. ACIS measurements at early cement hydration ages (>24hrs) can be performed using the final custom-cell design proposed, allowing this design to reduce the parasitic effects at high frequency.
2. ACIS response and parasitic effects are directly affected by electrode effects and cell design.
3. Cement conductivity and resistivity behaviour, and their variation as a function of time during hydration correlate with existing conceptual models developed from calorimetric and other data.
4. ACIS has been shown to be a sensitive and versatile technique for assessing the different stages of cement hydration, from the fresh to the hardened state, which is very difficult to probe truly continuously by any other single technique in a time-resolved manner. However, in order to fully understand this process

and its microstructural development, the behaviour and interpretation of ACIS measurements and the parasitic effects that complicate the data processing and analysis need further investigation, supported by other characterisation techniques.

Chapter 5:

PORTLAND CEMENT

Note: This chapter is based on the paper *"Early-age characterisation of Portland cement by impedance spectroscopy"* by A. F. Sosa Gallardo and J. L. Provis, [39], unpublished manuscript and submitted for publication, 2020, pp.1-39.

5.1 Introduction

The objective of this chapter is to assess the early hydration process of Portland cements at different sand, anhydrite, and water contents by evaluating the electrochemical (ACIS), thermochemistry (IC) setting time (Vicat) response, and by comparison with pore solution compositional data available in the literature. Comparison among these techniques is important to understand the major aspects that influence the electrochemical behaviour of cement pastes during the first 24 hrs after mixing, both before and after setting. Potential factors that may affect impedance measurements and data interpretation are also discussed, such as the complexity of cement chemical composition, its physical properties and hydration kinetics, and technique limitations. The impedance data obtained are benchmarked against different supporting techniques and literature data, showing a strong relationship among hydration rates as determined by thermochemistry, setting time measurements by physical approaches, pore fluid chemistry, electrical conductivity, and the impedance behaviour observed. The results demonstrate that ACIS is a sensitive technique to assess cement hydration, enabling differentiation of changes in the water and cement content, hydration degree, and microstructural development during the first 24 hour after mixing.

5.2 Sample specifications

To support ACIS data interpretation, five groups of Portland cements at different w/c ratios, and replacement levels of sand or anhydrite, were assessed by ACIS measurements and supported by calorimetry and setting tests. The first group consisted of wPc hydrated at different w/c ratios (0.35-0.60). Table 5-1 shows the sample specifications of each of the other groups, which were all formulated at a constant w/c ratio of 0.45. Grey cement was used as a comparison to the wPc results; three sand replacement levels and three dosages of anhydrite were tested.

Table 5-1. Sample specifications.

No.	Parameter	Amount			*w/c
1	wPc (%)	100			0.35-0.60
2	wPc (%)	100			0.45
3	gPc (%)	100			
4	wPc (%)	80	60	40	
	Sand (%)	20	40	60	
5	wPc (%)	100	99	90	
	Anhydrite (%)	0.5	1	10	

5.3 Results and discussion

5.3.1 White Portland cement and grey Portland cement (wPc and gPc)

The presence of significant quantities of Fe_2O_3 and MnO gives gPc, one of the most used cements, its grey colour. On the other hand, wPc which is usually used for aesthetic architectural applications, differs from gPc by having a limited amount of Fe_2O_3, and MnO, higher free CaO content, and a higher content of C_3A. It is sometimes often more finely ground, as is the case for the cements studied here. In

general wPc, due to the high energy consumption required for its production, is more expensive than Portland cement. [6], [7], [9]. The pore solution of wPc is slightly different from other Portland cements since it has a lower alkali content (i.e. K and Na), producing a decrease in the available content of SO_4^{2-} and OH^- ions available to react with C_3A during hydration, lowering the production of ettringite [66], [288].

The calorimetric curves of wPc and gPc during the first 24 hrs after mixing are shown in Fig. 5-1a. The hydration stage timings in wPc and gPc are similar, however a higher release of heat is observed for wPc paste due to the rapid hydration of C_3A, ettringite formation, and the smaller particle size and higher surface area of this cement. At the end of the acceleration period gPc shows two shoulders (between 6 and 8 hrs) which are attributed to the hydration of C_3S and C_3A, and the formation of C-S-H and ettringite [66], [81], [289], [290].

Fig. 5-1b shows the penetration depth of the Vicat needle into wPc and gPc. The initial and final setting times are reached at similar times, with setting observed for the gPc paste slightly faster than the wPc. This is attributed to a more stable transformation of ettringite into AFm and the formation of secondary phases as a result of a higher sulphate content in gPc paste, showing an earlier acceleration and more gradual heat release [80], [81].
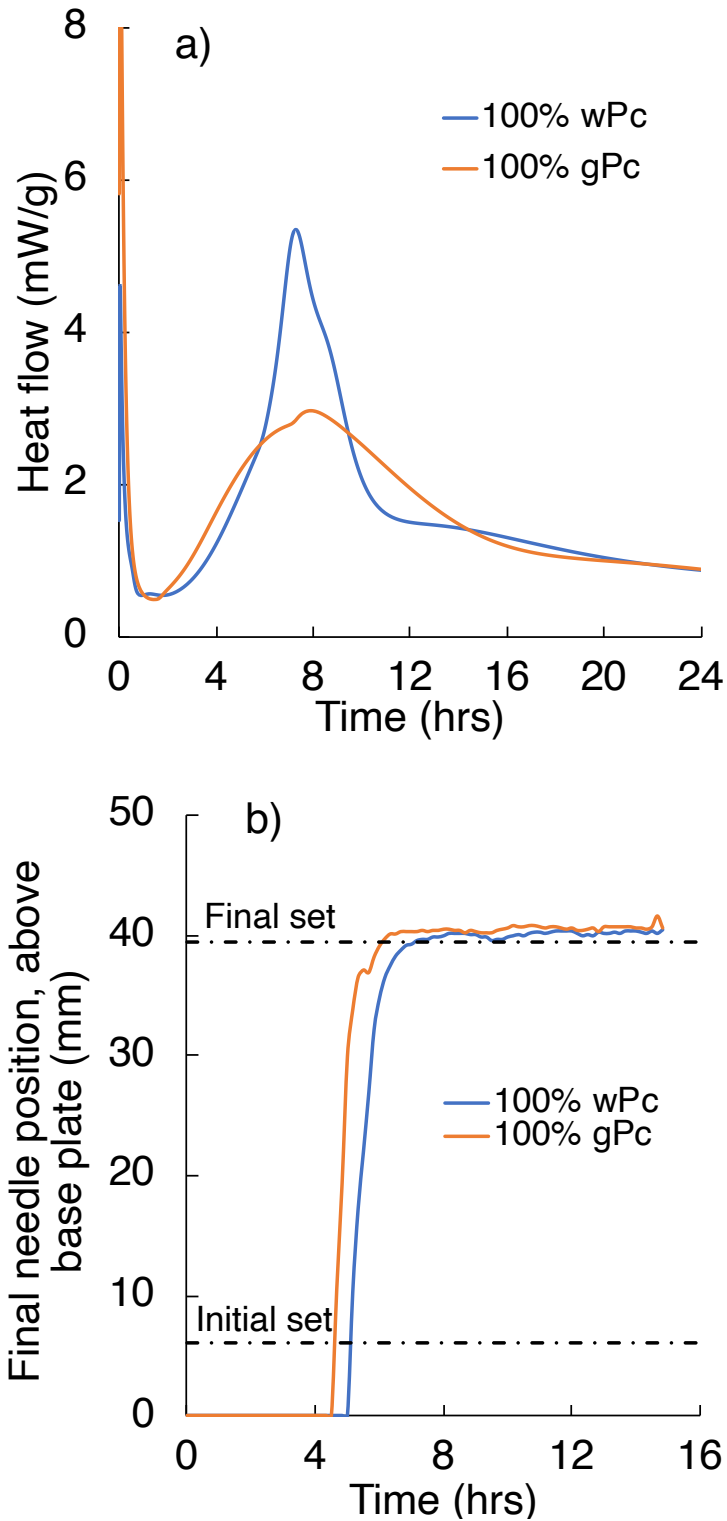
Fig. 5-1. wPc and gPc at w/c=0.45: a) heat flow, b) Vicat determination of setting time.

The ACIS and resistivity/conductivity measurements of wPc and gPc during the first 24 hrs after mixing are shown in in Fig. 5-2a-b. Fig. 5-2c-d show the ACIS response of wPc and gPc by representing the measurements in terms of resistance and reactance as a function of time and frequency.

At early ages and in both pastes, a semicircular arc of small impedance is obtained due to the high conductivity of the cement paste (Fig. 5-2a). At high frequency, wPc shows a higher impedance and resistance than gPc, an effect that is attributed to the higher particle surface area, the particle size distribution, and the conversion of C_3A to ettringite, leading to an early-age paste that contains a higher volume of hydrate products [108]. The wPc shows a conductivity perturbation at 1 hr after mixing, and gPc shows the same perturbation at approximately 2 hrs after mixing (Fig. 5-2b) [37]. Also, the dormant period in Fig. 5-1a is longer for wPc paste, but the ACIS measurements do not change.

During the acceleration period, the conductivity of the gPc paste drops considerably faster than that of the wPc paste, while the gPc and wPc bulk resistance increase sligthly. This drop is attributed to the decrease of ionic concentrations and their reduced mobility as the microstructure evolves [68], [291]. The wPc ACIS measurements are affected by parasitic effects at high frequency at around 4 hrs after mixing, while gPc ACIS measurements are affected at longer times. The appearance of parasitic effects in the impedance measurements was associated with the beginning of this period in which the ionic species concentrations and pH rises, incorporating alkaline species into the clinker and hydrated phases [37]. Also, during this period, the heat release increases as the crystallisation of CH and the precipitation-nucleation of C-S-H take place [4], [94], [292], [293].

During the deceleration period, both cement pastes show an increasing bulk resistance (Fig. 5-2c). At this point the capillary aqueous phase and pore connectivity are reduced, the microstructure is more fully developed (with limited available space for new hydrated products), and C-S-H gel keeps increasing (Fig. 5-3a-b), [148], [185],

[290]. At approximately 14 hrs, the high frequency ACIS data for gPc are affected by parasitic effects (Fig. 5-2c-d), which merits further investigation.

At later ages and at high frequency, where the wPc impedance and bulk resistance values are greater than in gPc pastes (Fig. 5-2c), there is a decreasing tendency in the conductivity and parasitic effects of both pastes due to the reduction of free water content, and limited space for growth of new hydrated products via constant microstructural development, leading to a larger bulk semicircular arc [13], [29], [36], [139], [293], [294].
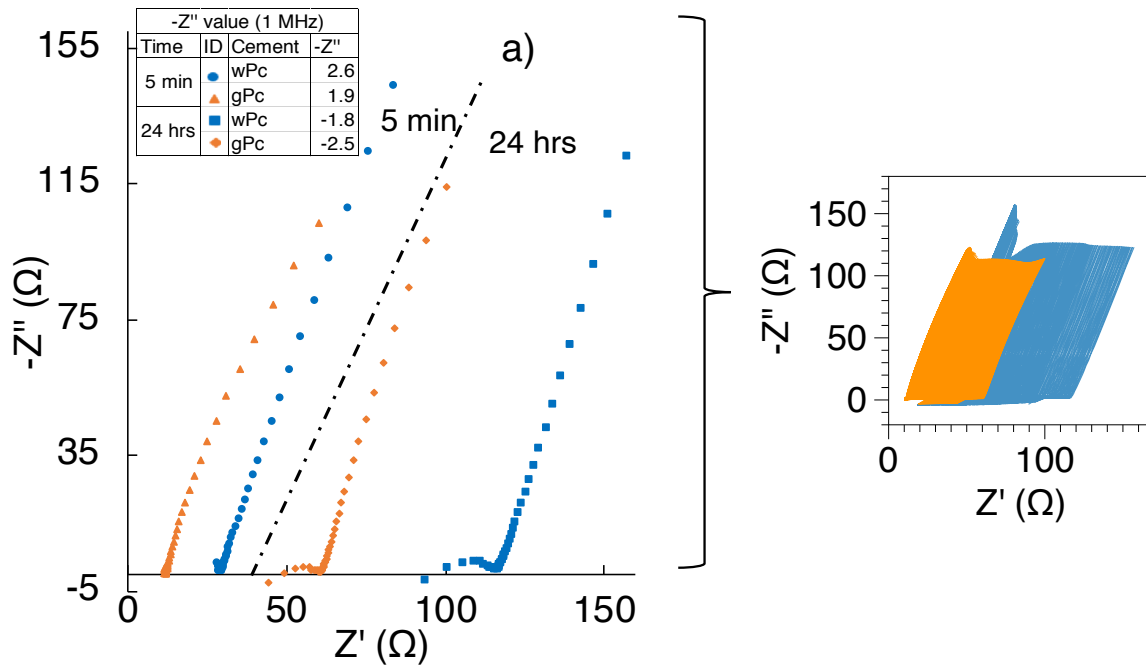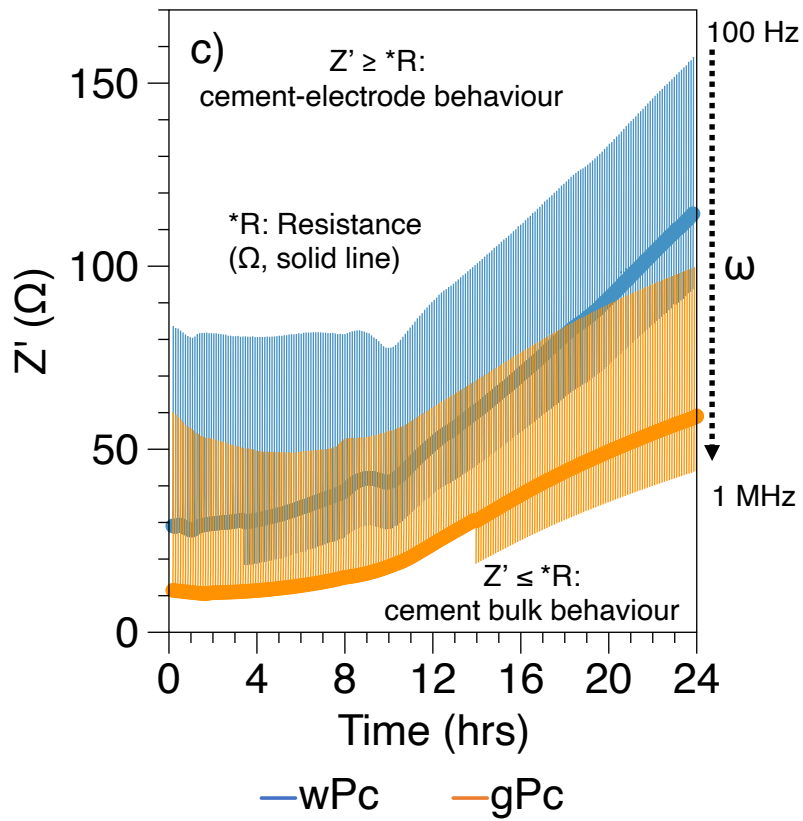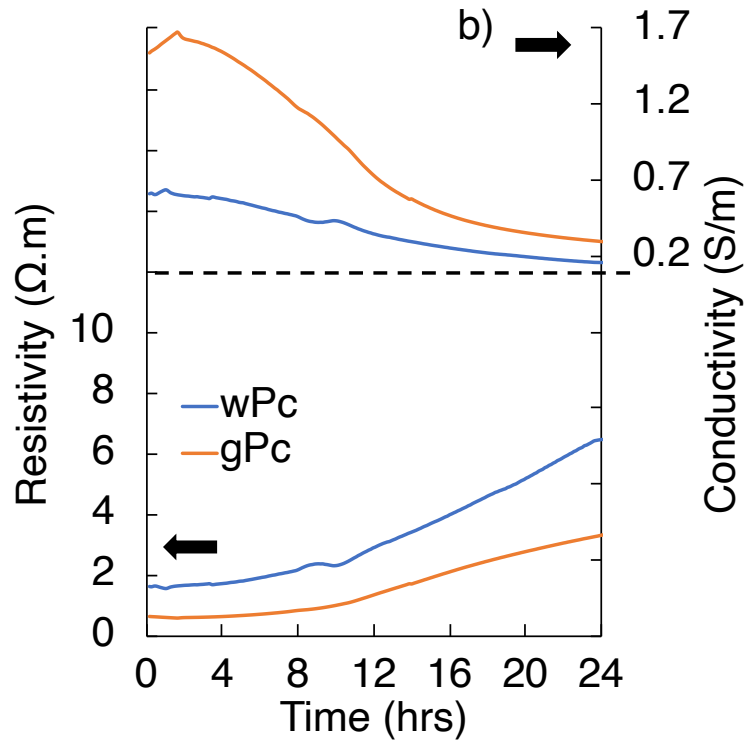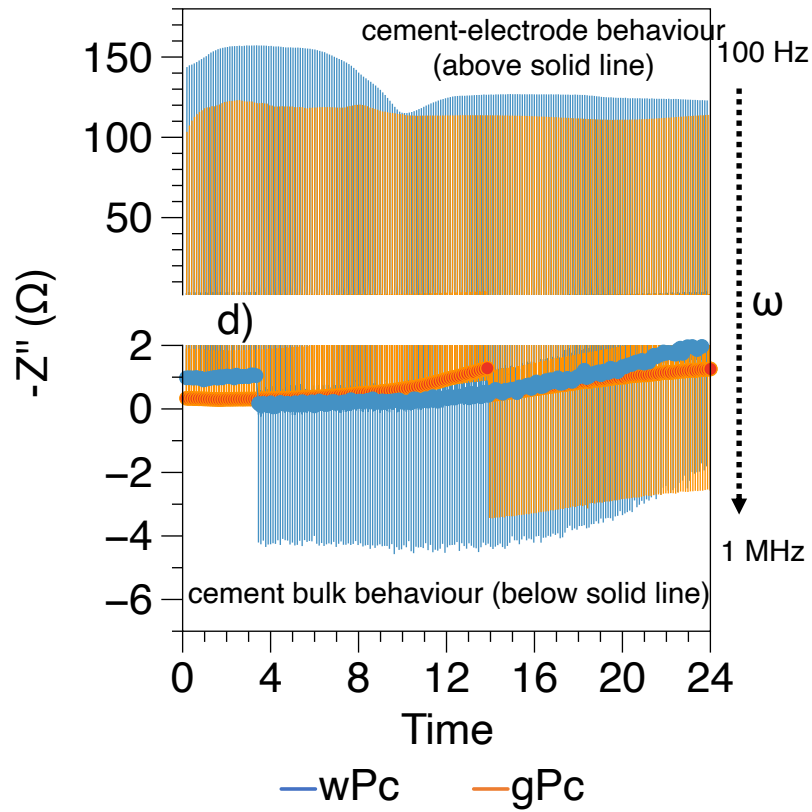
Fig. 5-2. ACIS response of wPc and gPc pastes at w/c = 0.45 as indicated in the legend: a) Nyquist plots; b) conductivity and resistivity; and from 1 MHz to 100 Hz c) real component and d) imaginary component.

a) gPc   24 hrs   500 μm

b) wPc   24 hrs   500 µm
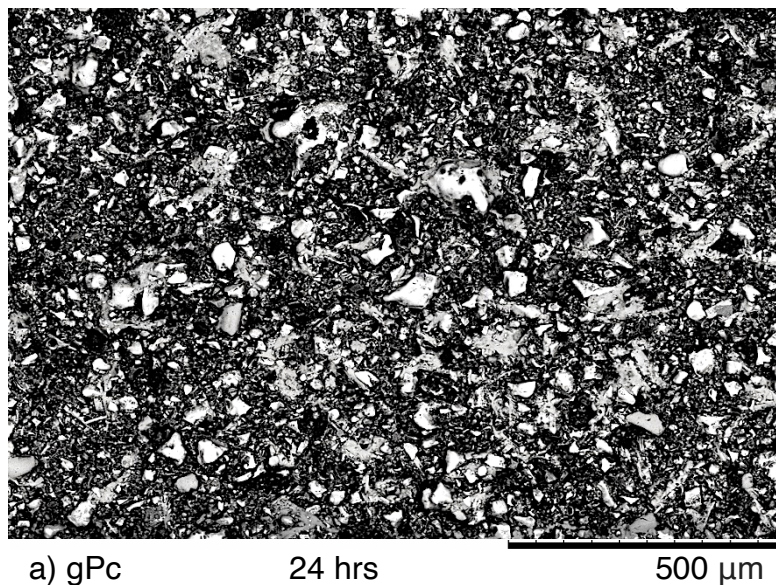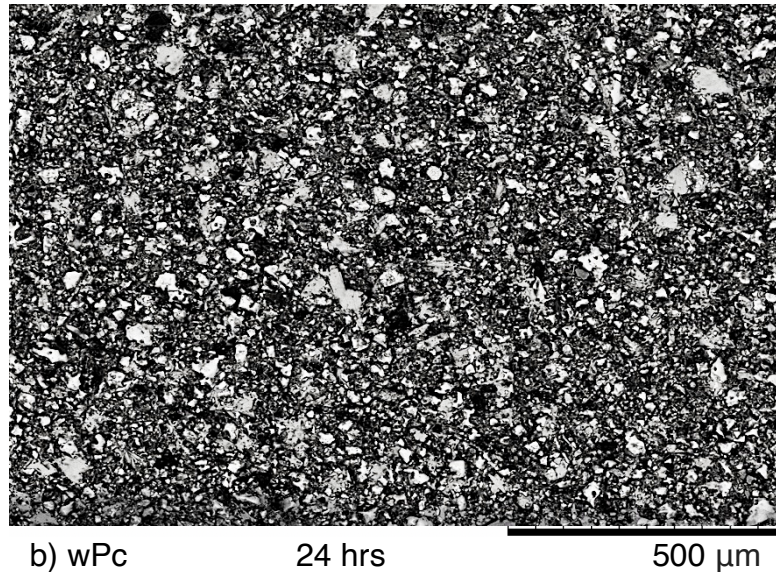
Fig. 5-3. SEM images of gPc (a) and wPc (b) paste at 24 hrs after mixing.

5.3.2 Effects of water to cement ratio (w/c)

As the w/c ratio affects the space among the cement particles, kinetics of hydration, setting-hardening times, and microstructure, the water content becomes a major factor influencing the hydration mechanisms and the final mechanical properties of cement [103], [109]. Regarding the pore solution, the w/c ratio influences the K, Na and alkali concentrations, while it slightly affects the concentrations of Si, Al, Ca and SO_4^{2-}. The concentrations of Ca and SO_4^{2-} are restricted due to the solubility limitations of $Ca(OH)_2$, and ettringite and AFm, respectively [56]. Ca, Si, Al and OH^- concentrations are affected as the hydration proceeds and pH rises, as a result of the calcium sulphate depletion and precipitation of CH [110].

The calorimetric curves of wPc at different w/c ratios during the first 24 hrs after mixing are shown in Fig. 5-4a. A slight influence of different w/c ratios on the wPc hydration kinetics at early ages is observed. As the w/c ratio increases, the degree of hydration increases and the maximum peak of heat release decreases due to the

higher degree of dilution, and the availability of more space for the precipitation, nucleation and crystallisation of hydrated products [1], [5], [103], [109], [295], [296]. As the hydration rate decreases, a delay in the acceleration period is observed due to the pore solution saturation being reached at longer times. However, the trends in all the calorimetric curves remain similar.

Fig. 5-4b shows the penetration depth of the Vicat needle into wPc at different w/c ratios. A faster initial time is observed, as the water content decreases, due to a lower degree of hydration, porosity and free water content make it easier to fill the space between the cement grains, producing a high-density cement paste [194]–[196].
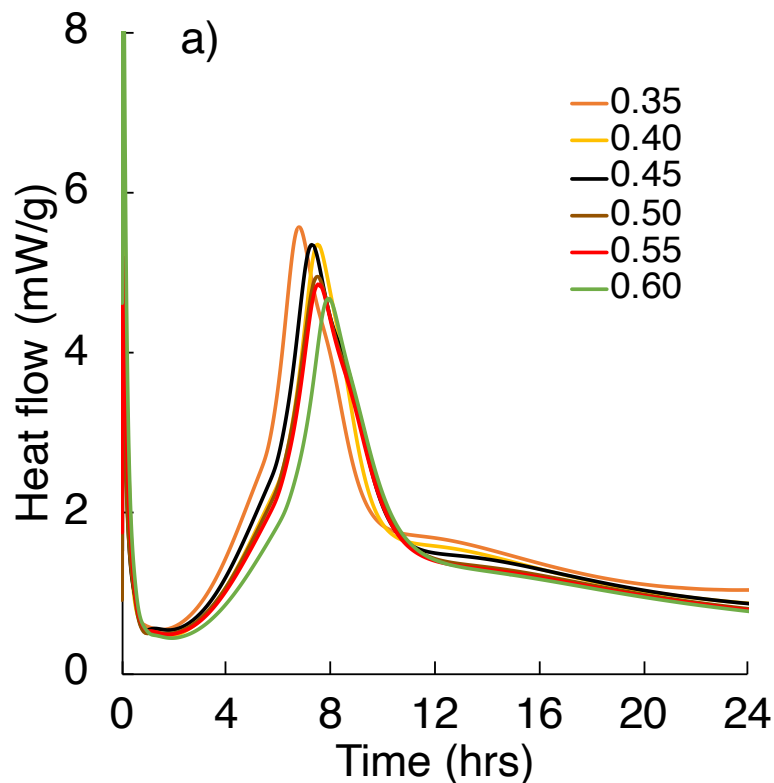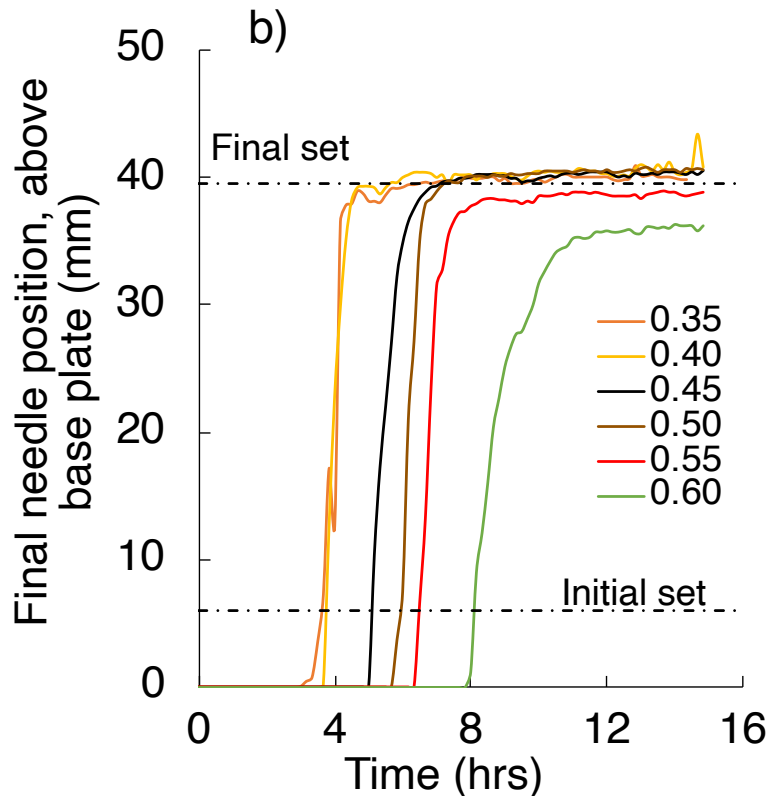
Fig. 5-4. wPc at different w/c ratios: a) heat flow, b) Vicat determination of setting time.

The ACIS data, and specifically resistivity/conductivity measurements, of wPc hydrating at different w/c ratios during the first 24 hrs after mixing are shown in Fig. 5-5a-b. Fig. 5-5c-d show a different perspective of the wPc ACIS response at different w/c ratios, by representing the measurements in terms of resistance (Z' axis), and reactance (linked to capacitance; -Z'' axis), over time and frequency.

At early hydration periods (5 min), a semicircular arc of small impedance values at high frequency and low bulk resistance are observed due to the high conductivity of cement paste, which is attributed to the initial dissolution of alkali sulphate phases into the aqueous solution surrounding the cement grains [25], [145], [159].

During the acceleration period, and as mentioned earlier, the impedance measurements at high frequency are affected by parasitic effects, obscuring the resistive and capacitive behaviour of the paste. The impedance measurements at high frequency are affected by some expected parasitic features from 3.5 to 8 hrs depending on the w/c ratio [6], [7], [9], [164], [226], [297].

In the impedance measurements at high frequency, a delay in the rise of parasitic effects is observed as the cement water content increases (Fig. 5-5d). This is due to an increase of the dilution degree, the available space, the porosity of the system, and a decrease in the hydration rate [150], [152], [298]. At this stage the pore solution is saturated or oversaturated with respect to $Ca(OH)_2$ [110].

As the hydration process continues and the concentrations of Ca and SO_4^{2-} decrease, due to the precipitation of $Ca(OH)_2$ and ettringite, the impedance and bulk resistance values increase. Bulk resistance and reactance perturbations (at low frequency) are observed between 8 to 12 hrs, during which time the maximum heat release (end of acceleration period), final setting time, and the beginning and middle stages of the deceleration period take place [1], [114], [122], [169].

At longer hydration ages (24 hrs), the calcium sulphate from the cement is fully consumed and, as the impedance and bulk resistance values increase, the parasitic effects show a decreasing tendency due to the reduction of free water content, low hydration rate and a more highly developed microstructure [6], [7], [9], [226], [297]. At this point, the conductivity of the sample maintains a decreasing tendency and the effect of pH within the pore solution is smaller. This is attributed to the microstructural percolation and lower OH^-, SO_4^2 (controlled by AFm) concentration in the pore solution. Also, as the w/c ratio decreases (Fig. 5-5b), the resistivity measurements increase due to a more refined pore size distribution and a lower free water content in the pores. Although the degree of hydration rises as the w/c ratio increases, lowering the alkali concentration and increasing the amount of hydrated products, higher resistivity values are obtained for pastes with lower w/c ratios. This demonstrates that

the impedance response at this stage is mainly controlled by the percolation and pore size distribution of the microstructure (Fig. 5-6a-b), [164], [299], [300].
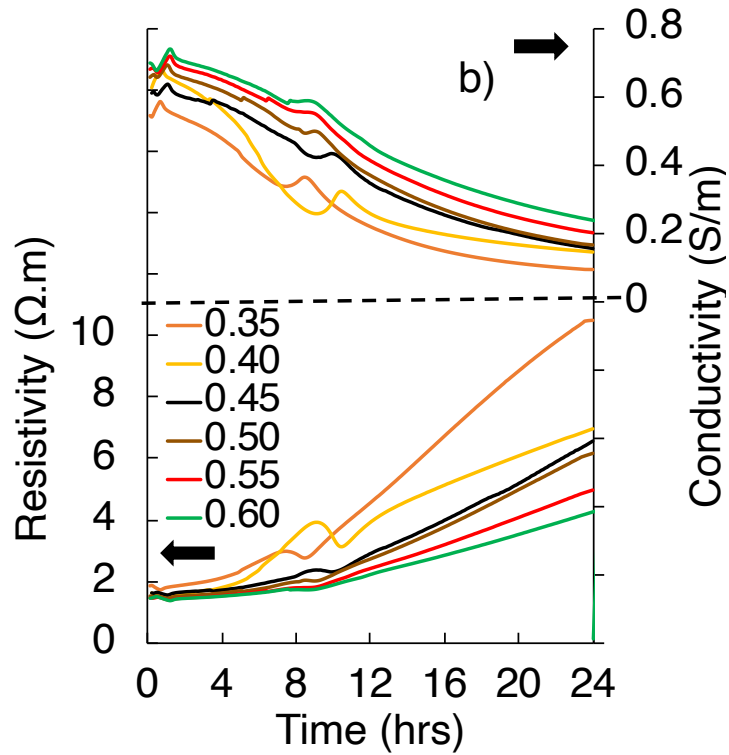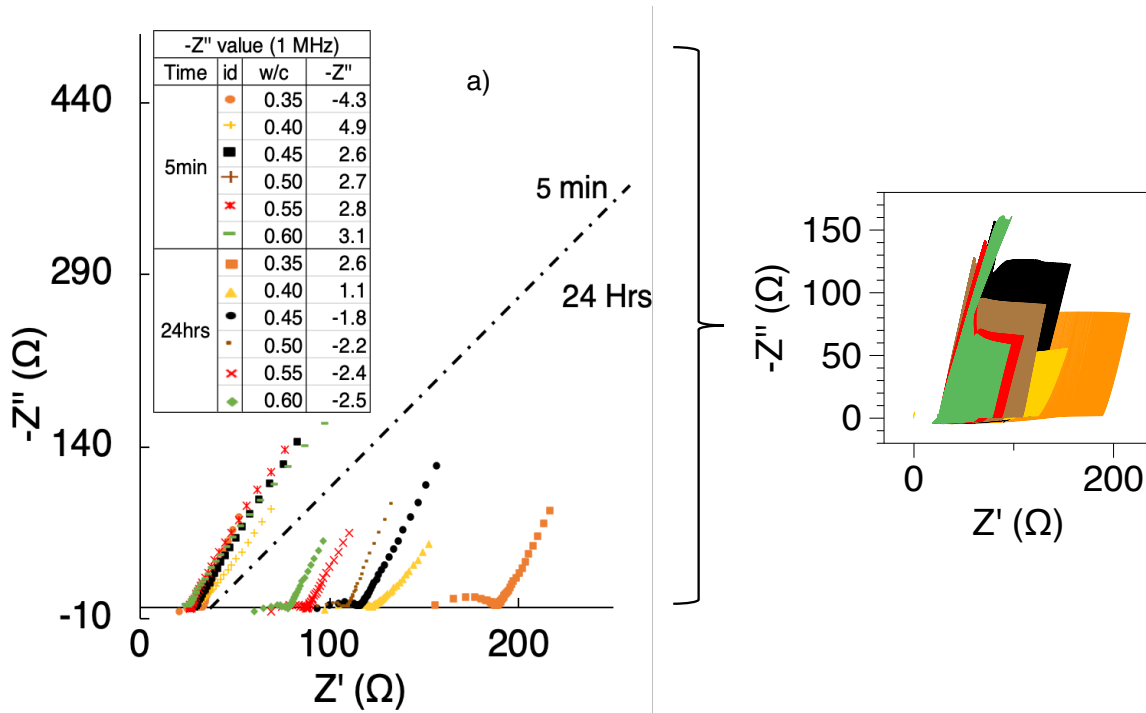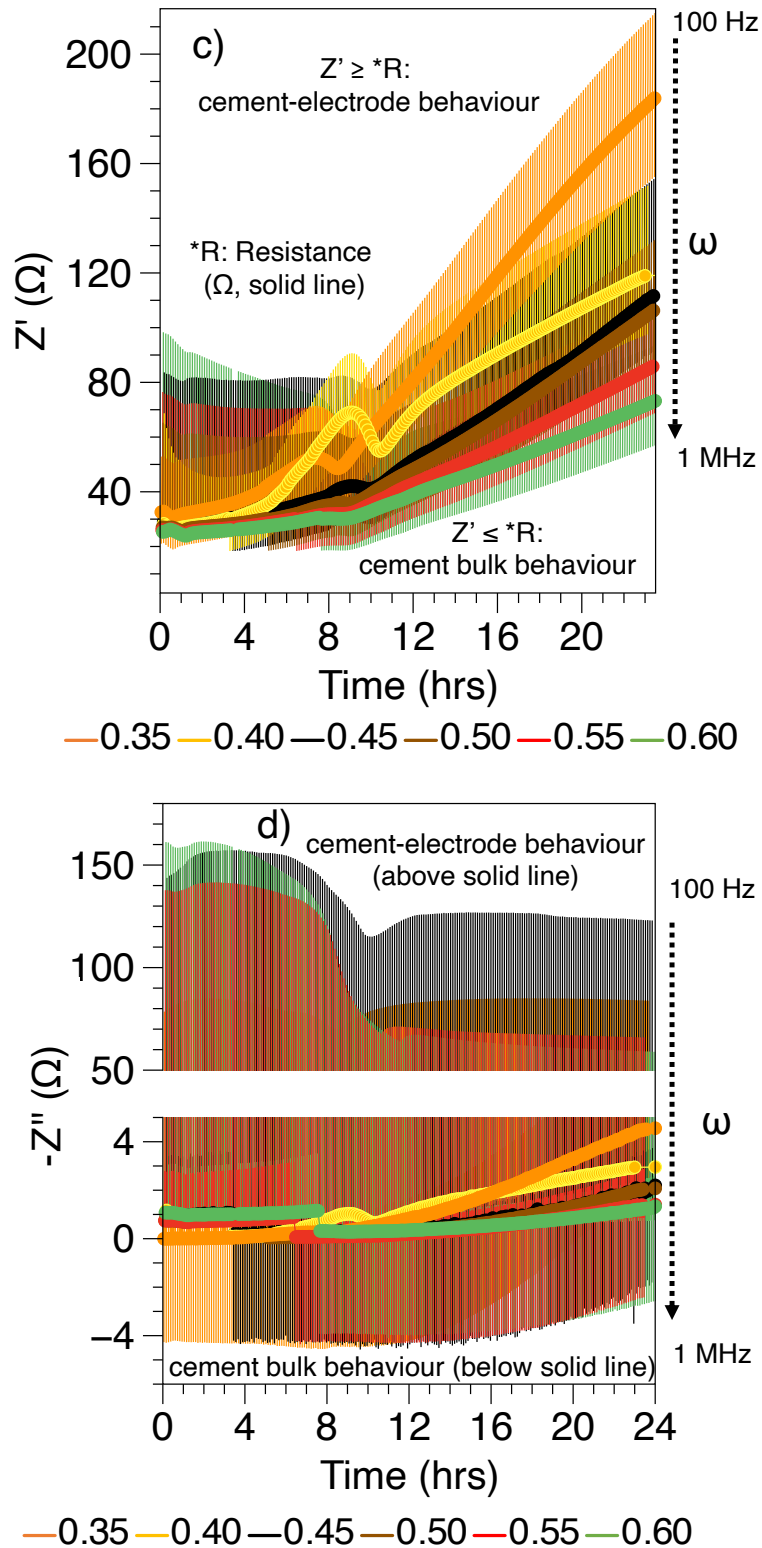
Fig. 5-5. ACIS response of wPc pastes with different w/c ratios as indicated in the legend, at 100 Hz and 1 MHz: a) Nyquist plots b) conductivity and resistivity, and at 100 Hz and 1 MHz c) real component, and d) imaginary component.
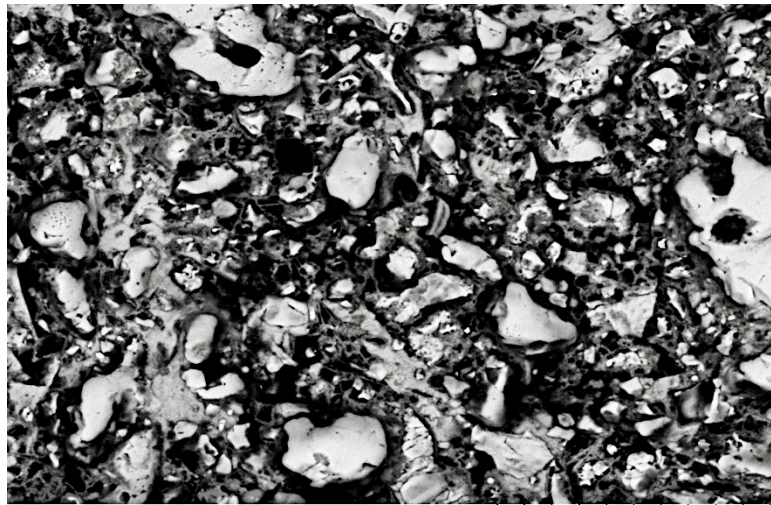
a) wPc (w/c:0.35)   24 hrs   50 µm

b) wPc (w/c:0.45)   24 hrs   50 µm

Fig. 5-6. SEM images of wPc pastes at 24 hrs after mixing: (a) w/c 0.35 (b) w/c: 0.45.

The wPc hydrated at w/c: 0.35 (Fig. 5-6a) shows a slightly denser pore size distribution, and higher percolation of the microstructure, while wPc at w/c: 0.45 (Fig. 5-6b) shows a higher capillary porosity and lower hydrated product content.

5.3.3 Effects of sand addition

Sand is used in cementitious materials as an inert aggregate material that behaves as a filler, changing the mechanical properties, alkali concentration in the pore solution, kinetics of reaction, and the development of the microstructure. Also, the use of aggregates such as sand can influence the air voids content, pore size distribution and pore volume of mortars and concretes [7], [139].

At early ages, the pore solution of mortars depends mainly on the alkali content in cement and the free water content in the system affecting the NaOH and KOH concentration and the rate of hydration and kinetics of reactions, respectively. At longer ages, the use of sand slightly affects the OH$^-$ concentration and reduces the pH due to a dilution effect [6], [301], [302].

Fig. 5-7a shows the calorimetric curves of wPc at different sand replacement levels during the first 24 hrs after mixing. As the sand replacement level is increased, a delaying effect on the hydration process, related to dilution associated to a filler effect, is observed. Also, the decrease in the amount of reactive constituents per volume of material as a result of the addition of sand reduces the heat release, and brings some change in the microstructural development due to nucleation and other effects [303], [304].

The appearance of C_3S and sulphate depletion peaks at lower heat and the same times after mixing, due to the hydration kinetics of cement, are observed. Sand is considered to be an inert material that does not affect the chemistry of cement; however, it has a notable impact on the hydration process by increasing the space among the cement particles, and by inducing an acceleration of the hydration reactions. The sulphate depletion peak is more noticeable for mortars than pastes due to a delayed conversion of ettringite into monosulphate [42], [184], [186], [190].

113

The penetration depth of the Vicat needle into wPc pastes at different sand replacement levels and w/c of 0.45 is observed in

Fig. 5-7b. As the amount of wPc is decreased, the initial and final setting times of mortar are reached at longer times, resulting in a delay in the hydration process, a lower hydration degree, and some change in the hydration kinetics of the system. Mortars with 40-60% sand content show a slowed setting behaviour, attributed to a low cement and water content and high content of pores and air voids in the microstructure, leading to a decrease in strength. These effects are attributed to the sand water uptake, and lower cement and water content [50], [305], [306].
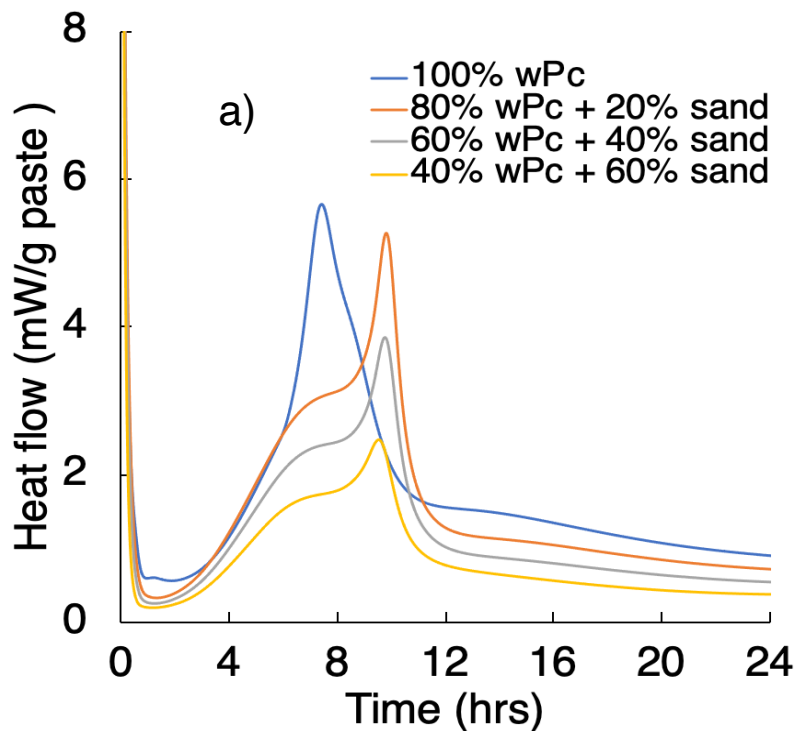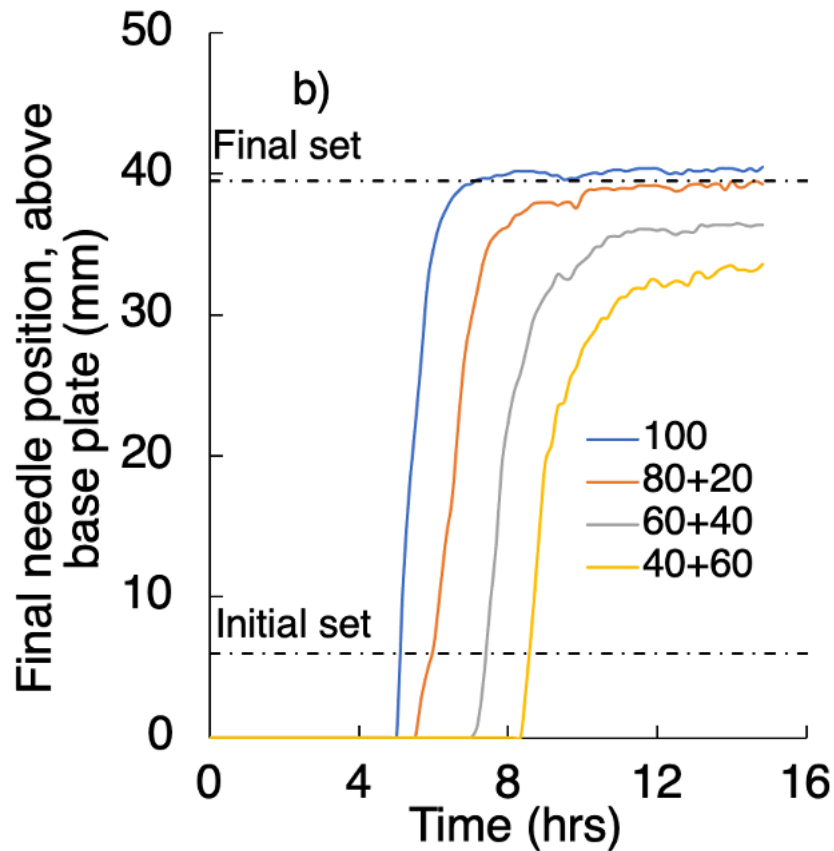
Fig. 5-7. wPc hydration at different sand replacement levels as indicated in the legend: a) heat flow (normalised to total sample mass), b) Vicat determination of setting time.

Fig. 5-8a-d shows the wPc ACIS, resistivity/conductivity, and impedance response in terms of resistance and reactance over time and frequency, at different sand replacement levels, during the first 24 hrs after mixing.

At early ages and comparing wPc paste to mortars (Fig. 5-8a), the results show an increasing tendency of the impedance and parasitic effects as the sand replacement level increases. This effect is attributed to an increase in the conductivity of the aqueous fluid surrounding the cement grains [26], [307]. There is also a filler effect produced by the addition of sand which increases the growth and the nucleation sites

for hydrated products. In Fig. 5-8b the bulk resistivity of the mortar increases due to a lower amount of C_3A per unit volume of material and fewer available wPc grains to react with water, leading to an increase in the dissolution rate of anhydrous compounds and the formation of hydration products around the cement particles (mainly $C\text{-}A\text{-}\bar{S}\text{-}H$ phases, and some early $C\text{-}S\text{-}H$). This response confirms that the addition of sand has a significant dilution and electrical insulating effect during the microstructural development of mortars, causing a decrease in their electrical conductivity [24], [26]. During the dormant period, as the amount of sand is increased, the impedance response in terms of bulk resistance (Fig. 5-8c) shows an increasing tendency at low and high frequency, confirming the impact of the mortar microstructure on the impedance response [307].

As wPc is replaced by sand, the reactance decreases at low frequency, and increases at high frequency, and it is also observed that the parasitic effects increase and emerge at earlier times (Fig. 5-8d). These behaviours are probably related to a decrease in the charge transfer resistance as a result of a higher ionic strength and a sand filler effect, demonstrating the impact on the hydration kinetics produced by the addition of sand [30], [157], [308].

At the beginning of the acceleration period, there is no change in the appearance rate of the main C_3S hydration peak (Fig. 5-7), but the mortars show a similar increasing trend in which the bulk resistance values are higher than the values for wPc (Fig. 5-8). This is attributed to a microstructural change produced by the sand-cement interface which affects the air voids and porosity of the mortars (Fig. 5-9a-b), leading to an increase in resistivity of the sample [309].

At the end of the acceleration period, the sulphate depletion peaks of mortars at different sand addition levels are observed at similar times, while the resistivity/conductivity measurements show a perturbation between 10-11 hrs that is delayed as the sand level is increased. This perturbation is not only related to the maximum release of heat (sulphate depletion peak,

116

Fig. 5-7a) but also to the impact of sand on the microstructural development, deposition of hydrated products such as CH, and pore size distribution and content [157].

At longer ages, mortars show similar impedance behaviour in which a bulk semicircular arc of higher resistance is obtained. However, the parasitic effects in the ACIS measurements are reduced at 20% to 40% sand replacement levels. Higher sand replacement (60%) shows a greater parasitic effect. This is due to an interfacial effect in which the total porosity, the pore size and the pore distribution increase at high sand replacement levels [308].
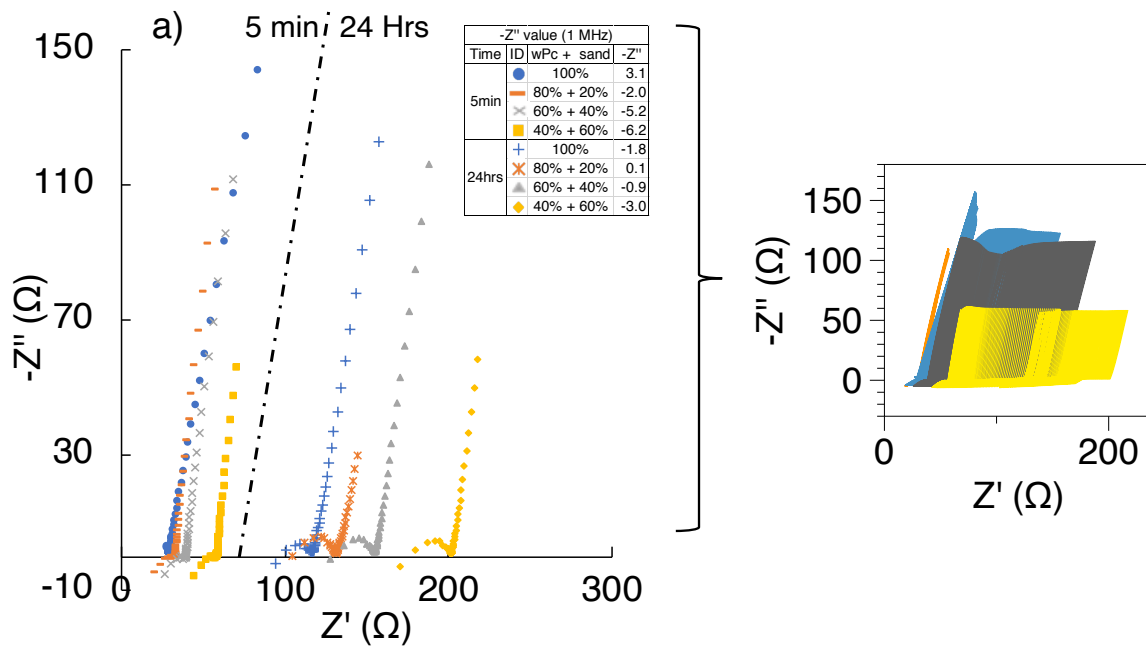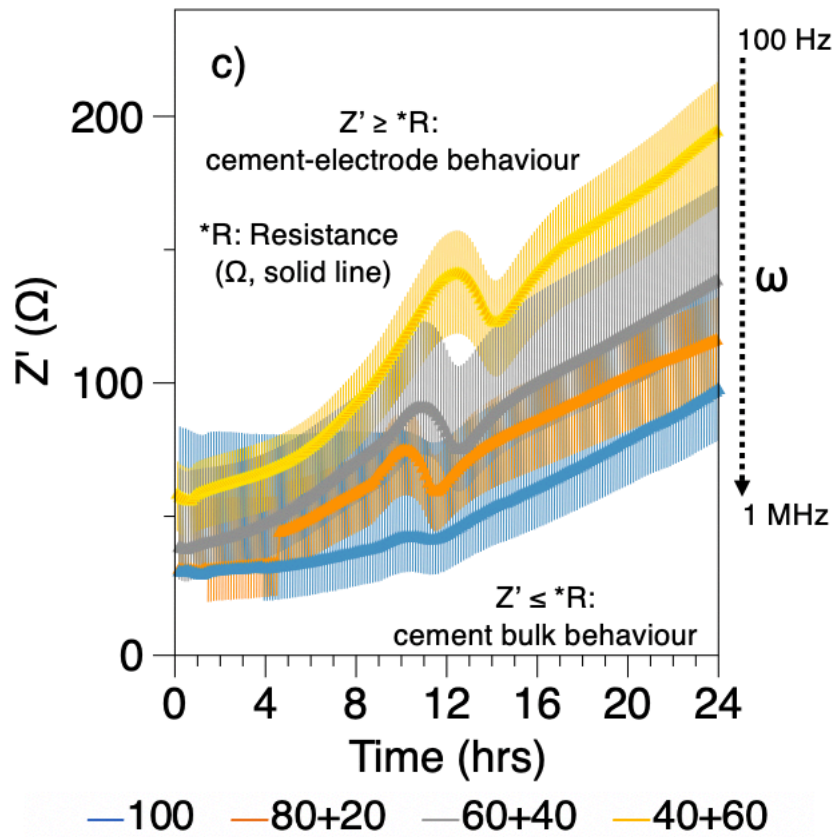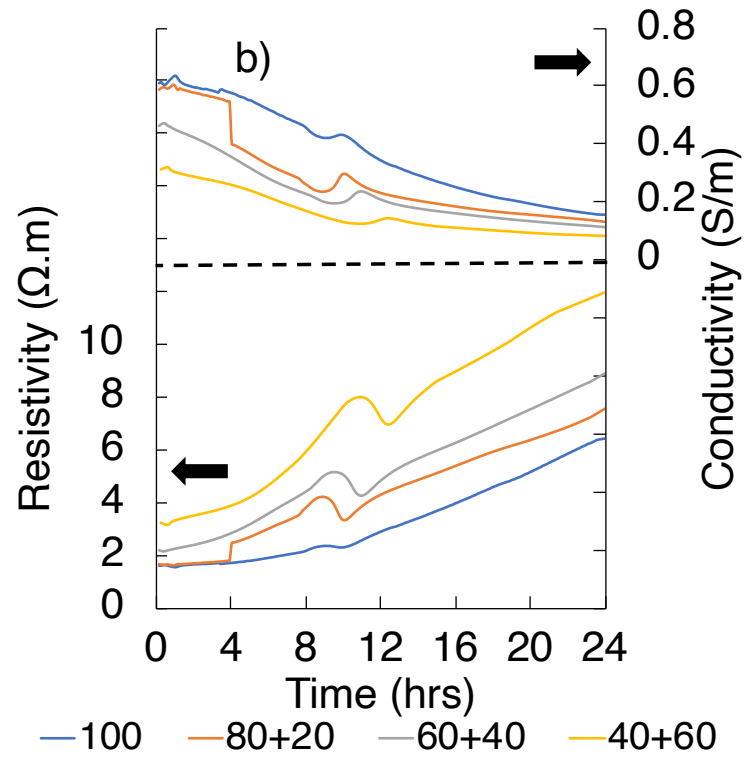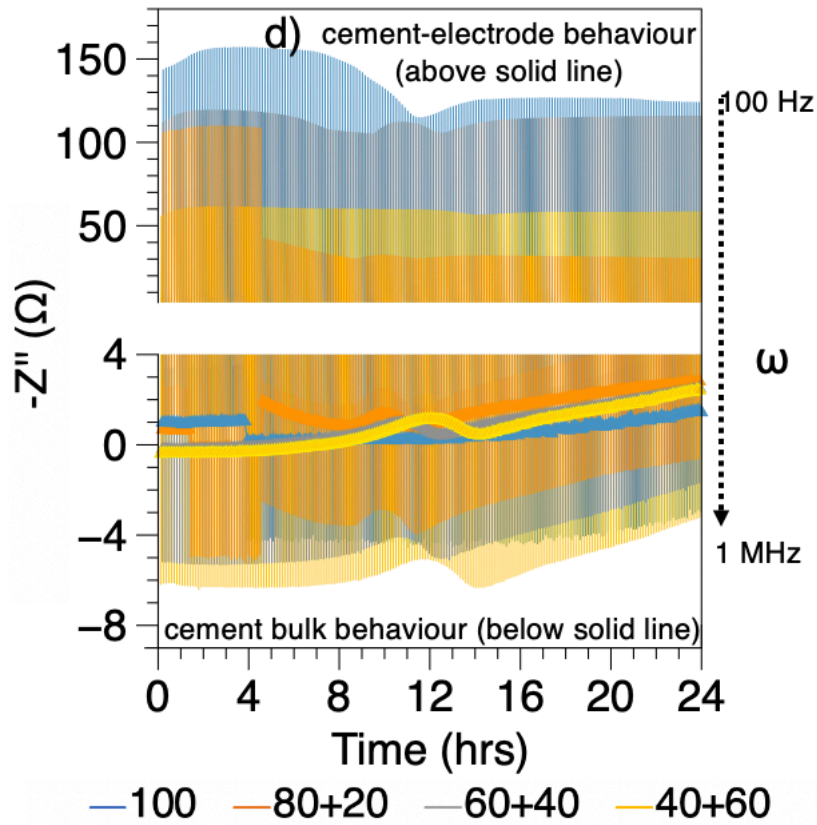
Fig. 5-8. ACIS response of wPc pastes at different sand replacement levels as indicated in the legend: a) Nyquist plots, b) conductivity and resistivity, and at 100 Hz and 1 MHz c) real component, and d) imaginary component.
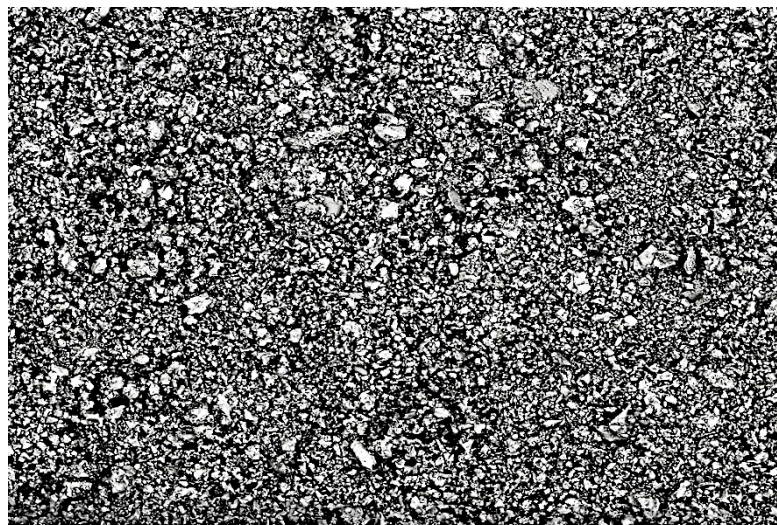
b) wPc/Sand   4 hrs   500 µm
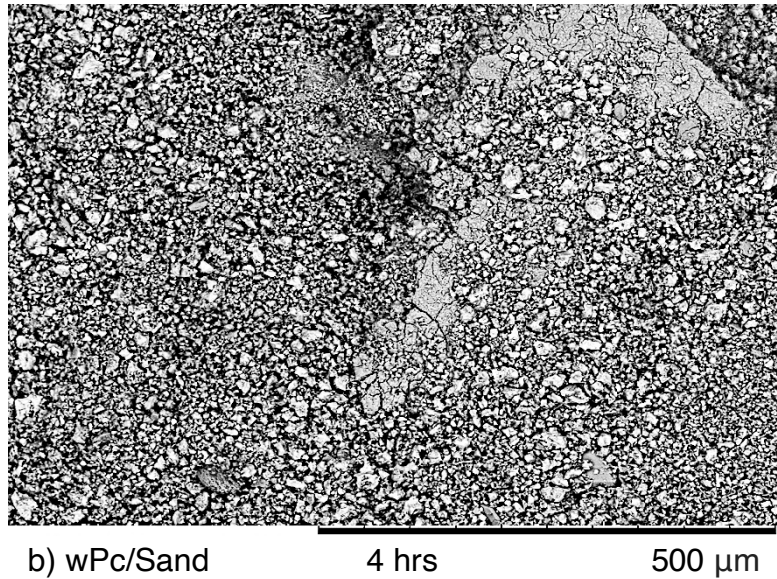
Fig. 5-9. SEM images of wPc paste (a) and mortar (b) at 4 hrs after mixing.

5.3.4 Anhydrite addition to cement

The reaction of C_3A during the cement hydration process is of great importance, as C_3A in contact with water reacts faster than other clinker phases, leading (if it is not controlled) to the formation of calcium aluminate products, rapid release of heat, and potentially quick/flash setting of cement if it is not controlled. To prevent this, the C_3A reaction is slowed down by the addition of a few wt.% of calcium sulphate sources such as gypsum ($CaSO_4 \cdot 2H_2O$), anhydrite ($CaSO_4$ or $C\bar{S}$) or hemihydrate ($CaSO_4 \cdot 0.5H_2O$) which are usually added during cement manufacturing to retard the C_3A hydration ($\approx$ 2%) [6], [7], [44].

The presence of these of the calcium sulphate can regulate the setting of Portland cement and control the sulphate concentration in the cement system, by changing the kinetics of reaction during hydration. The amount of calcium sulphate required for a particular cement will depend on the amount of sulphate and C_3A in the clinker (Fig. 2-6). An excessive addition of calcium sulphate can cause a false set and, at early

120

ages, a slight influence on the pore solution. Meanwhile, the rate at which Al^{3+} ions enter the pore solution and the hydrated product formation (i.e. ettringite and AFm) are strongly affected by the amount and source of calcium sulphate [207], [310].

The calorimetric curves of wPc at different anhydrite replacement levels during the first 24 hrs after mixing are shown in Fig. 5-10a. At small replacements (0.5-1%) of anhydrite in wPc pastes, the data show a similar trend to wPc paste. However, in the hydration process there is a retardation effect attributed to the slower dissolution of anhydrite, in which the release of heat decreases as the amount of anhydrite is increased. At high anhydrite replacement levels (10%) the calorimetric curve shows different behaviour, in which the heat release rate decreases significantly and the deceleration period increases in correlation to the sulphate depletion [311].

The dormant and acceleration periods, and the maximum exothermic peak, have similar heat evolution rate values in samples with 0 to 1% anhydrite content, Fig. 5-10a. At 10% of anhydrite replacement, the heat evolution rate values decrease due to an early and higher formation of AFt phase on cement grains [312], [313]. In the deceleration period, the heat evolution rate increases as the anhydrite replacement level increases. These effects suggest that the setting is prolonged as anhydrite amount increases, which is attributed to the anhydrite retardation effect on the reaction of C_3A and C_3S, the precipitation of ettringite and nucleation of AFm phases, and a reduction of the available space for reaction due to the amount of ettringite produced [105], [311], [313]–[316].

The penetration depth of the Vicat needle into wPc pastes at different anhydrite replacement levels is observed in Fig. 5-10b. The partial replacement of cement by anhydrite has only a slight effect on the initial setting time, and no false setting is observed even at the highest level of anhydrite addition. On the other hand, a higher retardation effect is observed in the final setting time as the amount of anhydrite is increased. The results agree with the thermochemistry data, attributed to the retardation of C_3A retardation effect due to the addition of anhydrite which produces

AFt and prolongs the sulphate depletion time. This effect is followed by the reaction of CH and ettringite with the remaining C_3A content, producing AFm phases [4], [317].
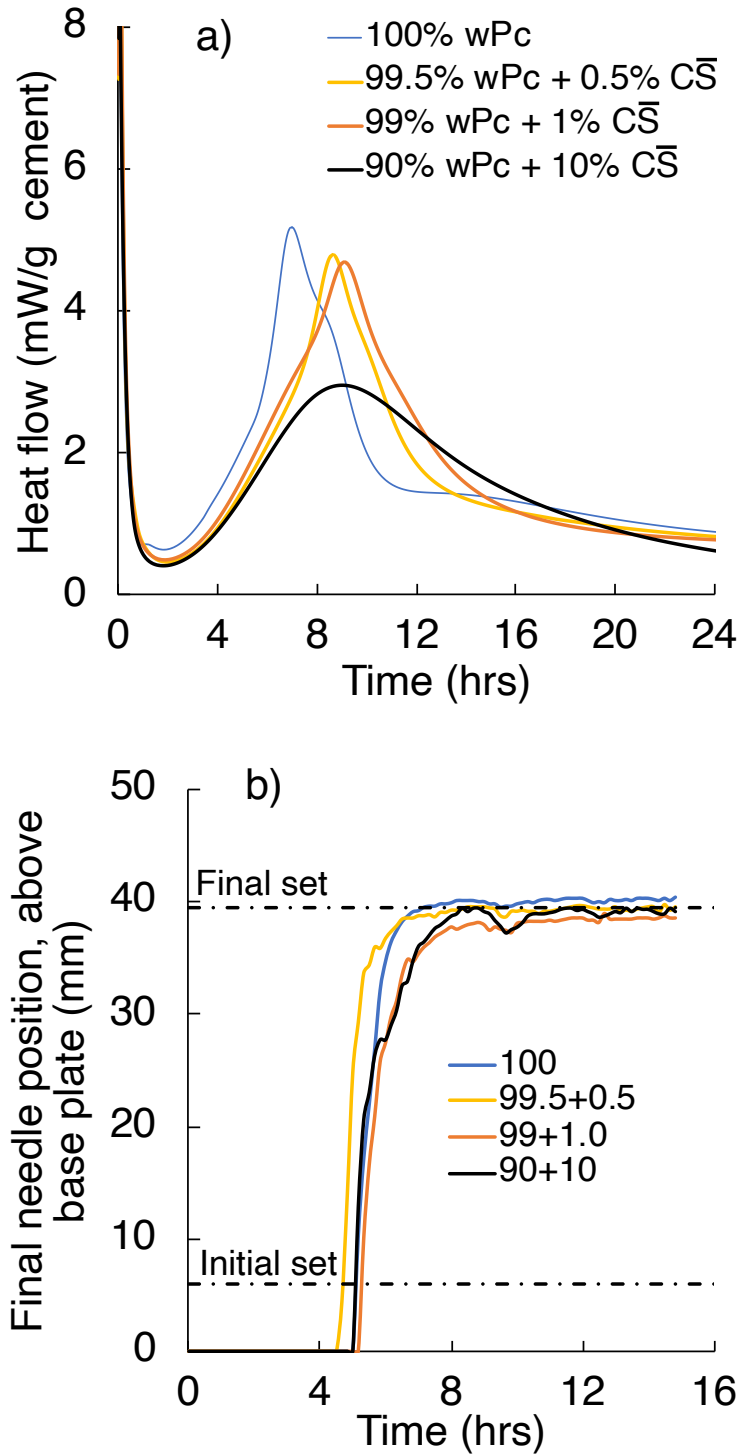
Fig. 5-10. wPc hydration at different anhydrite ($C\overline{S}$) replacement levels. as indicated in the legend: a) heat flow, b) Vicat determination of setting time.

Fig. 5-11a-d show the wPc ACIS data, resistivity/conductivity, and the impedance response in terms of resistance and reactance over time and frequency at different anhydrite replacement levels during the first 24 hrs after mixing.

At early ages, the conductivity/resistivity (Fig. 5-11b), and impedance behaviour (Fig. 5-11a) show similar behaviour in all samples. The -Z" values decrease as the anhydrite replacement level increases, showing a parasitic effect at 10% anhydrite replacement, and this effect needs further investigation. At high frequency and at approximately 1 hr after mixing, a perturbation in the conductivity, and in the real and imaginary impedance components, (Fig. 5-11c-d) is observed. Comparing these results with the thermochemical data, these perturbations are attributed to the beginning of the dormant period. This effect is followed by a decreasing tendency in the conductivity as the anhydrite replacement increases; at 1% anhydrite replacement, the data show a sharp and higher conductivity drop [318].

At approximately 2-4 hrs after mixing, the -Z" axis data show a sudden appearance of parasitic effects which increase as the replacement of anhydrite increases. The paste with 10% anhydrite is the first sample which shows this behaviour due to a dissolution rate decrease, followed by the paste with 0.5% anhydrite, while the paste with 1% anhydrite has a behaviour similar to wPc paste. The sudden appearance of parasitic effects is correlated to the beginning of the acceleration period.

The rate of dissolution of anhydrite and reaction of C_3A are accelerated as the calcium sulphate content increases and the dissolution of C_3S and C_2S begins. However, for all samples in the dormant period and the beginning of the acceleration period, the calorimetric curves (Fig. 5-10a) show a similar trend and the effect of anhydrite is not evident [318]–[320]. An increasing tendency in the conductivity measurements is observed 6 hours after mixing; this effect is attributed to greater formation of AFt due to the depletion of anhydrite, which decreases at later ages [207].

Around 8-12 hrs after mixing, at the end of the acceleration period and during the deceleration period, perturbations in resistivity and impedance values in terms of the

bulk resistance and reactance (Z' and -Z'' axis) are observed. However, the thermochemical and penetration displacement results are not enough to support full identification of the behaviour of the impedance spectra as wPc is replaced by anhydrite. Regarding the concentration of the ionic species in the pore solution and microstructural features at this stage of hydration, a more detailed investigation is needed to complement the interpretation of the impedance behaviour of wPc at different anhydrite replacement levels.

At longer ages and comparing to the ACIS response of wPc paste, the impedance values decrease for pastes with 0.5% and 1% anhydrite, and the parasitic effect increases as the replacement level increases. The sample with 10% anhydrite shows an increase of the impedance values and a higher resistivity bulk semicircular arc. Samples with 1% and 10% anhydrite replacement show conductivity values lower than those of wPc paste, while the 0.5% anhydrite sample shows a conductivity slightly higher than those of wPc paste. To understand and correlate the anhydrite replacement effect on the impedance behaviour, thermochemistry and initial and final setting times, further investigation, based on microstructural changes, is needed.

-Z'' value (1 MHz)			
Time	ID	wPc + anhydrite	-Z''
5min	●	100%	3.1
	▲	99.5% + 0.5%	2.9
	✕	99% + 1%	2.6
	+	90% + 10%	-4.4
24hrs	◆	100%	1.9
	✕	99.5% + 0.5%	-1.9
	─	99% + 1%	-2.6
	━	90% + 10%	5.6
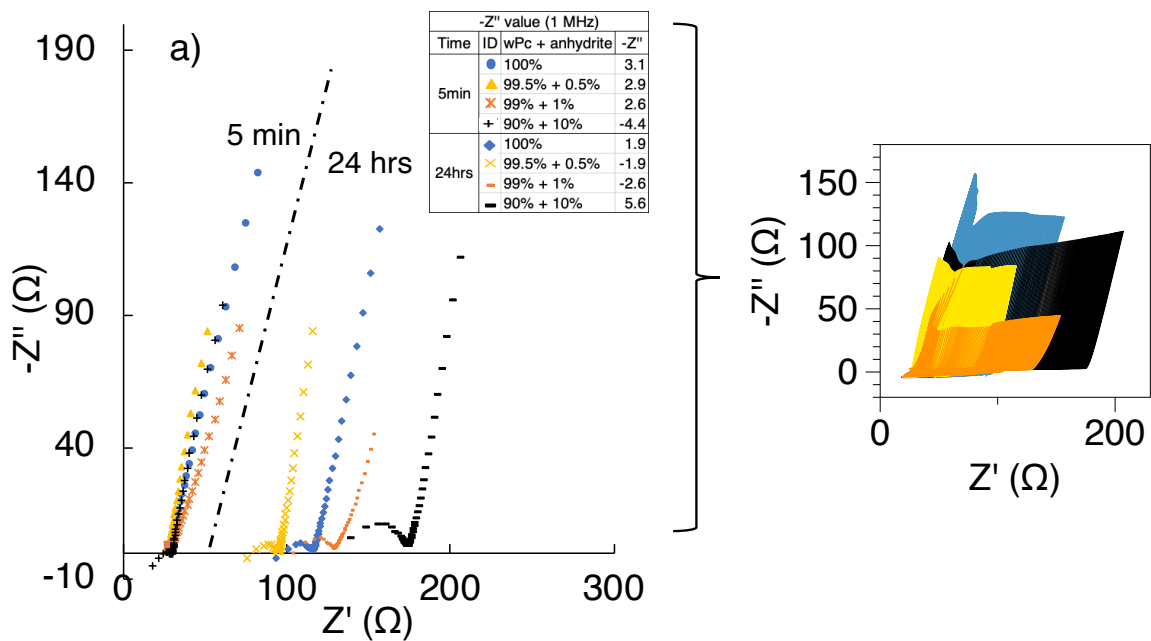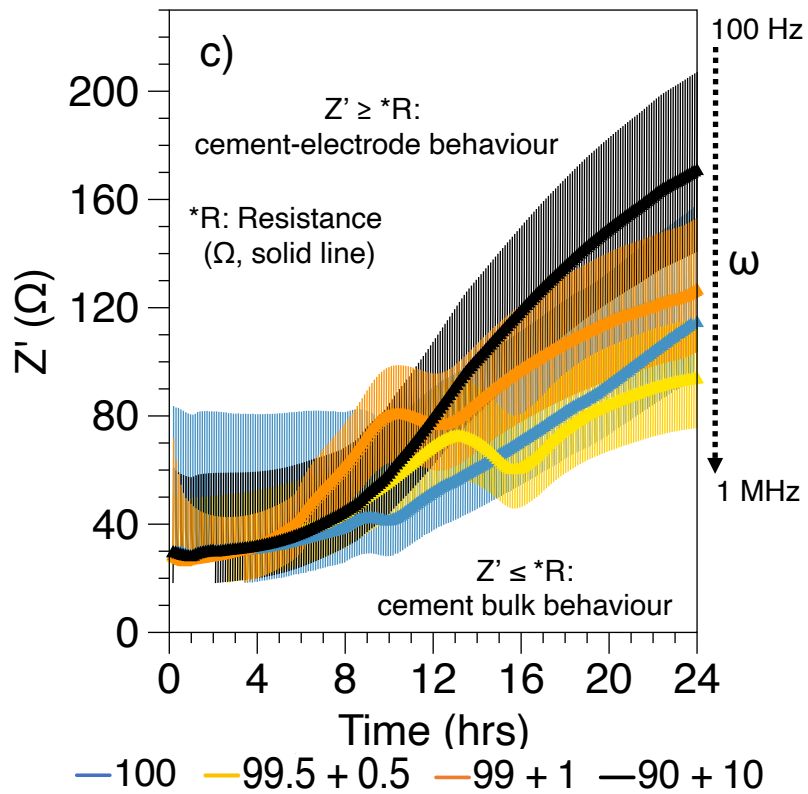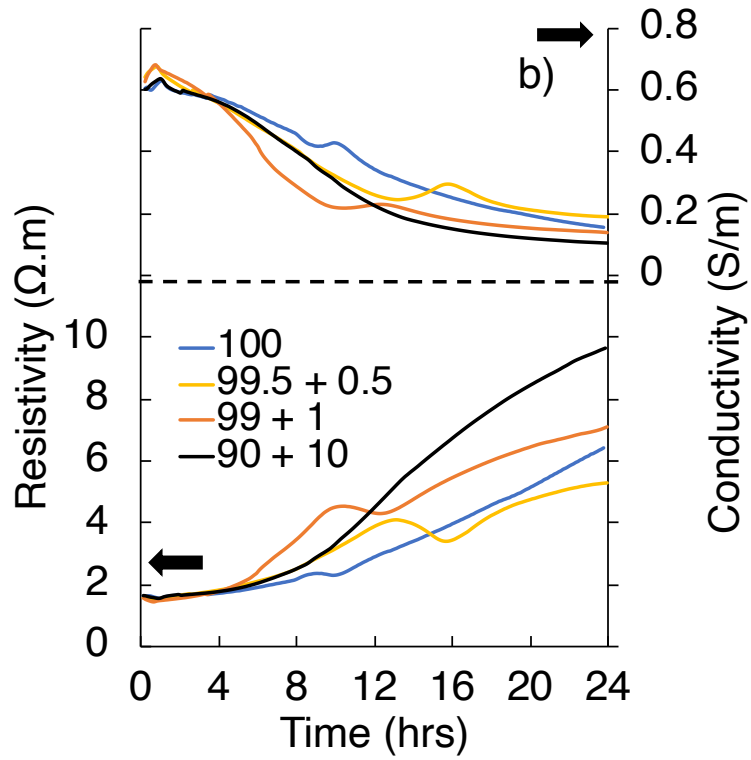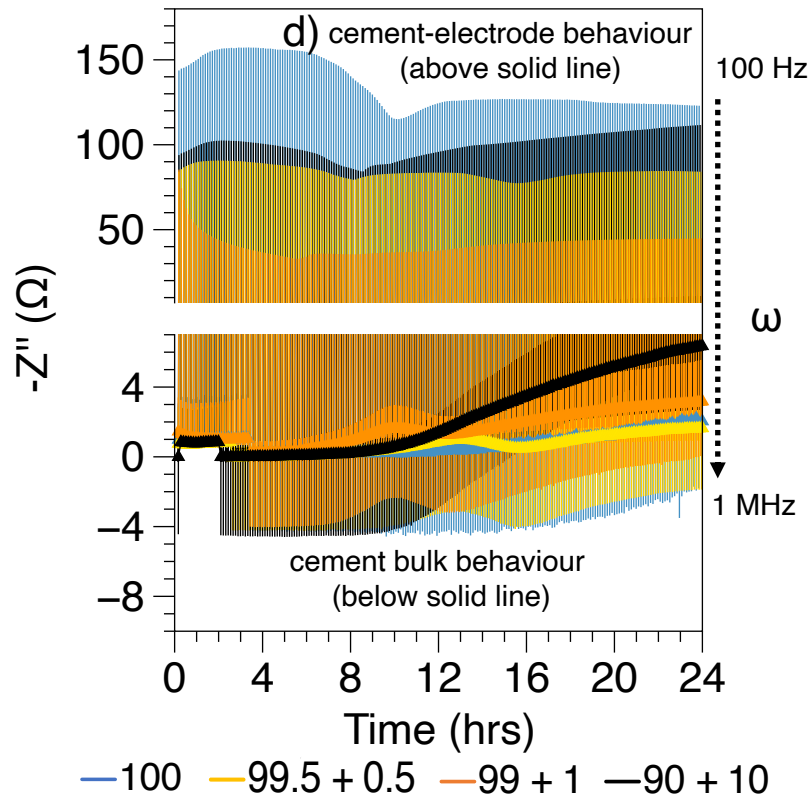
Fig. 5-11. ACIS response of wPc pastes at different anhydrite replacement levels as indicated in the legend: a) Nyquist plots, b) conductivity and resistivity, and at 100 Hz and 1 MHz c) real component, and d) imaginary component.

5.4 Conclusions

In this chapter different techniques have been used to assess, during the first 24 hrs after mixing, the electrochemical response and the microstructural development of Portland cement at different w/c ratios and different sand and anhydrite replacement levels. The experimental results highlighted the following conclusions:

- The thermochemistry results show only a slight variation between the heat flows measured at different w/c ratios. Conversely, the ACIS measurements show a significant variation, in which the appearance of parasitic effects on the

impedance measurements at high frequency can be correlated to the initial setting time.

- Perturbations in the electrical conductivity response are attributed to the dissolution of the clinker phases, and the precipitation of C-S-H, correlates with the thermochemistry results.

- The decreasing conductivity trends obtained as a function of time are related to the microstructural development of cementitious systems (hydrated product formation and disconnection of pores) and consumption of water/pore fluid.

- Microstructural changes during hydration are produced by altering the chemistry of the cementitious paste or mortar and can be observed via changes in the electrical resistivity and the impedance behaviour. These changes are correlated with some features in the thermochemistry and setting time results.

- Cement conductivity, resistivity and impedance behaviour, as a function of time, correspond to the results of previous investigations.

In summary, in spite of the fact that at early ages impedance measurements are affected by parasitic effects due to a highly conductive cement state and a low degree of microstructural development, the study of cement hydration and the influence of admixtures can be accomplished by ACIS. However, to obtain more robust impedance data interpretation, the appearance of parasitic effects on ACIS measurements and microstructural characterisation need further investigation.

Chapter 6:

PORTLAND CEMENT & BLENDS

Note: This chapter is based on the paper *"Early-age characterisation of Portland cement and blends by impedance spectroscopy"* by A. F. Sosa Gallardo and J. L. Provis, [38], unpublished manuscript and submitted for publication, 2020, pp.1-33.

6.1 Introduction

This chapter evaluates the influence of different supplementary cementitious materials on the electrochemical response of white Portland cement at early hydration periods by applying alternating current impedance spectroscopy (ACIS) and different supporting techniques (thermochemical and setting time measurements, and pore fluid compositional trends obtained from the literature). White Portland cement (wPc) was used in this investigation due to practical reasons such as:

- The wPc clinker composition is largely similar to grey Portland cement.
- Limited content of Fe_2O_3 in wPc (beneficial to other investigations in our laboratory, e.g. NMR analysis).
- Higher commercial availability of wPc as a commercial non-blended product; this is the only form of plain Portland cement (CEM I) that is sold in bags by local suppliers.
- To complement previous data interpretation and give continuity in the experimental protocol.

The support from additional techniques is of great importance to improve impedance data interpretation and to understand the major factors influencing the

kinetics of reaction, pore solution and microstructural development during blended cement hydration at an early age.

A strong relationship among the emergence of parasitic effects in the impedance measurements, electrical conductivity perturbations, and the increase of ionic strength of the pore solution is observed. The results demonstrate that ACIS can be used as a probe of the early-age cement hydration allowing the assessment of changes in the ionic strength of the pore solution, hydration degree and microstructural development. Possible causes which might affect ACIS measurements and its data interpretation such as cement chemical composition, kinetics of hydration, and technique drawbacks, are also discussed.

6.2 Sample specifications

To support ACIS data interpretation, three groups of Portland cements at different replacement levels of GGBFS, FA or SF, were assessed by ACIS measurements and supported by calorimetry and setting tests. Table 6-1 shows the sample specifications of each of the groups, which were all formulated at a constant water to binder ratio (w/b) of 0.45. Four GGBFS and FA replacement levels, and three SF replacement levels were tested.

Table 6-1. Sample specifications.

No.	Parameter	Amount				*w/b
1	wPc (%)	80	60	40	20	
	GGBFS (%)	20	40	60	80	
2	wPc (%)	80	60	40	20	0.45
	FA (%)	20	40	60	80	
3	wPc (%)	90	80	70		
	SF (%)	10	20	30		

6.3 Results and discussion

6.3.1 Ground-granulated blast-furnace slag (GGBFS)

GGBFS, the composition of which includes SiO_2, CaO, Al_2O_3, MgO, and 1-2% of S^{2-} in the form of a glass, is used as a partial cement substitute to produce mainly C-S-H gel and hydrotalcite (at longer ages) by reacting with water and $Ca(OH)_2$. The reactivity of GGBFS depends on the availability of water, the glass content, fineness and bulk composition of the system [321].

In comparison to Portland cements, at low GGBFS replacement levels, no meaningful changes in the alkali, Ca, Si and Al concentrations in the pore solution are observed. At high GGBFS replacement levels (>75%), the alkali and OH^- concentrations in the pore solution decrease. Also, the high GGBFS content in the system drops the pH values, an effect attributed to the OH^- consumption as a result of the GGBFS hydration and the reduced sulphur species (e.g. HS^-, SO_3^{2-} and $S_2O_3^{2-}$) produced [56], [322], [323]. The C-S-H gel produced in hydrated GGBFS cement pastes has lower Ca/Si ratios than in ordinary Portland cement, decreasing the reaction rate as a result of a higher alkali bonding, an effect attributed to the lower Ca content which increases the C-S-H degree of reactivity and level of substitution, and the uptake of Al to form C-A-S-H, leading to an increase in the polymerisation of Si chains [12], [324]–[326].

The hydration products and microstructure of GGBFS-blended cements are in many ways similar to those of Portland cement. The hydration of GGBFS is triggered by the release of OH^- ions, leading to a CH level decrease in the cementitious system [9]. The use of GGBFS in cement has been of great interest since it provides environmental and engineering advantages in manufacturing and construction: lower permeability, lower heat release and lower energy cost [44], [76].

Fig. 6-1a shows the calorimetric curves of wPc at different GGBFS replacement levels during the first 24 hrs after mixing. The replacement of part of the cement by GGBFS slightly decreases the dormant hydration period, and then for the beginning of the acceleration period a similar hydration rate and behaviour are observed in all pastes. During the acceleration period and as GGBFS replacement level is increased, a higher decrease in the heat release rate and a higher acceleration tendency of the hydration process is observed. At earlier ages and lower heat evolution rate values, the maximum exothermic peaks are reached as a result of a change in the pore solution and the kinetics of reaction, a filler effect (dilution), and an increase in the hydration degree (produced by the replacement of GGBFS, the lower amount of wPc, and the water demand of the system).

This effect is followed by a sharp heat rate decrease during the deceleration period, and the same previous trend attributed to the decrease of C_3S and C_3A. At later ages and during the long-term period, the heat rate decreases gradually as the GGBFS replacement level is increased, reaching similar heat rate values at 24 hrs [5], [76], [327], [328].

Fig. 6-1b shows the Vicat needle penetration displacement of wPc at different GGBFS replacement levels at 14 hrs after mixing. As the GGBFS replacement level is increased, the initial setting times are relatively similar in all samples. However, in samples with 20-40% GGBFS replacement level, the final setting time increases slightly. The sample with 60-80% GGBFS replacement level shows a major increase in the final setting time, confirming the thermochemistry results and the slower overall reaction effect produced by large amounts of GGBFS. At 60-80% GGBFSA replacement level and at around 5-7 hrs, the results show a step attributed to an increase of the yield stress of the paste produced by the deformation of the paste at early age, affecting the displacement of the needle and the interface between the paste and the needle.
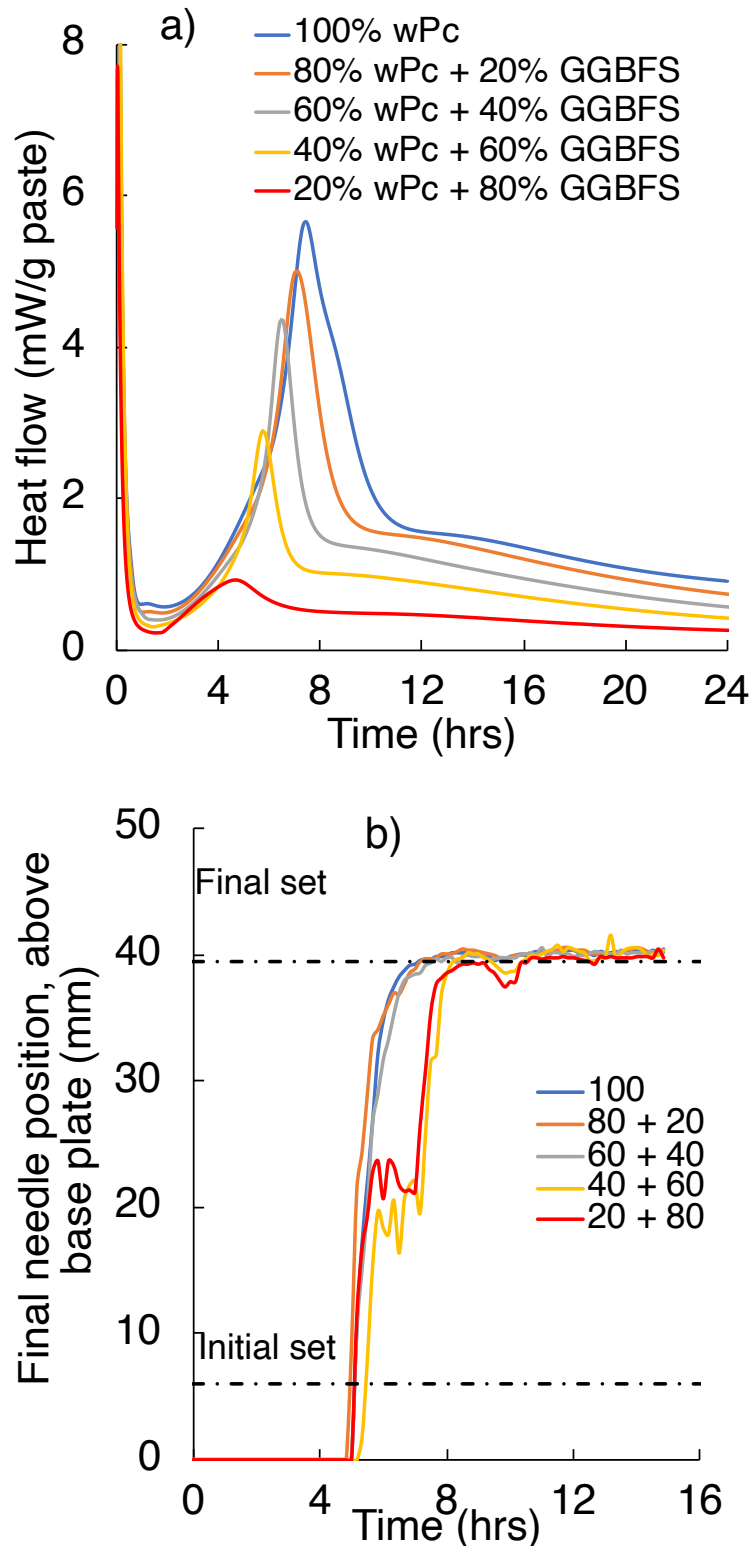
Fig. 6-1. wPc at different GGBFS replacement levels as indicated in the legend: a) heat flow (normalised to total sample mass), b) Vicat determination of setting time.

Fig. 6-2a-d show the ACIS, resistivity/conductivity, and the impedance response in terms of resistance and reactance at different GGBFS replacement levels in wPc, during the first 24 hrs after mixing.

At early ages (5 min; Fig. 6-2a), the impedance values and the parasitic effects increase slightly as the GGBFS replacement increases as a result of a decrease in the ionic strength produced by the replacement of cement clinker and the GGBFS filler effect, lowering the rapidly-soluble species (i.e. alkali, sulphates and gypsum) and increasing the water volume that reacts with cement particles [329].

At approximately 1 hr after mixing, the conductivity data show a small perturbation. The conductivity decreases slightly as the wPc content is reduced due to a change in the pore solution and kinetics of reaction (Fig. 6-2b). At the beginning of the dormant period, in both the real (Fig. 6-2c) and imaginary (Fig. 6-2d) components at high frequency and at small GGBFS replacement values (20-40%), this perturbation is observed (similar to the thermochemistry results).

Fig. 6-2d shows that impedance values at high frequency are affected by parasitic effects as the GGBFS replacement level increases, obscuring the resistive and capacitive behaviour of the pastes [76], [330], [331].

During the acceleration period (at approximately 3-8 hrs after mixing) and as the wPc content is reduced, the conductivity decreases due to a change in the pore solution of the system. The bulk resistance increases slightly as a result of a denser microstructure but remains the same at low frequency. The values of reactance remain almost the same, at high and low frequency.

Between 8-10 hrs after mixing, and contrasting with the setting time results, a perturbation in the conductivity measurements that corresponds with the final setting time of each sample is observed. This perturbation is followed by a decreasing

conductivity tendency in which the previous behaviour is inverted. Pastes with higher GGBFS content show a higher conductivity due to a higher pore interconnectivity, a decrease of AFm, a decrease of the degree of hydration, and a lower amount of portlandite which is needed to continue the slag hydration in the system [76], [101], [188], [332], [333].

At longer hydration periods, the impedance and conductivity values decrease at GGBFS replacement levels ≤40% due to the decrease of $Ca(OH)_2$ and OH^- ion concentration, as a result of slower hydration. However, the pastes with 40-80% GGBFS replacement show a lower conductivity than wPc paste, which is attributed to a lower ion transport resistance, a lower amount of hydrated products, lower hydration degree of GGBFS, and less mature microstructural development level [333].

Also at high GGBFS content, a decrease in the alkali concentrations is expected due to a higher available water content as a result of lower Portland cement content to react with water, higher amount of hydrotalcite (more alkalis to bind), and a higher unreacted GGBFS content containing encapsulated alkalis [329].

The paste with a 20% GGBFS content shows higher impedance values as a result of a filler effect, a dense pore structure (due to a higher pore refinement) and additional C-S-H formation [101]. At high frequency the semicircular arcs are affected by parasitic effects, which increase as the wPc amount is reduced. The conductivity values maintain a decreasing tendency in all samples.
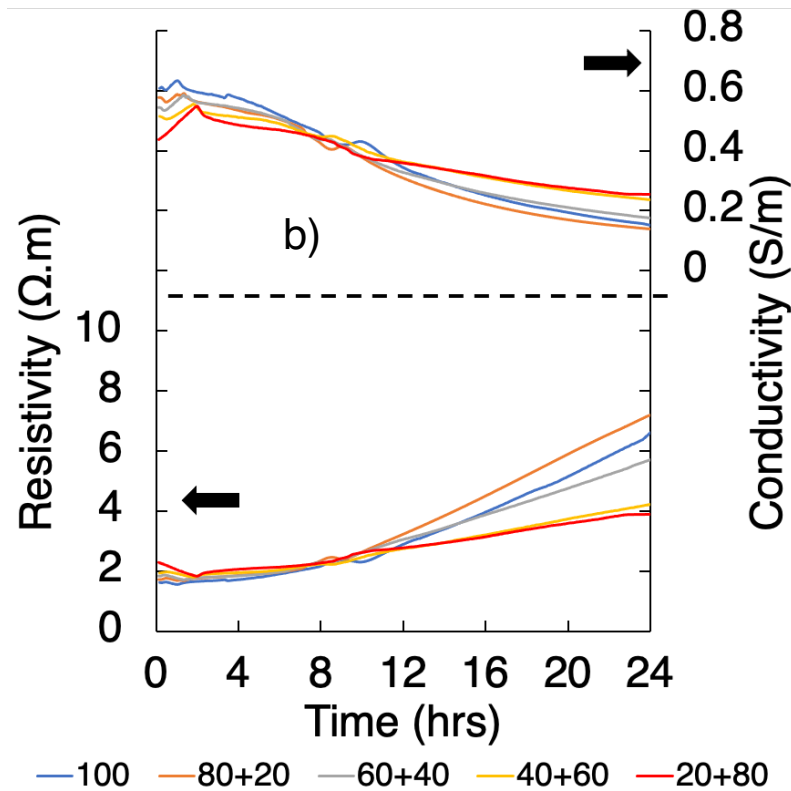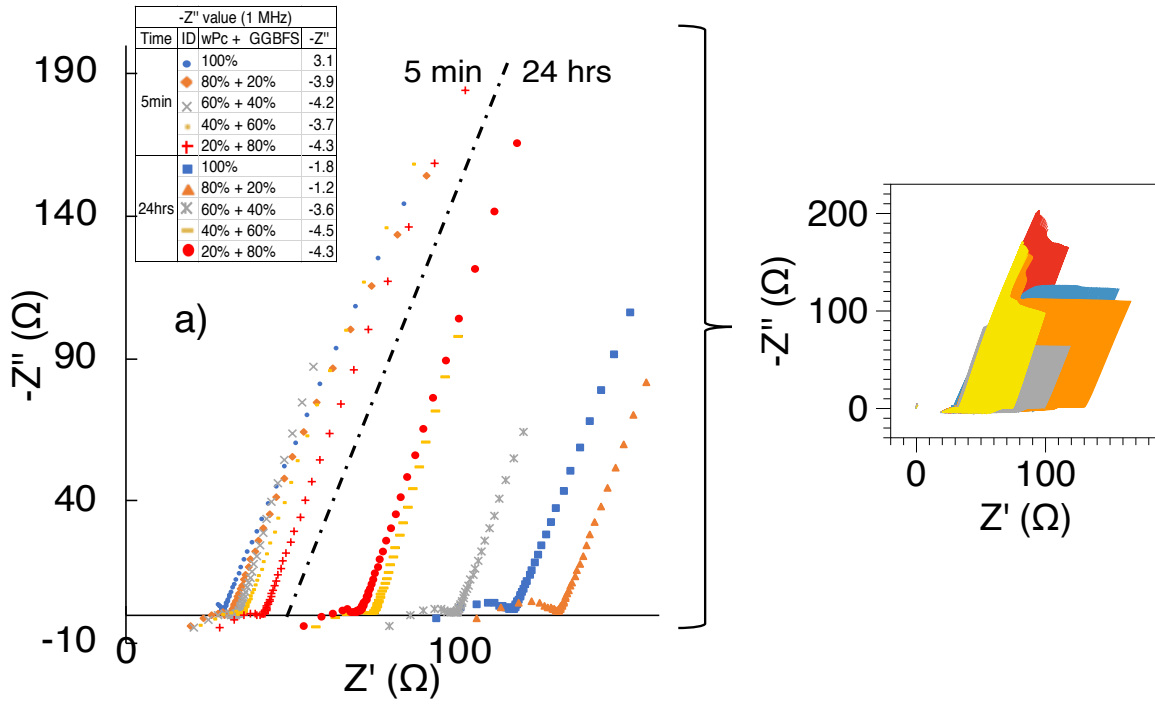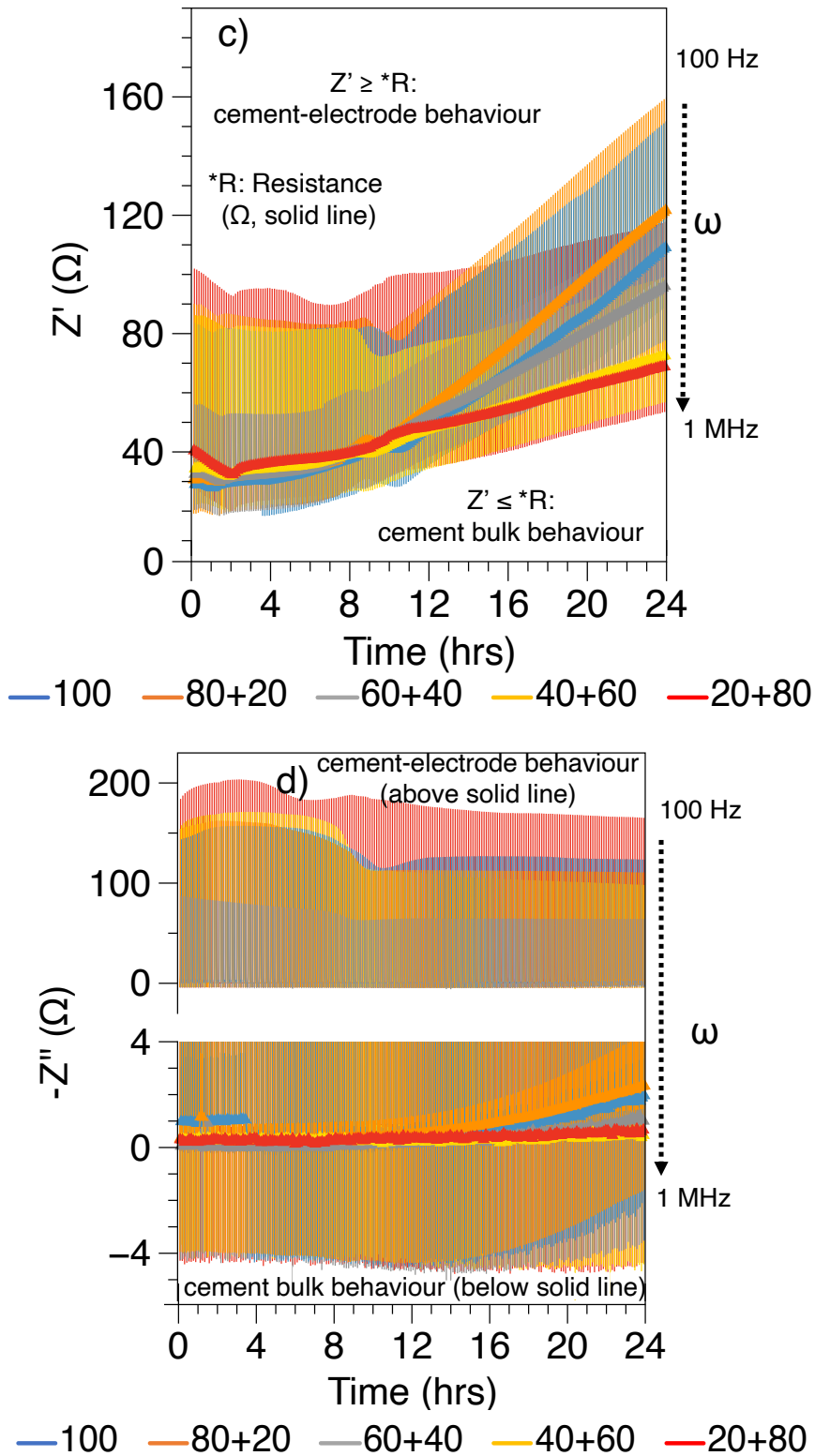
Fig. 6-2. ACIS response of wPc pastes at different GGBFS replacement levels as indicated in the legend: a) Nyquist plots, b) conductivity and resistivity, and c) the real component, and d) the imaginary component at 100 Hz and 1 MHz.

6.3.2 Fly ash (FA)

FA is a pozzolanic admixture, produced by the combustion of coal and used to reduce the manufacturing cost and/or enhance the performance of cement. This material can improve the mechanical properties of cement due to its properties such as its particle size and morphology which improve workability, reduce heat output, produce a filler effect and an increase in the amount of C-S-H with a lower Ca/Si ratio in which alkalis are bound, giving as a result lower permeability and bleeding, and higher strength at long-term ages [9], [42], [66]. However, FA shows some disadvantages for certain applications such as a lower surface area and a slower pozzolanic reaction, which lead to lower development rates of cement properties at early ages [6], [11], [334].

Depending on the type of cement and FA used in the mixture, FA replacement in the cement system can have Al and alkali contents in the pore solution higher than Portland cement. During hydration the Al content tends to increase while the alkali and OH$^-$ concentrations decrease as the FA replacement level is increased, an effect attributed to the FA pozzolanic reaction and the higher alkali binding in C-S-H and C-A-S-H of lower Ca/Si ratio. Na, Ca, Si, and SO$_4^{2-}$ concentrations in the aqueous solution are almost in the same range as they are in Portland cement [56], [335]–[338].

Fig. 6-3a shows the calorimetric curves of wPc at different FA replacement levels during the first 24 hrs after mixing. The replacement of part of the cement by FA increases the initial hydration period; however, a retardation effect is clearly observed in the dormant period as a result of a decrease in the Ca^{2+} in the pore solution due to the Al content in FA that delays the crystallization and nucleation of hydrated products such as C-S-H and CH. This effect is followed by the acceleration period, where the maximum exothermic peak, and a decrease in the heat rate values as a result of the wPc reduction, are observed. As the FA replacement level increases, the heat rate decreases and the beginning of the acceleration period is delayed. At 20% FA

replacement levels, in which the heat evolution rates of the blended paste and wPc are similar, a slight delay in the beginning of the acceleration period is observed. At 40-80% FA replacement levels, a higher decrease in the heat rate, a delayed main exothermic peak and a second exothermic peak (i.e. calcium sulphate depletion) are observed. These responses are mainly attributed to the lower cement clinker content and the retardation of the hydrated product formation (i.e. CH and C-S-H) as a result of Ca^{2+} decrease in the pore solution. The pozzolanic reaction of FA contributes to the heat release at longer ages [11], [339]–[342].

Fig. 6-3b shows the Vicat needle penetration displacement of wPc at different FA replacement levels at 14 hrs after mixing. At 20% FA replacement level, the initial and final setting times are similar to wPc values. At higher FA replacement content (≥40%), the initial and final setting times are delayed due to the retardation effect on the cement hydration as a result of a higher amount of water available to react with cement particles, leading to a decrease in the ionic strength of the pore solution and delaying the supersaturation, and a delay in the precipitation of hydrated products (i.e. CH and C-S-H) [66], [197], [198].

At 60% FA replacement level and at around 7 hrs, the results show a step attributed to an increase of the yield stress of the paste generated by the deformation of the paste at early age. These results agree with the thermochemistry measurements in which the influence of FA replacement in the cement hydration is observed, obtaining a strong correlation between the retardation of the initial and final setting times and the dormant and acceleration periods delay.
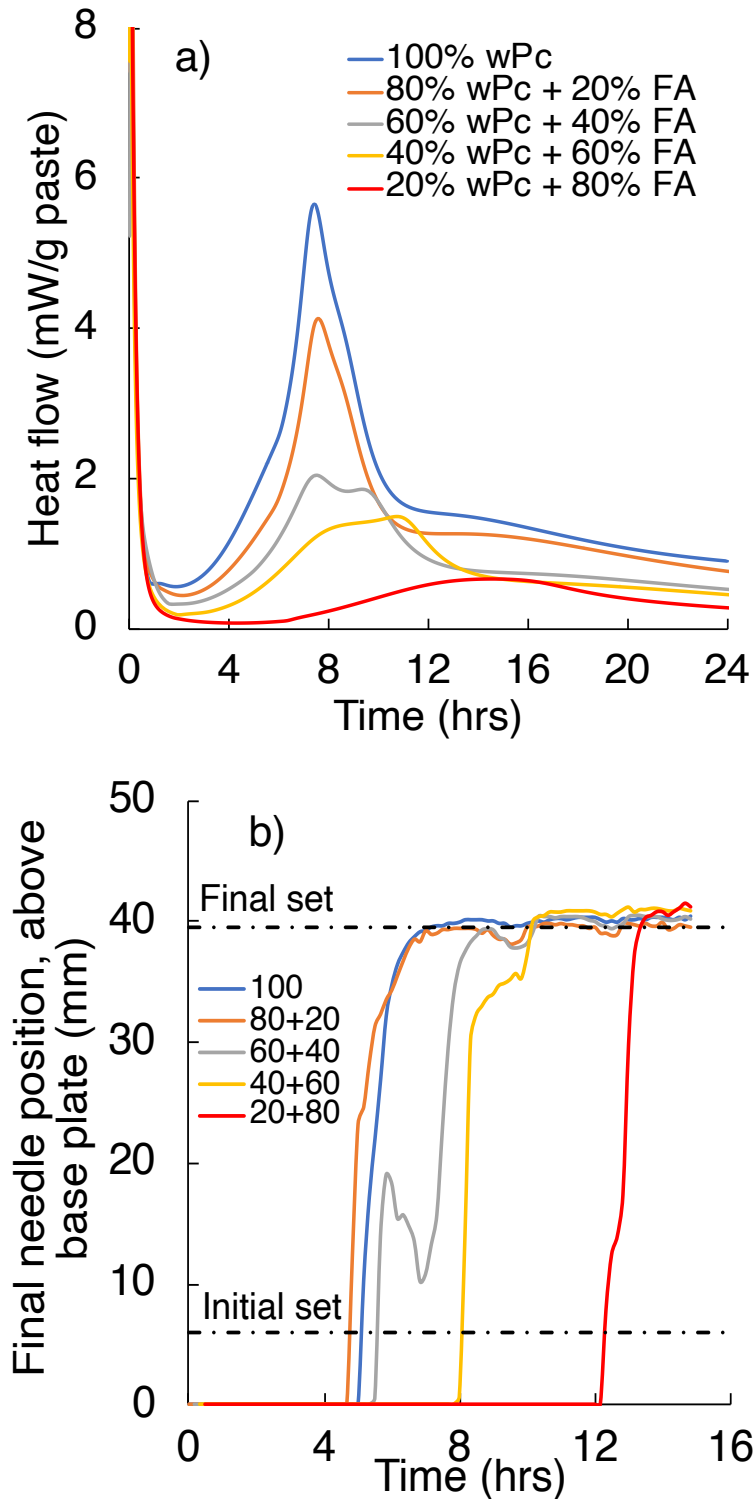
Fig. 6-3. wPc at different FA replacement levels as indicated in the legend: a) heat flow (normalised to total sample mass), b) Vicat determination of setting time.

The ACIS, resistivity/conductivity, and impedance response in terms of bulk resistance and reactance at different FA replacement levels during the first 24 hrs after mixing, are shown in Fig. 6-4a-d. At early age, the impedance response of pastes containing FA shows a behaviour similar to the response of wPc, with a slight increase in the bulk resistance values as FA content increases (Fig. 6-4a).

In samples with 0-60% FA content, a conductivity perturbation is observed 1-2 hrs after mixing (Fig. 6-4b). The increase of FA content delays the conductivity perturbations corresponding to the beginning of the dormant period observed in the thermochemistry results. In the 80% FA content paste, the conductivity perturbation appears at approximately 7 hrs after mixing, corresponding to the end of the dormant period. During the first 8 hrs after mixing, the pore solution changes slightly as the ionic species content is mainly controlled by the consumption of calcium sulphate species and the formation of $Ca(OH)_2$ [335]. The delay in the conductivity perturbation at high FA content needs further investigation since this response appeared several hours before the setting of this cement.

At high frequency, the wPc impedance response in terms of bulk resistance and reactance is affected by parasitic effects at approximately 4 hrs after mixing, while the pastes with FA replacement levels of 20% and 40% are affected by parasitic effects at approximately 7 and 16 hrs after mixing, respectively. The appearance of parasitic effects correlates to the beginning of the acceleration period; during this period the release of heat is mainly attributed to the wPc hydration reaction and the C-S-H produced [12], [66], [343]. However, pastes with high FA replacement content (60-80%) do not seem to be affected by parasitic effects, this is probably due to the higher effective w/c ratio in which cement particles react with a high volume of water, reducing the ionic strength of the pore solution and prolonging the supersaturation of the solution and precipitation reaction of hydrated products [335], [338].

A second conductivity and impedance (in terms of bulk resistance and reactance) perturbation trend is observed between 10-16 hrs after mixing. The appearance of the

conductivity perturbation delays as the FA replacement content increases, an effect attributed to the cement clinker content, the retardation of hydration and chemical reactions (e.g. sulphate depletion, diffusion of phases and ions, AFt formation), influencing the ionic strength and conductivity of the pore solution [344]–[346].

At longer hydration times, a decrease in conductivity is observed for all the pastes, and the paste with 80% FA content is the sample which shows the highest conductivity. The impedance spectra and the conductivity measurements show similar behaviour. The increase of FA content reduces the impedance and resistivity values, showing similar behaviour to that which is observed at early hydration periods. This effect is due to the retarded hydration and microstructural development, and the lower portlandite content, reducing the potential extent of the pozzolanic reaction of FA and leading to a higher pore size distribution and C-A-S-H phase production of lower Ca/Si ratio, taking more alkalis than C-S-H as a result of the alkali binding [14], [17], [66], [340], [347]. At low FA replacement levels, some densification of the microstructure due to the formation of new hydrated products and a decrease of the pore solution of the system results from the reaction of FA at longer ages (>1 d) [15], [337], [347].
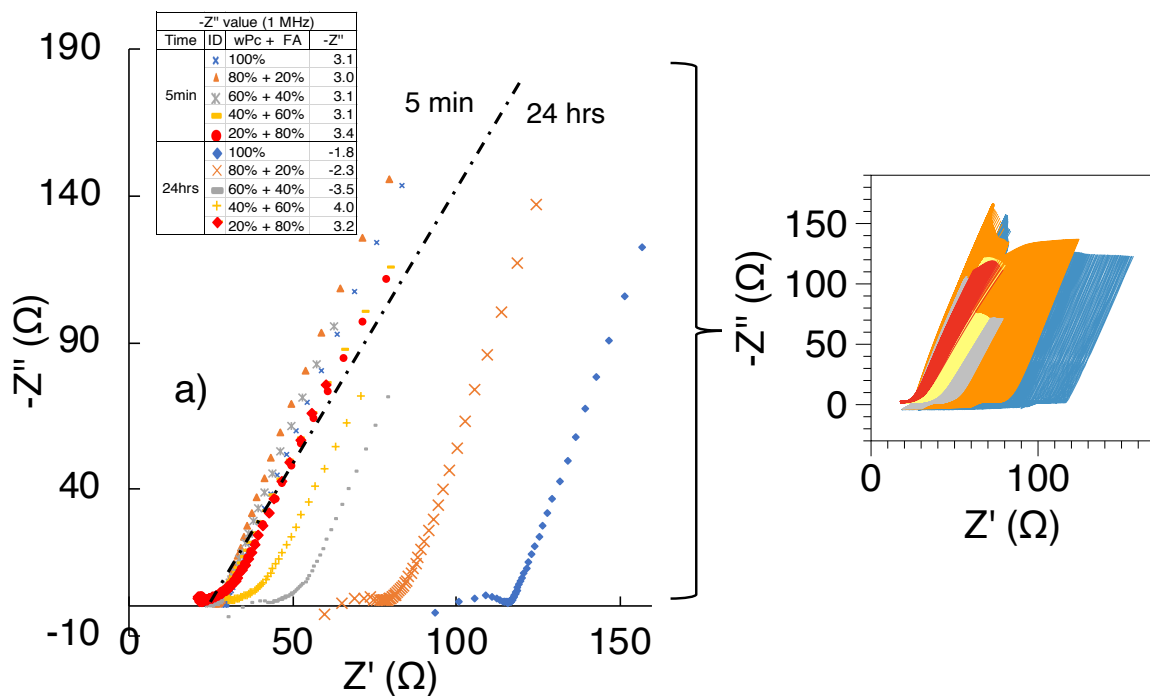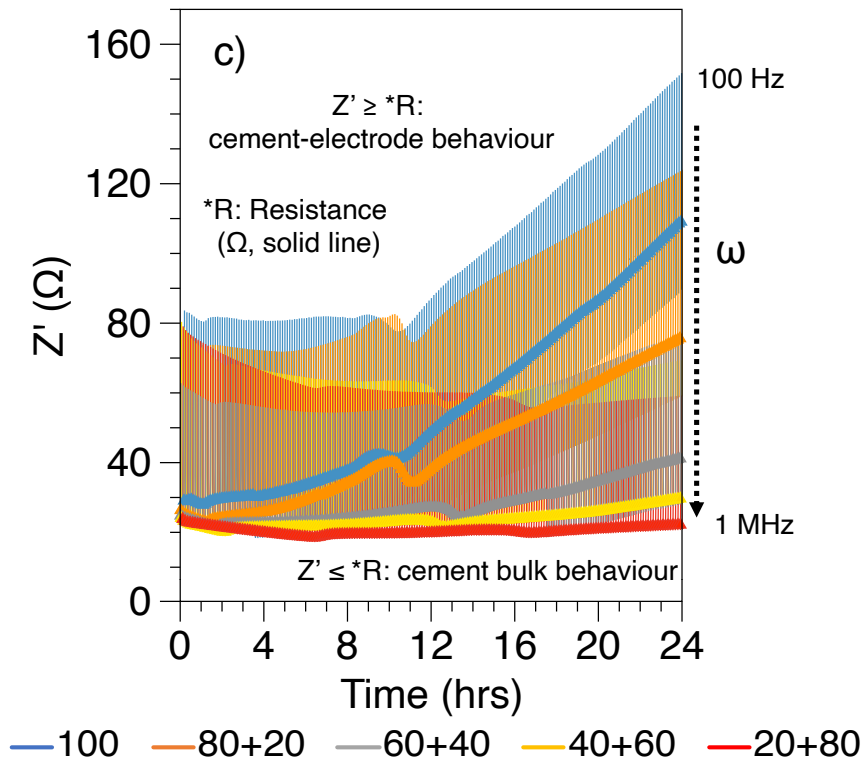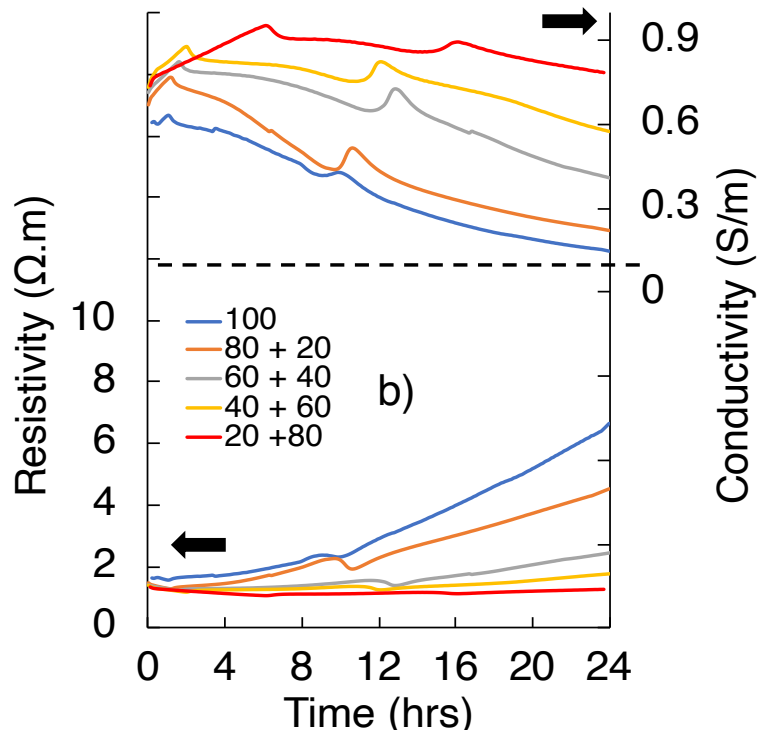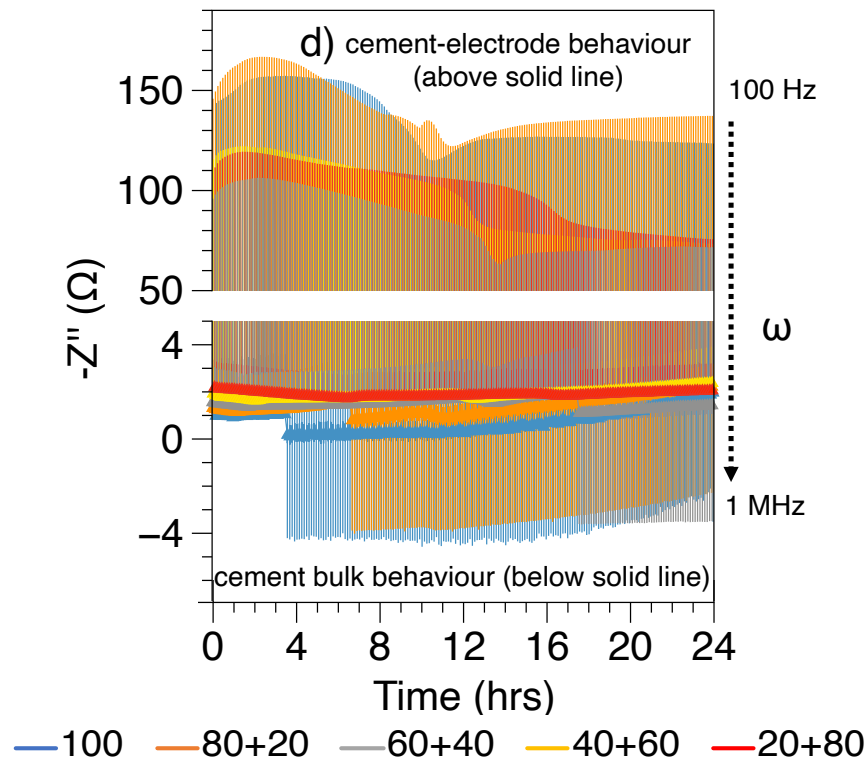
Fig. 6-4. ACIS response of wPc pastes at different FA replacement levels as indicated in the legend: a) Nyquist plots, b) conductivity and resistivity, and c) the real component, and d) the imaginary component at 100 Hz and 1 MHz.

6.3.3 Silica fume (SF)

SF is a pozzolanic admixture which can improve the mechanical properties, durability and refined pore structure of cement and concrete at certain concentrations [42]. SF is a highly reactive material, with a high amorphous silicon dioxide content, that reacts with CH to form additional calcium silicate hydrate (C-S-H).

The addition of SF in cement decreases the pore size, removes alkali hydroxide from the pore solution, and densifies the microstructure, enhancing the final mechanical properties of the system [52]. The addition of SF to cement pastes does not affect the Al and Si concentrations in the pore solution. However, after 1 day and

as a result of a dilution effect and the intake of C-S-H of lower Ca/Si ratio (produced by the SF pozzolanic reaction and the dissolved alkali and OH$^-$); it decreases the Ca^{2+}, K$^+$, Na$^+$, OH$^-$, sulphate and pH values [56], [348], [349]. The influence of SF in the pore solution of cement pastes increases as the SF content increases, however, the SF and wPc reaction depends on the available water content in the system [56], [349], [350].

The calorimetric curves of wPc at different SF replacement levels during the first 24 hrs after mixing are shown in Fig. 6-5a. During the dormant period a slight delaying effect due to the addition of SF is observed. This effect is attributed to the SF water adsorption behaviour, reduction of Ca^{2+} and OH$^-$ ions in the cement paste, and the formation of SF layer on the surface of cement particles decreasing the diffusion rate of water [11], [187]. An increase in the acceleration and deceleration period is observed as the SF content increases, producing new nucleation sites for the precipitation of hydrated products [351], [352].

Comparing the wPc samples, a higher maximum exothermic peak is observed at 10% SF replacement level, due to a dilution and nucleation effect [353], [354]. At 20% SF replacement level, a slightly similar exothermic peak is obtained. The sample with 30% SF replacement level has the lowest heat rate due to a lower cement content, higher portlandite consumption, and lower pH values (as a result of the lower alkali and higher Ca^{2+} concentration in the pore solution) [355]–[357].

As wPc content decreases, the end of the deceleration period is obtained at earlier ages and at higher heat rate values. During the long-term period, samples with 20% and 30% SF content show heat evolution rate values slightly lower than the wPc and 10% SF content pastes, an effect attributed to the exhaustion of Ca(OH)$_2$ in the system produced by a lower content of clinker in the system.

The Vicat needle penetration displacement of wPc pastes at different SF replacement levels is observed in Fig. 6-5b. At 20% SF content, the initial and final setting times slightly decrease, an effect related to the acceleration of hydration reactions and the rapid formation of C-S-H as a result of the faster availability of Si produced by the SF particles when reacting with the Ca released by the C_3S dissolution. The initial and final setting time in the sample with 30% SF content decrease considerably due to quick setting of the paste as a result of a higher water demand, faster precipitation of hydrated products and a denser microstructure [358]–[360].
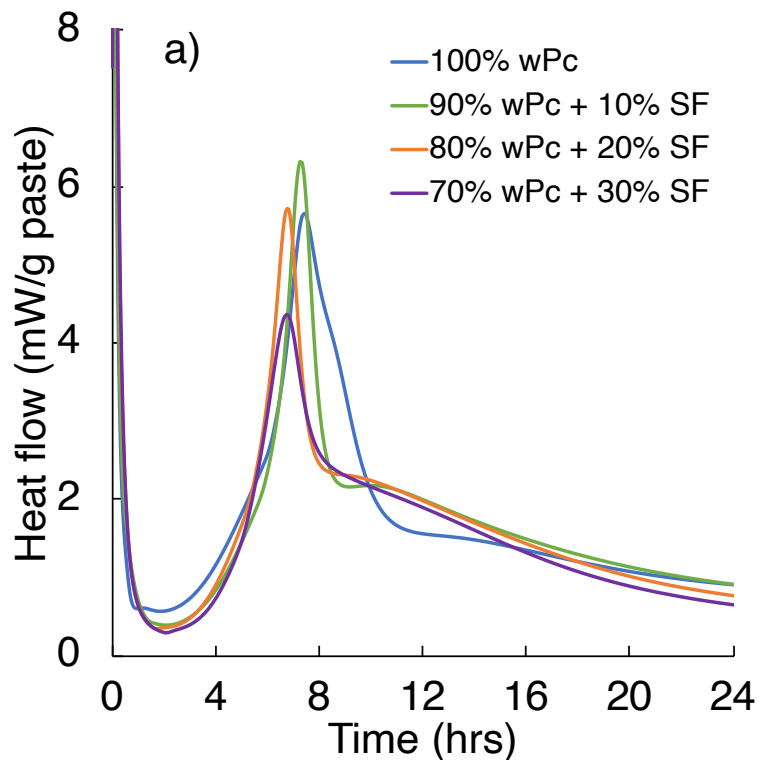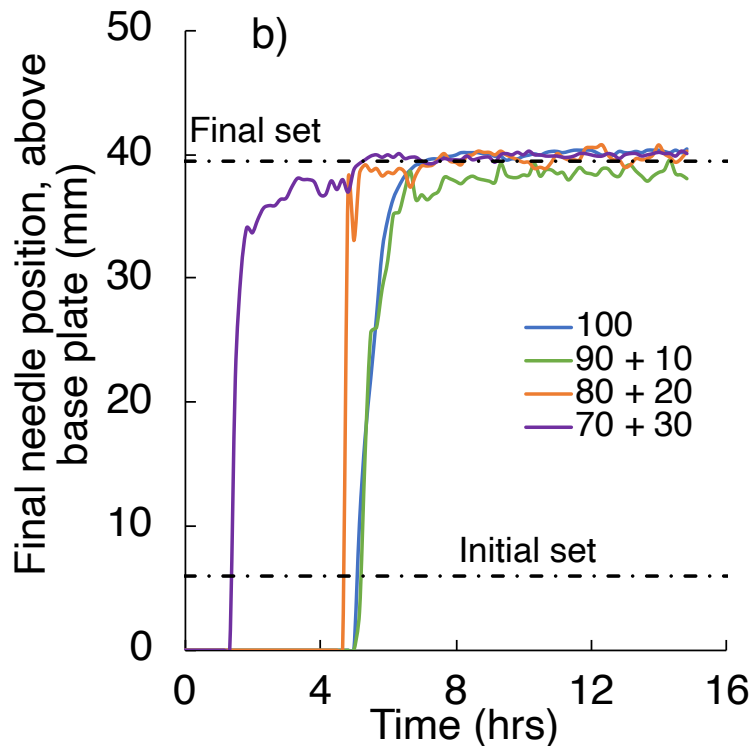
Fig. 6-5. wPc at different silica fume replacement levels as indicated in the legend: a) heat flow (normalised to total sample mass), b) Vicat determination of setting time.

Fig. 6-6a-d shows the wPc ACIS, resistivity/conductivity, and the impedance response in terms of bulk resistance and reactance at different SF replacement levels during the first 24 hrs after mixing.

In all samples, at early ages, a similar impedance behaviour is observed (Fig. 6-6a), however the Z' values decrease with the addition of SF. At 30% SF content, the impedance response is affected by parasitic effects from the beginning of the measurement. The samples with 10-20% SF content show a slight decrease in the -Z'' values. As the SF content increases, higher conductivity values, attributed to a dilution effect and the rapid dissolution of ionic species, are observed [15].

Between 1-1.5 hrs, a perturbation in conductivity and the Z' impedance component (at high frequency) is observed in Fig. 6-6b-c. As the SF content increases, the

perturbation is delayed slightly, corresponding to the beginning of the dormant period observed in the thermochemistry results and attributed to the rapid dissolution of SF, which increases both ion concentration and ion mobility in the system. After the perturbation, the conductivity drops due to the rapid formation of C-S-H, reducing the dissolved Ca^{2+} content and stimulating earlier development of the microstructure [361].

As was mentioned before, in the -Z'' data at high frequency and at approximately 4 hrs after mixing, the impedance response of wPc paste is affected by parasitic effects. The sudden appearance of parasitic effects is delayed as the wPc is replaced with SF (Fig. 6-6c-d), and the sample with 10% SF content is the paste with the longest parasitic effect delay. At high frequency, the pastes with a 20-30% SF content show two perturbations. The first perturbation appears at 5-6 hrs after mixing and the second perturbation at 7-8 hrs after mixing.

The effect of SF on the appearance of parasitic effects during the acceleration period correlates to the conductivity perturbation observed in Fig. 6-6b, attributed to the decrease of $Ca(OH)_2$ available, alkali uptake, and the formation of C-S-H in the system [362], [363].

The second parasitic perturbation is probably related to the increase of the ionic strength and the partial transformation of ettringite to monosulphate. This effect is followed by an increasing tendency in the resistivity as SF content increases due to the precipitation of hydrated products. The effect of parasitic effects and its delay on the impedance behaviour need further investigation.

At low frequency, a second perturbation in the conductivity, Z' and -Z'' impedance components is observed between 7-10 hrs after mixing, showing that the increase of SF content accelerates the emergence of these perturbations, which coincide with the maximum exothermic peak and the decrease of heat release during the deceleration

period. At this point the conductivity drops rapidly due to the densification of the microstructure and the reduced availability of water.

At 24 hrs after mixing and as the SF replacement level is increased, the impedance and resistivity measurements show a decreasing tendency attributed to the low pH, alkali content, permittivity, and the level of percolation of the microstructure. At longer hydration times, resistivity and impedance values higher than those of wPc are expected due to a major contribution of the SF pozzolanic reaction, pore refinement, and densification of the microstructure [168], [170], [364], [365].

b)

Resistivity (Ω.m) / Conductivity (S/m) vs Time (hrs)

100
90 + 10
80 + 20
70 + 30

c)

100 Hz

Z' ≥ *R:
cement-electrode behaviour

*R: Resistance
(Ω, solid line)

1 MHz

ω

1 MHz

Z' ≤ *R: cement bulk behaviour

Z' (Ω) vs Time (hrs)

—100 —90+ 10 —80 + 20 —70 + 30
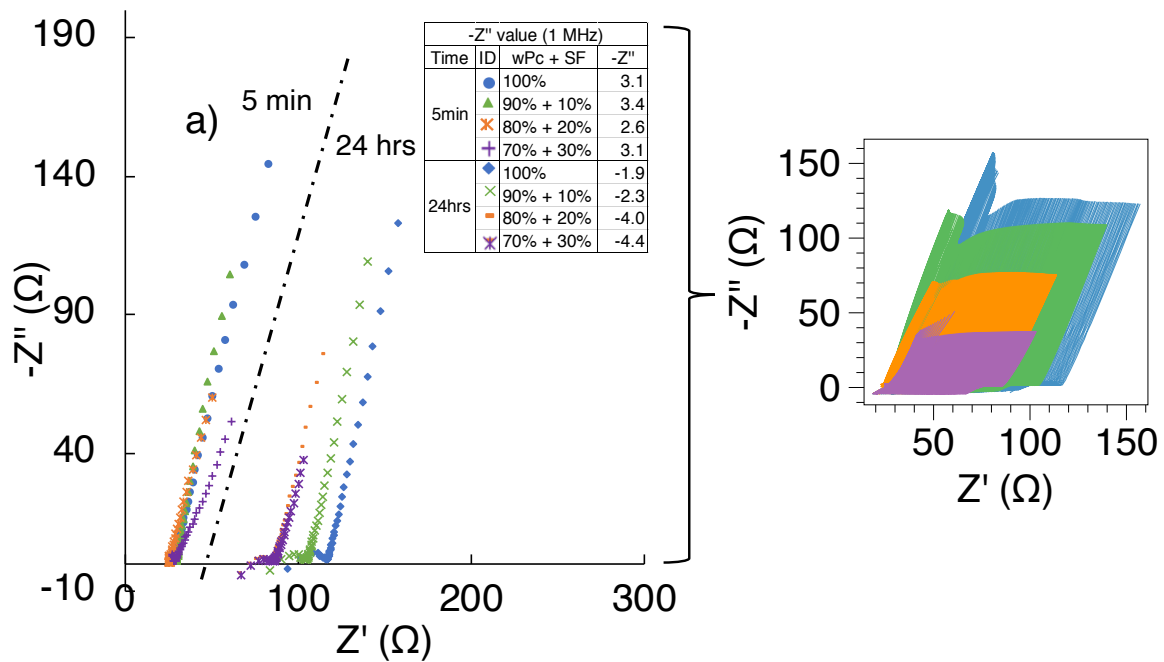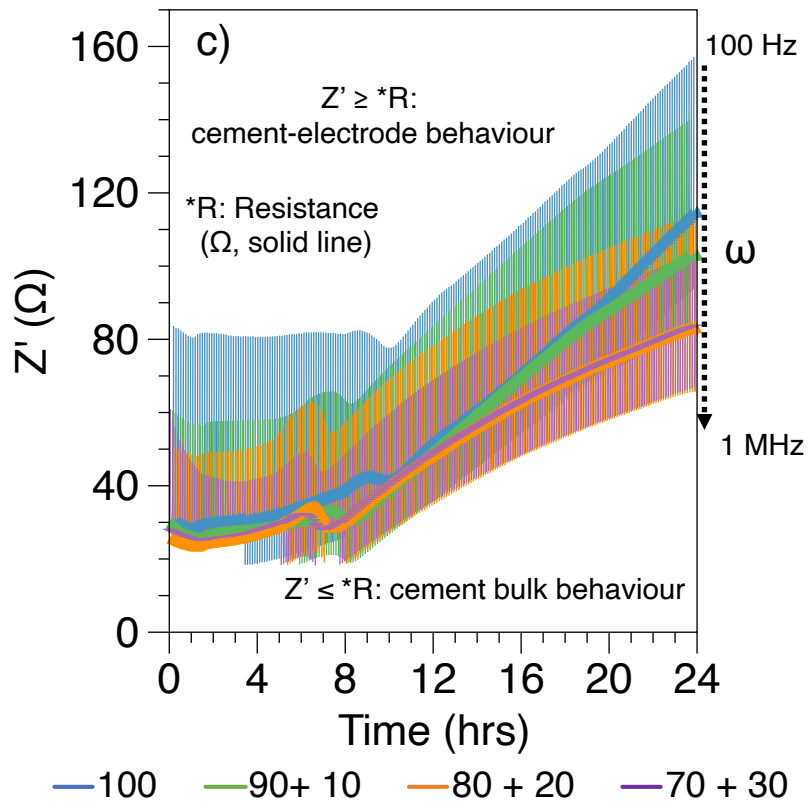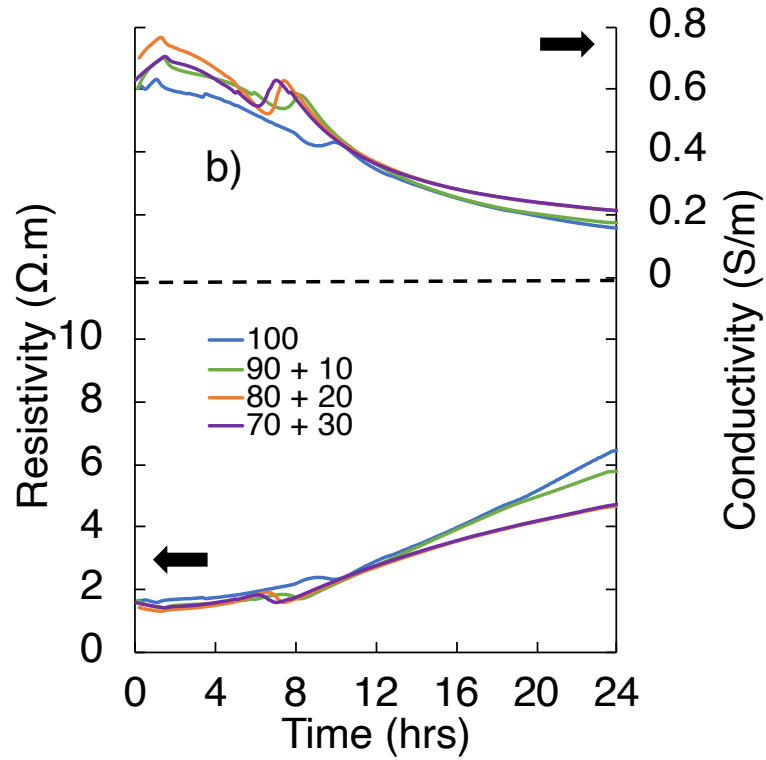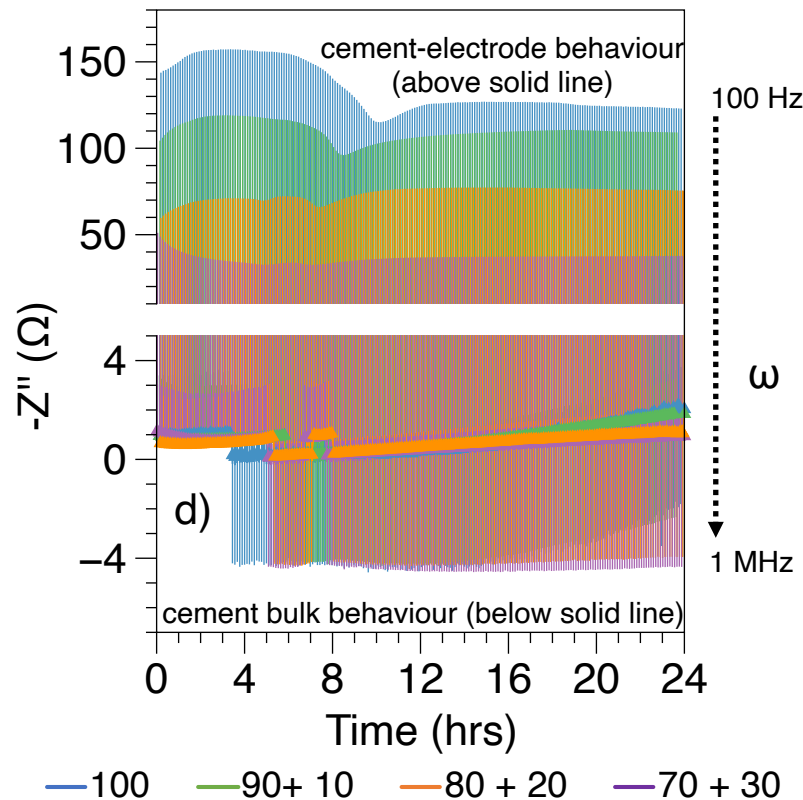
Fig. 6-6. ACIS response of wPc pastes at different SF replacement levels as indicated in the legend: a) Nyquist plots, b) conductivity and resistivity, and c) the real component, and d) the imaginary component at 100 Hz and 1 MHz.

6.4 Conclusions

In this chapter different techniques have been used to assess the electrochemical response of wPc at different replacement levels of GGBFS, FA and SF during the first 24 hrs after mixing. To improve the impedance data interpretation and understand the cement hydration process, electrochemical and thermochemical responses, and setting behaviour were assessed, in parallel with information on the effect of SCMs on the pore solution obtained from the literature.

The results emphasised the following conclusions:

- Microstructural changes produced by the addition of SCMs during hydration can be observed in the electrical resistivity and the impedance behaviour.

- ACIS measurements can enable researchers to assess and differentiate the influence of the addition of SCMs on the electrical properties and kinetics of hydration. However, cement ACIS measurements at longer ages (>1 d after mixing) are needed in order to differentiate the influence of the pore solution at different SCM replacement levels.

- Cement pastes with the addition of GGBFS show the appearance of inductance effects on the impedance measurements at early hydration periods (5 min after mixing) which are attributed to the GGBFS filler effect and the acceleration of wPc hydration. As the GGBFS content increases, a higher conductivity, attributed to an increase in the alkali bonding in the C-S-H produced by GGBFS, is observed.

- As the addition of FA increases, a delay in the emergence of inductance effects, higher conductivity and lower impedance values are observed as a result of a dilution effect, clinker phase dissolution and slow reactivity of FA, and a lower concentration of OH^- in the pore solution.

- Samples containing SF show a delay in the emergence of inductance effects and small differences in the conductivity and the impedance values attributed to the SF filler effect, the lower K^+ and Na^+ concentration in the pore solution, and lower available water to react with wPc.

- A correlation among the conductivity perturbation, the emergence of parasitic effects, hydration stages and setting times was observed. The results presented in this research have demonstrated that the ACIS technique and method of interpretation are robust and provide useful information, by being able to highlight correlations among the conductivity perturbation, the emergence of parasitic effects, hydration stages and setting times [37], [39]. However, ACIS data interpretation, the appearance and behaviour of inductance effects and the influence of the microstructure in the ACIS measurements need further investigation.

Chapter 7:

MICROSTRUCTURAL ASSESSMENT

Note: This chapter is based on the paper *"Microstructural characterisation of Portland cement and blends"* by A. F. Sosa Gallardo and J. L. Provis, [40], unpublished manuscript and submitted for publication, 2020, pp.1-51.

7.1 Introduction

In this chapter, alternating current impedance spectroscopy (ACIS) and imaging using a scanning electron microscope (SEM) are used to assess the electrochemical response and the microstructural development of Portland cement at different water to cement ratios, and dosages of admixtures and supplementary cementitious materials, in the early stages of hydration.

The main objective of this chapter is to evaluate microstructural development of cement and blends at early hydration ages ($\geq$ 24 hrs) by assessing the electrochemical response and other properties. In particular, we seek to use information from well-established techniques such as electron microscopy, calorimetry and Vicat setting times to aid in the interpretation of the rich but complex relationships between the electrical response of cement during hydration and its microstructural development features (e.g. morphology, particle and pore size distribution).

A strong correlation among the changes in the electrical response and microstructural development of cement and blends is reported. However, the influence and behaviour of the parasitic inductive effects observed in the impedance measurements at high frequency need further investigation.

7.2 Sample specifications

To conduct a more detailed study, eight groups of Portland cement blends, previously assessed by ACIS measurements and supported by thermochemistry and setting tests in previous chapters (5 and 6), were selected by incorporating a microstructural development analysis. The first group consisted of wPc hydration analysis at a w/c ratio of 0.35. The remaining samples were produced at a water to binder (w/b) ratio of 0.45 and are described in Table 7-1.

Table 7-1. Sample specifications.

No.	Parameter	Amount		
1	wPc (%)	100	*w/c: 0.35	
2	wPc (%)			Chapter 5 [39]
3	gPc (%)	100	*w/c: 0.45	
4	wPc (%)	80		
	Sand (%)	20		
5	wPc (%)	99		
	Anhydrite (%)	1		
6	wPc (%)	80	*w/b: 0.45	Chapter 6 [38]
	GGBFS (%)	20		
7	wPc (%)	80		
	FA (%)	20		
8	wPc (%)	80		
	SF (%)	20		

*w/c: water to cement ratio and w/b: water to binder ratio.

7.3 Results and discussion

7.3.1 Portland cement, w/c ratio and admixtures

Fig. 7-1a shows the calorimetric curves of gPc, wPc and blends at the specified replacement concentrations, during the first 24 hrs after mixing. Fig. 7-1b shows the corresponding Vicat needle penetration displacement measurements for the first 14 hrs after mixing.

The gPc paste shows a heat of hydration lower than wPc paste due to a lower surface area, higher particle size and higher C_3A content (Fig. 7-1a). Also, the emergence of a peaks at the acceleration period, as a result of the hydration of C_3A and C_3S, and the formation of C-S-H and ettringite, is observed. The initial and final setting times of the gPc are obtained at earlier ages as a result of a lower alkali content and a more stable formation and transformation of AFt into AFm and the formation of secondary phases [66], [80], [81], [289], [290].

The w/c ratio slightly affects the heat of hydration; a small delay in the dormant and acceleration period and a lower maximum in the heat release peak are observed due to the longer time it takes for the pore solution to be saturated. Also, a dilution effect which increases the particle spacing and degree of hydration is observed. However, the w/c ratio shows a stronger effect on the setting time of cement pastes, in which at lower w/c ratio a faster initial and final setting are obtained; this is due to the lower capillary porosity and available water [103], [109], [194], [195], [295], [296].

The addition of sand decreases the sulphate content and produces a filler effect, obtaining early conversion of ettringite into monosulphate and delaying the acceleration and the deceleration periods. Also, the heat release of the C_3S peak is decreased and the sulphate depletion peak is delayed. The setting times are delayed in wPc/sand paste due to the sand water uptake and lower cement content in the system [42], [50], [184], [186], [305], [306].

154

Likewise, the addition of anhydrite shows a decrease in the maximum heat release peak and a delay in the acceleration and deceleration periods. However, the addition of $CaSO_4$ gave a small retardation in the initial and final setting times. These effects are attributed to the rapid dissolution of anhydrite, retardation of C_3A hydration, and the nucleation of hydrated products limiting the space for reaction and prolonging the sulphate depletion time [311], [313]–[317].
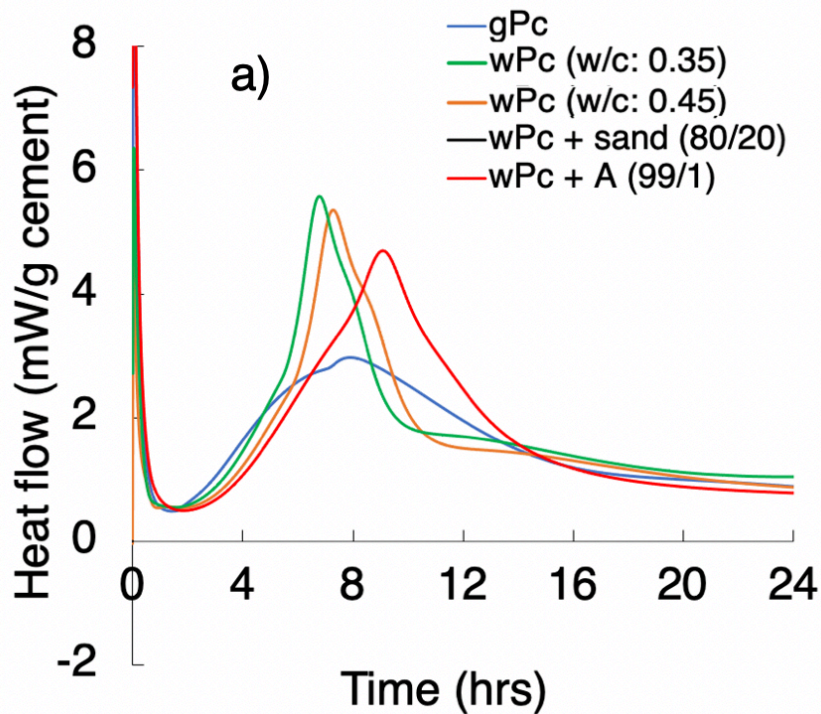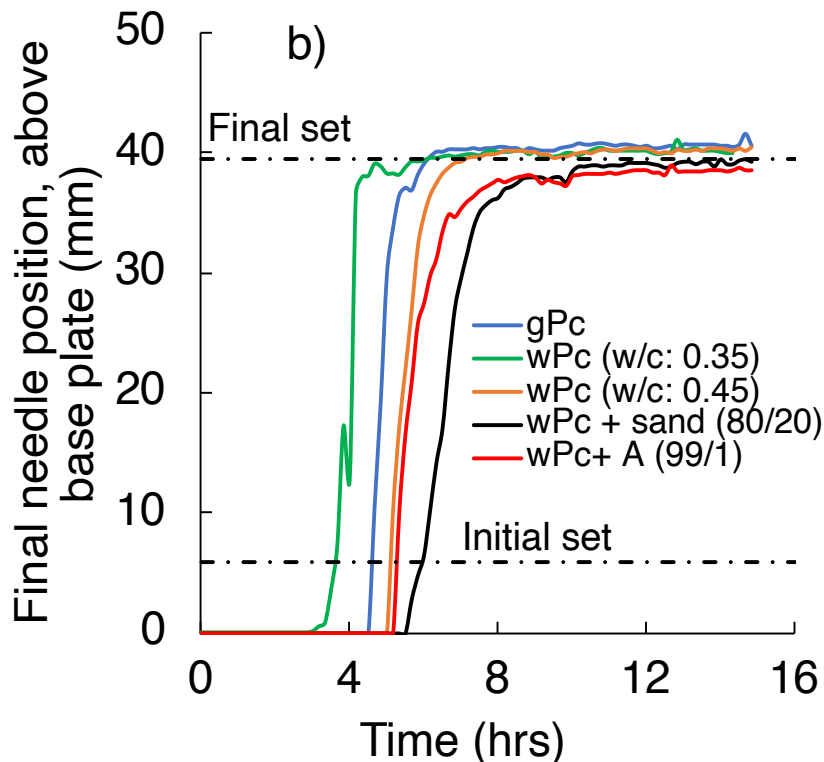
Fig. 7-1. Hydration of gPc, and wPc at different replacement levels and w/c ratios: a) heat flow, b) Vicat determination of setting time. Experimental data were obtained from Chapter 5 [39].

Fig. 7-2 a-b shows the conductivity and resistivity response of gPc, wPc, and blends at the specified replacement concentrations during the first 24 hrs after mixing. A correlation between the hydration stages and the conductivity perturbations is observed. Approximately between 1-2 hours after mixing (during the dormant period), samples show a small perturbation in conductivity which is attributed to the quick dissolution of ionic species into the aqueous solution (e.g. alkalis, sulphate, Ca^{2+} and OH^-). Also, as the new hydrated products are formed and free water content decreases, the conductivity decreases [100], [366]. At approximately 7-11 hrs, a perturbation in the resistivity and conductivity measurements, related to the maximum release of heat and the deceleration period, is observed in all samples (Chapter 5) [39].

At longer hydration ages, the increasing bulk resistance attributed to densification of the microstructure, and a decrease of free water content in all the pastes, is observed [13], [29], [36], [293]. gPc paste shows resistivity values lower than that of the wPc paste as a result of a smaller surface area and lower conversion of C_3A.

These changes lead to a higher capillary porosity, a lower hydration rate and a lower volume of hydrate products [108]. wPc (w/c: 0.35) shows the highest resistivity values due to a denser microstructure obtained as a result of a faster hydration rate, and more limited space and available water [226], [297]. Similarities in the bulk resistance behaviour of wPc/sand and wPc/anhydrite pastes require further investigation.
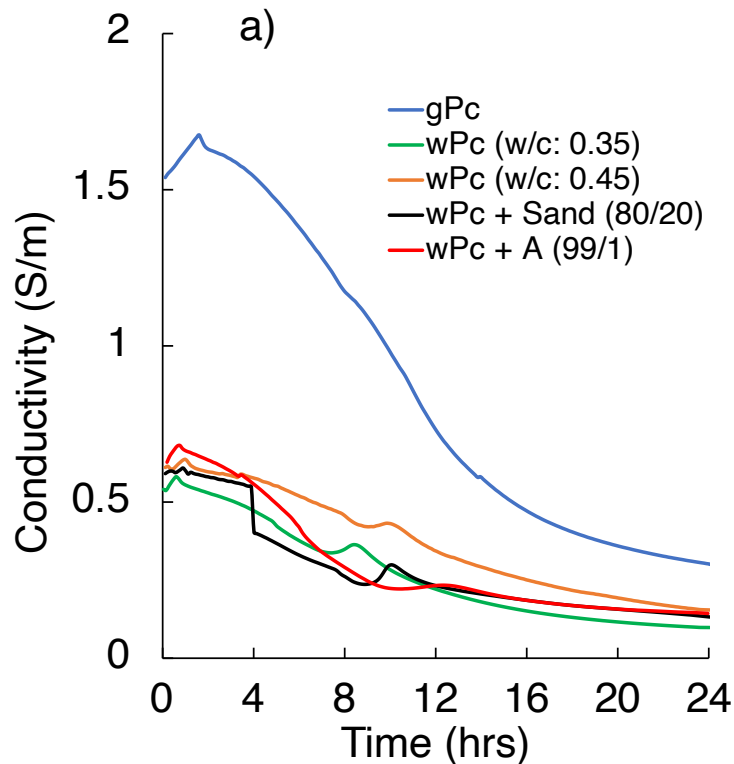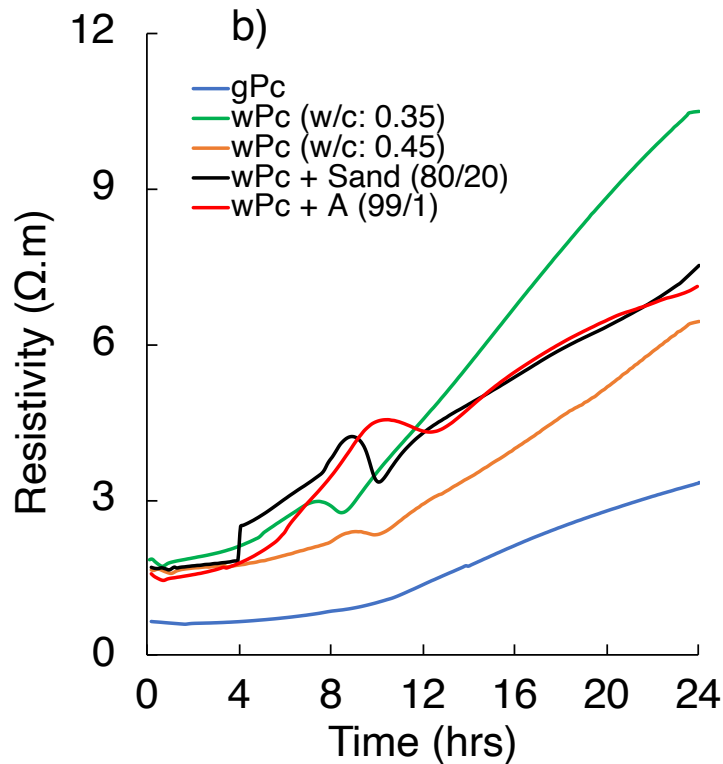
Fig. 7-2. a) Conductivity and b) resistivity of gPc, wPc, and blends at the specified replacement concentrations and w/c ratios. Experimental data were obtained from Chapter 5 [39].

7.3.2 White Portland cement (w/c: 0.35 and 0.45)

Fig. 7-3a-d show SEM images of wPc (w/c: 0.35 and 0.45, respectively) at different stages of hydration.

At 4 hrs after mixing, wPc$_{(w/c:\ 0.35)}$ paste (Fig. 7-3a) shows a denser microstructure attributed to rapid dissolution of C$_3$S and unfilled space leading to a faster setting of the paste, corroborating the Vicat test measurements obtained (Fig. 7-1). By comparison, the wPc$_{(w/c:\ 0.45)}$ paste (Fig. 7-4a) shows a larger capillary voids size and a higher amount of C-S-H due to a higher degree of hydration and interparticle spacing (dilution effect) [88], [194]. At 8 hrs after mixing, wPc$_{(w/c:\ 0.35)}$ (Fig. 7-3b) shows, an

amount of C-S-H and AFt formation(as observed in EDX analysis) higher than the wPc$_{(w/c:\ 0.45)}$ paste (Fig. 7-4b) as a result of the reaction of C$_3$A in presence of gypsum and sulphate depletion [80].

At 12 hrs, a denser microstructural development with a slightly higher growth of hydrated products (i.e. C-S-H, CH and AFt) is observed in both wPc pastes. Also, the formation of voids surrounded by hydrated products can be identified as a result of the complete reaction of some of the cement grains [203].

As the hydration continues to 24 hrs, the wPc$_{(w/c:\ 0.35)}$ paste, Fig. 7-3d, shows a microstructure with higher connectivity between the cement phases and a lower capillary porosity attributed to the free water content and the limited space. wPc$_{(w/c:\ 0.45)}$ paste (Fig. 7-4d) shows a lower connectivity between cement phases, higher capillary porosity and higher hydrated calcium aluminate content as a result of the dilution effect which increases the initial pore space and the degree of hydration [72], [367], [368].

a) wPc $_{(w/c:0.35)}$ 4 hrs   50 µm
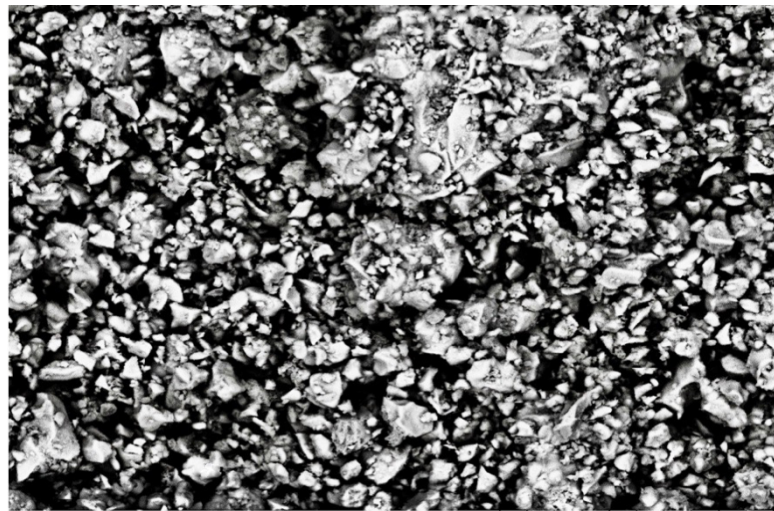
b) wPc (w/c:0.35)   8 hrs   50 µm

c) wPc (w/c:0.35)   12 hrs.   50 µm

d) wPc (w/c:0.35)   24 hrs   50 µm
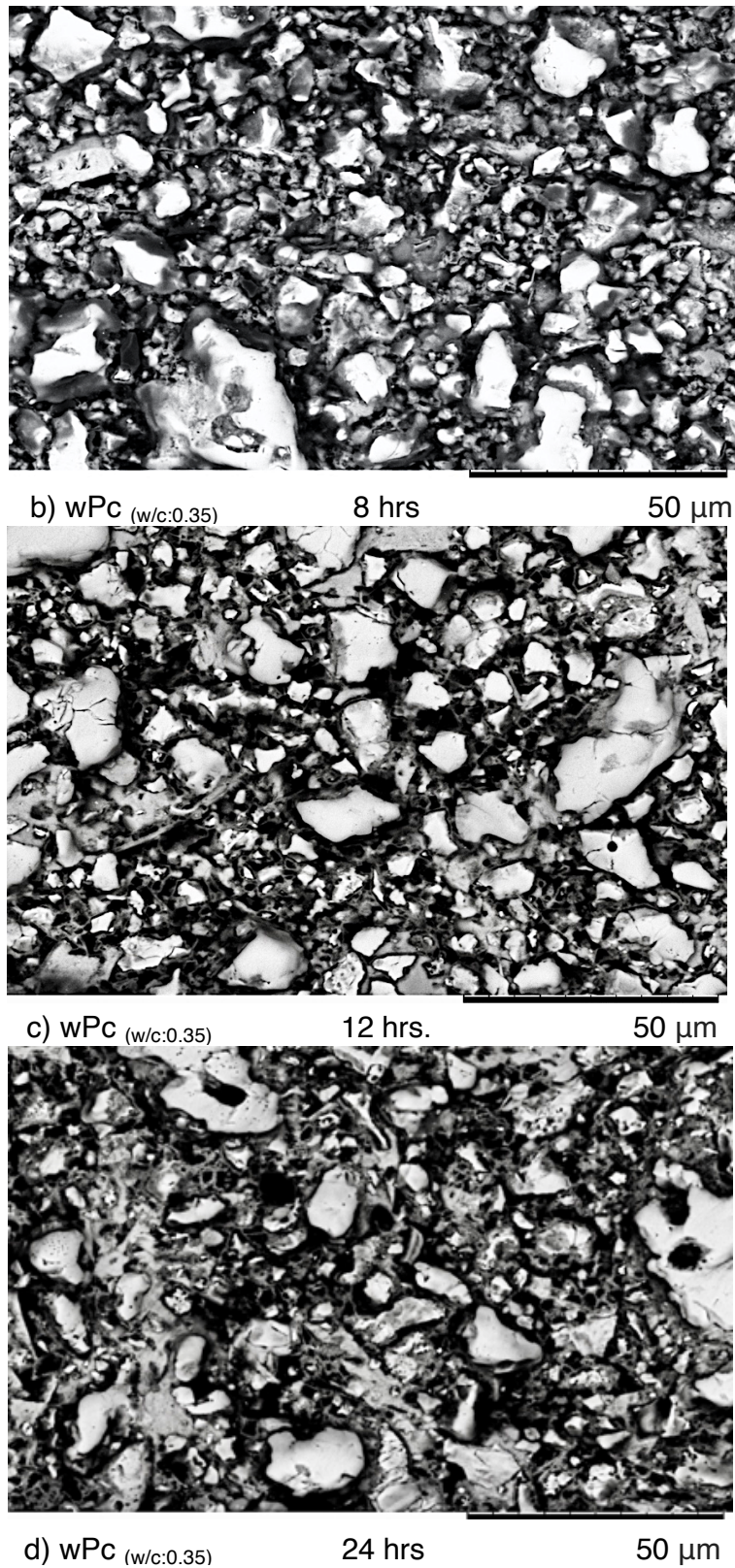
Fig. 7-3. SEM images of wPc (w/c: 0.35) paste at different hydration stages: a) 4 hrs, b) 8 hrs, c) 12 hrs and d) 24 hrs after mixing.
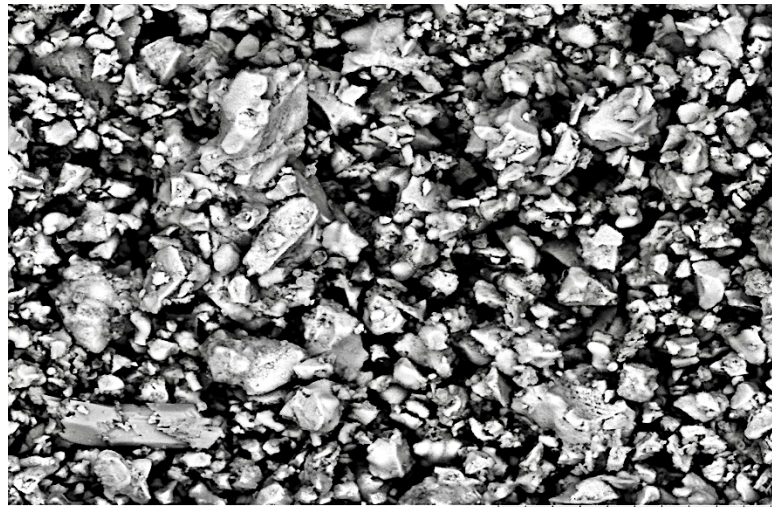
a) wPc (w/c:0.45)   4 hrs   50 µm
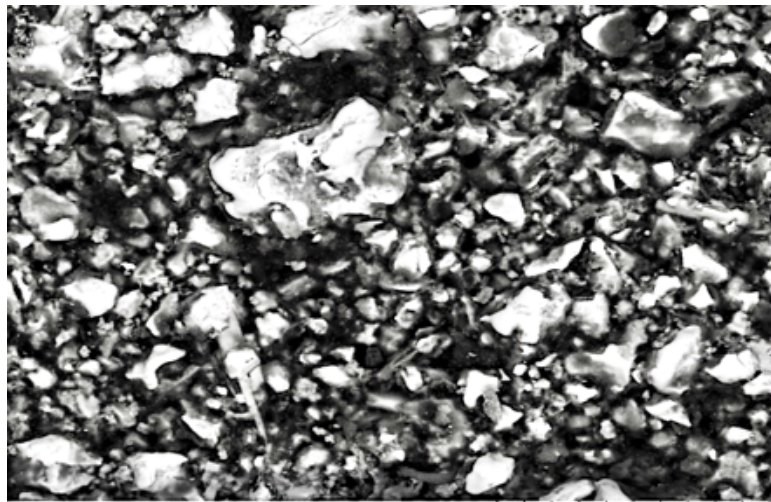
b) wPc (w/c:0.45)   8 hrs   50 µm
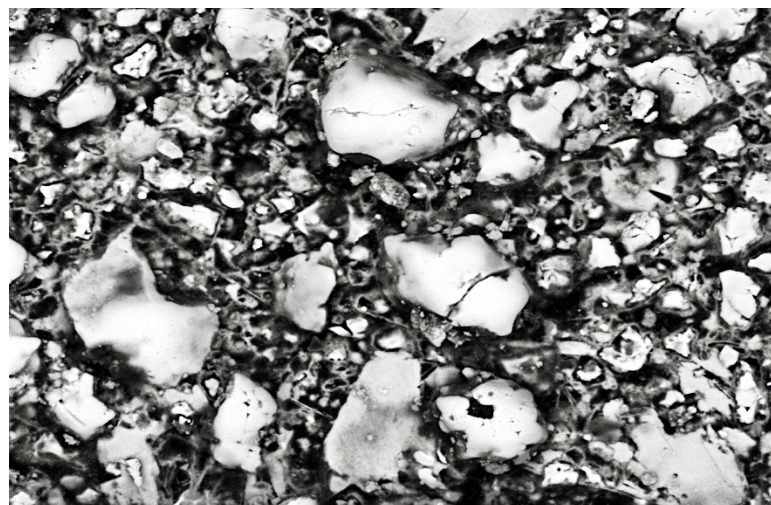
c) wPc (w/c:0.45)   12 hrs   50 µm

d) wPc (w/c:0.45)   24 hrs   50 µm

Fig. 7-4. SEM images of wPc (w/c: 0.45) paste at different hydration stages: a) 4 hrs, b) 8 hrs, c) 12 hrs and d) 24 hrs after mixing.

Fig. 7-5a-b show the impedance response of wPc pastes at w/c ratios of 0.35 and 0.45, respectively, during the first 24 hrs after mixing. At 5 min after mixing, a semicircular arc of low impedance is observed for both pastes. However, the impedance measurements for wPc$_{(w/c:\,0.35)}$ are affected by the parasitic effects at high frequency, which is probably attributed to rapid dissolution and a higher content of ionic species in the aqueous solution (e.g. Ca^{2+}, Na^+, K^+, OH^- and SO_4^{2-}) as a result of a lower water content [56], [66], [288], [369].

At 4 hrs after mixing, the wPc$_{(w/c:\,0.45)}$ paste impedance response is affected by parasitic effects, and the resistance and impedance values slightly increase due to the consumption of water and the increase of ionic species in the aqueous solution [164].

Between 4 and 12 hrs after mixing, the impedance and resistance values continue increasing, and at longer hydration ages the parasitic effects at high frequency decrease for both pastes. These trends are attributed to the evolution of the microstructure in which the nucleation and crystallisation of hydrated products is

ongoing [169]. wPc$_{(w/c:\,0.35)}$ paste shows impedance and resistance values higher than that of the wPc$_{(w/c:\,0.45)}$, attributed to a lower capillary porosity and a lower degree of hydration which decrease the space between the cement particles and accelerate the cement setting time. These results corroborate the Vicat test measurements (Fig 7-1) and SEM characterisation (Fig. 7-3 and Fig. 7-4) [159], [169].

At 24 hrs after mixing, a more developed semicircular arc and a major increase in resistivity are observed for both pastes. However, the impedance measurements for wPc$_{(w/c:\,0.35)}$ paste at high frequency are no longer affected by parasitic effects due to a lower free water content, denser pore size distribution, and higher percolation of the microstructure. wPc$_{(w/c:\,0.45)}$ shows a smaller semicircular arc of a lower impedance, in which parasitic effects are slightly affecting impedance measurements at high frequency, attributed to a higher capillary porosity and higher free water content [164], [367].

At this stage, the thermochemistry and Vicat test measurements of both wPc pastes show a similar behaviour (Fig. 7-1); however, the impedance response differs in each sample, as changes in the bulk resistance and impedance values demonstrate the influence of w/c ratio in determining the microstructural development and electrical properties of the cement pastes, in a way that is not readily captured by calorimetry or Vicat measurements.
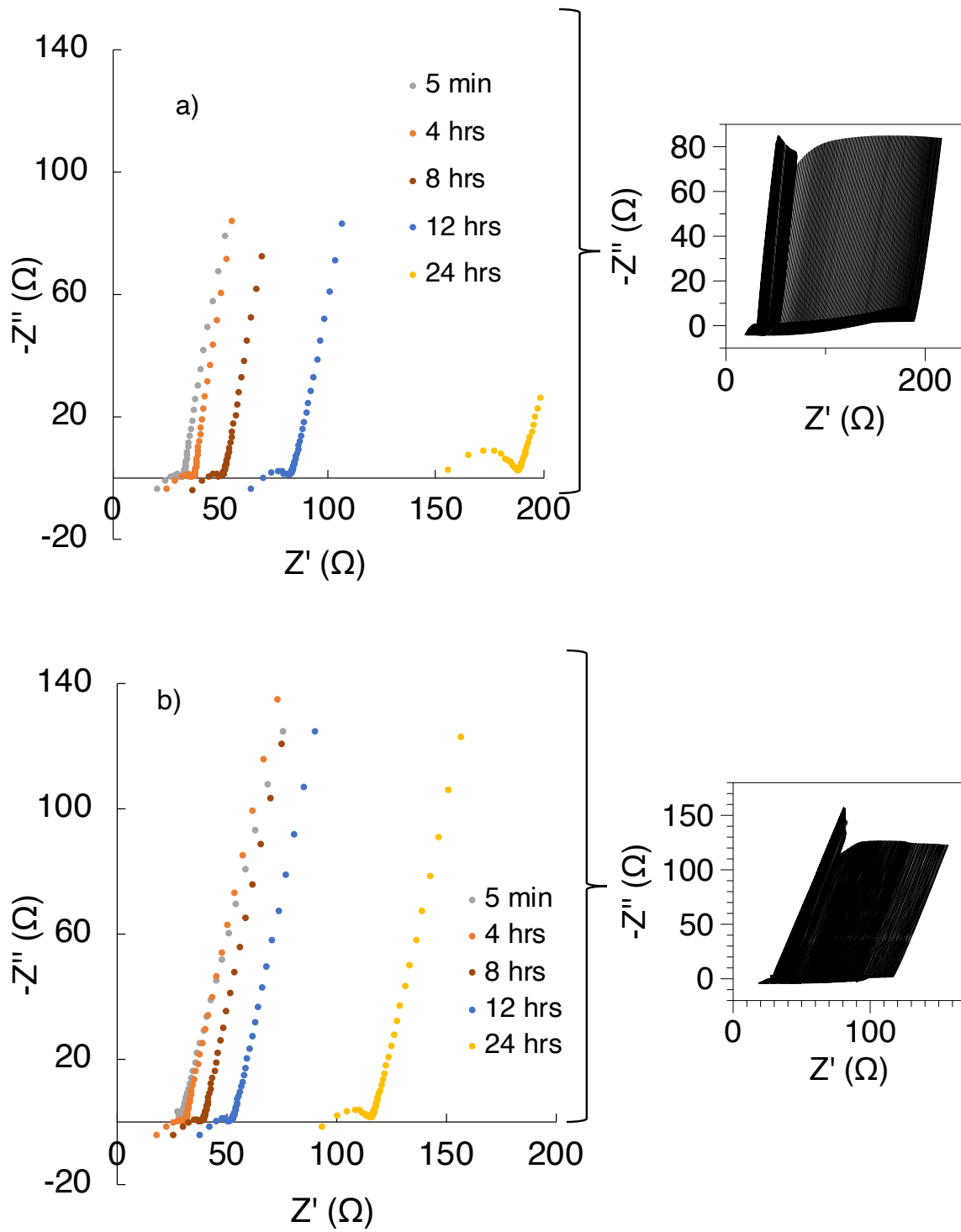
Fig. 7-5. ACIS response of wPc paste at different w/c ratios: a) 0.35 and b) 0.45.

7.3.3 Grey Portland cement

Fig. 7-6a-d shows SEM images, and Fig. 7-7 displays the impedance response, of gPc at different hydration stages.

At 4 hrs after mixing, a small difference in morphology between gPc (Fig. 7-6a) and wPc(w/c: 0.45) cement grains is observed. However, gPc shows a larger particle size which leads to an earlier beginning of the setting and the acceleration period. These effects are produced due to a more stable transformation of AFt into AFm, the formation of secondary phases (as a result of a higher sulphate content in gPc paste) and a lower degree of hydration that agree with the gPc calorimetric curve and setting time results [370]. The relationship among the water content, the particle size and the surface area of gPc cause a decrease in the impedance and resistance values, attributed to a slower dissolution rate of the clinker phases and a higher ionic strength [108], [294].

At 8-12 hrs after mixing, SEM images of gPc (Fig. 7-6b-c) show a more developed microstructure in which a higher content of hydrated products and an increase in the connectivity between the phases are observed. However, the impedance values of gPc are lower than of the wPc(w/c: 0.45) paste, showing a higher conductivity and porosity attributed to a lower degree of reaction and a higher ion concentration in the pore solution (section 5.3.1) [371].

At 24 hrs after mixing, the SEM image of gPc (Fig. 7-6d) shows a denser microstructure attributed to a major consumption of the clinker phases and growth of hydrated products. An increase in the gPc impedance measurements is obtained due to a partial dissolution of C_3S and a surface area lower than wPc which decreases the nucleation sites for hydrated product growth (making it more difficult for water to diffuse and reach anhydrous C_3S). Also, the appearance of new available space from the partial consumption of the clinker phases can be identified.

Comparing the results of wPc(w/c: 0.45) (Fig. 7-4d) and gPc paste, a more disconnected microstructure with lower connectivity between the phases and higher porosity is observed in gPc paste [57], [148], [372], [373]. However, at 24 hrs, the emergence of parasitic effects in the impedance measurements of gPc at high frequencies needs further investigation.
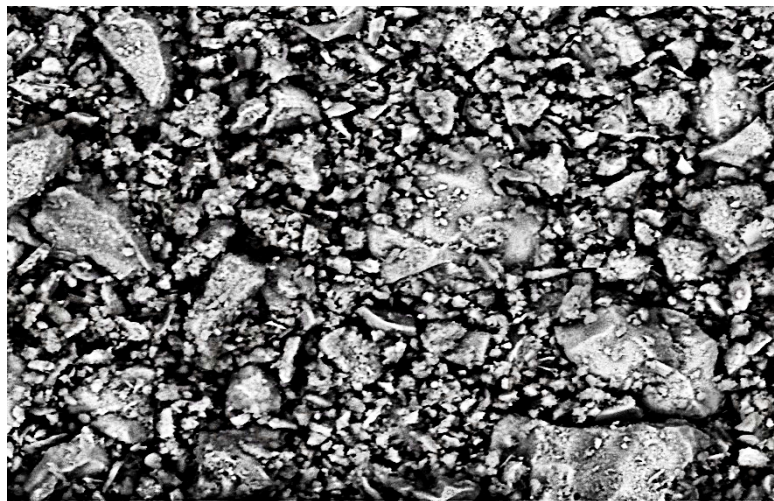
a) gPc (w/c:0.45)   4 hrs   50 µm
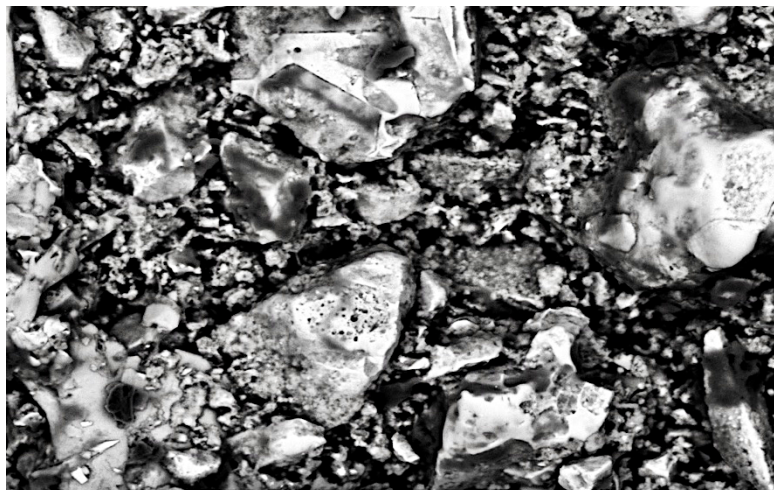
b) gPc (w/c:0.45)   8 hrs   50 µm
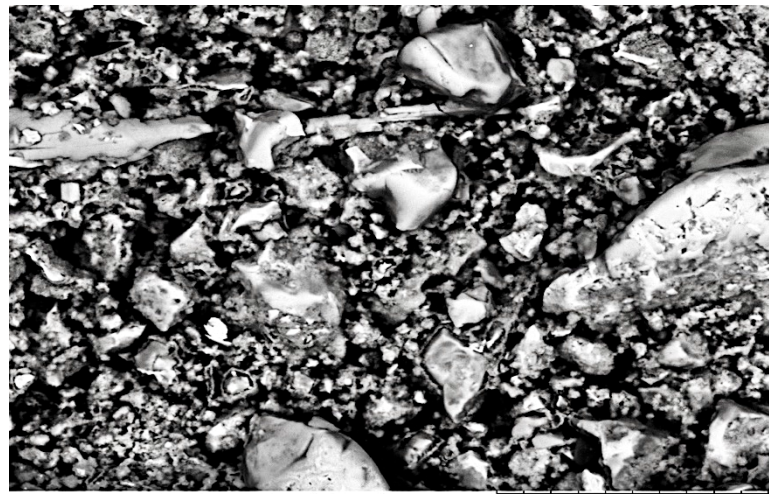
c) gPc (w/c:0.45)   12 hrs   50 µm
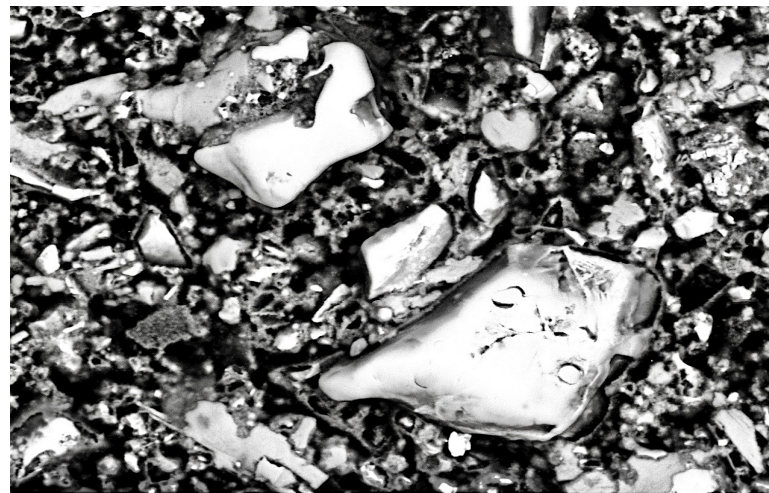
d) gPc (w/c:0.45)   24 hrs   50 µm
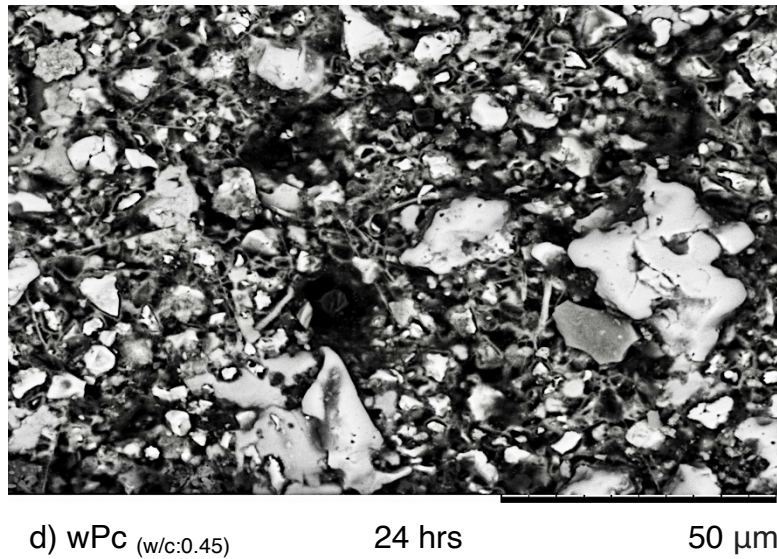
Fig. 7-6. SEM images of gPc paste at different hydration stages: a) 4 hrs, b) 8 hrs, c) 12 hrs and d) 24 hrs after mixing.
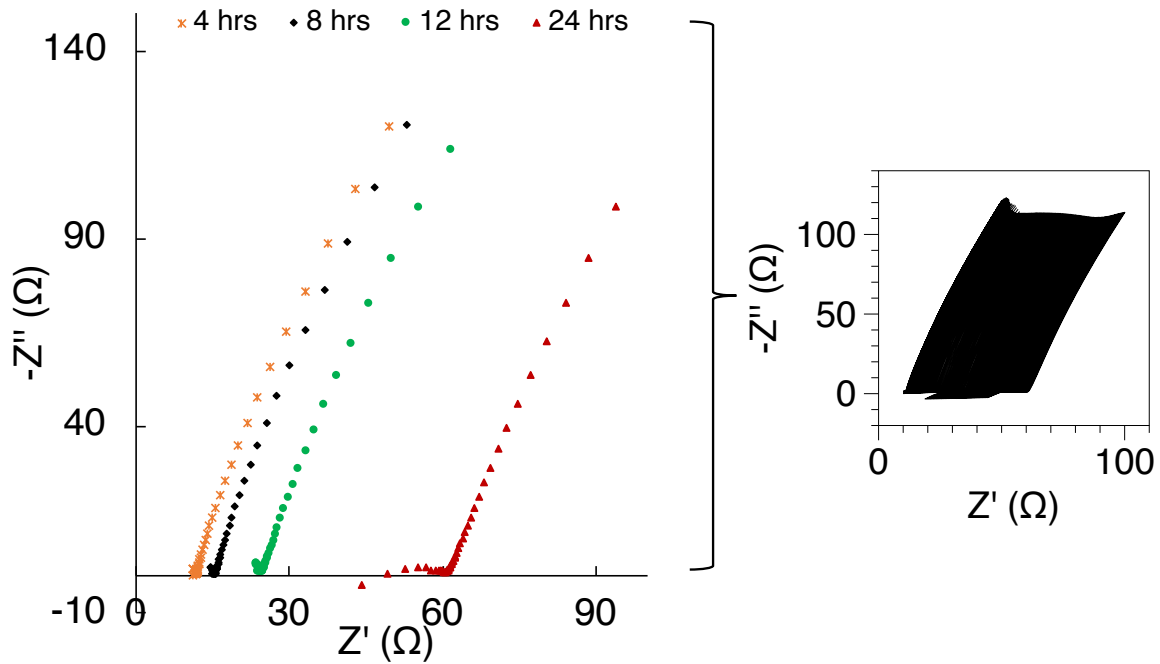
Fig. 7-7. ACIS response of gPc paste at different ages (w/c: 0.45).

7.3.4 Anhydrite (A)

Fig. 7-8a-d shows SEM images. Fig. 7-9 displays the impedance response, for wPc paste at 1% anhydrite replacement level (in addition to the gypsum that is already interground with this commercial cement, ≈ 2%) at different hydration stages.

At 4 hrs after mixing, in comparison to the $wPc_{(w/c:\ 0.45)}$ paste (Fig. 7-4a), no notable changes in the microstructure by the replacement of wPc with this quantity of anhydrite (Fig. 7-8a) are observed. However, the addition of 1% anhydrite slightly decreases the impedance measurements due to a change in the pore solution (Ca^{2+} and SO_4^{2-} content), leading to a small increase in the conductivity [207]. The influence of parasitic effects in the impedance measurements at high frequency remains similar.

At 8 to 12 hrs after mixing, although the addition of anhydrite caused a delay in the acceleration-deceleration periods and the final setting time, the wPc/anhydrite paste (Fig. 7-8b) shows a similar microstructure with a porosity lower than that of the $wPc_{(w/c:}$

0.45) paste. These changes in the wPc/anhydrite microstructure and the conductivity in the system are attributed to a higher formation of AFt and pore structure refinement, agreeing with the increase of the impedance measurements observed.

At 12 hrs (Fig. 7-8c), the impedance values of wPc/anhydrite and the conductivity of the system increase due to a change in the ionic strength as a result of anhydrite consumption, C_3A hydration, and a partial conversion of AFt to AFm [313], [318], [374]. These results agree with the thermochemistry measurements (Fig 7-1). The heat evolution rate of the wPc/anhydrite paste is similar to that of the wPc(w/c: 0.45) paste. However, the heat flow peaks (corresponding to the C_3S and AFt transformation) are observed at longer times due to a retardation effect attributed to the sulphate provided by the dissolution of anhydrite.

At 24 hrs after mixing, wPc/anhydrite paste shows an impedance semicircle arc higher than that of the wPc(w/c: 0.45) paste, in which the influence of parasitic effects on the impedance measurements of wPc/anhydrite paste disappear at early hydration ages. At this stage, wPc/anhydrite paste shows a slightly higher resistance than that of the wPc(w/c: 0.45) paste [319], [375]. However, the influence on the impedance measurements by the replacement of wPc with anhydrite needs further investigation, since there is not a strong correlation among thermochemistry, the setting behaviour and the microstructural changes.

a) wPc/Anhydrite   4 hrs   50 µm
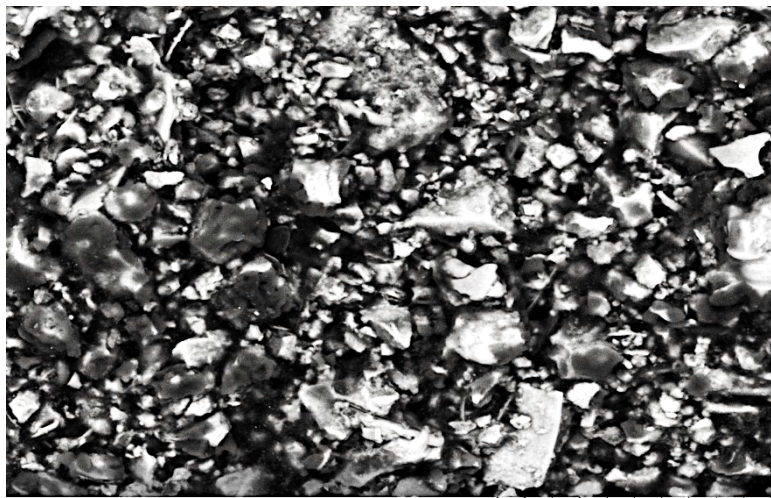
b) wPc/ Anhydrite   8 hrs   50 µm
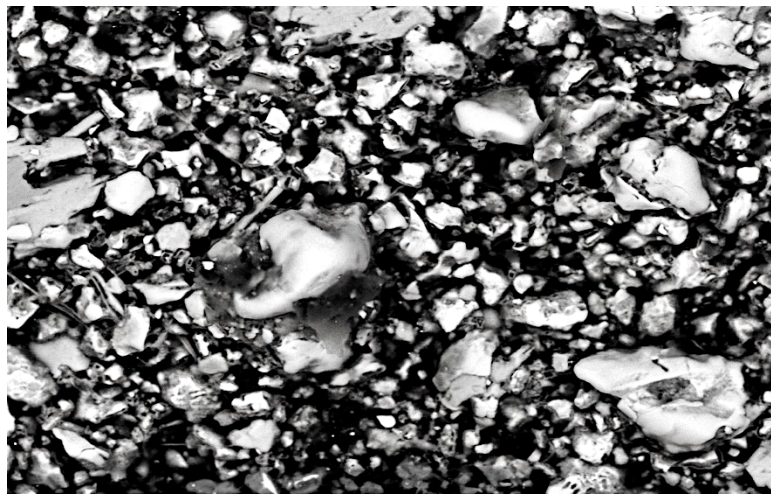
c) wPc/Anhydrite   12 hrs   50 µm
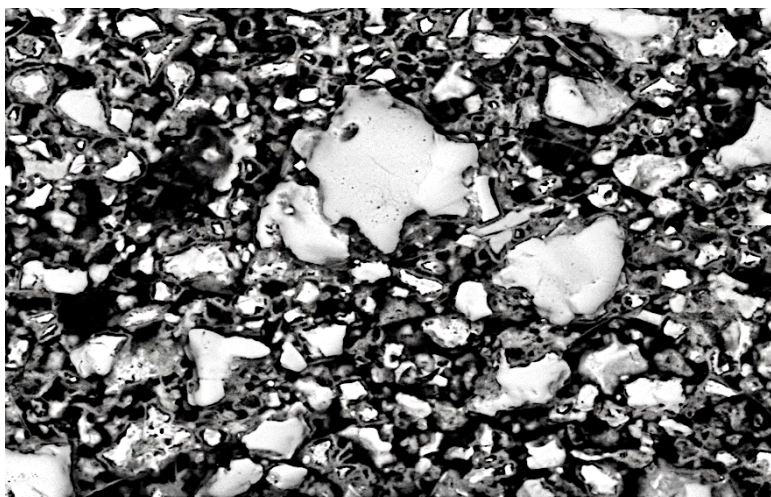
d) wPc/Anhydrite   24 hrs   50 µm

Fig. 7-8. SEM images of wPc/ Anhydrite (99/1) paste at different hydration stages: a) 4 hrs, b) 8 hrs, c) 12 hrs and d) 24 hrs after mixing.
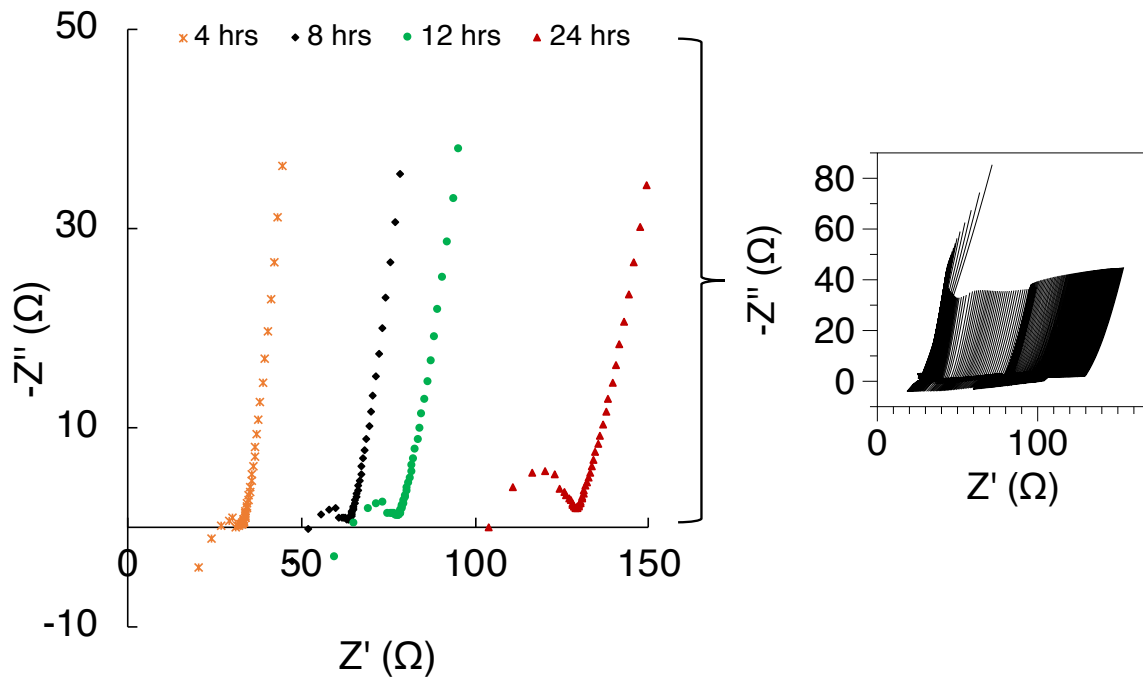
Fig. 7-9. ACIS response of wPc paste at 1% anhydrite replacement level.

7.3.5 Sand

Fig. 7-10a-d shows SEM images and Fig. 7-11 displays the impedance response, of wPc paste at a 20% sand (wPc/sand) replacement level at different hydration stages. At 4 hrs after mixing, wPc/sand (Fig. 7-11) shows an increase in the impedance measurements leading to an increase in the resistivity of the system. The previous effects agree with the changes observed in the microstructure, with a slightly denser microstructure and a decrease in the pore size distribution attributed to a filler effect. [157].

Thermochemistry measurements, in comparison to wPc$_{(w/c:\ 0.45)}$ paste (Fig. 7-1a), show that the addition of sand delays the acceleration period and the sulphate depletion peak. Also, during the acceleration hydration stage, a rapid decrease in conductivity and a higher increase in the impedance measurements are observed.

This behaviour is attributed to the reduced paste content in the system and the microstructural changes produced by the replacement of wPc with sand, as the particle and the pore size distribution have an influence on the ionic conduction paths [30], [309].

At 8 hrs after mixing, the final setting of the wPc/sand paste is reached, showing a relatively dense microstructure (Fig. 7-10b) with an amount of C-S-H generated higher than that of the wPc$_{(w/c:\ 0.45)}$ paste, agreeing with the high impedance values obtained.

At 11 hrs after mixing, an increase in the conductivity that agrees with the thermochemistry results (Fig. 7-1) with a secondary heat peak during the end of the acceleration period, is observed. The changes in the thermochemistry and electrical response are attributed to depletion of sulphate ions from the pore solution [184]. This is followed by a decrease in conductivity due to densification of the microstructure as a result of the crystallisation and growth of CH and C-S-H phases. At 12 hrs after mixing, Fig. 7-10c shows a small development of the microstructure with a higher connectivity between the phases. The impedance and the resistivity measurements slightly increase at the end of the deceleration period [152].

At 24 hrs after mixing, wPc/sand paste shows a denser microstructure (Fig. 7-10d) with a higher degree of percolation. The increase of the impedance measurements agrees with the densification of the microstructure showing, at high frequency, a semicircle arc of higher impedance attributed to the sand/cement interface and a decrease of Ca^{2+} ions in the pore solution. At this stage, the mortar impedance measurements at high frequency are no longer affected by the parasitic effects. The small difference in impedance and conductivity values between the mortar and wPc paste implies that the conductivity contribution of the sand/cement interfacial transition zone is not strongly different from that of the wPc$_{(w/c:\ 0.45)}$ paste.

Also, the deposition of hydrated products around the sand/cement interface, attributed to an increase in the nucleation sites and the crystallisation of CH due to better stability and nucleation conditions, is observed [26], [104], [140], [308].

a) wPc/Sand   4 hrs   500
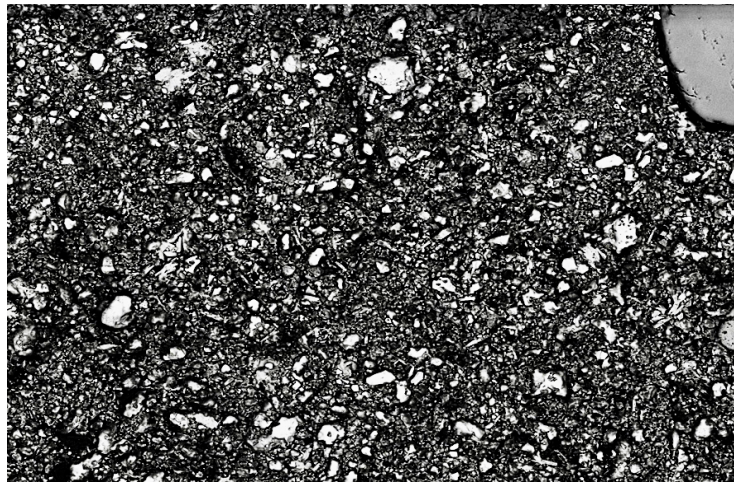
b) wPc/Sand   8 hrs   500 µm
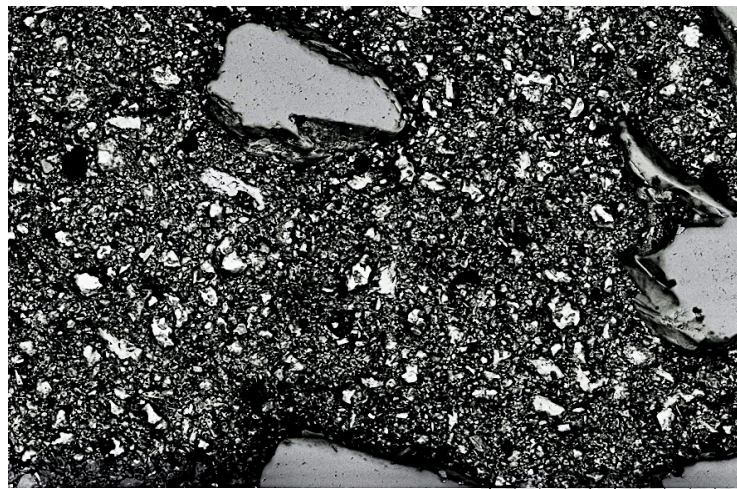
c) wPc/Sand   12 hrs   500 µm
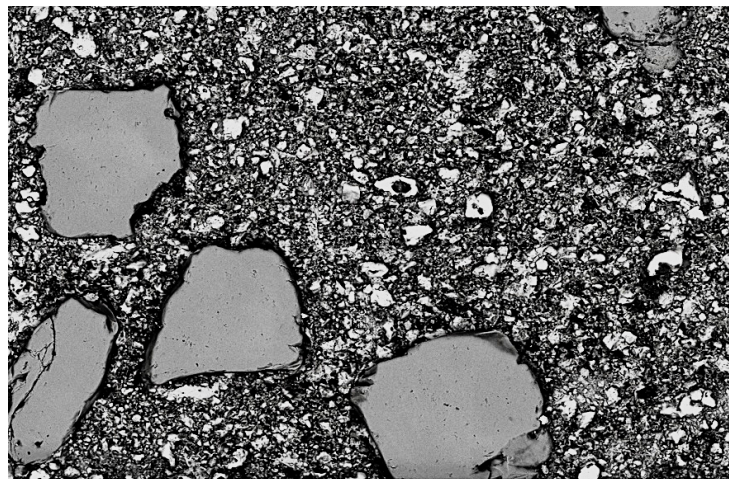
d) wPc/Sand   24 hrs   500 µm

Fig. 7-10. SEM images of wPc/sand (80/20) paste at different hydration stages: a) 4 hrs, b) 8 hrs, c) 12 hrs and d) 24 hrs after mixing.
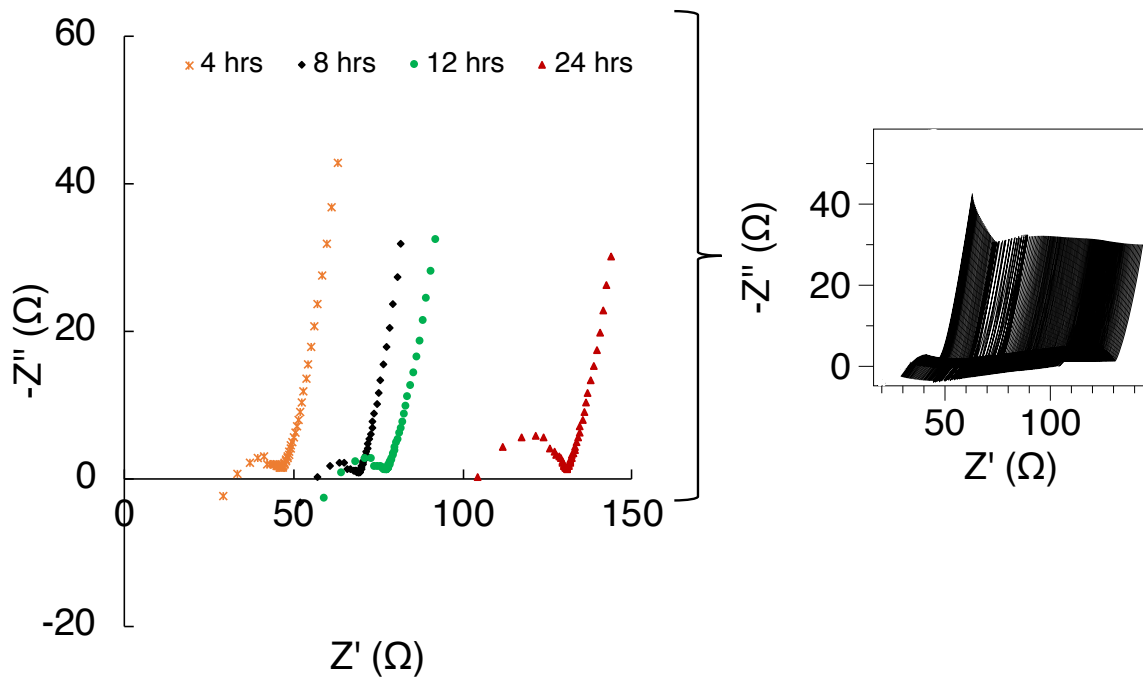
Fig. 7-11. ACIS response of wPc paste at a 20% sand replacement level.

7.3.6 White Portland cement and supplementary cementitious materials

Fig. 7-12a shows the calorimetric curves of wPc at different SCM replacement levels during the first 24 hrs after mixing. Fig. 7-12b shows the corresponding Vicat needle penetration displacement measurements, up to 14 hrs after mixing.

These thermochemistry measurements show a heat release increase in the initial hydration period in all wPc blends. During the induction and acceleration periods, wPc pastes with GGBFS show similar trends to those of the $wPc_{(w/c:\ 0.45)}$ paste. In the case of wPc replacement with the addition of FA, the induction and acceleration periods are delayed and the height of the maximum exothermic peak at the end of the acceleration period is decreased, whereas the wPc replacement with SF slightly delays the induction and the beginning of the acceleration period (section 6.3.3).

At approximately 5 hrs after mixing and during the acceleration period, wPc/SF paste shows a slight increase in the heat rate (observing the maximum exothermic peak at an earlier time than that of the wPc paste) while the heat rate of wPc/GGBFS and the wPc/FA pastes decreases. The changes in the thermochemical behaviour, due to the replacement of wPc with GGBFS, FA and SF at early hydration ages, are mainly attributed to a dilution effect which has an influence on the ionic concentration of the pore solution, the particle size distribution, the water available for the cement reaction, and on the nucleation sites needed for the growth hydrated products [11], [328], [334], [339], [351]. The changes observed, due to the replacement of wPc with GGBFS, FA, SF in the thermochemistry measurements, agree with the setting time measurements (Fig. 7-12b) with a decrease in the initial setting time as result of a filler effect. The final GGBFS and FA paste setting times are similar to that of the wPc$_{(w/c: 0.45)}$, whereas with SF the final setting time decreases considerably due to a quick setting of the paste as a result of a lower particle size, a higher water demand and a higher growth of hydrated products leading to a denser microstructure [359], [360], [376].

During the deceleration period, wPc paste shows a rapid decrease of the heat release, whereas the replacement of wPc with GGBFS/FA/SF expedite this period of hydration. The deceleration period is followed by a gradual decline of the heat release into the long-term period.

Also, during the deceleration-long-term period, wPc/SF paste shows the highest influence in the heat release rate, showing a high release of heat until 18 hrs after mixing. This effect is attributed to sulphate depletion, AFt transformation and partial reaction of SF with CH, (Fig. 7-12a) [327], [351], [354].
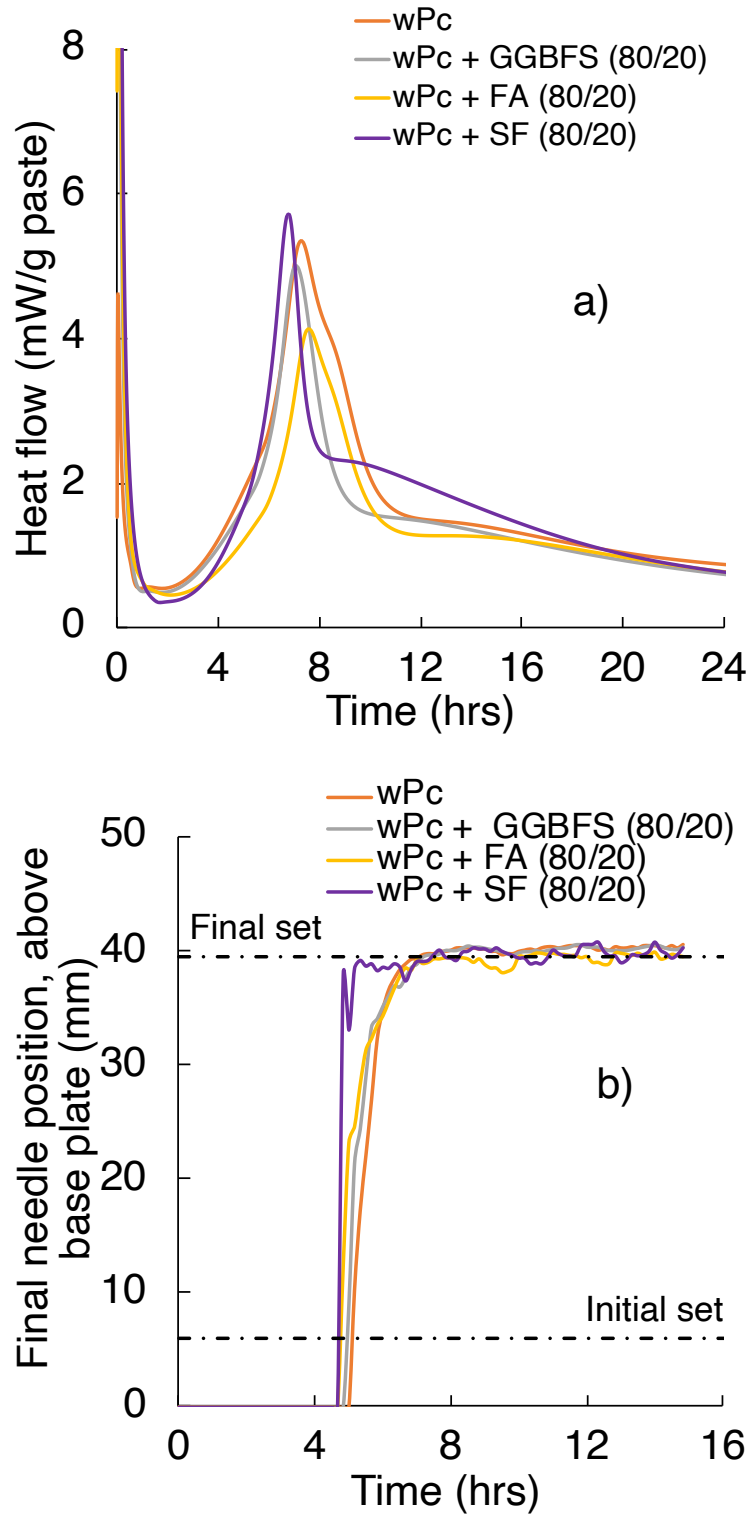
Fig. 7-12. wPc hydration at different SCM replacement concentrations: a) heat flow (normalised to total sample mass), b) Vicat determination of setting time. Experimental data were obtained from Chapter 6 [38].

Fig. 7-13a-b shows the conductivity and resistivity response of wPc at different SCM replacement concentrations during the first 24 hrs after mixing.

At approximately 1-2 hr after mixing, the conductivity measurements (Fig. 7-13a) show a perturbation followed by a decreasing tendency, that agrees with the beginning of the induction period and its changes produced by the replacement of wPc with SCM's. These perturbations are related to the particle size distribution and its influence on the diffusion of ions in the pore solution (section 6.3.3).

At around 4 hrs after mixing, a second perturbation in the conductivity attributed to a decrease in the charge transfer resistance controlled by the chemical potential of the ionic species, is observed. The replacement of wPc with SCMs delays the appearance of a second perturbation that corresponds to the changes in the pore solution, and particularly its ionic strength. Between 7 and 11 hrs after mixing, a third perturbation in the conductivity measurements attributed to a decrease in the heat flow and Ca^{2+} & SO_4^{2-} content, and followed by an increase in OH^-, K^+ & Na^+ content in the pore solution at the end of the deceleration period, is observed. This behaviour agrees with the thermochemistry results (Fig. 7-12). At longer hydration ages and as the microstructure densifies, conductivity values follow a decreasing tendency [76], [330], [361].

Through the resistivity change rate and its perturbations and after the microstructure has reached a certain level where it is constrained by space for further hydrated growth (Fig. 7-13b), it is possible to follow the microstructural development of cement and the beginning of the hardening process, and identify the influence exerted by the reaction of the clinker phases. At this early stage of hydration, the replacement of wPc with SF or FA decreases the resistivity at early and longer hydration ages (up to 24 hrs) as a result of a lower percolation of the microstructure and pore structure refinement, a decrease in the CH content, and the generation of C-S-H with lower Ca/Si ratio [337], [364]. The addition of GGBFS increases the resistivity

values due to a higher densification of the microstructure as a result of a filler effect which increases the nucleation sites for hydrate product formation [188], [332].
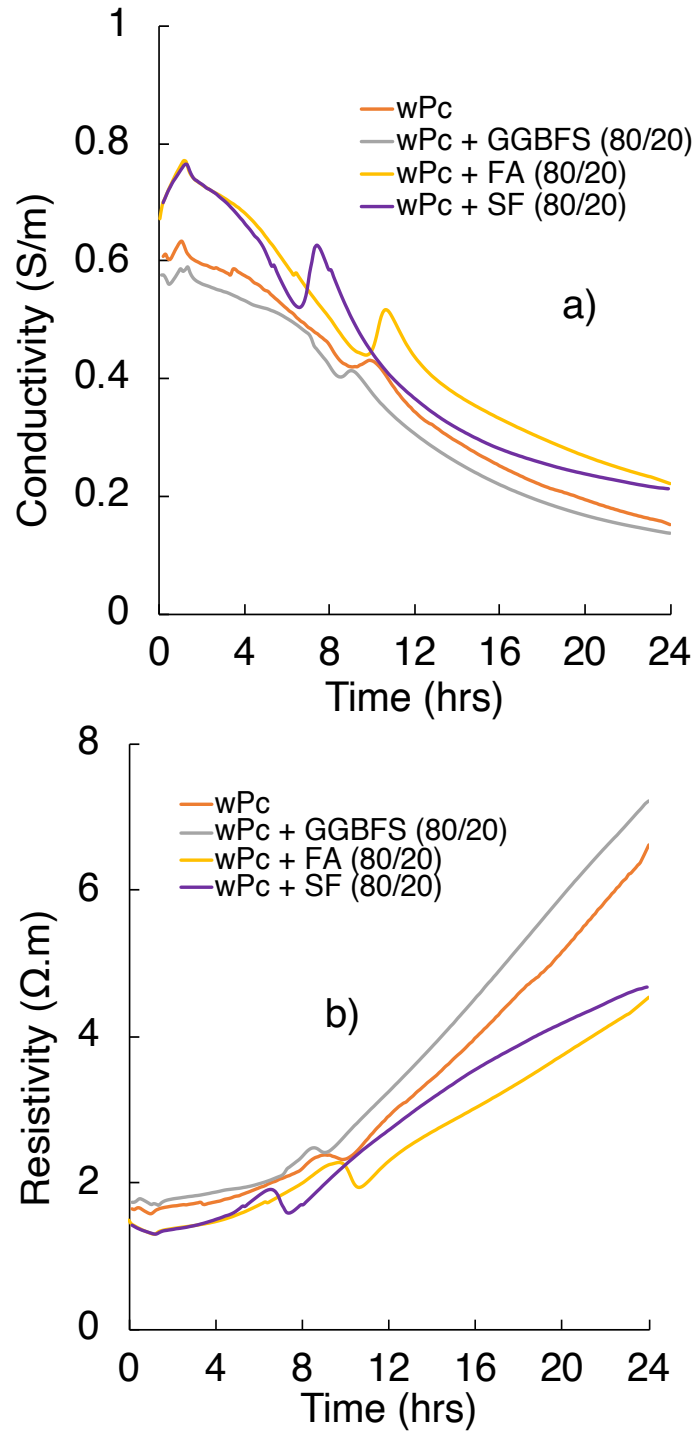
Fig. 7-13. a) Conductivity and b) resistivity of wPc pastes at different SCM replacement concentrations.

7.3.7 Ground-granulated blast-furnace slag

Fig. 7-14a-d shows SEM images and Fig. 7-15 shows the impedance response of wPc at a 20% GGBFS (wPc/GGBFS) replacement level and different hydration stages.

At 4 hrs after mixing, wPc/GGBFS (Fig. 7-14a) shows a microstructure with a similar morphology to that of the wPc$_{(w/c:\,0.45)}$ paste (Fig. 7-4) with a small decrease in porosity and higher C-S-H gel formation. These differences in the wPc/GGBFS paste microstructure agree with a slight increase in the impedance values attributed to a filler effect which influences the hydrated product formation and grain distribution, and the decrease in the ionic strength, Fig. 7-15 [76], [340].

At early ages (5 min; Fig. 7-15a), the impedance values and the parasitic effects increase slightly as the GGBFS replacement increases as a result of a decrease in the ionic strength produced by the replacement of cement clinker by the slower-reacting GGBFS, lowering the concentrations of rapidly-soluble species (i.e. alkali, sulphates and gypsum) and increasing the water volume that reacts with cement particles.

At 8 to 12 hrs after mixing, the wPc/GGBFS microstructure (Fig. 7-14b-c) compared to wPc$_{(w/c:\,0.45)}$ (

Fig. 7-4b-c), shows a small development and small differences in the connectivity between the phases and the porosity content. The impedance measurements and resistivity values of wPc/GGBFS remain slightly higher than those of wPc$_{(w/c:\,0/45)}$ paste (Fig. 7-5b). The small differences in the microstructure and the electrical response agree with the setting and the thermochemical measurements [377], [378].

At 24 hrs after mixing, wPc/GGBFS (Fig. 7-14d) shows a more developed microstructure with a higher level of percolation, similar to wPc$_{(w/c:\,0/45)}$ paste, with

small differences in phase connectivity and porosity. However, wPc/GGBFS paste shows a significant difference in the impedance and resistivity measurements due to a slight decrease in the pore size and ion species concentration (OH⁻, alkalis and sulphur species), and additional C-S-H formation, which lead to resistivity values higher than those of the wPc paste [101].
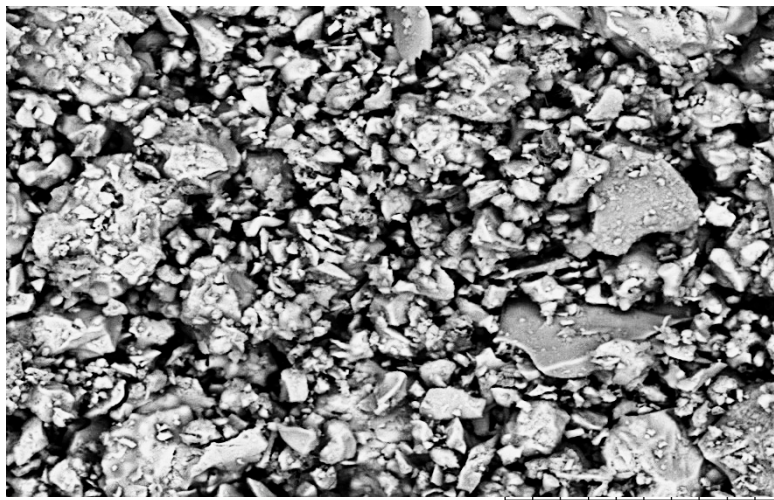
a) wPc/GGBFS   4 hrs   50 µm
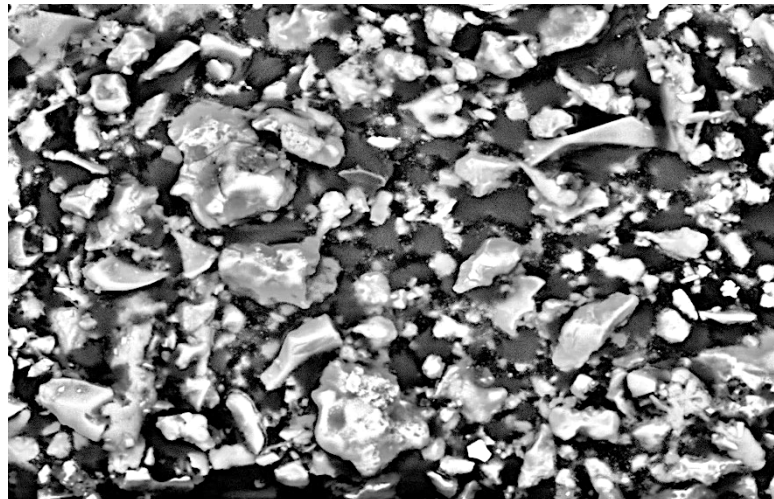
b) wPc/GGBFS   8 hrs   50 µm
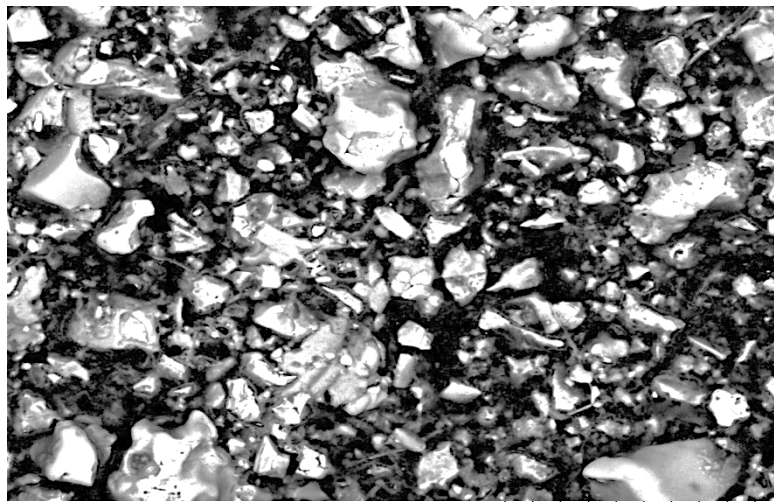
c) wPc/GGBFS   12 hrs   50 µm

d) wPc/GGBFS   24 hrs   50 µm

Fig. 7-14. SEM images of wPc/GGBFS (80/20) paste at different hydration stages: a) 4 hrs, b) 8 hrs, c) 12 hrs and d) 24 hrs after mixing.

Fig. 7-15. ACIS response of wPc paste at a 20% GGBFS replacement level.

7.3.8 Fly ash

Fig. 7-16a-d shows SEM images and Fig. 7-17 shows the impedance response of wPc at a 20% FA (wPc/FA) replacement level and different hydration stages.

At 4 hrs after mixing, the microstructure of wPc/FA (Fig. 7-16a) shows a dense arrangement between the phases. A high content of hydrated products formed around the cement grains, and major differences in the particle morphology and size distribution, can be observed. Even though the wPc/FA microstructure displays a lower porosity and a higher amount of occupied space, the impedance measurements (Fig. 7-17) show impedance and resistivity values lower than for the wPc$_{(w/c: 0.45)}$ paste (Fig. 7-5b). This electrical response is probably related to a higher pore connectivity (generated around FA particles) and a rapid dissolution of ionic species [335], [379]. However, this effect needs further investigation.

At 8 hrs after mixing, wPc/FA microstructure (Fig. 7-6b) shows a major consumption of cement clinker phases, a higher porosity and a more remarkable difference in morphology and particle size distribution between the cement and FA particles. These changes in the microstructure, due to a higher porosity and a lower hydrated product formation, agree with a small decrease in the impedance measurements of wPc/FA paste, obtaining a slightly more conductive system. A delay in the appearance of parasitic effects in the impedance measurements at high frequency, probably related to a decrease in the ionic strength of the system as a result of the replacement of wPc with FA, is observed [338].

At 12 to 24 hrs after mixing, wPc/FA paste shows a slight development in the impedance measurements compared to wPc$_{(w/c:\ 0.45)}$ paste measurements (Fig. 7-5b), obtaining the highest conductivity values in all the supplementary cementitious systems. This behaviour agrees with the changes observed in the microstructure of the wPc/FA paste (Fig. 7-16c-d) attributed to the addition of FA and its slow reaction which decreases the CH content and level of percolation, and increases the pore size [14], [337], [347].
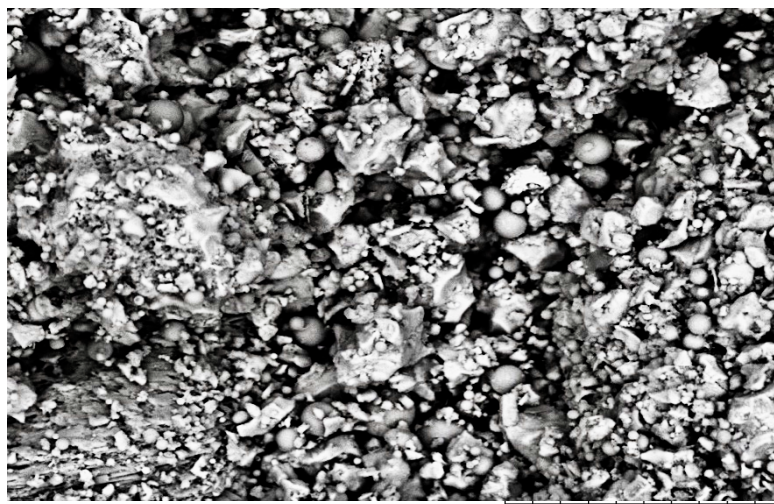
a) wPc/FA   4 hrs   50 µm
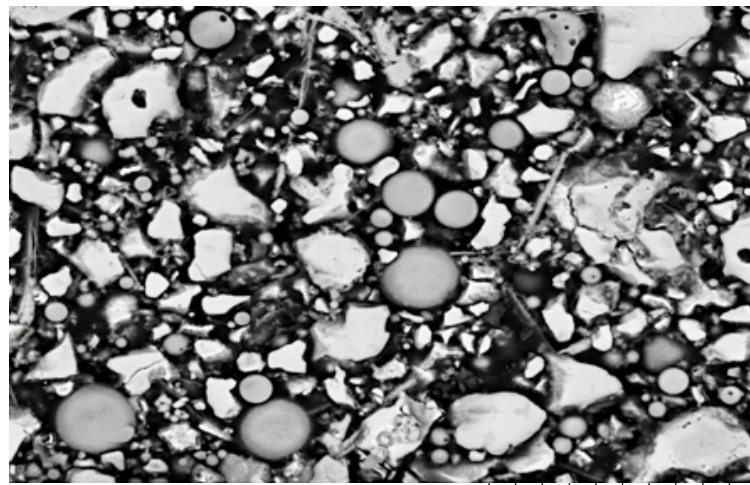
b) wPc/FA   8 hrs   50 µm
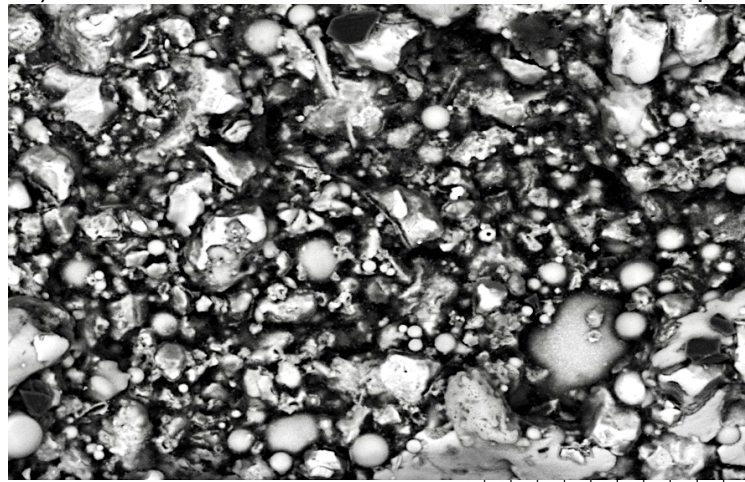
c) wPc/FA   12 hrs   50 µm
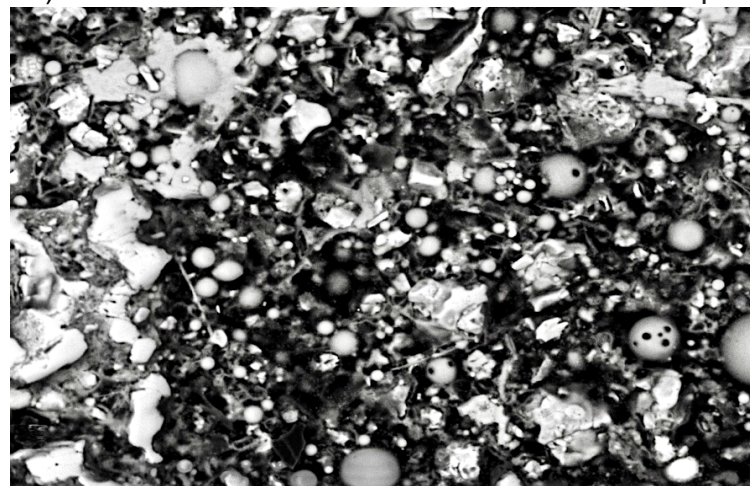
d) wPc/FA   24 hrs   50 µm

Fig. 7-16. SEM images of wPc/FA (80/20) paste at different hydration stages: a) 4 hrs, b) 8 hrs, c) 12 hrs and d) 24 hrs after mixing.
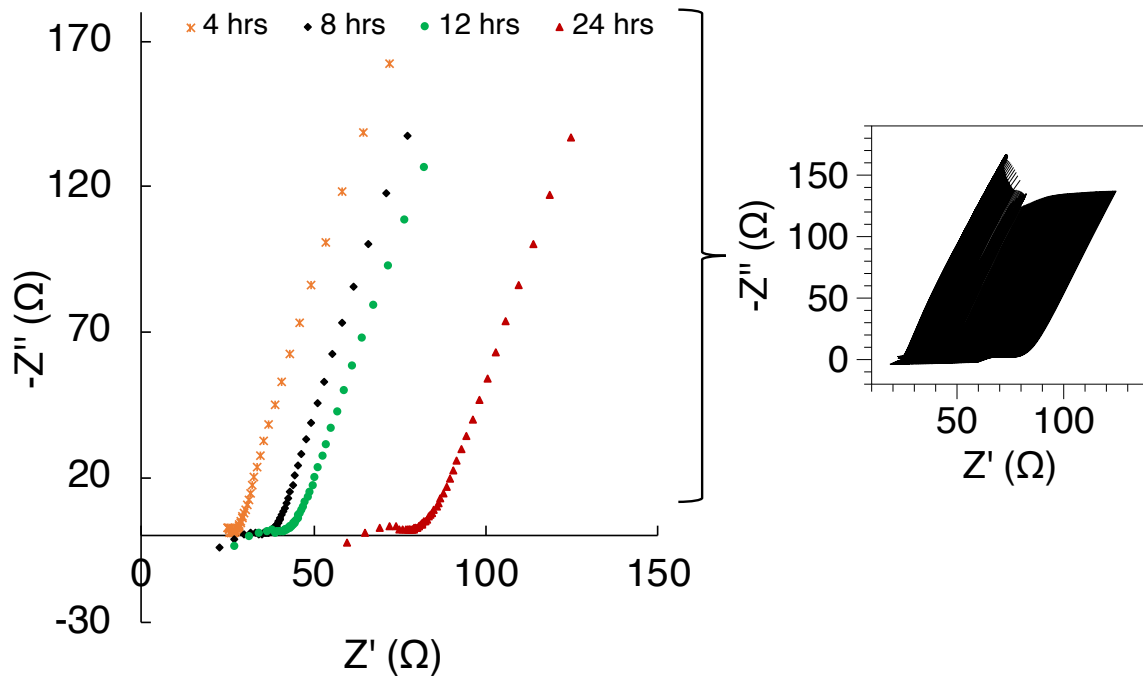
Fig. 7-17. ACIS response of wPc paste at a 20% FA replacement level.

7.3.9 Silica fume

Fig. 7-18a-d shows SEM images and Fig. 7-19 shows the impedance response of wPc at a 20% SF (wPc/SF) replacement level at different hydration stages.

At 4 hrs after mixing, the replacement of wPc with 20% SF (Fig. 7-18a) has a great impact on the microstructure of the system. At first instance, the microstructure shows a denser composition with lower available space for hydrated product growth, attributed to the smaller SF particle size and hydrated product formation around the SF particles. Higher conductivity and lower impedance values (Fig. 7-19) are obtained by the replacement of wPc with SF. These changes in the electrical response are attributed to a strong filler effect which affects the dissolution rate of the clinker phases and the content of ionic species in the pore solution, e.g. Ca^{2+}, K^+, Na^+, OH^- [170], [362], [363], [380]. At this stage, the impedance measurements at high frequency are

not affected by parasitic effects due to a decrease in the ionic strength and a lower densification of the microstructure probably related to a lower CH, alkali content and ion mobility. As a result, the supersaturation of the pore solution and the formation of hydrated products is delayed [175].

At 8 hrs after mixing a slight increase in the wPc/SF paste impedance measurements, a microstructure with higher connectivity between the pores (Fig. 7-18b), and similar conductivity values, are observed. These effects are correlated to a lower content of CH, a decrease in the heat flow rate, and an increase in the OH^- content.

At 12 to 24 hrs after mixing, wPc/SF paste (Fig. 7-18c-d) shows a rapid development of the microstructure with a slight decrease in porosity attributed to the consumption of the clinker phases, and a different morphology and particle size of the hydrated products formed. These changes in the microstructure agree with a gradual increase in the impedance measurements as a result of the percolation of the microstructure, the precipitation of new hydrated products and the small contribution of the pozzolanic reaction of SF. The wPc/SF conductivity values are higher than those of the wPc$_{(w/c:\ 0.45)}$ paste (Fig. 7-13a) at early ages due to a higher pore connectivity and a stronger ionic strength. At later ages (< 3d), a higher densification and resistivity of the system is expected as a result of strong influence of the SF pozzolanic reaction on the microstructure [168], [170], [363].

a) wPc/SF   4 hrs   50 µm

b) wPc/SF   8 hrs   50 µm
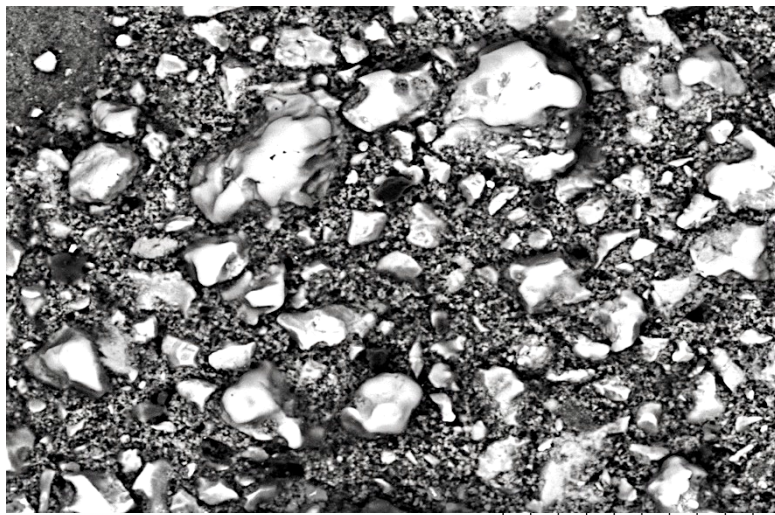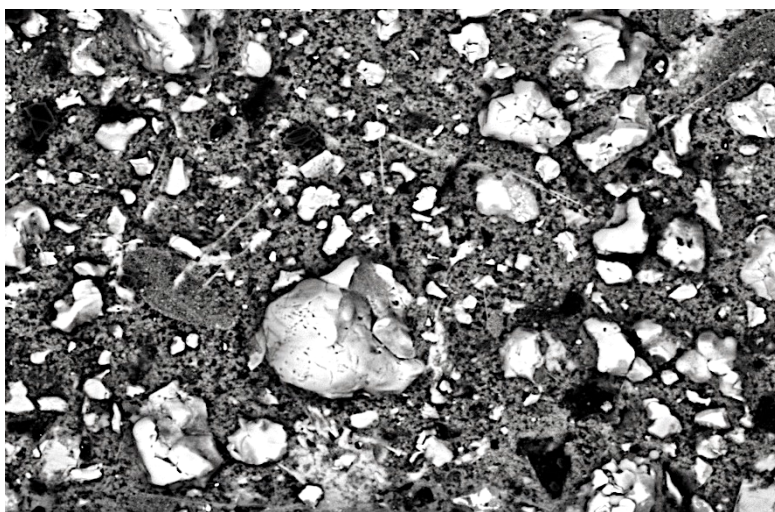
c) wPc/SF   12 hrs   50 µm

d) wPc/SF   24 hrs   50 µm
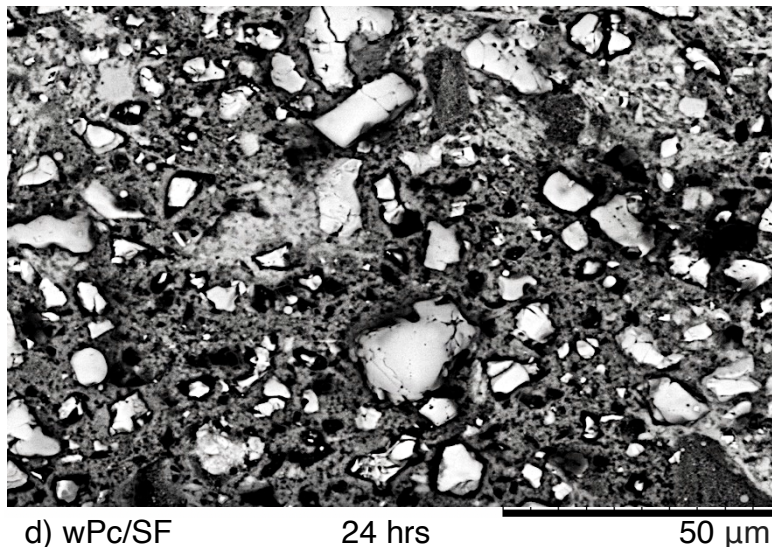
Fig. 7-18. SEM images of wPc/SF (80/20) paste at different hydration stages: a) 4 hrs, b) 8 hrs, c) 12 hrs and d) 24 hrs after mixing.
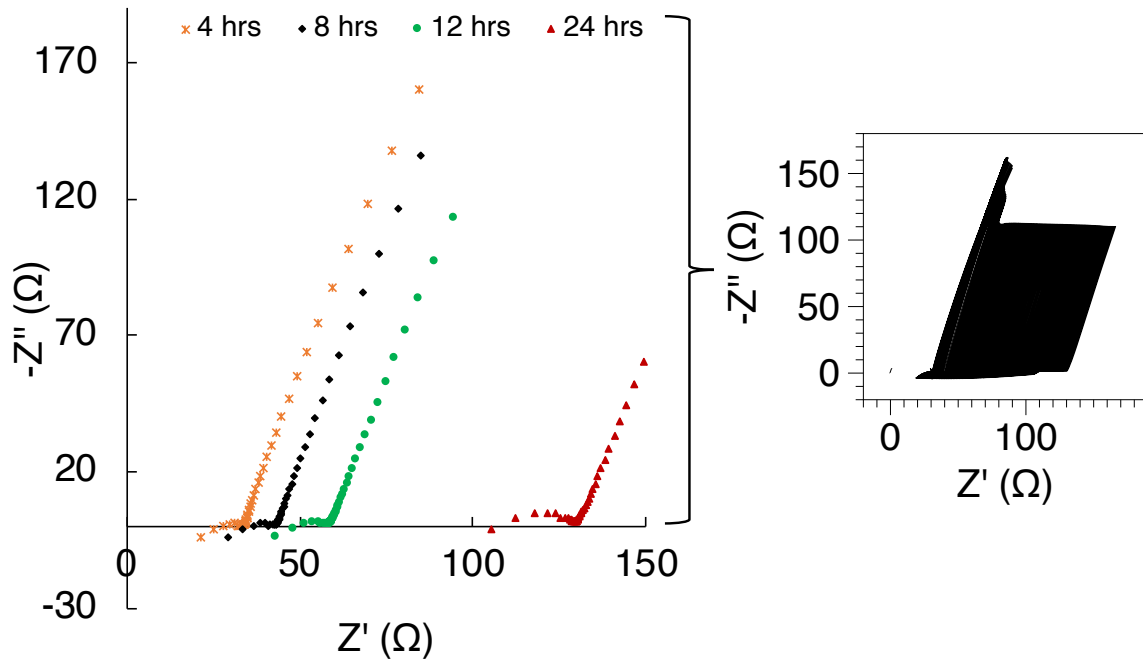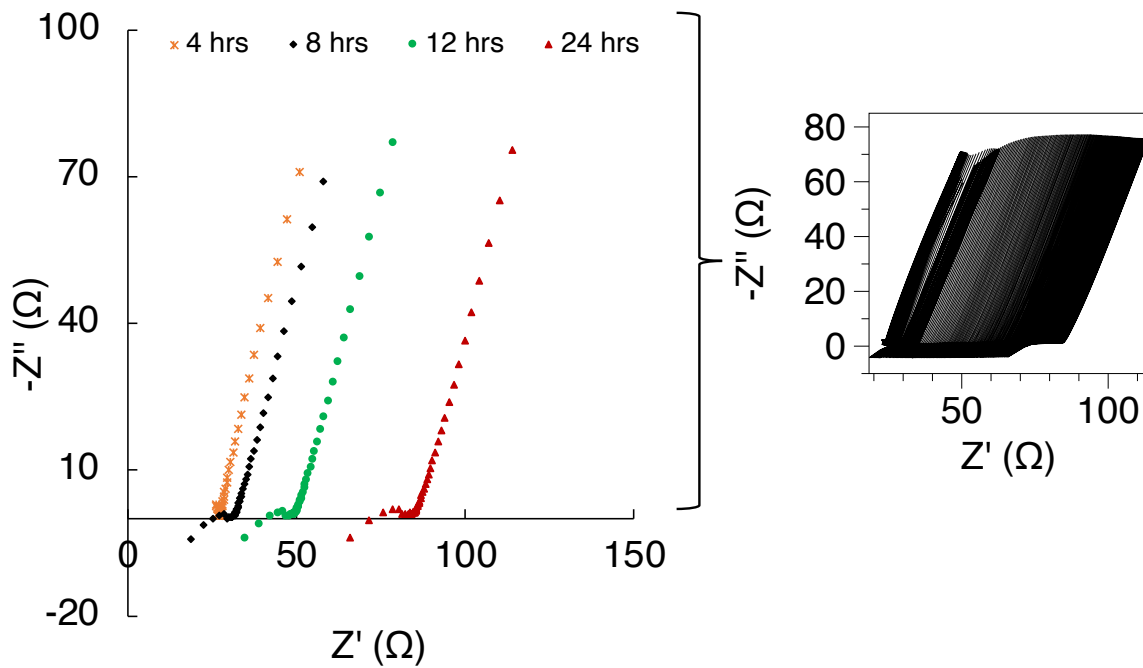

Fig. 7-19. ACIS response of wPc paste at a 20% SF replacement level.

7.4 Conclusions

This chapter has evaluated the microstructural development of Portland cement and blends at early ages (≥24 hrs) by assessing the electrochemical response and other properties. The results demonstrate that ACIS can be a useful and sensitive technique to obtain a better understanding of the relationships between the electrical response of cement during hydration and its microstructural development and features (e.g. morphology, particle and pore size distribution). However, in order to obtain a better ACIS data interpretation, the support of different characterisation techniques is needed.

Summarising:

- The hydration kinetics and microstructural changes produced by the partial replacement of wPc with sand, $CaSO_4$, or mineral admixtures (e.g. morphology, particle size, chemistry) at early hydration stages, influence the electrochemical behaviour of wPc.

- Water to cement ratio and particle size distribution plays an important role in controlling the ionic strength of the pore solution and the microstructural development, which in turn affect the electrochemical response of the system.

- The emergence and behaviour of parasitic effects in the impedance measurements at high frequency are strongly related to a decrease in the charge transfer resistance as a result of an increase in the ionic strength in the pore solution.

- The decrease in electrical resistivity of wPc due to the addition of sand, $CaSO_4$, FA and SF is mainly attributed to a filler effect and the concentration of ionic species in the pore solution.

- Regarding the conductivity perturbations observed, the first perturbation is associated to the rapid dissolution of the ionic species in the pore solution. The second is attributed to the charge transfer resistance decrease, and the third is related to a decrease in Ca^{2+} & SO_4^{2-} content and an increase of the OH^-, K^+ & Na^+ content in the pore solution.

Chapter 8:

Modelling and simulation

Note: This chapter is based on the paper *"Simulation of the impedance response of hydrating tricalcium silicate at early stages of hydration"* by A. F. Sosa Gallardo, J. L. Provis and J. Dean, [249], unpublished manuscript and submitted for publication, 2020, pp.1-32.

8.1 Introduction

Numerous techniques and theoretical modelling methods have been used in attempts to correlate the electrical response of Portland cement with its microstructural development. However, understanding these relationships remains challenging due to the complexity of cement chemistry and the kinetics of hydration.

Here we develop a finite element model (FEM) to simulate the impedance response for C_3S, representing a simplified description of Portland cement, at different stages of hydration. The model proposed is composed of three phases: water/pore solution, C_3S and C-S-H. The intrinsic properties (i.e. conductivity and permittivity) of these phases are assigned based on the degree of hydration (i.e. amount of C_3S that has fully reacted with water) and the volume fraction of each phase (Table 8-1).

Table 8-1. Approximate electrical properties and specifications of phases present in the simulation [381]–[383].

t	Water/Pore solution [294], [384]–[386]		C$_3$S			C-S-H (high density)	
	σ	ε	σ	ε	DoH	σ	ε
0.08	0.005				0.00	0.0140	2.50
4	2.03				0.05		1.0×10^3
8	1.79	80.06	0.014	2.50	0.14		5.0×10^4
12	1.30				0.22	0.008	8.5×10^5
24	0.20				0.40		4.0×10^5
	C-S-H (low density)*						
672	0.001	1.0×10^6			1.00		4.0×10^6

t: time (hrs), σ: conductivity (S/m) and ε: permittivity (F/m) [36], [156], [384], [387], and DoH: degree of hydration (%) [100], [226], [299], [381], [383], [388]–[390].

The intrinsic properties of Portland cement depend on different aspects such as the random arrangement of its constituents, particle size, morphology, curing conditions, ionic concentration, among others. These properties are defined to vary with time, as during the hydration process these phases go through different reactions, changes and stages (hydrolysis, oversaturation of the pore solution, and hydrated product precipitation, nucleation, and crystallisation) that lead to paste setting and changes in the intrinsic properties. As a result, the reaction and the contribution of each these phases to the physical and mechanical properties of the paste varies through time [59], [79], [80], [326], [391].

The hydration process of C$_3$S is thus similar to that of Portland cement [7], [44], [56] [57]:

- Rapid dissolution of C$_3$S
- Pore solution formation
- Hydrated product formation (mainly C-S-H, and CH)

- Release of heat

- Consumption of water

- Setting and hardening of the paste

However, the kinetics of reaction of C₃S, mainly attributed to chemical composition and the reaction between their constituents, are different from those of Portland cement. A schematic representation of C₃S hydration is provided in Fig. 8-1.
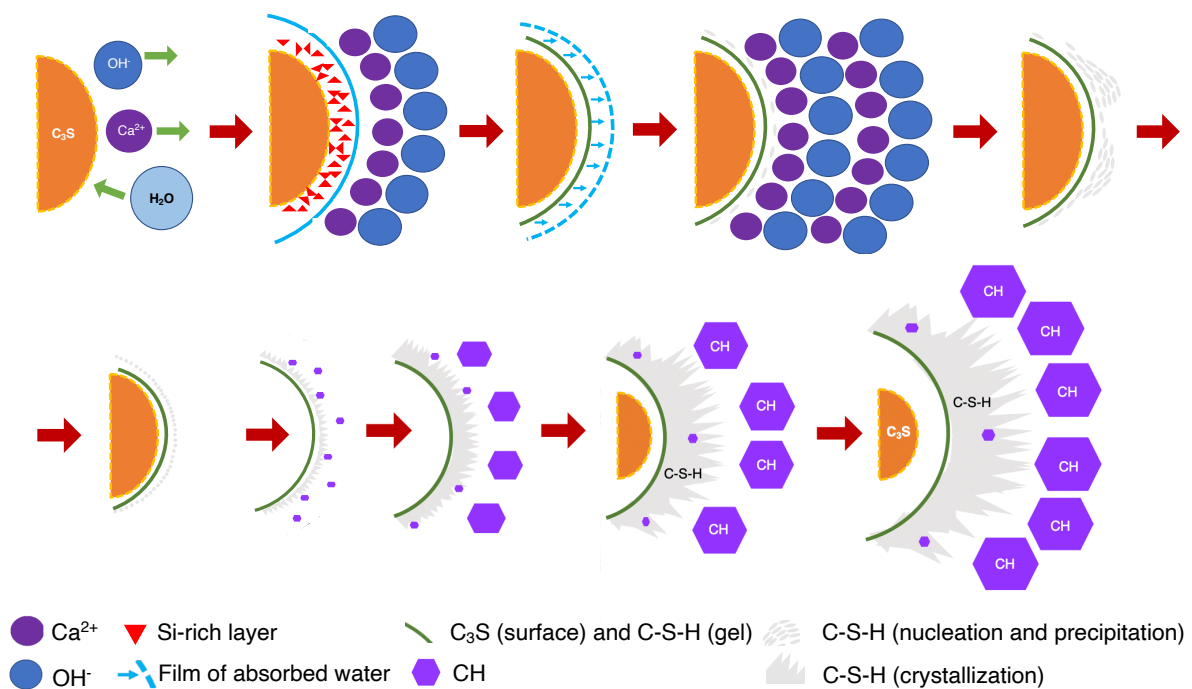
Fig. 8-1. Schematic representations of C₃S hydration, based on information from [3], [7], [80], [203], [343].

The degree of hydration of C₃S was estimated in the model at different hydration times (0.08 to 672 hrs) [383], [388]–[390]. Immediately after C₃S is mixed with water, the C₃S surface is rapidly dissolved leading to the supersaturation of the pore solution with respect to C-S-H and the precipitation of the C-S-H phase. This is followed by an increase in the concentration of Ca^{2+} and OH^- in the pore solution, leading to supersaturation of the pore solution with respect to calcium hydroxide, and precipitation of CH (<4 hrs). At this stage, the reaction of C₃S decreases).

Approximately 4-8 hrs after mixing, C_3S hydration is accelerated and controlled by the C-S-H growth rate. After the hydrated products cover unreacted C_3S grains, the reaction rate of C_3S is decreased and becomes diffusion controlled, lasting weeks/months. The reaction of C_3S ends when there is not enough available space for hydrated product growth or when C_3S is fully consumed, Table 8-2 [381]–[383].

Table 8-2. Mechanism of hydration and microstructural details of C_3S hydrates.

Mechanism of hydration	Microstructure
*t 1. Protonolysis of SiO_4^{4-} and O^{2-}. 2. Rapid dissolution of C_3S. 3. Ca^{2+}, $SiO_4^{4,}$ and OH^- ions enter the pore solution. 4. Oversaturation of the pore solution. 5. C-S-H(I) starts to precipitate at C_3S surface. 6. C_3S reaction rate decreases. 7. C-S-H nucleation (slow process). 8. Acceleration of C_3S dissolution. 9. Crystallisation and growth of a 2nd stage C-S-H(II) and CH. 10. Hydrated products fill available space and the pore solution are reduced. 11. Hydration of C_3S is slowed down until C_3S is consumed. 12. Hydration process ends (limited available space for hydrated product growth or fully consumption of C_3S).	1. Pore structure: a. Contains pores of different size. b. Decreases as hydration continues. c. Increases as water to solid ratio increases. 2. Hydrated products formed: d. Hydrated products surface area varies. e. High density C-S-H or inner product: C-S-H formed from C_3S grains. f. Low density C-S-H or outer product: C-S-H formed the initial water-filled pore spaces. g. Morphology of C-S-H varies fibres, flakes and honeycombs h. CH is formed in the initial water-filled space. i. Morphology of CH: large crystals.

*t: initial time after C_3S is mixed with water; **C-S-H: amorphous or nearly amorphous calcium silicate hydrate products; CH: $Ca(OH)_2$ [3], [7], [80], [203], [343].

The main objective of this chapter is to highlight the use of FEM to aid the interpretation of ACIS data for cement hydration. An impedance FEM package previously used to analyse dielectric materials for microstructural effects (i.e. core-shell, porosity and electrical pathways) [212], [215], [217], is applied to model and simulate the impedance response of cement microstructure at different hydration stages by integrating basic cement microstructural and intrinsic properties.

The simulated data are compared to alternating current impedance spectroscopy (ACIS) experimental results obtained from white Portland cement paste at different stages of hydration. A strong correlation between the simulation and the trends in the experimental ACIS results is observed, demonstrating the combination of FEM and ACIS to be a promising approach to assess microstructural changes in cement. However, the differences and limitations observed when comparing the simulation values to the experimental ACIS results, attributed to the simplicity of the model proposed, require further development of the FEM and deconvolution of the intrinsic material properties of each phase present within the cement microstructure.

8.2 Sample specifications

To compare the simulated impedance response of C_3S, the impedance response of white Portland cement (wPc) was assessed at different hydration stages. wPc paste samples were prepared at a water to cement ratio (w/c) of 0.45.

8.3 Results and discussion

8.3.1 Model setup

To provide verification of the model, the capacitance and resistance values were extracted from the simulated impedance response to allow permittivity and conductivity values to be calculated. A simple cube with lateral dimensions of 200 μm

195

was created, and ten trial core-shell spheres, each with a diameter of 20 μm (Fig. 8-2) were meshed using tetrahedron and prism elements and placed into a box. The intrinsic material properties of all the phases were set to be the same (σ: 1.0×10^{-4} S/m, ε: 1.0×10^{3} F/m, selected according to a defined reference analytical solution), so that the model was verified against the reference analytical solution.
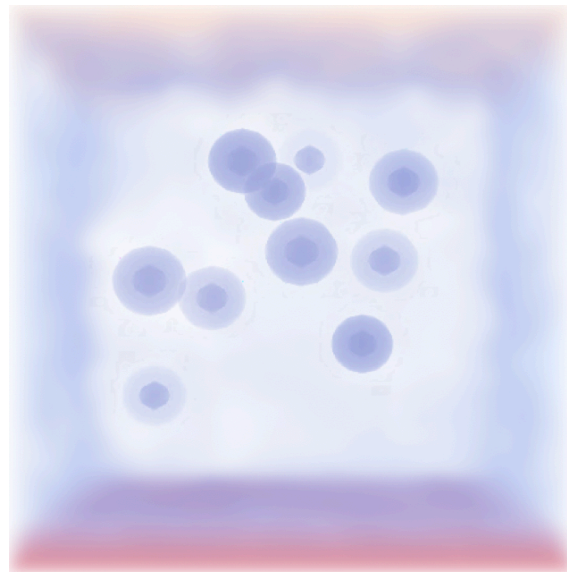
Fig. 8-2. Basic model: ten 20 μm spheres in a 200 μm box.

The analytical resistance (R) and capacitance (C) values of the model were determined to be R: 50.0 MΩ and C: 1.77 pF using Eq. 1 (ε_0: permittivity of free space, ε: material permittivity, σ: conductivity l: thickness and A:cross-sectional area).

$$R = \frac{l}{A \cdot \sigma}, \qquad C = \frac{\varepsilon_0 \cdot \varepsilon \cdot A}{l} \tag{1}$$

The impedance response of the basic model was then simulated using the FEM approach and the immittance response associated Z* and electric modulus (M*, where M* = jwC$_o$Z* with w = angular frequency and C$_o$ = vacuum capacitance of the cell) generated (Fig. 8-3). The intercepts were then obtained from the Nyquist plots of Z*

(Fig. 8-3a) and M* (Fig. 8-3b) providing the R and 1/C values respectively [153], [218], [234]–[236]. The values extracted were R: 50.0 MΩ and C: 1.77 pF, which matched extremely well to the analytical solution, providing verification that an accurate impedance response simulation can be generated for this microstructure.
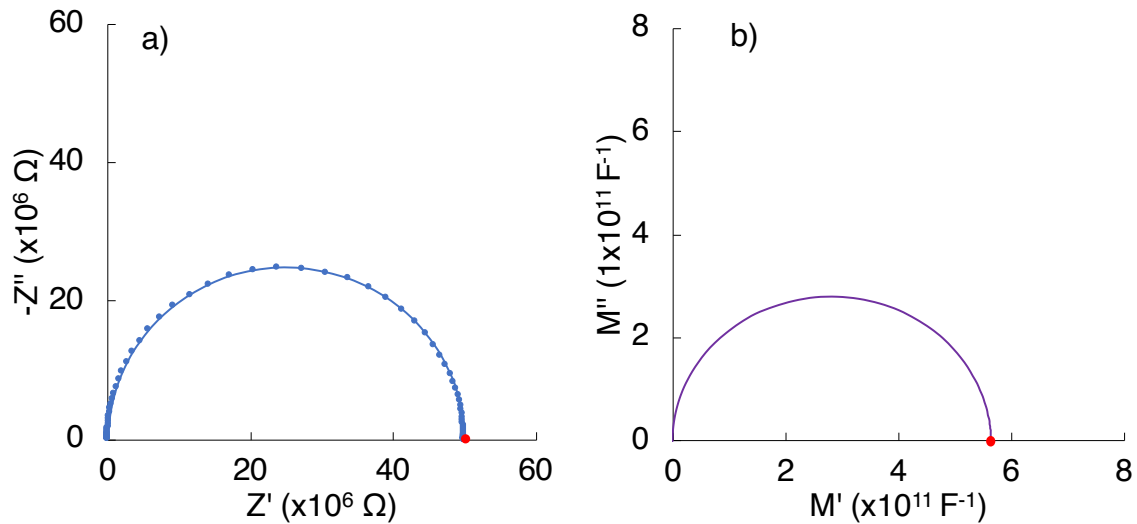
Fig. 8-3.Basic model Nyquist plots: a) impedance and b) electric modulus.

To test the effect of particle volume fraction and demonstrate the influence of the number of particles in the simulated impedance response, three models, made up of 400, 600 and 800 particles respectively, were generated (Fig. 8-4a-c). Particles were randomly dispersed inside a cube of 200 μm and shrunk to form a core-shell structure. The individual regions were then assigned intrinsic material properties as follows: the space (solution) surrounding the particle σ_1: 1 x 10^{-4} S/m and ε_1:1.0 x 10^3 F/m, the particle shells σ_2: 8 x 10^{-3} S/m and ε_2: 50.0 F/m, and the particle core: σ_3: 5 x 10^{-3} S/m and ε_3: 25.0 F/m. These properties were assigned to validate the relationship between the number of particles and the influence impedance response (as the number of particles increases, the impedance values decrease; shell/core conductivity is higher than the solution). Fig. 8-4d shows the phase distribution of a single particle model.
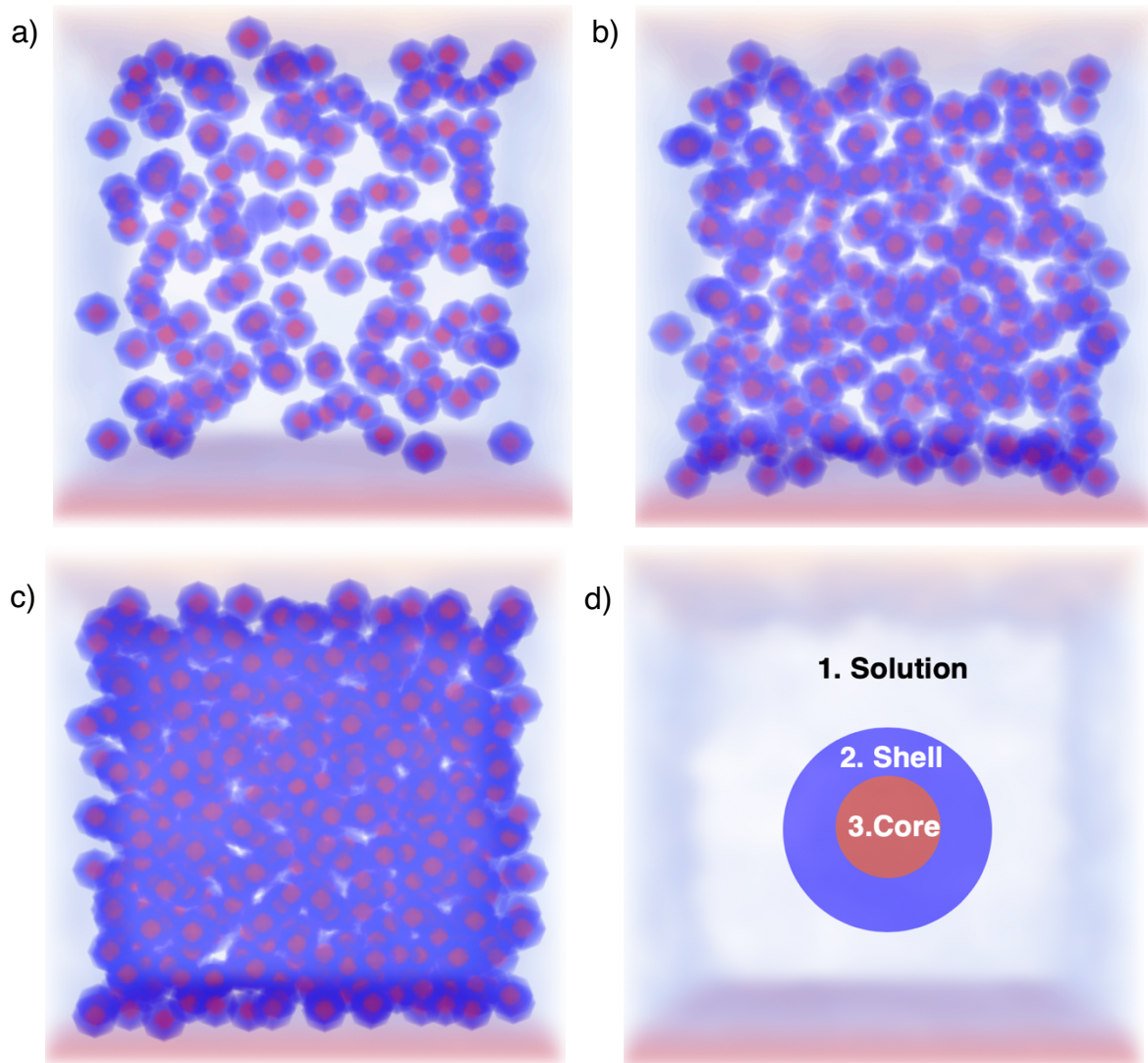
Fig. 8-4. Volume fraction models: a) 400 particles, b) 600 particles, c) 800 particles and d) phases distribution.

The impedance simulations of three different models with different particle volume fractions were calculated as shown in Fig. 8-5. As the volume of the particles decreases, the results show an increase in the simulated Z^* response, providing good agreement between the intrinsic properties of each phase and the model specifications. The models with 450 and 600 particles display, by distributing the resistance and capacitance in the system, an overlapping response of the solution and core/shell (single semicircle arc), attributed to a higher influence of the solution over

the core/shell particles. Conversely, the 800-particle model shows an inclined spike at high frequency related to a slight increase in the relaxation times between the solution and the core/shell phases; making it possible to differentiate the phases in the system.
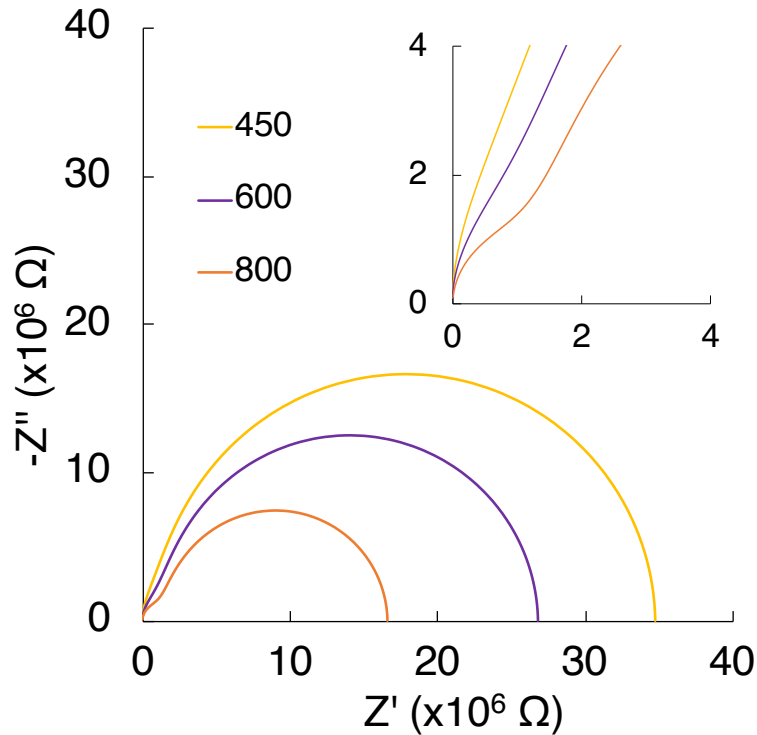
Fig. 8-5. Z* plots of the impedance response simulations for different particle volume fractions (represented as number of particles in the simulation box).

To optimise the accuracy of the impedance response and verify the mesh independency of the model, a mesh refinement process was assessed by evaluating the convergence of the solution in terms of resistivity and the number of elements generated by the mesh refinement. The purpose of the mesh refinement was to obtain a mesh-independent solution (i.e. intrinsic material properties and the impedance simulation are not mesh size dependent) without compromising computational resources and time [208], [392], [393].

To obtain convergence of the solution, four different mesh sizes (i.e. 0.5, 0.4, 0.3, and 0.1 μm) were evaluated by considering the same intrinsic material properties of the phases used in the volume fraction test and using a structure of 780 randomly dispersed particles inside a 200 μm cube. Fig. 8-6a-d shows the mesh structure and cross-sectional area for each mesh size, in which can be observed the influence of the mesh size on the geometry of the particles (i.e. shell and core).

As the mesh size decreases, the geometry of the phases becomes smoother as a result of an increase in the number of nodes and elements in a specific region of the model. However, the decrease of the element number/size through this method can generate a combination of different geometries due to an insufficient or excessive mesh refinement in certain regions (the code controls the mesh refinement without a preferential region selection).

a)
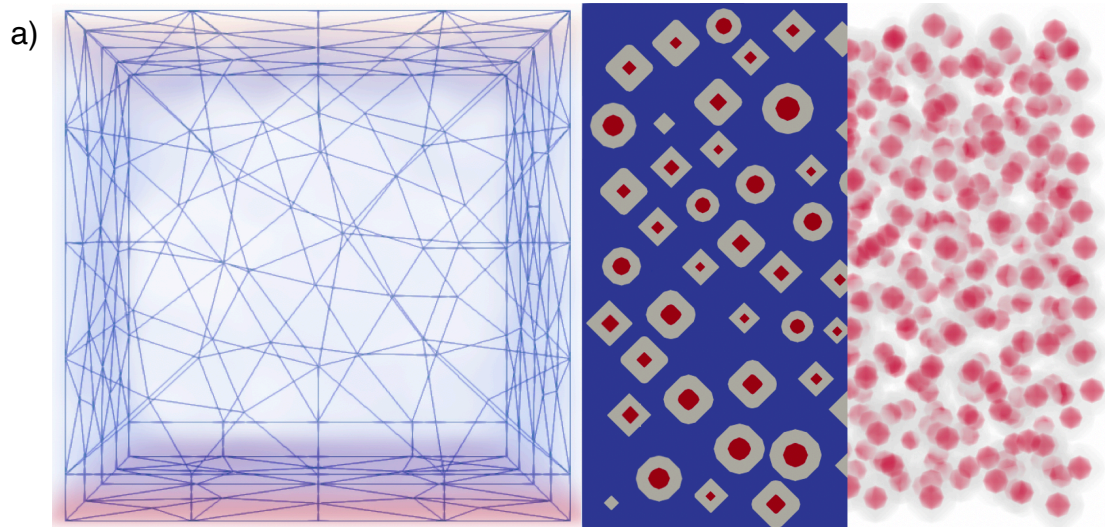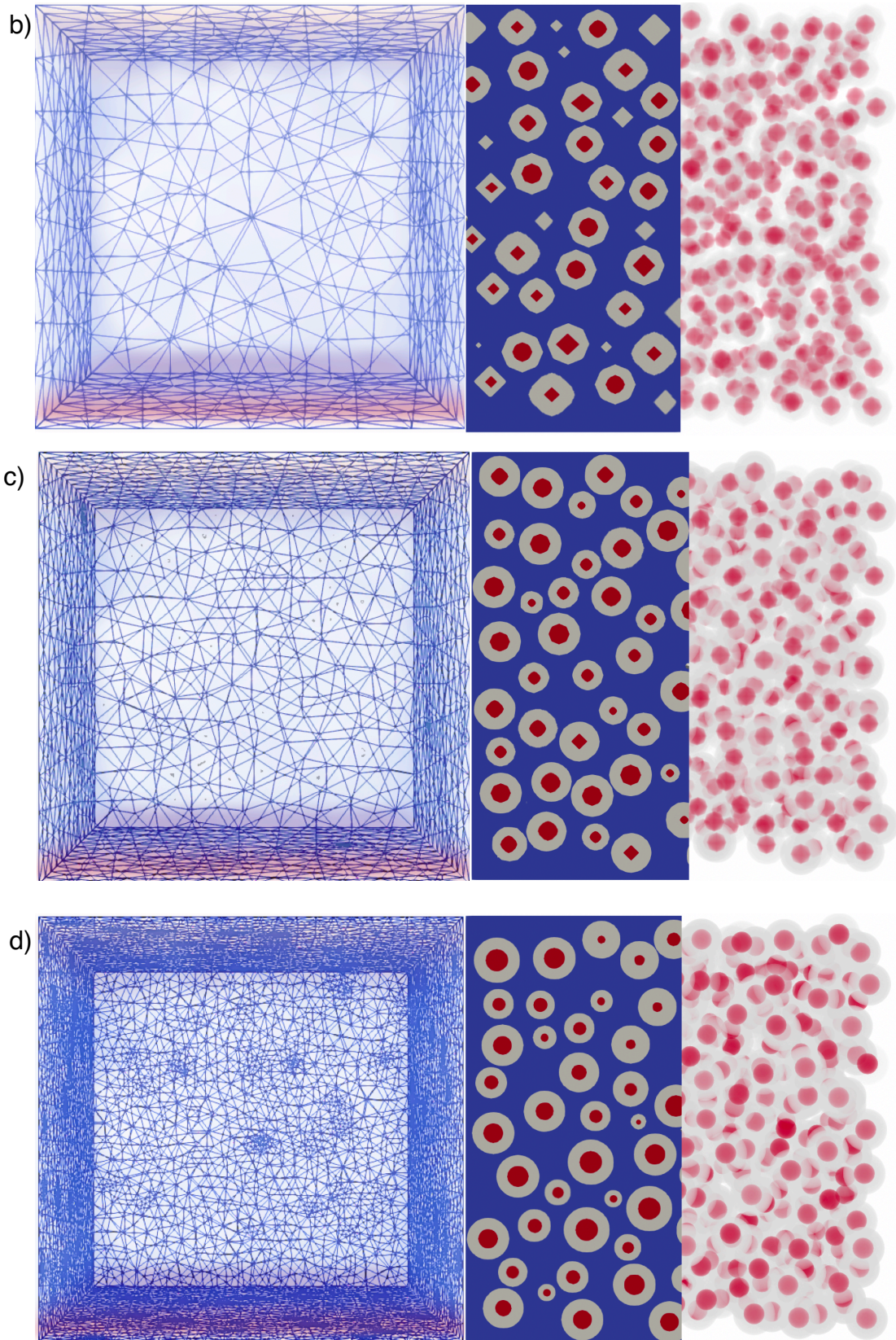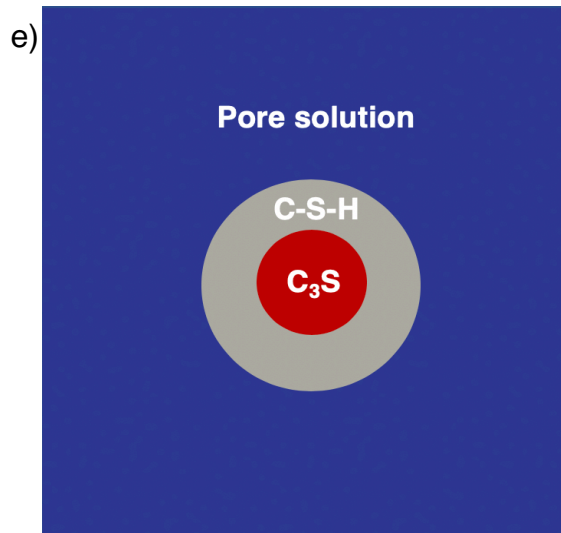
Fig. 8-6. Mesh size structure, and cube cross-sectional/volume fraction view: a) 0.5 µm, b) 0.4 µm, c) 0.3 µm, d) 0.1 µm, and e) phases distribution.

Fig. 8-7 shows the mesh refinement convergence plot using four different mesh sizes. As the mesh becomes finer, the results show an increase in the number of elements and resistivity values, reaching a point at which the resistivity starts to emerge at a mesh size of 0.4 µm and the changes in its behaviour become small enough to consider the solution to be converged at 0.2% element change.

Through this, a maximum mesh size of 0.3 µm was found to be needed to simulate the impedance response of the model generated (200k tetrahedron and prism elements on a 200 µm lateral dimension cube), slightly compromising the time and computer resources to generate the solution.
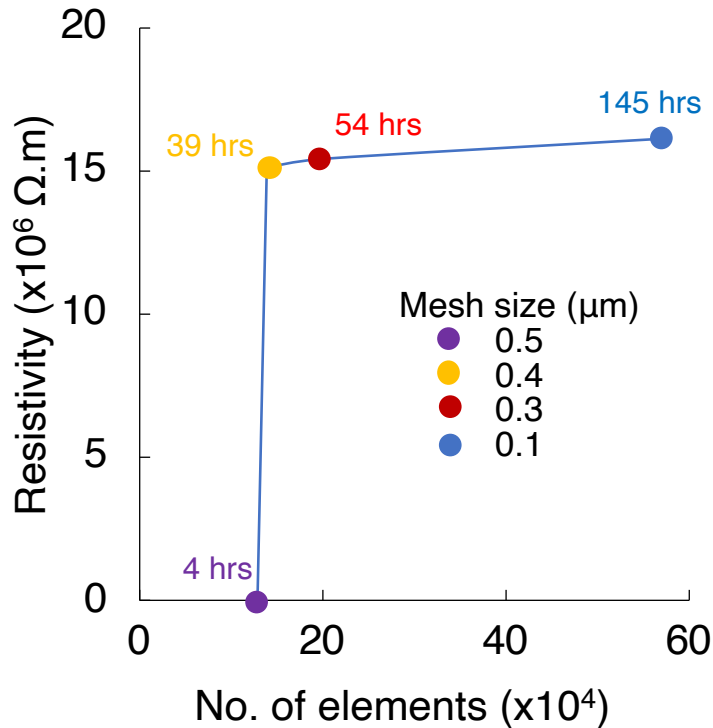
Fig. 8-7. Mesh refinement convergence.

8.3.2 Impedance response of cement microstructure

The initial cement hydration model was based on a 200 μm lateral dimension cube and considering the particles to be the major clinker phase (C_3S) with a particle size of 20 μm at a water to cement ratio (w/c) of 0.45. The cement system volume distribution at w/c of 0.45 was 41% C_3S (780 particles) and 59% water. The impedance responses were simulated for microstructures representing six different hydration times, considering the intrinsic electrical properties of system constituents at the corresponding time and the volume of each phase present, Table 8-1.

To complement and compare the impedance simulation of each hydration time, wPc was assessed in previous investigations by impedance spectroscopy and other supporting techniques (Chapter 4-7) [37]–[40]. The experimental results for wPc showed small impedance and bulk resistance response (5 min after mixing) followed by a perturbation in the conductive response as a result of the rapid dissolution of the

ionic species in the pore solution. At 4 hrs after mixing, wPc impedance measurements were affected by parasitic effects at high frequency. The emergence of these parasitic effects was attributed to a decrease in the charge-transfer resistance of the paste due to the supersaturation of the pore solution and an acceleration in the reaction rate of wPc constituents.

From 4-24 hrs after mixing, wPc results showed an increase tendency in the impedance and resistivity measurements due to the precipitation and growth of hydrated products, densification of the microstructure, and water consumption [13], [29], [139], [292]–[294]. However, there are significant differences between the kinetics of hydration of wPc and C_3S pastes that are attributed to chemical composition and the interaction between wPc constituents (e.g. reaction rate, ionic species concentration, heat rate, setting behaviour, formation of AFm and AFt phases). Nevertheless, these differences in the kinetics of hydration of wPc and C_3S pastes have a slight influence on the primary hydration mechanisms, making it possible to evaluate the simulated impedance response of C_3S by comparison with the experimental impedance response of wPc [6], [44], [67].

Fig. 8-8a-d shows the experimental and simulated impedance, resistivity and conductivity.

At 5 minutes after mixing, the experimental results show a semicircular arc of small impedance at high frequency (Fig. 8-8a). Between 4 hrs and 24 hrs, the experimental impedance measurements at high frequency were affected by parasitic effects (values below the Z' component) attributed to the high cement paste conductivity as a result of a rapid dissolution of ionic species in the pore solution, decrease in the charge transfer resistance (controlled by the ionic strength) and water content in the system [56], [148], [185], [288].

The simulated impedance response at 5 min to 12 hrs (Fig. 8-8b) shows a good agreement with the experimental data, showing an increase in the calculated impedance values as the hydration continues. The simulation also allows analysis of

the impedance spectra at high frequency. This is obscured by parasitic effects in experimental measurements. The impedance values obtained in the simulations are much higher than the experimental ones. These higher values are attributed to the parameters selected, and the reaction kinetics and microstructural features which were not considered in the model (water-filled pores, C-S-H porosity, diffusion of water between the cement grains and hydrated products). For this reason, just a qualitative analysis was conducted.

At 24 hrs, the simulated impedance follows the same behaviour observed in the experimental measurements. A further increase in the simulated impedance values attributed to a higher percolation of the microstructure, reduction of free water, and C-S-H growth, is observed. Conversely, at high frequency, the simulation shows a more developed semicircular arc with an impedance higher than the one observed in the experimental measurements. An effect attributed to the characteristics of the parameters selected in the model design (e.g. complete connectivity between the phases) and the lack of other different parameters (e.g. entrained air, capillary pores, water remain in the pores, and reaction kinetics) [331], [366], [372].

At 672 hrs (28 days) after mixing, the experimental impedance measurements are no longer affected by the parasitic effects. At high frequency a more developed semicircular arc, of higher impedance and significant increase in resistance, is observed. These changes in the electrical response of wPc are attributed to the level of percolation of the microstructure and the degree of hydration (around 70-75%). This is a stage at which the available space for new hydrated products and free water content is limited and the porosity of the system has decreased significantly [164], [294], [367].

The simulated impedance data show one semicircular arc and an inclined spike, which are attributed mainly to the high-density C-S-H and low-density C-S-H respectively. These values are one order of magnitude greater that the experimental values and could be due to the cement hydration model not taking into consideration the reaction kinetics, pore structure and its connectivity, capillary water and ion strength of the pore solution. As the model only considers the connection between the

clinker phase and the hydrated products without any kind of disruption higher impedance values are obtained. Also, the impedance result obtained from the simulation depends on the accuracy of the input parameters and the sensitivity of the model to these parameters. Further work is required to estimate uncertainties and the influence of different parameters in the impedance simulation (porosity, air voids and degree of percolation).

At the early hydration stages (i.e. initial, dormant, acceleration periods), the experimental measurements (Fig. 8-8c) show high conductivity values related to the ionic strength, free water content, and plastic state of the mixture. As the hydrated products are formed and the connectivity between the pores is reduced, a rapid decrease in the conductivity during the deceleration period, leading to the densification of microstructure and consumption of water, is observed. At longer hydration periods, the resistivity of the cement system increases gradually as the hydration process and development of the microstructure continues [13], [29], [100], [293], [366].

The conductivity and resistivity measurements obtained from the simulated impedance response show a good correlation with the experimental trends (Fig. 8-8d). However, the C_3S model does not represent the real complexity of cement hydration and its electrical response (it shows resistance and impedance values higher than those ones observed in wPc paste) due to:

- Assumptions and input parameters used in the model
- Differences in the experimental setup
    - Cell design, electrode properties and current dispersion
- Differences in the wPc response attributed to:
    - Chemical composition
    - Particle size and morphology
    - Kinetics of hydration
- Other aspects
    - Influence of parasitic effects at high frequency
    - Formation of an electric double layer between the electrode and cement paste

As a result, the simulated impedance response shows a different evolution of the semicircle arcs at high frequency (material bulk response) and low frequency (material-electrode response).
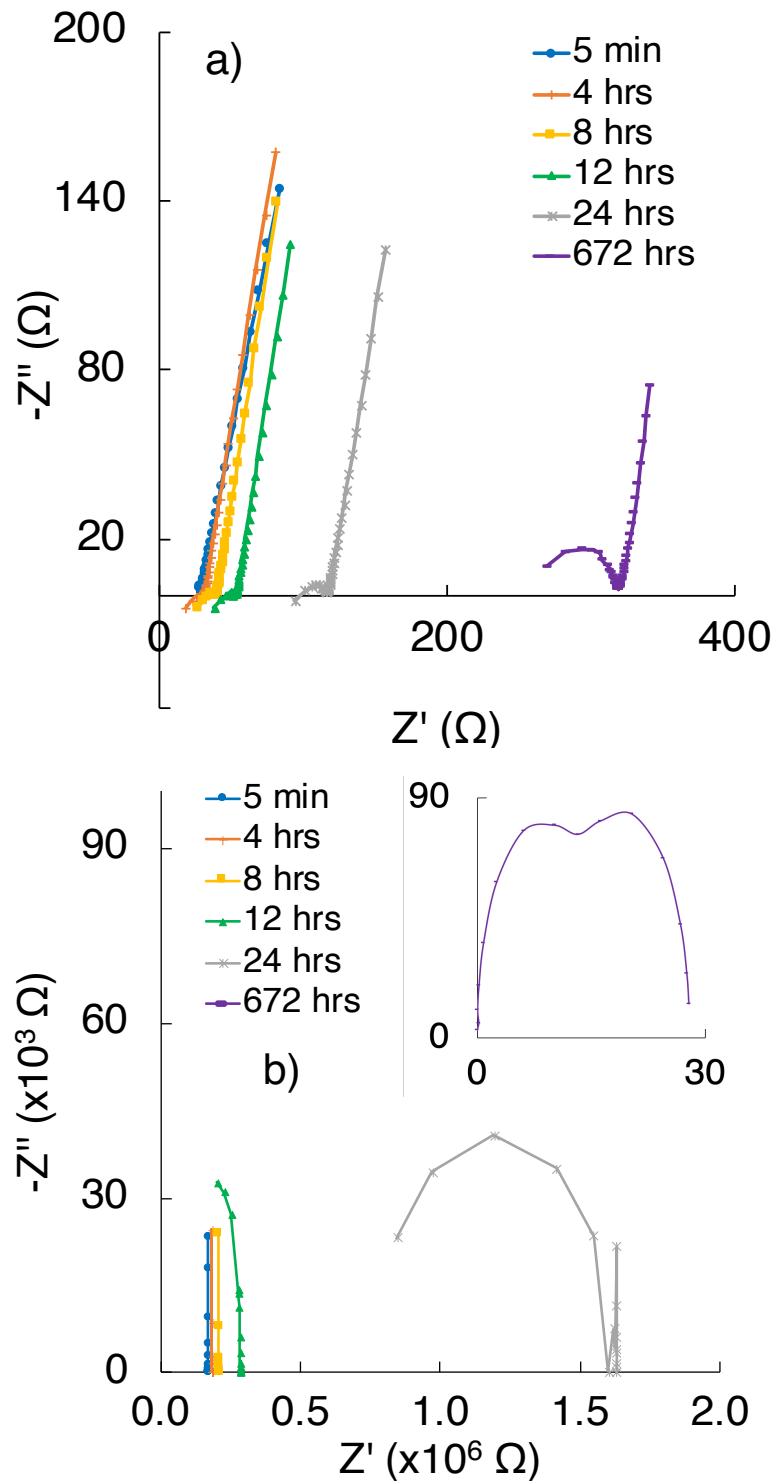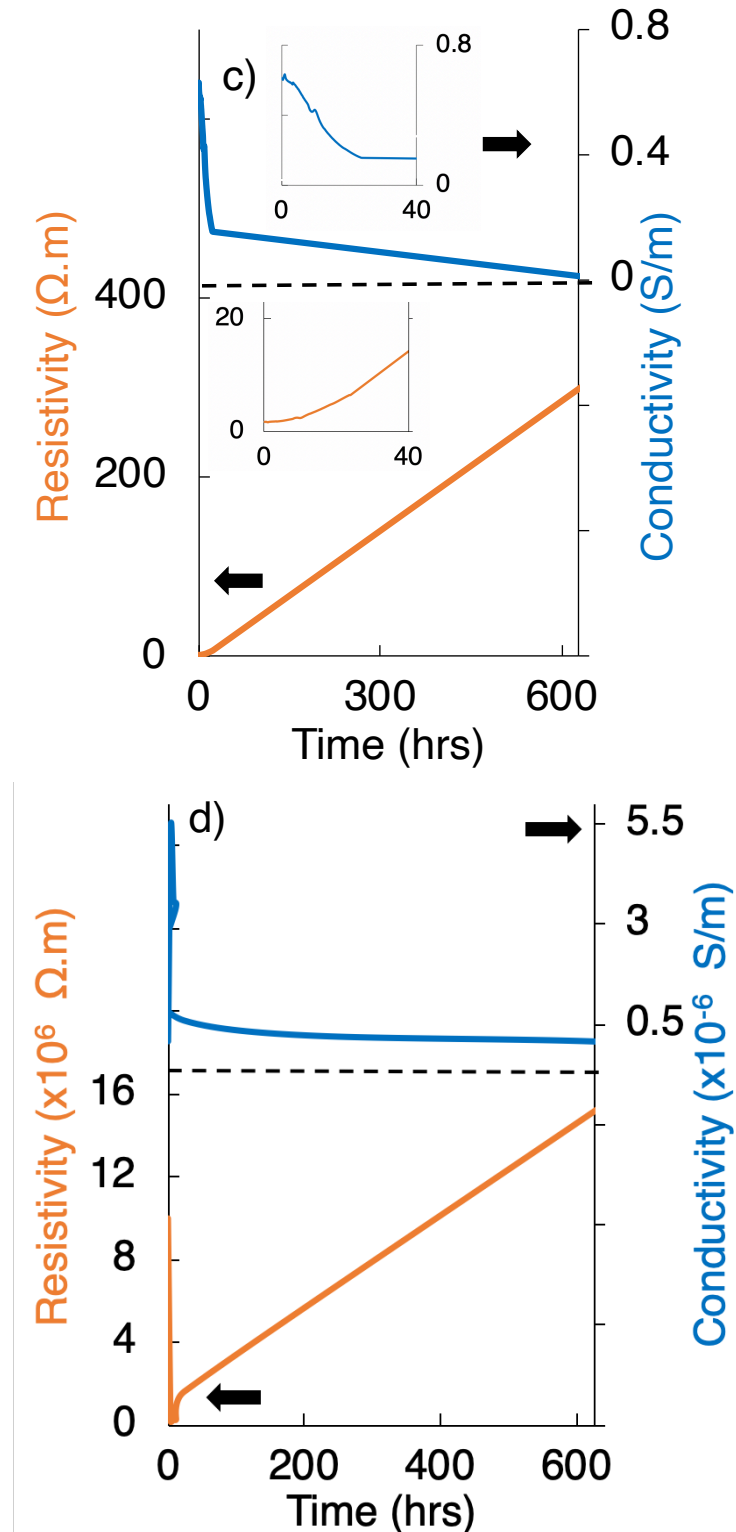
Fig. 8-8. ACIS response of wPc: a) experimental Nyquist spectra; b) simulated Nyquist spectra c) experimental conductivity and resistivity d) simulated conductivity and resistivity.

8.4 Conclusions

This chapter assesses the capabilities of a FEM to simulate the impedance response of the evaluation of the cement hydration process. The results show that the FEM method can be a useful tool to assess the impedance behaviour of cement, overcome experimental impedance spectroscopy limitations (e.g. parasitic effects, electrode effects and current dispersion), and obtain a better understanding of the relationship among the liquid phase, hydrated product formation and the electrochemical response of cement pastes during hydration. A good correlation between the simulated and experimental electrical response (i.e. impedance, conductivity and resistivity) were observed. Further work is required to obtain a more accurate impedance simulation and include changes in the different chemical (e.g. pore solution, phase composition), microstructural (e.g. particle size and morphology), thermochemical and kinetics parameters.

Chapter 9:
CONCLUSIONS

In this research, alternating current impedance spectroscopy (ACIS) was used, in parallel with other supporting techniques, to assess its capabilities for measuring the electrical response of Portland cements and blends at early hydration ages (0-24 hrs). The assessment was accomplished by exploring four areas:

1) Electrochemical cell design, experimental procedure, sources of parasitic effects at high frequency and impedance response of Portland cement at early hydration stages.
2) Electrical properties of Portland cement and blends, and the effect of water to cement ratio and partial replacement of cement with different replacement levels of admixtures on the electrical response of Portland cement.
3) Microstructural characterisation of Portland cements and blends.
4) Microstructural modelling and impedance simulation of cement.

9.1 Electrochemical cell design (Ch. 4)

The results show the importance of evaluating different cell parameters, i.e. experimental procedure, cell geometry, leads positioning and length, electrode properties and its attachment method to the cell. These parameters can affect impedance data acquisition and interpretation through nonlinear effects, noise, polarisation and parasitic effects at high frequency (Fig. 9-1).

A significant decrease of the parasitic effects at high frequencies (caused mainly by leads and electrode effects) can be achieved through an optimal cell design and impedance measurements correction, making it possible to correlate the electrical

210

response to the rate of cement hydration. However, due to the limited solid phase microstructural development and the highly conductive condition of cement at early hydration periods, the parasitic effects could not be fully corrected.
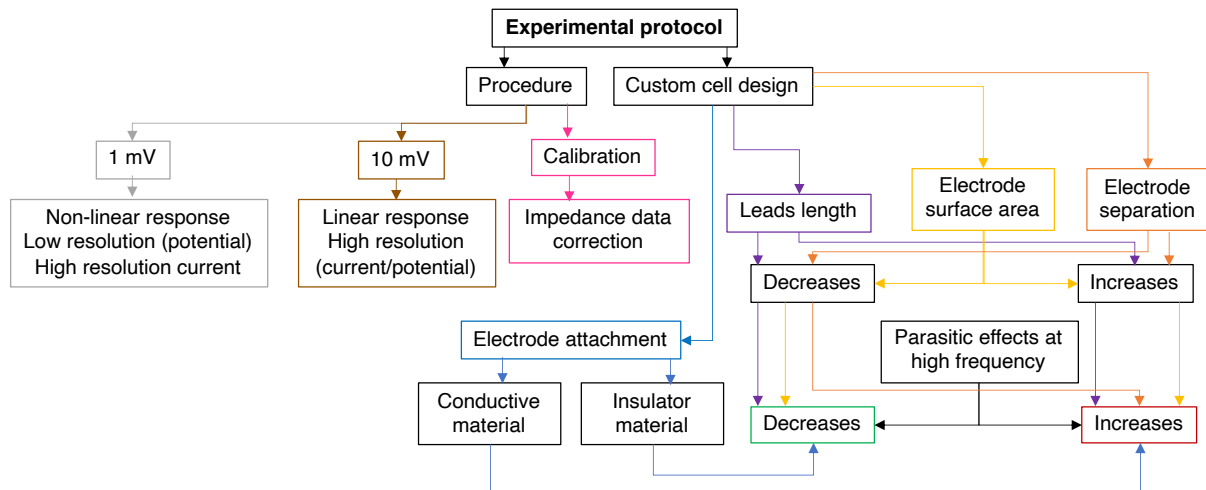
Fig. 9-1.Experimental protocol highlights.

9.2 Electrical properties of Portland cement and blends (Ch. 5-6)

The results demonstrate that ACIS is a sensitive technique capable to assess the early-age cement hydration and the influence on Portland cement of partial replacement with admixtures, or different water to cement ratios. This enabled, through the analysis of the electrical response of cement paste, the differentiation of changes in:

- Rate of hydration (Fig. 9-2a)
- Microstructural development (Fig. 9-2b)
- The ionic strength of the pore solution ((Fig. 9-2c)
- Electrical and physicochemical properties at different water to cement ratios and admixture replacement levels
- Emergence of parasitic effects (Fig. 9-2a)

211
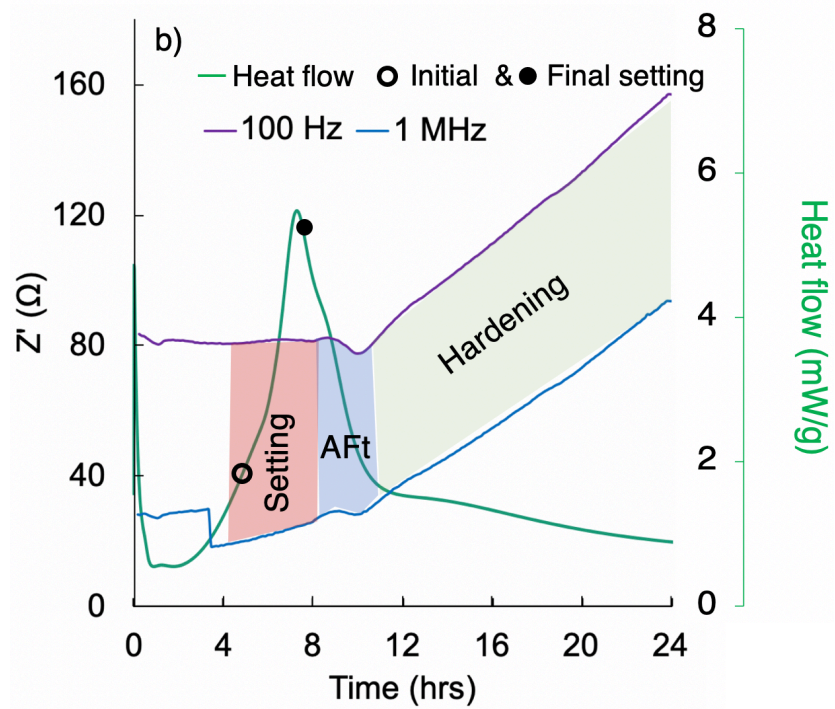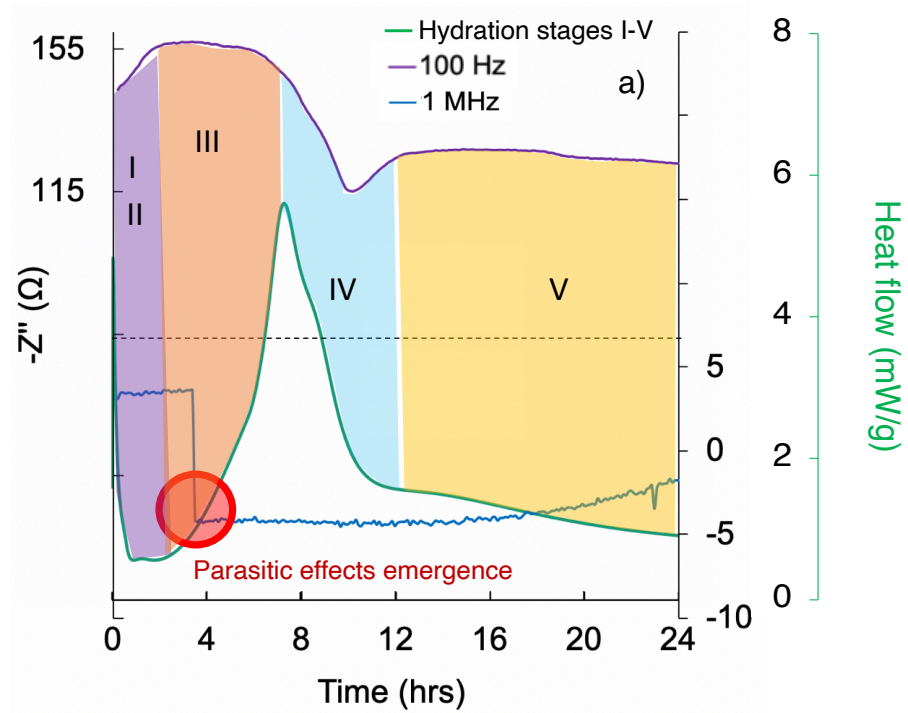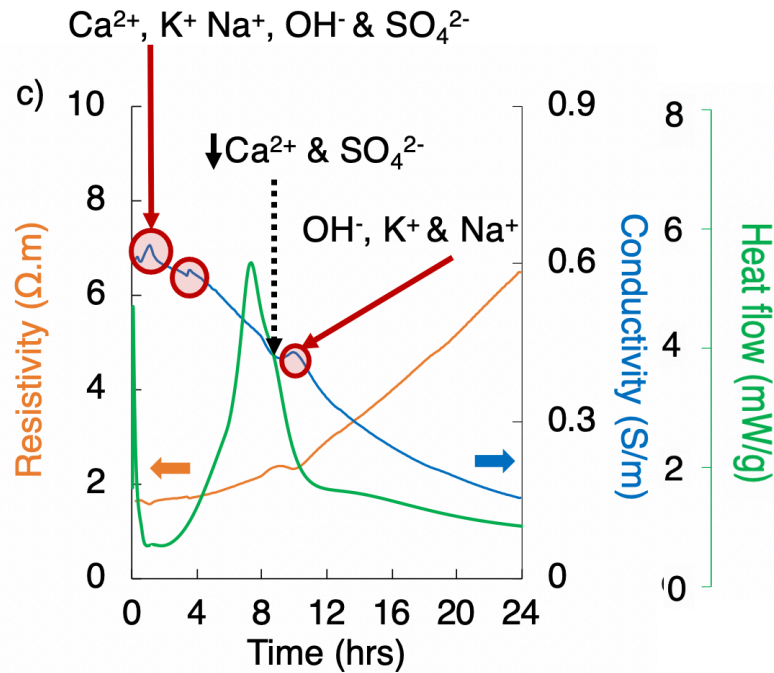
Fig. 9-2. wPc property correlations: a) reactance and rate of hydration; b) resistance and setting behaviour; c) conductivity and pore solution behaviour.

9.3 Microstructural characterisation of Portland cement and blends (Ch. 7)

A strong correlation among the changes in the electrical response and microstructural development of cement and blends was observed. The results demonstrate the capabilities of ACIS, in parallel with other techniques, to assess the influence of different parameters (filler and dilution effects, water to cement ratio) on the microstructural development (hydrated product formation and degree of percolation) at early hydration stages, e.g. Fig. 9-3. However, the influence of more complex cementitious systems on the parasitic inductive effects observed in the impedance measurements at high frequency needs further investigation. As a result of the pozzolanic reaction of FA and SF, the electrical response of wPc/FA/SF at longer ages (> 1d) is expected to be significantly different from that obtained at early ages (≤ 24 hrs).
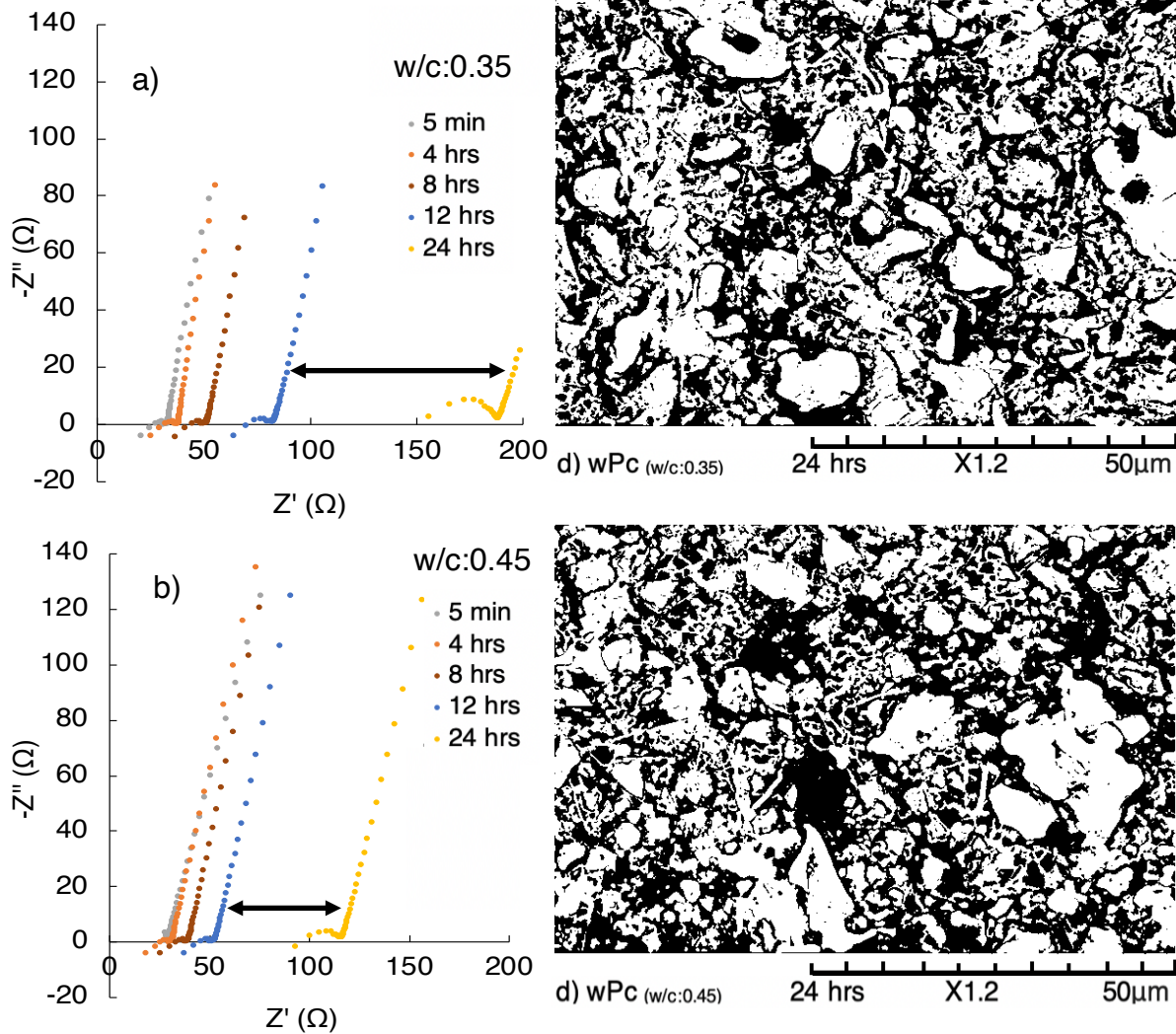
Fig. 9-3. wPc impedance response and microstructure percolation: a) w/c:0.35; b) w/c:0. 45.

9.4 Modelling and simulation (Ch. 9)

A strong correlation between the simulation and the trends in the experimental ACIS results is observed, demonstrating combined FEM and ACIS to be a promising approach to assess microstructural changes in cement. However, the differences and limitations observed when comparing the simulation values to the experimental ACIS results, attributed to the simplicity of the model proposed, require further development of the FEM and deconvolution of the intrinsic material properties of each phase present within the cement microstructure.

9.5 Further research

Although the results of this research may contribute to demonstrate the capabilities and sensitivity of ACIS as a useful characterisation technique to assess the early hydration and microstructural development of Portland cement, further work is needed in different areas, Fig. 9-4.
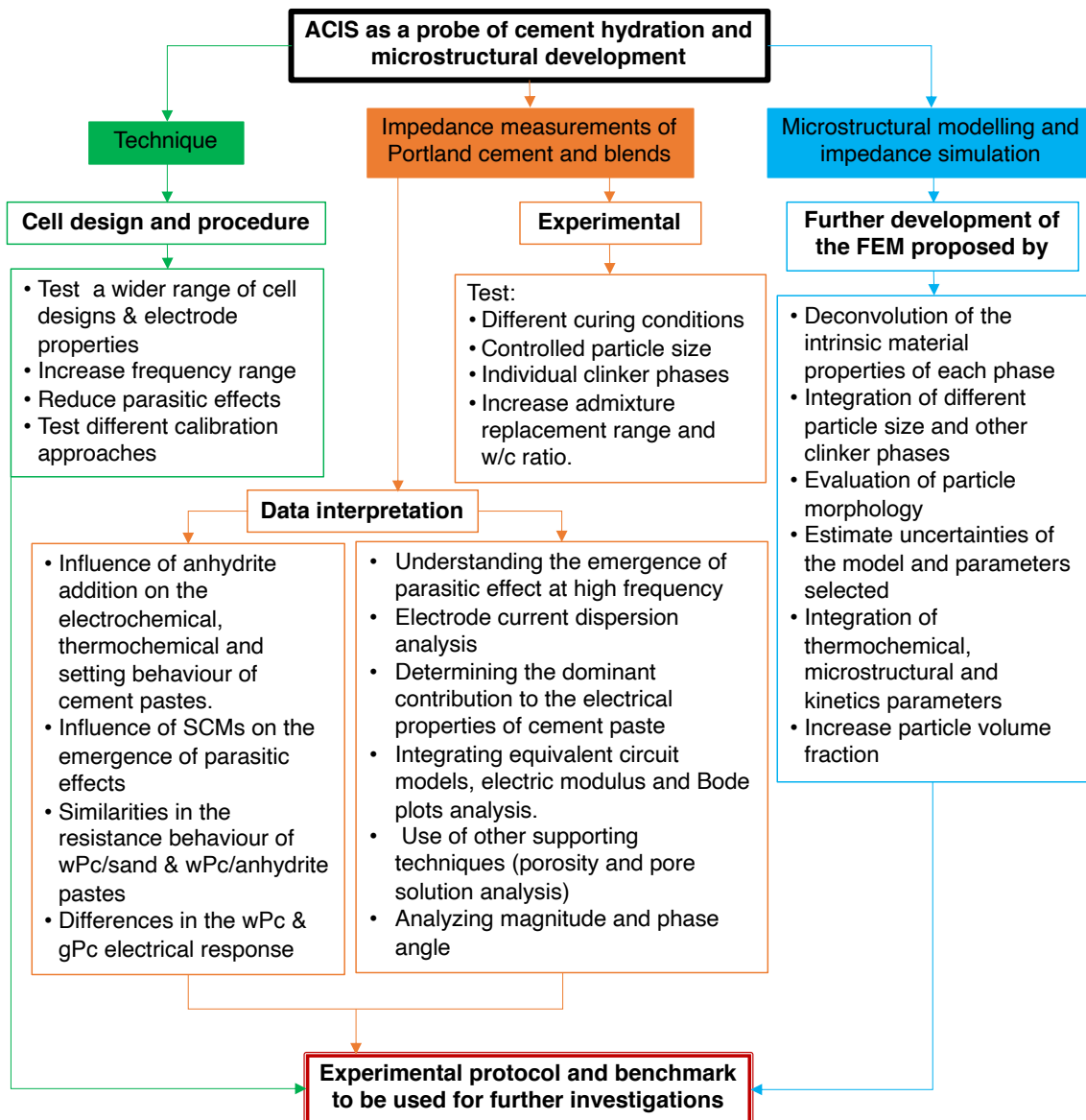
Fig. 9-4. Further research framework.

References

[1] K. L. Scrivener, P. Juilland, and P. J. M. Monteiro, "Advances in understanding hydration of Portland cement," *Cem. Concr. Res.*, vol. 78, pp. 38–56, 2015.

[2] A. Schöler, B. Lothenbach, F. Winnefeld, M. Ben Haha, M. Zajac, and H. M. Ludwig, "Early hydration of SCM-blended Portland cements: A pore solution and isothermal calorimetry study," *Cem. Concr. Res.*, vol. 93, pp. 71–82, 2017.

[3] H. Justnes, "How SCMs improve concrete durability. A fundamental view," *Sustain. Constr. Mater. Technol.*, vol. 7–11, pp. 1–18, 2016.

[4] J. W. Bullard *et al.*, "Mechanisms of cement hydration," *Cem. Concr. Res.*, vol. 41, no. 12, pp. 1208–1223, 2011.

[5] X. Xiong and K. Van Breugel, "Isothermal calorimetry study of blended cements and its application in numerical simulations," *HERON*, vol. 46, no. 3, pp. 150–159, 2001.

[6] P. K. Mehta and P. J. M. Monteiro, *Concrete: Microstructure, Properties, and Materials*, 3rd ed. California: McGraw-Hill, 2006.

[7] P. C. Hewlett and M. Liska, *Lea's Chemistry of Cement and Concrete*, 5th ed. United Kingdom: Elsevier, 2019.

[8] B. Kohlhaas, *Cement Engineers' Handbook*, 4th ed. Wiesbaden; Berlin: Bauverlag, 1983.

[9] H. F. W. Taylor, *Cement Chemistry*, 2nd ed. London: Thomas Telford, 1997.

[10] O. Linderoth and P. Johansson, "A comparative study of thermogravimetric analysis conducted on two different instruments," in *15th International Congress on the Chemistry of Cement*, 2019.

[11] B. W. Langan, K. Weng, and M. A. Ward, "Effect of silica fume and fly ash on heat of hydration of Portland cement," *Cem. Concr. Res.*, vol. 32, no. 7, pp. 1045–1051, 2002.

[12] B. Lothenbach, K. Scrivener, and R. D. Hooton, "Supplementary cementitious materials," *Cem. Concr. Res.*, vol. 41, no. 12, pp. 1244–1256, 2011.

[13] W. J. McCarter, "A parametric study of the impedance characteristics of cement-aggregate systems during early hydration.," *Cem. Concr. Res.*, vol. 24, no. 6,

pp. 1097–1110, 1994.

[14] J. M. Cruz, I. C. Fita, L. Soriano, J. Payá, and M. V Borrachero, "The use of electrical impedance spectroscopy for monitoring the hydration products of Portland cement mortars with high percentage of pozzolans," *Cem. Concr. Res.*, vol. 50, pp. 51–61, 2013.

[15] S. W. Tang *et al.*, "The review of early hydration of cement-based materials by electrical methods," *Constr. Build. Mater.*, vol. 146, pp. 15–29, 2017.

[16] H. le Chatelier, "Crystalloids against colloids in the theory of cements," *Trans. Faraday Soc.*, vol. 14, pp. 8–11, 1919.

[17] R. Snellings, G. Mertens, and J. Elsen, "Supplementary cementitious materials," *Rev. Mineral. Geochemistry*, vol. 41, no. 12, pp. 211–278, 2012.

[18] J. Duchesne and M. A. Bérubé, "The effectiveness of supplementary cementing materials in suppressing expansion due to ASR: Another look at the reaction mechanisms. Part 1: concrete expansion and portlandite depletion," *Cem. Concr. Res.*, vol. 24, pp. 221–230, 1994.

[19] A. D. Neuwald, "Supplementary cementitious material. Part I: Pozzolanic SCMs, what are SCMs and how can you use them to your advantage," *Manufactured Concrete*, pp. 8–16, 2004.

[20] L. Wadsö and M. Arndt, "An international round robin test on isothermal (conduction) calorimetry for measurement of three-day heat of hydration of cement," *Cem. Concr. Res.*, vol. 79, pp. 316–322, 2016.

[21] British Standards Institute, *BS EN 196-3 Methods of testing cement - Part 3: Determination of setting times and soundness*. 2016.

[22] K. Scrivener, R. Snellings, and B. Lothenbach, *A pratical guide to microstructural analysis of cementitious materials*, 1st ed. Boca Raton, Florida: CRC Press, 2016.

[23] J. S. Dolado and K. Van Breugel, "Recent advances in modeling for cementitious materials," *Cem. Concr. Res.*, vol. 41, no. 7, pp. 711–726, 2011.

[24] K. Brantervik and G. A. Niklasson, "Circuit models for cement based materials obtained from impedance spectroscopy," *Cem. Concr. Res.*, vol. 21, pp. 496–508, 1991.

[25] Z. Xu, P. Gu, P. Xie, and J. J. Beaudoin, "Application of A.C. impedance techniques in studies of porous cementitious materials (III): ACIS behaviour of very low porosity cementitious systems.," *Cem. Concr. Res.*, vol. 23, pp. 1007–1015, 1993.

[26] P. J. Tumidajski, "Electrical conductivity of Portland cement mortars," *Cem. Concr. Res.*, vol. 26, no. 4, pp. 529–534, 1996.

[27] D. E. Macphee, D. C. Sinclair, and S. L. Stubbs, "Electrical characterization of pore reduced cement by impedance spectroscopy," *J. Mater. Sci. Lett.*, vol. 15, pp. 1566–1568, 1996.

[28] D. E. Macphee and S. L. Cormack, "AC impedance spectroscopy of pore reduced cements : Influence of contact resistance," *J. Mater. Sci.*, vol. 35, pp. 4823–4826, 2000.

[29] W. J. McCarter, "The a.c. impedance response of concrete during early hydration," *J. Mater. Sci.*, vol. 31, no. 23, pp. 6285–6292, 1996.

[30] W. J. McCarter and S. Garvin, "Dependence of electrical impedance of cement-based materials on their moisture condition," *J. Phys. D. Appl. Phys.*, vol. 22, no. 11, pp. 1773–1776, 1989.

[31] T. O. Mason, S. J. Ford, J. D. Shane, J.-H. Hwang, and D. D. Edwards, "Experimental limitations in impedance spectroscopy of materials systems," *Adv. Cem. Res.*, pp. 143–150, 1998.

[32] G. Hsieh, T. O. Mason, and L. R. Pederson, "Experimental limitations in impedance spectroscopy: Part II- electrode artifacts three-point measurements on Pt/YSZ," *Solid State Ionics*, pp. 203–212, 1996.

[33] J. H. Hwang, K. S. Kirkpatrick, T. O. Mason, and E. J. Garboczi, "Experimental limitations in impedance spectroscopy: Part IV. Electrode contact effects," *Solid State Ionics*, pp. 93–104, 1997.

[34] R. Spragg, C. Villani, K. Snyder, D. Bentz, J. Bullard, and J. Weiss, "Factors that influence electrical resistivity measurements in cementitious systems," *Transp. Res. Rec.*, vol. 2342, pp. 1–12, 2013.

[35] X. Hu, C. Shi, X. Liu, J. Zhang, and G. de Schutter, "A review on microstructural characterization of cement-based materials by AC impedance spectroscopy,"

Cem. Concr. Compos., vol. 100, pp. 1–14, 2019.

[36] B. J. Christensen *et al.,* "Impedance spectroscopy of hydrating cement-based materials: measurement, interpretation, and application," *J. Am. Ceram. Soc.*, vol. 77, no. 11, pp. 2789–2804, 1994.

[37] A. F. Sosa Gallardo and J. L. Provis, "Electrochemical ell design and characterisation of cement hydration by impedance spectroscopy," *J. Mater. Sci.*, vol. 56, pp. 1203–1220, 2020.

[38] A. F. Sosa Gallardo and J. L. Provis, "Early-age characterisation of Portland cement and blends by impedance spectroscopy," *Unpubl. Manuscr. Submitt. Publ.*, pp. 1–33, 2020.

[39] A. F. Sosa Gallardo and J. L. Provis, "Early-age characterisation of Portland cement by impedance spectroscopy," *Unpubl. Manuscr. Submitt. Publ.*, pp. 1–39, 2020.

[40] A. F. Sosa Gallardo and J. L. Provis, "Microstructural characterisation of Portland cement and blends," *Unpubl. Manuscr. Submitt. Publ.*, pp. 1–51, 2020.

[41] ASTM International, *ASTM C150, Standard specification for Portland cement.* 2020.

[42] A. M. Brandt, *Cement Based Composites*, 2nd ed. Milton Park, Abingdon, Oxon: Taylor and Francis, 2009.

[43] E. Durgun, H. Manzano, R. J. M. Pellenq, and J. C. Grossman, "Understanding and controlling the reactivity of the calcium silicate phases from first principles," *Chem. Mater.*, vol. 24, no. 7, pp. 1262–1267, 2012.

[44] V. S. Ramachandran, *Concrete Admixtures Handbook. Properties, Science, and technology*, 2nd ed. Ottawa, Ontario, Canada.: Noyes Publications, 1995.

[45] ASTM International, *ASTM C595-05. Standard specification for blended hydraulic cements*. Philadelphia, 2005.

[46] British Standards Institute, *BS EN 197-1: Composition, specifications and conformity criteria for common cements*. 2011.

[47] European Committee for Standardization, *EN 197-1. Cement - Part 1: Composition, specifications and conformity criteria for common cements*. Brussels, Belgium, 2011.

[48] K. Humphreys and M. Mahasenan, *Towards a sustainable cement industry. Substudy 8: Climate change*. Switzerland, 2002.

[49] M. M. C. Canut, "Pore structure in blended cement pastes," Technical University of Denmark, 2011.

[50] R. Siddique and P. Cachim, *Waste and Supplementary Cementitious Materials in Concrete*. Duxford, United Kingdom: Woodhead Publishing Limited, 2018.

[51] P. Suraneni, A. Hajibabaee, S. Ramanathan, Y. Wang, and J. Weiss, "New insights from reactivity testing of supplementary cementitious materials," *Cem. Concr. Compos.*, vol. 103, pp. 331–338, 2019.

[52] S. Chandra and L. Berntsson, *Supplementary Cementing Materials*. Heidelberg: Springer, 2011.

[53] W. H. J. Tchamdjou, T. Cherradi, M. L. Abidi, and L. A. P. De Oliveira, "Influence of different amounts of natural pozzolan from volcanic scoria on the rheological properties of Portland cement pastes," *Energy Procedia*, vol. 139, pp. 696–702, 2017.

[54] F. Gurbuz and G. A. Codd, "Microcystin removal by a naturally-occurring substance: Pumice," *Bull. Environ. Contam. Toxicol.*, vol. 81, no. 3, pp. 323–327, 2008.

[55] R. Snellings and K. L. Scrivener, "Rapid screening tests for supplementary cementitious materials: past and future," *Mater. Struct.*, vol. 49, no. 8, pp. 1–15, 2015.

[56] A. Vollpracht, B. Lothenbach, R. Snellings, and J. Haufe, "The pore solution of blended cements: a review," *Mater. Struct.*, vol. 49, no. 8, pp. 3341–3367, 2015.

[57] F. Liu, "Early-age hydration studies of Portland cement," University of Lousville, 2014.

[58] I. Jelenić-Bezjak, "Kinetics of hydration of cement phases," *Adv. Cem. Technol.*, pp. 397–440, 1983.

[59] P. E. B. Moses and Perumal, "Hydration of cement and its mechanisms," *J. Mech. Civ. Eng.*, vol. 13, no. 6, pp. 2278–1684, 2016.

[60] M. Bishop, S. G. Bott, and A. R. Barron, "A new mechanism for cement hydration inhibition: Solid-state chemistry of calcium nitrilotris(methylene)triphosphonate,"

Chem. Mater., vol. 15, no. 16, pp. 3074–3088, 2003.

[61] G. Bye, P. Livesey, and L. Struble, *Portland Cement*, 3rd ed. London: ICE Publishing, 2011.

[62] C. E. Hughes *et al.*, "Exploiting in-situ solid-state NMR spectroscopy to probe the early stages of hydration of calcium aluminate cement," *Solid State Nucl. Magn. Reson.*, vol. 99, pp. 1–6, 2019.

[63] B. Z. Dilnesa, B. Lothenbach, G. Renaudin, A. Wichser, and E. Wieland, "Stability of monosulfate in the presence of iron," *J. Am. Ceram. Soc.*, vol. 95, no. 10, pp. 3305–3316, 2012.

[64] G. Möschner, B. Lothenbach, F. Winnefeld, A. Ulrich, R. Figi, and R. Kretzschmar, "Solid solution between Al-ettringite and Fe-ettringite ($Ca_6[Al_{1-x}Fe_x(OH)_6]_2(SO_4)_3 \cdot 26H_2O$)," *Cem. Concr. Res.*, vol. 39, no. 6, pp. 482–489, 2009.

[65] L. B. Skinner, S. R. Chae, C. J. Benmore, H. R. Wenk, and P. J. M. Monteiro, "Nanostructure of calcium silicate hydrates in cements," *Phys. Rev. Lett.*, vol. 104, no. 19, p. #195502, 2010.

[66] I. G. Richardson, A. V. Girão, R. Taylor, and S. Jia, "Hydration of water- and alkali-activated white Portland cement pastes and blends with low-calcium pulverized fuel ash," *Cem. Concr. Res.*, vol. 83, pp. 1–18, 2016.

[67] J. J. Thomas *et al.*, "Modeling and simulation of cement hydration kinetics and microstructure development," *Cem. Concr. Res.*, vol. 41, no. 12, pp. 1257–1278, 2011.

[68] H. J. H. Brouwers and R. J. Van Eijk, "Alkali concentrations of pore solution in hydrating OPC," *Cem. Concr. Res.*, vol. 33, no. 2, pp. 191–196, 2003.

[69] B. Lothenbach, F. Winnefeld, C. Alder, E. Wieland, and P. Lunk, "Effect of temperature on the pore solution, microstructure and hydration products of Portland cement pastes," *Cem. Concr. Res.*, vol. 37, no. 4, pp. 483–491, 2007.

[70] P. Lura and B. Lothenbach, "Influence of pore solution chemistry on shrinkage of cement paste," *Adv. Civ. Eng. Mater.*, pp. 191–200, 2008.

[71] F. Caruso, S. Mantellato, M. Palacios, and R. J. Flatt, "ICP-OES method for the characterization of cement pore solutions and their modification by

polycarboxylate-based superplasticizers," *Cem. Concr. Res.*, vol. 91, pp. 52–60, 2017.

[72] H. S. Wong and N. R. Buenfeld, "Determining the water-cement ratio, cement content, water content and degree of hydration of hardened cement paste: Method development and validation on paste samples," *Cem. Concr. Res.*, vol. 39, no. 10, pp. 957–965, 2009.

[73] H. A. F. Dewah, S. A. Austin, and M. Maslehuddin, "Effect of cement alkalinity on pore solution chemistry and chloride-induced reinforcement corrosion," *ACI Mater. J.*, vol. 97, no. 3, pp. 227–233, 2002.

[74] P. Lura, K. Friedemann, F. Stallmach, S. Mönnig, M. Wyzykowski, and L. P. Esteves, "Kinetics of water migration in cement-based system containing superabsorbent polymers," in *Application of Super Absorbent Polymers (SAP) in Concrete Construction*, RILEM, 2012, pp. 21–37.

[75] B. Lothenbach, "Thermodynamic equilibrium calculations in cementitious systems," *Mater. Struct.*, vol. 43, no. 10, pp. 1413–1433, 2010.

[76] W. Chen, "Hydration of slag cement. Theory, modeling and application," University of Twente, 2007.

[77] K. Andersson, B. Allard, M. Bengtsson, and B. Magnusson, "Chemical composition of cement pore solutions," *Cem. Concr. Res.*, vol. 19, pp. 327–332, 1989.

[78] E. Gallucci, P. Mathur, and K. Scrivener, "Microstructural development of early age hydration shells around cement grains," *Cem. Concr. Res.*, vol. 40, no. 1, pp. 4–13, 2010.

[79] W. Chen, Y. Li, P. Shen, and Z. Shui, "Microstructural development of hydrating Portland cement paste at early ages investigated with non-destructive methods and numerical simulation," *J. Nondestruct. Eval.*, vol. 32, no. 3, pp. 228–237, 2013.

[80] R. Ylmén, U. Jäglid, B. M. Steenari, and I. Panas, "Early hydration and setting of Portland cement monitored by IR, SEM and Vicat techniques," *Cem. Concr. Res.*, vol. 39, no. 5, pp. 433–439, 2009.

[81] I. F. Sáez del Bosque, S. Martínez-Ramírez, and M. T. Blanco-Varela,

"Calorimetric study of white Portland cement hydration. Effect of nanosilica and temperature," in *International Congress on the Chemistry of Cement*, 2015.

[82] H. Singh, *Steel fiber reinforced concrete: Behavior, modelling and design*. Punjab: Springer, 2017.

[83] I. G. Richardson, "Nature of C-S-H in hardened cements," *Cem. Concr. Res.*, vol. 29, no. 8, pp. 1131–1147, 1999.

[84] P. A. Bhat and N. C. Debnath, "Theoretical and experimental study of structures and properties of cement paste: The nanostructural aspects of C-S-H," *J. Phys. Chem. Solids*, vol. 72, no. 8, pp. 920–933, 2011.

[85] J. W. Bullard and R. J. Flatt, "New insights into the effect of calcium hydroxide precipitation on the kinetics of tricalcium silicate hydration," *J. Am. Ceram. Soc.*, vol. 93, no. 7, pp. 1894–1903, 2010.

[86] P. C. Aïtcin, *Portland Cement*. Elsevier Ltd, 2016.

[87] H. M. Jennings, "Refinements to colloid model of C-S-H in cement: CM-II," *Cem. Concr. Res.*, vol. 38, no. 3, pp. 275–289, 2008.

[88] T. R. Naik, "Concrete durability as influenced by density and/or porosity," *Cem. Concr. Inst. Mex. Symp.*, pp. 1–13, 1997.

[89] L.-O. Nilsson, "Durability concept; pore structure and transport processes," in *Adv. Concr. Technol. Set*, vol. 1, 2003, pp. 3–29.

[90] G. Sant, D. Bentz, and J. Weiss, "Capillary porosity depercolation in cement-based materials: Measurement techniques and factors which influence their interpretation," *Cem. Concr. Res.*, vol. 41, no. 8, pp. 854–864, 2011.

[91] P. J. McDonald, M. Mitchell, and M. Mulheron, "Cement products: Characterisation by NMR and MRI," *Encycl. Mater. Sci. Technol.*, pp. 1–9, 2005.

[92] P. J. McDonald, V. Rodin, and A. Valori, "Characterisation of intra- and inter-C–S–H gel pore water in white cement based on an analysis of NMR signal amplitudes as a function of water content," *Cem. Concr. Res.*, vol. 40, pp. 1656–1663, 2010.

[93] S. Jia and I. G. Richardson, "Micro- and nano-structural evolutions in white Portland cement/pulverized fuel ash cement pastes due to deionized-water leaching," *Cem. Concr. Res.*, vol. 103, pp. 191–203, 2018.

[94] M. W. Bligh, M. N. D'Eurydice, R. R. Lloyd, C. H. Arns, and T. D. Waite, "Investigation of early hydration dynamics and microstructural development in ordinary Portland cement using ^{1}H NMR relaxometry and isothermal calorimetry," *Cem. Concr. Res.*, vol. 83, pp. 131–139, 2016.

[95] S. Ahmari and L. Zhang, *The properties and durability of alkali-activated masonry units*. Woodhead Publishing Limited, 2015.

[96] J. Haramis, K. N. E. Verghese, and J. J. Lesko, *Freeze-thaw durability of composites for civil infrastructure*. Plastics Design Library, 2001.

[97] M. Wyrzykowski, P. J. McDonald, K. L. Scrivener, and P. Lura, "Water redistribution within the microstructure of cementitious materials due to temperature changes studied with ^{1}H NMR," *J. Phys. Chem. C*, vol. 121, no. 50, pp. 27950–27962, 2017.

[98] A. M. Gajewicz, E. Gartner, K. Kang, P. J. McDonald, and V. Yermakou, "A ^{1}H NMR relaxometry investigation of gel-pore drying shrinkage in cement pastes," *Cem. Concr. Res.*, vol. 86, pp. 12–19, 2016.

[99] P. J. McDonald, O. Istok, M. Janota, A. M. Gajewicz-Jaromin, and D. A. Faux, "Sorption, anomalous water transport and dynamic porosity in cement paste: A spatially localised ^{1}H NMR relaxation study and a proposed mechanism," *Cem. Concr. Res.*, vol. 133, p. 106045, 2020.

[100] F. Lin and C. Meyer, "Hydration kinetics modeling of Portland cement considering the effects of curing temperature and applied pressure," *Cem. Concr. Res.*, vol. 39, no. 4, pp. 255–265, 2009.

[101] J. M. Ortega, I. Sánchez, and M. A. Climent, "Impedance spectroscopy study of the effect of environmental conditions in the microstructure development of OPC and slag cement mortars," *Arch. Civ. Mech. Eng.*, vol. 15, no. 2, pp. 569–583, 2014.

[102] T. Xie and J. J. Biernacki, "The origins and evolution of cement hydration models," *Comput. Concr.*, vol. 8, no. 6, pp. 1–29, 2011.

[103] J. Hu, Z. Ge, and K. Wang, "Influence of cement fineness and water-to-cement ratio on mortar early-age heat of hydration and set times," *Constr. Build. Mater.*, vol. 50, pp. 657–663, 2013.

[104] J. A. Larbi and J. M. J. M. J. M. Bijen, "Effects of water-cement ratio, quantity and fineness of sand on the evolution of lime in set Portland cement systems," *Cem. Concr. Res.*, vol. 20, pp. 783–794, 1990.

[105] A. Kumar *et al.*, "The filler effect: The influence of filler content and type on the hydration rate of tricalcium silicate," *J. Am. Ceram. Soc.*, vol. 100, no. 7, pp. 3316–3328, 2017.

[106] J. Bensted, "Early hydration of portland cement - effects of water/cement ratio," *Cem. Concr. Res.*, vol. 13, no. 4, pp. 493–498, 1983.

[107] Y. Aikawa, D. Atarashi, T. Nakazawa, and E. Sakai, "Dependence of the hydration rate of Portland cement on particle size distribution," *J. Ceram. Soc. Japan*, vol. 122, no. 9, pp. 810–816, 2014.

[108] Y. M. Zhang and T. J. Napier-Munn, "Effect of particle size distribution, surface area and chemical composition on Portland cement strength," *Powder Technol.*, vol. 83, pp. 245–252, 1995.

[109] D. P. Bentz, M. A. Peltz, and J. Winpigler, "Early-age properties of cement-based Materials. II: Influence of water-to-cement ratio," *J. Mater. Civ. Eng.*, vol. 21, no. 9, pp. 512–517, 2009.

[110] D. Rothstein, J. J. Thomas, B. J. Christensen, and H. M. Jennings, "Solubility behavior of Ca-, S-, Al-, and Si-bearing solid phases in Portland cement pore solutions as a function of hydration time," *Cem. Concr. Res.*, vol. 32, no. 10, pp. 1663–1671, 2002.

[111] S.-G. Kim and K. Wang, "Effect of heat generation from cement hydration on mass concrete placement," Iowa State University, 2010.

[112] F. Puertas, A. Fernández-Jiménez, and M. T. Blanco-Varela, "Pore solution in alkali-activated slag cement pastes. Relation to the composition and structure of calcium silicate hydrate," *Cem. Concr. Res.*, vol. 34, no. 1, pp. 139–148, 2004.

[113] K. Scrivener, A. Ouzia, P. Juilland, and A. Kunhi Mohamed, "Advances in understanding cement hydration mechanisms," *Cem. Concr. Res.*, vol. 124, p. 105823, 2019.

[114] X.-Z. Yuan, C. Song, H. Wang, and J. Zhang, *Electrochemical impedance spectroscopy in PEM fuel cells*. London: Springer, 2010.

225

[115] O. Heaviside, *Electromagnetic theory*, 3rd ed. New York: IEEE, 1925.

[116] A. Finkelstein, "Über passives eisen," *Z. Phys. Chemie*, vol. 39, pp. 91-110., 1902.

[117] H. A. Kramers, "Die Dispersion und Absorption von Röntgenstrahlen," *Z. Phys.*, vol. 30, pp. 522–523, 1894.

[118] E. Warburg, "Über das Verhalten Sogenannter Unpolarisierbare Elektroden gegen Wechselstrom," *Annu. Phys. Chemie*, vol. 67, pp. 493–499., 1899.

[119] R. de L. Kronig and H. A. Kramers, "Zur Theorie der Absorption und Dispersion in den Röntgenspektren," *Z. Phys.*, vol. 48, pp. 174–179, 1928.

[120] R. de L. Kronig, "On the theory of dispersion," *J. Opt. Soc. Am.*, vol. 12, no. 6, pp. 547–557, 1926.

[121] M. E. Orazem and B. Tribollet, *Electrochemical impedance spectroscopy*. Hoboken: Wiley, 2008.

[122] E. Barsoukov and J. R. Macdonald, *Impedance spectroscopy theory, experiment, and applications*, 2nd ed. Hoboken, New Jersey: Wiley-Interscience, 2005.

[123] E. Levart and D. Schuhmann, "General determination of transition behavior of a rotating disc electrode submitted to an electrical perturbation of weak amplitude," *J. Electroanal. Chem.*, vol. 28, p. 45, 1970.

[124] E. Levart and D. Schuhmann, "Sur la détermination générale de l'impédance de concentration (diffusion convective et réaction chimique) pour une électrode à disque tournant," *J. Electroanal. Chem.*, vol. 53, pp. 77–94, 1974.

[125] J. S. Newman, "Frequency dispersion in capacity measurements at a disk electrode," *J. Electrochem. Soc.*, vol. 117, pp. 198–203, 1970.

[126] B. Tribollet and J. S. Newman, "Analytic expression for the Warburg impedance for a rotating disk electrode," *J. Electrochem. Soc.*, vol. 130, pp. 822-824., 1993.

[127] K. S. Cole, "Electric impedance of suspensions of spheres," *J. Gen. Physiol.*, vol. 12, pp. 29–36, 1928.

[128] P. I. Dolin and B. V. Ershler, "Kinetics of processes on the platinum electrode: I. The kinetics of the ionization of hydrogen adsorbed on a platinum electrode," *Acta Physicochim. URSS*, vol. 13, pp. 747-778., 1940.

[129] J. E. B. Randles, "Kinetics of rapid electrode reactions," *Faraday Discuss.*, vol. 1, pp. 11–19, 1947.

[130] R. de Levie, *Electrochemical Responses of Porous and Rough Electrodes*, P. Delahay., vol. 6, no. 1. New York: Interscience, 1967.

[131] I. Epelboin and G. Loric, "Sur un phénoméne de résonance observé en basse fréquence au cours des electrolyses accompagnées d'une forte surtension anodique," *J. Phys. le Radium*, vol. 21, pp. 75–76, 1960.

[132] A. Frumkin, "The study of the double layer at the metal-solution interface by electrokinetic and electrochemical methods," *Trans. Faraday Soc.*, vol. 33, pp. 117–127, 1940.

[133] B. A. Boukamp, "A Nonlinear Least Squares fit procedure for analysis of immittance data of electrochemical systems," *Solid State Ionics, Diffus. React.*, vol. 20, pp. 31–44, 1986.

[134] J. R. Macdonald, J. Schoonman, and A. P. Lehnen, "The applicability and power of complex nonlinear least squares for the analysis of impedance and immittance data," *J. Electroanal. Chem.*, vol. 131, pp. 77–95, 1982.

[135] B. A. Boukamp and J. R. Macdonald, "Alternatives to Kronig-Kramers transformation and testing, and estimation of distributions," *Solid State Ionics*, vol. 74, pp. 85–101, 1994.

[136] C. Deslouis, I. Epelboin, C. Gabrielli, and B. Tribollet, "Impédance électromécanique obtenue au courant limite de diffusion à partir d'une modulation sinusoidale de la vitesse de rotation d'une électrode à disque," *J. Electroanal. Chem.*, vol. 82, pp. 251-269., 1977.

[137] C. Gabrielli and B. Tribollet, "A transfer function approach for a generalized electrochemical impedance spectroscopy," *J. Electrochem. Soc.*, vol. 141, pp. 1147–1157, 1994.

[138] C. Deslouis, I. Epelboin, C. Gabrielli, P. Sainte-Rose Fanchine, and B. Tribollet, "Relationship between the electrochemical impedance and the electrohydrodynamical impedances measured using a rotating disc electrode," *J. Electroanal. Chem.*, vol. 107, pp. 193–195, 1980.

[139] B. Dong, Q. Qiu, J. Xiang, C. Huang, F. Xing, and N. Han, "Study on the

carbonation behavior of cement mortar by electrochemical impedance spectroscopy," *Materials (Basel).*, vol. 7, pp. 218–231, 2014.

[140] L. Kong, L. Hou, Y. Wang, and G. Sun, "Investigation of the interfacial transition zone between aggregate-cement paste by AC impedance spectroscopy," *J. Wuhan Univ. Technol. Mater. Sci. Ed.*, vol. 31, no. 4, pp. 865–871, 2016.

[141] J. M. Torrents, P. Juan-Garcia, and A. Aguado, "Electrical impedance spectroscopy as a technique for the surveillance of civil engineering structures : considerations on the galvanic insulation of samples," *Meas. Sci. Technol.*, vol. 18, pp. 1958–1962, 2007.

[142] Y. Shimizu, "An electrical method for measuring the setting time of Portland cement," *Mill Sect. Concr.*, vol. 32, no. 5, pp. 111–113, 1928.

[143] J. Calleja, "Effect of current frequency on measurement of electrical resistance of cement pastes," *J. Am. Concr. Inst.*, vol. 49, p. 329, 1952.

[144] S. Michelsen, "Beitrag zur Bindezeit Bestimmung," *Zement*, vol. 22, no. 3, pp. 457–461, 1933.

[145] H. W. Whittington, W. J. McCarter, and M. C. Forde, "The conduction of electricity through concrete," *Proc. Inst. Civ. Eng.*, vol. 33, no. 114, pp. 48–60, 1981.

[146] J. Calleja, "New techniques in the study of setting and hardening of hydraulic materials," *Am. Concr. Inst. J. Proc.*, vol. 48, no. 3, pp. 525–536, 1952.

[147] D. D. MacDonald, "Reflections on the history of electrochemical impedance spectroscopy," *Electrochim. Acta*, vol. 51, pp. 1376–1388, 2006.

[148] G. Dotelli and C. M. Mari, "The evolution of cement paste hydration process by impedance spectroscopy," *Mater. Sci. Eng.*, vol. 303, pp. 54–59, 2001.

[149] J. L. Provis and S. A. Bernal, "Geopolymers and related alkali-activated materials," *Annu. Rev. Mater. Res.*, vol. 44, pp. 299–330, 2014.

[150] N. Neithalath and J. Jain, "Applications of electrical impedance methods in linking the structure of micro- and macro-porous concretes to their transport properties," *ACI Spec. Publ.*, vol. 270, pp. 33–50, Mar. 2010.

[151] W. J. McCarter, T. M. Chrisp, G. Starrs, and J. Blewett, "Characterization and monitoring of cement-based systems using intrinsic electrical property

measurements," *Cem. Concr. Res.*, vol. 33, pp. 197–206, 2003.

[152] R. K. Manchiryal and N. Neithalath, "Electrical property-based sensing of concrete: Influence of material parameters on dielectric response," *Am. Concr. Inst. SP252*, pp. 23–40, 2008.

[153] J. L. Provis, P. A. Walls, and J. S. J. van Deventer, "Geopolymerisation kinetics. 3. Effects of Cs and Sr salts," *Chem. Eng. Sci.*, vol. 63, no. 4480–4489, 2008.

[154] N. Shafiq and M. F. Nuruddin, "Degree of hydration of OPC and OPC/FA pastes dried in different relative humidity," *Concr. Res. Lett.*, vol. 1, pp. 81–89, 2010.

[155] R. T. Coverdale, B. J. Christensen, T. O. Mason, H. M. Jennings, and E. J. Garboczi, "Interpretation of impedance spectroscopy of cement paste via computer modelling," *J. Mater. Sci.*, vol. 29, no. 19, pp. 712–719, 1995.

[156] R. T. Coverdale, B. J. Christensen, T. O. Mason, H. M. Jennings, and E. J. Garboczi, "Interpretation of the impedance spectroscopy of cement paste via computer modeling. Part II dielectric response," *J. Mater. Sci.*, vol. 29, no. 19, pp. 4984–4992, 1994.

[157] J. Bu, Z. Tian, S. Zheng, and Z. Tang, "Effect of sand content on strength and pore structure of cement mortar," *J. Wuhan Univ. Technol. Mater. Sci. Ed.*, vol. 32, no. 2, pp. 382–390, 2017.

[158] W. Lai, "Impedance spectroscopy as a tool for the electrochemical study of mixed conducting ceria," California Institute of Technology, 2007.

[159] B. Christensen *et al.*, "Impedance spectroscopy of hydrating cement-based materials: measurement, interpretation, and application," *J. Am. Ceram. Soc.*, vol. 77, no. 11, pp. 2789–2804, 1994.

[160] P. Gu, P. Xie, J. J. Beaudoin, and R. Brousseau, "A.C. impedance spectroscopy (I): A new equivalent circuit model for hydrated portland cement paste," *Cem. Concr. Res.*, vol. 22, no. 5, pp. 833–840, 1992.

[161] P. Xie, P. Gu, Z. Xu, and J. J. Beaudoin, "A rationalized a.c. impedance model for microstructural characterization of hydrating cement systems," *Cem. Concr. Res.*, vol. 23, no. 2, pp. 359–367, 1993.

[162] C. Andrade, V. M. Blanco, A. Collazo, M. Keddam, X. R. Nóvoa, and H. Takenouti, "Cement paste hardening process studied by impedance

spectroscopy," *Electrochim. Acta*, vol. 44, no. 24, pp. 4313–4318, 1999.

[163] G. Song, "Equivalent circuit model for AC electrochemical impedance spectroscopy of concrete," *Cem. Concr. Res.*, vol. 30, no. 11, pp. 1723–1730, 2000.

[164] C. A. Scuderi, T. O. Mason, and H. M. Jennings, "Impedance spectra of hydrating cement pastes," *J. Mater. Sci.*, vol. 26, no. 2, pp. 349–353, 1991.

[165] O. Poupard, A. Aït-Mokhtar, and P. Dumargue, "Corrosion by chlorides in reinforced concrete: Determination of chloride concentration threshold by impedance spectroscopy," *Cem. Concr. Res.*, vol. 34, no. 6, pp. 991–1000, 2004.

[166] L. Y. Woo, S. Wansom, A. D. Hixson, M. A. Campo, and T. O. Mason, "A universal equivalent circuit model for the impedance response of composites," *J. Mater. Sci.*, vol. 38, no. 10, pp. 2265–2270, 2003.

[167] M. Shi, Z. Chen, and J. Sun, "Determination of chloride diffusivity in concrete," *Cem. Concr. Res.*, vol. 29, pp. 1111–1115, 1999.

[168] G. Ping, X. Zhingzi, X. Ping, and J. J. Beaudoin, "Application of A.C impedance techniques in studies of porous cementitious materials. (I): Influence of solid phase and pore solution on high frequency resistance," *Cem. Concr. Res.*, vol. 23, no. I, pp. 531–540, 1993.

[169] S. L. Cormack, D. E. Macphee, and D. C. Sinclair, "An AC impedance spectroscopy study of hydrated cement pastes," *Adv. Cem. Res.*, vol. 10, no. 4, pp. 151–159, 1998.

[170] P. Gu, P. Xie, J. J. Beaudoin, and R. Brousseau, "A.C. impedance spectroscopy (II): Microstructural characterization of hydrating cement-silica fume systems," *Cem. Concr. Res.*, vol. 23, no. 1, pp. 157–168, 1993.

[171] S. Prabhakaran and C. R. Sullivan, "Impedance-analyzer measurements of high-frequency power passives : Techniques for high power and low impedance," in *Conference Record of the 2002 IEEE Industry Applications Conference. 37th IAS Annual Meeting*, 2002, pp. 1360–1367.

[172] L. Xiao and X. Wei, "Early age compressive strength of pastes by electrical resistivity method and maturity method," *J. Wuhan Univ. Technol. Mater. Sci.*

Ed., vol. 26, no. 5, pp. 983–989, 2011.

[173] X. Wei, L. Xiao, and Z. Li, "Prediction of standard compressive strength of cement by the electrical resistivity measurement," *Constr. Build. Mater.*, vol. 31, pp. 341–346, 2012.

[174] Y. Liao and X. Wei, "Penetration resistance and electrical resistivity of cement paste with superplasticizer," *Mater. Struct.*, vol. 47, no. 4, pp. 563–570, 2014.

[175] Y. Bu and J. Weiss, "The influence of alkali content on the electrical resistivity and transport properties of cementitious materials," *Cem. Concr. Compos.*, vol. 51, pp. 49–58, 2014.

[176] D. D. Macdonald, "Some advantages and pitfalls of electrochemical impedance spectroscopy," *Corrosion*, vol. 46, no. 3, pp. 229–242, 1990.

[177] C. Pastor-Fernández, K. Uddin, G. H. Chouchelamane, W. D. Widanage, and J. Marco, "A Comparison between electrochemical impedance spectroscopy and incremental capacity-differential voltage as Li-ion diagnostic techniques to identify and quantify the effects of degradation modes within battery management systems," *J. Power Sources*, vol. 360, pp. 301–318, 2017.

[178] A. S. Hamdy, E. El-Shenaw, and T. El-Bitar, "Electrochemical impedance spectroscopy study of the corrosion behavior of some niobium bearing stainless steels in 3.5% NaCl," *Int. J. Electrochem. Sci.*, vol. 1, no. 4, pp. 171–180, 2006.

[179] J. R. Scully, D. C. Silverman, and M. W. Kendig, *Electrochemical Impedance : Analysis and Interpretation*. Philadelphia: ASTM International, 1993.

[180] G. W. H. Höhne, W. F. Hemminger, and H.-J. Flammersheim, *Differential Scanning Calorimetry*, 2nd ed. Laupheim: Springer, 2003.

[181] W. Zielenkiewicz and E. Margas, *Theory of calorimetry*, vol. 1. 2004.

[182] M. Gerstig and L. Wadsö, "A method based on isothermal calorimetry to quantify the influence of moisture on the hydration rate of young cement pastes," *Cem. Concr. Res.*, vol. 40, no. 6, pp. 867–874, 2010.

[183] T. Lemke, "An eight channel isothermal heat flow calorimeter for cement / concrete research and production control use in the mW range," *C3 Prozess- und Anal. GmbH*, pp. 1–41.

[184] L. Frølich, L. Wadsö, and P. Sandberg, "Using isothermal calorimetry to predict

one day mortar strengths," *Cem. Concr. Res.*, vol. 88, pp. 108–113, 2016.

[185] X. Pang, D. P. Bentz, C. Meyer, G. P. Funkhouser, and R. Darbe, "A comparison study of Portland cement hydration kinetics as measured by chemical shrinkage and isothermal calorimetry," *Cem. Concr. Compos.*, vol. 39, pp. 23–32, 2013.

[186] Q. Xu, J. Hu, J. M. Ruiz, K. Wang, and Z. Ge, "Isothermal calorimetry tests and modeling of cement hydration parameters," *Thermochim. Acta*, vol. 499, no. 1–2, pp. 91–99, 2010.

[187] I. Pane and W. Hansen, "Investigation of blended cement hydration by isothermal calorimetry and thermal analysis," *Cem. Concr. Res.*, vol. 35, pp. 1155–1164, 2004.

[188] E. Gruyaert, N. Robeyst, and N. De Belie, "Study of the hydration of Portland cement blended with blast-furnace slag by calorimetry and thermogravimetry," *Therm. Anal. Calorim.*, vol. 2, pp. 941–951, 2010.

[189] A. O. Adamtsevich, A. P. Pustovgar, S. A. Pashkevich, and A. V Eremin, "Calorimetric methods in analysis of composite building materials," *Appl. Eng. Res.*, vol. 11, no. 3, pp. 1609–1611, 2016.

[190] P. J. Haines, *Principles of thermal analysis and calorimetry*. Cambridge, England, 2002.

[191] R. C. O. Romano, M. A. Cincotto, and R. G. Pileggi, "Hardening phenomenon of Portland cement suspensions monitored by Vicat test, isothermal calorimetry and oscillatory rheometry," *IBRACON*, vol. 11, no. 5, pp. 949–959, 2018.

[192] H. F. Gonnerman, "Development of cement performance tests and requirements," *P.C.A. Res. Bull*, vol. 93, pp. 22–25, 1958.

[193] B. L. Bean and J. R. Dise, "Causes of variation in chemical analyses and physical tests of Portland cement," *U.S. Natl. Bur. Stand.*, pp. 1–30, 1961.

[194] H. N. Atahan, O. N. Oktar, and M. A. Taşdemir, "Effects of water-cement ratio and curing time on the critical pore width of hardened cement paste," *Constr. Build. Mater.*, vol. 23, no. 3, pp. 1196–1200, 2009.

[195] G. D. Stefanou and C. Larsinos, "Influence of mixing water on the setting time of concrete," *Int. J. Cem. Compos. Light. Concr.*, vol. 3, pp. 45–48, 1981.

[196] K. Marar and Ö. Eren, "Effect of cement content and water/cement ratio on fresh

concrete properties without admixtures," *Int. J. Phys. Sci.*, vol. 6, no. 24, pp. 5752–5765, 2011.

[197] W. Fajun, M. W. Grutzeck, and D. M. Roy, "The retarding effects of fly ash upon the hydration of cement pastes: The first 24 hours," *Cem. Concr. Res.*, vol. 15, no. 1, pp. 174–184, 1985.

[198] D. P. Bentz and C. F. Ferraris, "Rheology and setting of high volume fly ash mixtures," *Cem. Concr. Compos.*, vol. 32, no. 4, pp. 265–270, 2010.

[199] S. Amziane, "Setting time determination of cementitious materials based on measurements of the hydraulic pressure variations," *Cem. Concr. Res.*, vol. 36, no. 2, pp. 295–304, Feb. 2006.

[200] J. F. Lamond and J. H. Pielert, *Significance of tests and properties of concrete & concrete-making materials*. West Conshohocken: ASTM International, 2006.

[201] P. Echli, *Handbook of sample preparation for scanning electron microscopy and x-ray microanalysis*. New York: Springer, 2009.

[202] D. H. Krinsley, P. Kenneth, S. Boggs, and T. Keith, *Backscattered scanning electron microscopy and image analysis of sediments and sedimentary rocks*. Cambridge, UK: Cambridge University Press, 2019.

[203] K. L. Scrivener, "The development of microstructure of Portland cement mortars," University of London, 1984.

[204] Z. Hong and D. David, "Quantitative backscattered electron analysis of cement paste," The University of Kansas, 1990.

[205] T. Gareth, "Modern electron microscopy for materials characterization," *J. Electron Microsc. Tech.*, no. 1, pp. 465–468, 1986.

[206] P. Stutzman, "Scanning electron microscopy imaging of hydraulic cement microstructure," *Cem. Concr. Compos.*, vol. 26, no. 8, pp. 957–966, 2004.

[207] L. Pelletier-Chaignat, F. Winnefeld, B. Lothenbach, G. Le Saout, C. J. Müller, and C. Famy, "Influence of the calcium sulphate source on the hydration mechanism of Portland cement-calcium sulphoaluminate clinker-calcium sulphate binders," *Cem. Concr. Compos.*, vol. 33, no. 5, pp. 551–561, 2011.

[208] F. L. Matthews, G. A. O. Davies, D. Hitchings, and C. Soutis, *Finite element modelling of composite materials and structures*. Cambridge, England:

Woodhead Publishing Limited, 2000.

[209] M. Rappaz, M. Bellet, and M. Deville, *Numerical modeling in materials Science and Engineering*. Heidelberg, 2003.

[210] S. Huclova, "Modeling of cell suspensions and biological tissue for computational electromagnetics," ETH Zurich, 2011.

[211] C. D. Kennedy, D. C. Sinclair, I. M. Reaney, and J. S. Dean, "Predicting the energy storage density in poly(methyl methacrylate)/methyl ammonium lead iodide composites," *J. Appl. Phys.*, vol. 125, no. 21, 2019.

[212] G. Dale, M. Strawhorne, D. C. Sinclair, and J. S. Dean, "Finite element modeling on the effect of intra-granular porosity on the dielectric properties of $BaTiO_3$ MLCCs," *J. Am. Ceram. Soc.*, vol. 101, no. 3, pp. 1211–1220, 2018.

[213] A. Goncharov, G. Hrkac, J. D. Dean, and T. S. Schrefl, "Finite element modelling of impedance spectroscopy data in composite electroceramics," *Comput. Mater. Sci.*, pp. 1–14, 2012.

[214] T. D. Shook and R. S. Reddy Gorla, "Finite element analysis and redesign of a compressor hub spinner," *Finite Elem. Anal. Des.*, vol. 28, no. 1, pp. 19–31, 1997.

[215] S. S. Faouri *et al.*, "High quality factor cold sintered Li_2MoO_4-$BaFe_{12}O_{19}$ composites for microwave applications," *Acta Mater.*, vol. 166, pp. 202–207, 2019.

[216] J. S. Dean, J. H. Harding, and D. C. Sinclair, "Simulation of impedance spectra for a full three-dimensional ceramic microstructure using a finite element model," *Am. Ceram. Soc.*, vol. 97, no. 3, pp. 885–891, 2014.

[217] J. P. Heath, J. S. Dean, J. H. Harding, and D. C. J. Sinclair, "Simulation of impedance spectra for core-shell grain structures using finite element modeling," *J. Am. Ceram. Soc.*, vol. 98, no. 6, pp. 1925–1931, 2015.

[218] J. P. Heath, J. H. Harding, D. C. Sinclair, and J. S. Dean, "The analysis of impedance spectra for core–shell microstructures: why a multiformalism approach is essential," *Adv. Funct. Mater.*, vol. 29, no. 38, pp. 1–10, 2019.

[219] J. Koruza *et al.*, "Formation of the core–shell microstructure in lead-free $Bi_{1/2}Na_{1/2}TiO_3$-$SrTiO_3$ piezoceramics and its influence on the electromechanical

properties," *J. Eur. Ceram. Soc.*, vol. 36, pp. 1009–1016, 2016.

[220] Singeresu S. Rao, *The finite element method in engineering*, 6th ed. Elsevier, 2018.

[221] B. Zhu, *The finite element method*, vol. 53, no. 9. Singapore, 2018.

[222] M. Zhang, G. Ye, and K. Van Breugel, "Multiscale lattice Boltzmann-finite element modelling of chloride diffusivity in cementitious materials. Part I: Algorithms and implementation," *Mech. Res. Commun.*, vol. 58, pp. 53–63, 2014.

[223] J. A. Teixeira De Freitas, P. T. Cuong, R. Faria, and M. Azenha, "Modelling of cement hydration in concrete structures with hybrid finite elements," *Finite Elem. Anal. Des.*, vol. 77, pp. 16–30, 2013.

[224] B. R. Indriyantho and Nuroji, "Finite element modeling of concrete fracture in tension with the Brazilian splitting test on the case of plane-stress and plane-strain," *Procedia Eng.*, vol. 95, pp. 252–259, 2014.

[225] N. De Jager, P. Pallav, and A. J. Feilzer, "Finite element analysis model to simulate the behavior of luting cements during setting," *Dent. Mater.*, vol. 21, no. 11, pp. 1025–1032, 2005.

[226] P. Navi and C. Pignat, "Simulation of cement hydration and the connectivity of the capillary pore space," *Adv. Cem. Based Mater.*, vol. 4, no. 2, pp. 58–67, 1996.

[227] R. T. Coverdale, E. J. Garboczi, H. M. Jennings, B. J. Christensen, and T. O. Mason, "Computer simulations of impedance spectroscopy in two dimensions: application to cement paste," *J. Am. Ceram. Soc.*, vol. 76, no. 6, pp. 1513–1520, 1993.

[228] British Standards Institute, *BS EN 450-1, Fly Ash for Concrete, Part 1: Definition, Specifications and Conformity Criteria*. 2012.

[229] European Committee for Standardization, *EN 13263-1:2005+A1:2009 Silica fume for concrete. Definitions, requirements and conformity criteria*. Brussels, Belgium, 2009.

[230] M. Autolab B.V, "Electrochemical cell setup," in *Autolab application note EC08*, 2011, pp. 1–3.

[231] G. Raikova, P. Carpanese, Z. Stoynov, D. Vladikova, M. Viviani, and A. Barbucei, "Inductance correction in impedance studies of solid oxide fuel cells," *Bulg. Chem. Commun.*, vol. 41, no. 2, pp. 199–206, 2009.

[232] T. Soboleva, Z. Xie, Z. Shi, E. Tsang, T. Navessin, and S. Holdcroft, "Investigation of the through-plane impedance technique for evaluation of anisotropy of proton conducting polymer membranes," *J. Electroanal. Chem.*, vol. 622, no. 2, pp. 145–152, 2008.

[233] ASTM International, *ASTM C1679 -17. Standard practice for measuring hydration kinetics of hydraulic cementitious mixtures using isothermal calorimetry.* 2017.

[234] National Institute of Standards and Technology, "Primary standards and standard reference materials for electrolytic conductivity." pp. 1–31, 2004.

[235] Setting Standards in Analytical Science, "Preparation of calibration curves," vol. 32, pp. 1–27, 2003.

[236] Rosemount Analytical, "Conductance data for commonly used chemicals," vol. 44, pp. 1–33, 2010.

[237] C. J. Haecker *et al.*, "Modeling the linear elastic properties of Portland cement paste," *Cem. Concr. Res.*, vol. 35, no. 10, pp. 1948–1960, 2005.

[238] S. P. Martinović, M. M. Vlahović, J. B. Majstorović, and T. D. Volkov Husović, "Anisotropy analysis of low cement concrete by ultrasonic measurements and image analysis," *Sci. Sinter.*, vol. 48, no. 1, pp. 57–70, 2016.

[239] M. M. Shahzamanian and W. J. Basirun, "Modeling of cementitious representative volume element with additives," *J. Multiscale Model.*, vol. 8, no. 2, pp. 1–29, 2017.

[240] H. Mazaheripour, R. Faria, G. Ye, E. Schlangen, J. Granja, and M. Azenha, "Microstructure-based prediction of the elastic behaviour of hydrating cement pastes," *Appl. Sci.*, vol. 8, no. 442, pp. 2–20, 2018.

[241] D. P. Bentz, "CEMHYD3D: A three-dimensional cement hydration and microstructure development modeling package," vol. 8. National Institute of Standards and Technology, pp. 227–235, 2000.

[242] V. Šmilauer and Z. Bittnar, "Microstructure-based micromechanical prediction of

elastic properties in hydrating cement paste," *Cem. Concr. Res.*, vol. 36, pp. 1708–1718, 2006.

[243] E. Stora, B. Bary, Q. He, E. Deville, and P. Montarnal, "Modelling and simulations of the chemo – mechanical behaviour of leached cement-based materials. Leaching process and induced loss of stiffness," *Cem. Concr. Res.*, vol. 39, no. 9, pp. 763–772, 2009.

[244] L. Prasittisopin and D. Trejo, "Characterization of chemical treatment method for rice husk ash cementing materials," *Am. Concr. Inst. SP294*, pp. 94–106, 2012.

[245] S. K. Al-Bahar *et al.*, "Evaluation of Kuwaiti argillaceous materials as a replacement of sand for clinker Production," *Arab. J. Sci. Eng.*, vol. 39, no. 6, pp. 4485–4506, 2014.

[246] F. Méducin, B. Bresson, N. Lequeux, M. N. de Noirfontaine, and H. Zanni, "Calcium silicate hydrates investigated by solid-state high resolution ^{1}H and ^{29}Si nuclear magnetic resonance," *Cem. Concr. Res.*, vol. 37, no. 5, pp. 631–638, 2007.

[247] J. W. Bullard and E. J. Garboczi, "A model investigation of the influence of particle shape on Portland cement hydration," *Cem. Concr. Res.*, vol. 36, no. 6, pp. 1007–1015, 2006.

[248] Z. Qian, E. J. Garboczi, G. Ye, and E. Schlangen, "Anm: a geometrical model for the composite structure of mortar and concrete using real-shape particles," *Mater. Struct.*, vol. 49, no. 1–2, pp. 149–158, 2016.

[249] A. F. Sosa Gallardo, J. L. Provis, and J. S. Dean, "Simulation of the impedance response of hydrating tricalcium silicate at early stages of hydration," *Unpubl. Manuscr. Submitt. Publ.*, pp. 1–32, 2020.

[250] A. F. Sosa Gallardo, "The study of cement hydration by alternating current impedance spectroscopy and isothermal calorimetry," University of Sheffield, 2016.

[251] M. Autolab B.V, "Raw data from FRA measurements ,Technical note 15," pp. 1–15.

[252] Autolab, "Electrochemical impedance spectroscopy (EIS), Part 6 – Measuring raw signals in EIS," *Spectroscopy*, pp. 1–3, 2011.

237

[253] A. I. Zia and S. C. Mukhopadhyay, "Impedance spectroscopy and experimental setup," in *Electrochemical sensing: carcinogens in beverages*, New Zealan., Switzerland: Springer International, 2016, pp. 21–67.

[254] B. Hirschorn, B. Tribollet, and M. E. Orazem, "On selection of the perturbation amplitude required to avoid nonlinear effects in impedance measurements," *Isr. J. Chem.*, vol. 48, pp. 133–142, 2008.

[255] A. Yerokhin, E. V. Parfenov, C. J. Liang, V. R. Mukaeva, and A. Matthews, "System linearity quantification for in-situ impedance spectroscopy of plasma electrolytic oxidation," *Electrochem. commun.*, vol. 27, pp. 137–140, 2013.

[256] J. J. Giner-Sanz, E. M. Ortega, and V. Pérez-Herranz, "Harmonic analysis based method for perturbation amplitude optimization for EIS measurements," *J. Electrochem. Soc.*, vol. 164, no. 13, pp. H918–H924, 2017.

[257] A. Lasia, *Electrochemical impedance spectroscopy and its applications*. New York: Springer, 2014.

[258] C. R. Paul, "Partial Inductance," *IEEE EMC Soc. Newsletters*, no. 226, pp. 34–42, 2010.

[259] S. J. Shah, "Field wiring and noise considerations for analog signals," *Natl. Instruments Corp.*, pp. 1–22, 2001.

[260] O. Reid, F. S. Saleh, and E. B. Easton, "Determining electrochemically active surface area in PEM fuel cell electrodes with electrochemical impedance spectroscopy and its application to catalyst durability," *Electrochim. Acta*, vol. 114, pp. 278–284, 2013.

[261] G. Breit, *High-frequency resistance of inductance coils*, vol. 17, no. 4. National Bureau of Standards, 1922.

[262] J. G. Coffin, "The influence of frequency upon the self-inductance of coils," *Proc. Am. Acad. Arts Sci.*, vol. 41, no. 34, pp. 275–296, 1906.

[263] BioLogic Science Instruments, "Application note #5: Precautions for good impedance measurements," pp. 1–5, 2010.

[264] Gamry Instruments, "Verification of low impedance: EIS using a 1 mΩ Resistor," pp. 1–6, 2010.

[265] Chomerics, "EMI shielding theory & gasket design guide," in *EMI shielding*

engineering handbook, pp. 191–220.

[266] C. Bünzli, H. Kaiser, and P. Novák, "Important aspects for reliable electrochemical impedance spectroscopy measurements of Li-ion battery electrodes," *J. Electrochem. Soc.*, vol. 162, no. 1, pp. A218–A222, 2015.

[267] G. Hsieh, T. O. Mason, E. J. Garboczi, and L. R. Pederson, "Experimental limitations in impedance spectroscopy: Part III. Effect of reference electrode geometry/position," *Solid State Ionics*, vol. 96, no. 3–4, pp. 153–172, 1997.

[268] J. A. Grubb, H. S. Limaye, and A. M. Kakade, "Testing pH of concrete," *Concr. Int.*, vol. 29, no. 04, pp. 78–83, 2007.

[269] X. Jiang, S. Nešić, and F. Huet, "The effect of electrode size on electrochemical noise measurements and the role of chloride on localized CO2 corrosion of mild steel," *NACE Int.*, pp. 1–17, 2009.

[270] N. Ogihara, Y. Itou, T. Sasaki, and Y. Takeuchi, "Impedance spectroscopy characterization of porous electrodes under different electrode thickness using a symmetric cell for high-performance lithium-ion batteries," *J. Phys. Chem.*, vol. 119, pp. 4612–4619, 2015.

[271] H. Zhou, R. D. Tilton, and L. R. White, "The role of electrode impedance and electrode geometry in the design of microelectrode systems," *J. Colloid Interface Sci.*, vol. 297, no. 2, pp. 819–831, 2006.

[272] S. Mohtashami, "Electrochemical properties of flexible electrodes for implanted neuromuscular excitation applications," Thesis, McMaster University, 2011.

[273] Z. Wu, L. Li, J. M. Yan, and X. B. Zhang, "Materials design and system construction for conventional and new-concept supercapacitors," *Adv. Sci.*, vol. 4, pp. 1–48, 2017.

[274] Y. Suda, A. Mizutani, T. Harigai, H. Takikawa, H. Ue, and Y. Umeda, "Influences of internal resistance and specific surface area of electrode materials on characteristics of electric double layer capacitors," *Am. Inst. Phys. Conf. Proc.*, pp. 1–12, 2016.

[275] B. Li, Y. Huan, and W. Zhang, "Passivation and corrosion behavior of P355 carbon steel in simulated concrete pore solution at pH 12.5 to 14," *Int. J. Electrochem. Sci.*, pp. 10402–10420, 2017.

[276] S. H. Lee, J. H. Jung, Y. M. Chae, J. K. F. Suh, and J. Y. Kang, "Fabrication and characterization of implantable and flexible nerve cuff electrodes with Pt, Ir and IrO films deposited by RF sputtering," *J. Micromech. Microeng.*, vol. 20, no. 3, 2010.

[277] U. Nürnberger, "Stainless steel in concrete–state of the art report," *Inst. Mater. (UK), pp.30, 1996*, no. 18, p. 30, 1996.

[278] A. Nishikata, Y. Ichihara, and T. Tsuru, "An application of electrochemical impedance spectroscopy to atmospheric corrosion study," *Corros. Sci.*, vol. 37, no. 6, pp. 897–911, 1995.

[279] V. A. Alves and C. M. A. Brett, "Characterisation of passive films formed on mild steels in bicarbonate solution by EIS," *Electrochim. Acta*, vol. 47, no. 13–14, pp. 2081–2091, 2001.

[280] J. Hu, D. A. Koleva, J. H. W. De Wit, P. Petrov, and K. Van Breugel, "Corrosion performance of carbon steel in micelle-containing cement extract," *ECS Trans.*, vol. 28, no. 24, pp. 113–121, 2010.

[281] Arminox, *Corrosion aspects of galvanic coupling between carbon steel and stainless steel reinforcement in concrete*. Brondby, 1999.

[282] S. J. Ford, T. O. Mason, B. J. Christensen, R. T. Coverdale, H. M. Jennings, and E. J. Garboczi, "Electrode configurations and impedance spectra of cement pastes," *J. Mater. Sci.*, vol. 30, pp. 1217–1224, 1995.

[283] H. Cesiulis, N. Tsyntsaru, A. Ramanavicius, and G. Ragoisha, "The study of thin films by electrochemical impedance spectroscopy," in *Nanostructures and thin films for multifunctional applications*, Moldova: Springer International, 2016, pp. 3–43.

[284] R. Ahmed and K. Reifsnider, "Study of influence of electrode geometry on impedance spectroscopy," *Int. J. Electrochem. Sci*, vol. 6, pp. 1159–1174, 2011.

[285] F. Zhang *et al.*, "Reference and counter electrode positions affect electrochemical characterization of bioanodes in different bioelectrochemical systems," *Biotechnol. Bioeng.*, vol. 111, pp. 1931–1939, 2014.

[286] W. Yan, S. Hong, and R. Chaoshi, "Optimum design of electrode structure and parameters in electrical impedance tomography," *Physiol. Meas.*, vol. 27, no. 3,

pp. 291–306, 2006.

[287] Corporate Circular: BTD2007/11, "Horizontal reinforcement for crack control in walls and wall type piers," *Bridge technical direction*. .

[288] M. Á. Sanjuán, E. Estévez, and C. Argiz, "Alkali ion concentration estimations in cement paste pore solutions," *Appl. Sci.*, vol. 9, no. 5, p. 992, 2019.

[289] Q. Li and N. J. Coleman, "Hydration kinetics, ion-release and antimicrobial properties of white Portland cement blended with zirconium oxide nanoparticles," *Dent. Mater. J.*, vol. 33, no. 6, pp. 805–810, 2014.

[290] R. Ylmén, L. Wadsö, and I. Panas, "Insights into early hydration of Portland limestone cement from infrared spectroscopy and isothermal calorimetry," *Cem. Concr. Res.*, vol. 40, no. 10, pp. 1541–1546, 2010.

[291] K. R. Backe, O. B. Lile, S. K. Lyomov, and N. U. Science, "Characterizing curing cement slurries by electrical conductivity," *SPE Drill. Complet.*, pp. 201–207, 2001.

[292] J. M. Cruz, J. Payá, L. F. Lalinde, and I. C. Fita, "Evaluación de las propiedades eléctricas de morteros de cemento con puzolanas," *Mater. Constr.*, vol. 61, no. 301, pp. 7–26, 2011.

[293] P. Azarsa and R. Gupta, "Electrical resistivity of concrete for durability evaluation: A review," *Adv. Mater. Sci. Eng.*, pp. 1–30, 2017.

[294] G. M. Moss, B. J. Christensen, T. O. Mason, and H. M. Jennings, "Microstructural analysis of young cement pastes using impedance spectroscopy during pore solution exchange," *Adv. Cem. Based Mater.*, vol. 4, no. 2, pp. 68–75, 1996.

[295] L. Wadsö, C. P. Cooper-Jensen, and P. M. Bentley, "Assessing hydration disturbances from concrete aggregates with radiation shielding properties by isothermal calorimetry," *Phys. Rev. Accel. Beams*, vol. 20, no. 4, pp. 1–8, 2017.

[296] A. Sedaghat, "Cement heat of hydration and thermal control," University of South Florida, 2016.

[297] G. Renaudin, A. Mesbah, B. Z. Dilnesa, M. Francois, and B. Lothenbach, "Crystal chemistry of iron containing cementitious AFm layered hydrates," *Curr. Inorg. Chem.*, vol. 2, pp. 1–10, 2015.

[298] P. Gu, P. Xie, and J. J. Beaudoin, "Some applications of AC impedance spectroscopy in cement research," *Cem. Concr. Aggr.*, vol. 17, no. 2, pp. 113–118, 1995.

[299] S. Zhutovsky and K. Kovler, "Effect of water to cement ratio and degree of hydration on chemical shrinkage of cement pastes," *Concr. Durab. Serv. Life Plan.*, no. April 2016, pp. 47–54, 2009.

[300] S. J. Kwon, M. Q. Feng, and S. S. Park, "Characterization of electromagnetic properties for durability performance and saturation in hardened cement mortar," *NDT E Int.*, vol. 43, no. 2, pp. 86–95, 2010.

[301] Z. Owsiak, "Dependence between the composition of pore solution and the expansion of mortar containing reactive aggregate," *Ceram. - Silikáty*, vol. 49, no. 2, pp. 109–114, 2004.

[302] L. J. Buckley, M. A. Carter, M. A. Wilson, and J. D. Scantlebury, "Methods of obtaining pore solution from cement pastes and mortars for chloride analysis," *Cem. Concr. Res.*, vol. 37, no. 11, pp. 1544–1550, 2007.

[303] L. Zeghichi, Z. Benghazi, and L. Baali, "The effect of the kind of sands and additions on the mechanical behaviour of S.C.C," *Phys. Procedia*, vol. 55, pp. 485–492, 2014.

[304] J. Topič and Z. Prošek, "Hydration process and mechanical properties of cement paste with recycled concrete powder and silica sand powder," *Acta Polytech. CTU Proc.*, vol. 13, pp. 125–129, 2017.

[305] S. Suresh and J. Revathi, "Effect of M-sand on setting time of high performance concrete," *Asian J. Res. Soc. Sci. Humanit.*, vol. 6, no. 10, p. 1648, 2016.

[306] M. Bouasker, P. Mounanga, P. Turcry, A. Loukili, and A. Khelidj, "Chemical shrinkage of cement pastes and mortars at very early age: Effect of limestone filler and granular inclusions," *Cem. Concr. Compos.*, pp. 1–10, 2017.

[307] F. He *et al.*, "Differential analysis of AC impedance spectroscopy of cement-based materials considering CPE behavior," *Constr. Build. Mater.*, vol. 143, pp. 179–188, 2017.

[308] R. F. Feldman, "The effect of sand/cement ratio and silica fume on the microstructure of mortars," *Cem. Concr. Res.*, vol. 16, pp. 31–39, 1986.

[309] J. Cao and D. D. L. Chung, "Microstructural effect of the shrinkage of cement-based materials during hydration, as indicated by electrical resistivity measurement," *Cem. Concr. Res.*, vol. 34, pp. 1893–1897, 2004.

[310] C. McCague, Y. Bai, Q. Zhou, and P. A. M. Basheer, "Effect of calcium sulfates on the early hydration of calcium sulfoaluminate cement and the stability of embedded aluminium," in *International Symposium on Cement-Based Materials for Nuclear Wastes*, 2014, pp. 1–12.

[311] R. Novotný, E. Bartoní, J. Ĝ. Švec, and M. Mon, "Influence of active alumina on the hydration process of Portland cement," in *International Conference on Ecology and new Building materials and products,* 2016, vol. 151, pp. 80–86.

[312] G. Jen, S. Skalamprinos, M. Whittaker, I. Galan, M. S. Imbabi, and F. P. Glasser, "The impact of intrinsic anhydrite in an experimental calcium sulfoaluminate cement from a novel, carbon-minimized production process," *Mater. Struct. Constr.*, vol. 50, no. 2, 2017.

[313] L. Xu, P. Wang, and G. Zhang, "Calorimetric study on the influence of calcium sulfate on the hydration of Portland cement–calcium aluminate cement mixtures," *J. Therm. Anal. Calorim.*, vol. 110, pp. 725–731, 2012.

[314] D. Bentz, F. Zunino, and D. Lootens, "Chemical vs. physical acceleration of cement hydration," *Concr. Int.*, vol. 38, no. 11, pp. 37–44, 2016.

[315] S. Pourchet *et al.*, "Early C_3A hydration in the presence of different kinds of calcium sulfate.," *Cem. Concr. Res.*, vol. 39, pp. 989–996, 2009.

[316] V. Tydlitát and P. Tesárek, "Effects of the type of calorimeter and the use of plasticers and hydrophobizers on the measured hydration heat development of gypsum," *J. Therm. Anal. Calorim.*, vol. 91, pp. 791–796, 2008.

[317] R. Ylmén, "Early hydration of Portland cement - An infrared spectroscopy perspective complemented by calorimetry and scanning electron microscopy," Chalmers University of Technology, 2013.

[318] M. García-maté, A. G. De, L. León-reina, E. R. Losilla, M. A. G. Aranda, and I. Santacruz, "Effect of calcium sulfate source on the hydration of calcium sulfoaluminate eco-cement," *Cem. Concr. Compos.*, vol. 55, pp. 53–61, 2015.

[319] C. Xiong, L. Jiang, Y. Zhang, H. Chu, and P. Jiang, "Characterization of sulfate

diffusion into cement paste by low frequency impedance spectroscopy," *Mater. Lett.*, vol. 174, pp. 234–237, 2016.

[320] A. Quennoz, "Hydration of C_3A with calcium sulfate alone and in the presence of calcium silicate," École polytechnique fédérale de Lausanne, 2011.

[321] S. Sujin and H. M. Jennings, "Pore solution chemistry of alkali-activated ground blast-furnace slag," *Cem. Concr. Res.*, vol. 29, pp. 159–170, 1999.

[322] J. Kempl and O. Çopuroglu, "The interaction of pH , pore solution composition and solid phase composition of carbonated blast furnace slag cement paste activated with aqueous sodium monofluorophosphate," in *15th Euroseminar on Microscopy Applied to Building Materials*, 2015, pp. 287–296.

[323] B. Lothenbach, G. Le Saout, M. Ben Haha, R. Figi, and E. Wieland, "Hydration of a low-alkali CEM III/B-SiO₂ cement (LAC)," *Cem. Concr. Res.*, vol. 42, no. 2, pp. 410–423, 2012.

[324] W. Kunther, B. Lothenbach, and J. Skibsted, "Influence of the Ca/Si ratio of the C-S-H phase on the interaction with sulfate ions and its impact on the ettringite crystallization pressure," *Cem. Concr. Res.*, vol. 69, pp. 37–49, 2015.

[325] A. M. Harrisson, N. B. Winter, and H. F. W. Taylor, "Microstructure and microchemistry of slag cement pastes," *Mater. Res. Soc. Symp. Proc.*, vol. 85, no. 9, pp. 213–221, 1987.

[326] I. G. Richardson and G. W. Groves, "Microstructure and microanalysis of hardened cement pastes involving ground granulated blast-furnace slag," *J. Mater. Sci.*, vol. 27, no. 22, pp. 6204–6212, 1992.

[327] Y. A. Villagrán Zaccardi, E. Gruyaert, N. M. Alderete, and N. De Belie, "Influence of particle size distribution of slag , limestone and fly ash on early hydration of cement," *Int. RILEM Conf. Mater. Syst. Struct. Civ. Eng. Conf. Segm. Concr. with Suppl. Cem. Mater.*, pp. 31–40, 2016.

[328] C. Hwang and D. Shen, "The effects of blast-furnace slag and fly ash on the hydration of Portland cement," *Cem. Concr. Res.*, vol. 21, pp. 410–425, 1991.

[329] W. Chen and H. J. H. Brouwers, "A method for predicting the alkali concentrations in pore solution of hydrated slag cement paste," *J. Mater. Sci.*, vol. 46, no. 10, pp. 3622–3631, 2011.

[330] J. I. Escalante-García and J. H. Sharp, "Effect of temperature on the hydration of the main clinker phases in Portland cements: Part I, neat cements," *Cem. Concr. Res.*, vol. 28, no. 9, pp. 1245–1257, 1998.

[331] N. B. Singh, K. N. Bhattacharjee, and A. K. Shukla, "Hydration of Portland blended cements," *Cem. Concr. Res.*, vol. 25, no. 5, pp. 1023–1030, 1995.

[332] L. Courard and F. Michel, "Limestone fillers cement based composites: Effects of blast furnace slags on fresh and hardened properties," *Constr. Build. Mater.*, vol. 51, pp. 439–445, 2014.

[333] Q. Qiu *et al.*, "Influence of slag incorporation on electrochemical behavior of carbonated cement," *Constr. Build. Mater.*, vol. 147, pp. 661–668, 2017.

[334] S. K. Nath, S. Mukherjee, S. Maitra, and S. Kumar, "Kinetics study of geopolymerization of fly ash using isothermal conduction calorimetry," *J. Therm. Anal. Calorim.*, vol. 127, no. 3, pp. 1953–1961, 2017.

[335] F. Deschner *et al.*, "Hydration of Portland cement with high replacement by siliceous fly ash," *Cem. Concr. Res.*, vol. 42, no. 10, pp. 1389–1400, 2012.

[336] M. Kawamura, O. A. Kayyali, and M. N. Haque, "Effects of a flyash on pore solution composition in calcium and sodium chloride-bearing mortars," *Cem. Concr. Res.*, vol. 18, no. 5, pp. 763–773, 1988.

[337] K. L. Aughenbaugh, R. T. Chancey, P. Stutzman, M. C. Juenger, and D. W. Fowler, "An examination of the reactivity of fly ash in cementitious pore solutions," *Mater. Struct.*, vol. 46, no. 5, pp. 869–880, 2013.

[338] M. H. Shehata, M. D. A. Thomas, and R. F. Bleszynski, "The effects of fly ash composition on the chemistry of pore solution in hydrated cement pastes," *Cem. Concr. Res.*, vol. 29, no. 12, pp. 1915–1920, 1999.

[339] G. Baert, S. Hoste, G. De Schutter, and N. De Belie, "Reactivity of fly ash in cement paste studied by means of thermogravimetry and isothermal calorimetry," *J. Therm. Anal. Calorim.*, vol. 94, no. 2, pp. 485–492, 2008.

[340] S. W. Tang, Z. J. Li, H. Y. Shao, and E. Chen, "Characterization of early-age hydration process of cement pastes based on impedance measurement," *Constr. Build. Mater.*, vol. 68, pp. 491–500, 2014.

[341] E. Sakai, S. Miyahara, S. Ohsawa, S. H. Lee, and M. Daimon, "Hydration of fly

ash cement," *Cem. Concr. Res.*, vol. 35, no. 6, pp. 1135–1140, 2005.

[342] V. Rahhal and R. Talero, "Influence of two different fly ashes on the hydration of Portland cements," *J. Therm. Anal. Calorim.*, vol. 78, no. 1, pp. 191–205, 2004.

[343] E. Berodier and K. Scrivener, "Understanding the filler effect on the nucleation and growth of C-S-H," *J. Am. Ceram. Soc.*, vol. 97, no. 12, pp. 3764–3773, 2014.

[344] S. Hanjitsuwan, P. Chindaprasirt, and K. Pimraksa, "Electrical conductivity and dielectric property of fly ash geopolymer pastes," *Int. J. Miner. Metall. Mater.*, vol. 18, no. 1, pp. 94–99, 2011.

[345] L. Xiao and Z. Li, "Early-age hydration of fresh concrete monitored by non-contact electrical resistivity measurement," *Cem. Concr. Res.*, vol. 38, no. 3, pp. 312–319, 2008.

[346] I. B. Topu, T. Uygunolu, and I. Hocaolu, "Electrical conductivity of setting cement paste with different mineral admixtures," *Constr. Build. Mater.*, vol. 28, no. 1, pp. 414–420, 2012.

[347] J. M. Ortega, I. Sánchez, and M. Á. Climent, "Impedance spectroscopy study of the effect of environmental conditions on the microstructure development of sustainable fly ash cement mortars," *Materials (Basel).*, vol. 10, pp. 1–15, 2017.

[348] V. Yogendran, B. W. Langan, and M. A. Ward, "Hydration of cement and silica fume paste," *Cem. Concr. Res.*, vol. 21, pp. 691–708, 1991.

[349] S. Diamond, "Effects of microsilica (silica fume) on pore-solution chemistry of cement pastes," *J. Am. Ceram. Soc.*, vol. 66, no. 5, p. C-82-C-84, 1983.

[350] Rasheeduzzafar and S. Ehtesham Hussain, "Effect of microsilica and blast furnace slag on pore solution composition and alkali-silica reaction," *Cem. Concr. Compos.*, vol. 13, no. 3, pp. 219–225, 1991.

[351] V. Rahhal, O. Cabrera, R. Talero, and A. Delgado, "Calorimetry of Portland cement with silica fume and gypsum additions," *J. Therm. Anal. Calorim.*, vol. 87, no. 2, pp. 331–337, 2007.

[352] A. C. A. Muller, K. L. Scrivener, J. Skibsted, A. M. Gajewicz, and P. J. McDonald, "Influence of silica fume on the microstructure of cement pastes: New insights from ^{1}H NMR relaxometry," *Cem. Concr. Res.*, vol. 74, pp. 116–125, 2015.

[353] V. Rahhal and R. Talero, "Calorimetry of Portland cement with silica fume,

diatomite and quartz additions," *Constr. Build. Mater.*, vol. 23, no. 11, pp. 3367–3374, 2009.

[354] H. Cheng-Yi and R. F. Feldman, "Hydration reactions in Portland cement–silica fume blends," *Cem. Concr. Res.*, vol. 15, pp. 585–592, 1985.

[355] M. H. Shehata and M. D. A. Thomas, "Use of ternary blends containing silica fume and fly ash to suppress expansion due to alkali-silica reaction in concrete," *Cem. Concr. Res.*, vol. 32, no. 3, pp. 341–349, 2002.

[356] J. S. Kim, S. Kwon, J. W. Choi, and G. C. Cho, "Properties of low-pH cement grout as a sealing material for the geological disposal of radioactive waste," *Nucl. Eng. Technol.*, vol. 43, no. 5, pp. 459–468, 2011.

[357] A. Estokova, M. Kovalcikova, A. Luptakova, and M. Prascakova, "Testing silica fume-based concrete composites under chemical and microbiological sulfate attacks," *Materials (Basel).*, vol. 9, no. 5, 2016.

[358] E. A. El-Alfi, A. M. Radwan, and H. Abu-El-naga, "Influence of substitution of ordinary Portland cement by silica fume on the hydration of slag-Portland cement pastes," *Ceram. - Silikaty*, vol. 55, no. 2, pp. 147–152, 2011.

[359] V. M. Sounthararajan, K. Srinivasan, and A. Sivakumar, "Micro filler effects of silica-fume on the setting and hardened properties of concrete," *J. Appl. Sci. Eng. Technol.*, vol. 6, no. 14, pp. 2649–2654, 2013.

[360] M. A. A. Abd Elaty and M. F. Ghazy, "Performance of Portland cement mixes containing silica fume and mixed with lime-water," *HBRC J.*, vol. 10, no. 3, pp. 247–257, 2014.

[361] S. A. Abo El-Enein, M. F. Kotkata, G. B. Hanna, M. Saad, and M. M. Abd El Razek, "Electrical conductivity of concrete containing silica fume," *Cem. Concr. Res.*, vol. 25, no. 8, pp. 1615–1620, 1995.

[362] T. M. Salem, "Electrical conductivity and rheological properties of ordinary Portland cement-silica fume and calcium hydroxide-silica fume pastes," *Cem. Concr. Res.*, vol. 32, no. 9, pp. 1473–1481, 2002.

[363] B. J. Christensen, T. O. Mason, and H. M. Jennings, "Influence of silica fume on the early hydration of Portland cements using impedance spectroscopy," *J. Am. Ceram. Soc.*, vol. 75, no. 4, pp. 939–945, 1992.

[364] D. D. L. Chung, "Electrical conduction behavior of cement-matrix composites," *J. Mater. Eng. Perform.*, vol. 11, no. 2, pp. 194-204(11), 2002.

[365] J. Yajun and J. H. Cahyadi, "Simulation of silica fume blended cement hydration," *Mater. Struct.*, vol. 37, no. 270, pp. 397–404, 2004.

[366] H. C. Kim, S. Y. Kim, and S. S. Yoon, "Electrical properties of cement paste obtained from impedance spectroscopy," *J. Mater. Sci.*, vol. 30, no. 15, pp. 3768–3772, 1995.

[367] D. P. Bentz and E. J. Garboczi, "Percolation of phases in a three-dimensional cement paste microstructural model," *Cem. Concr. Res.*, vol. 21, pp. 325–344, 1991.

[368] L. Evangelista and M. Guedes, "Microstructural studies on recycled aggregate concrete," *New Trends Eco-efficient Recycl. Concr.*, vol. 24, no. 11, pp. 425–451, 2018.

[369] W. Chen, P. Shen, and Z. Shui, "Determination of water content in fresh concrete mix based on relative dielectric constant measurement," *Constr. Build. Mater.*, vol. 34, pp. 306–312, 2012.

[370] D. P. Bentz, E. J. Garboczi, C. J. Haecker, and O. M. Jensen, "Effects of cement particle size distribution on performance properties of Portland cement-based materials," *Cem. Concr. Res.*, vol. 29, no. 10, pp. 1663–1671, Oct. 1999.

[371] A. Van Beek and M. A. Hilhorst, "Dielectric measurements to characterize the microstructural changes of young concrete," *Heron*, vol. 44, no. 1, pp. 3–17, 1999.

[372] I. Sharpley, "The effect of hydration on the microstructural properties of individual Phases of ordinary Portland cement," University College London, 2015.

[373] D. P. Bentz, P. E. Stutzman, C. J. Haecker, and S. Remond, "SEM/X-ray imaging of cement-based materials," in *Euroseminar on microscopy applied to building materials*, 1999, pp. 457–466.

[374] I. Jelenić, A. Panović, R. Halle, and T. Gaćeša, "Effect of gypsum on the hydration and strength development of commercial Portland cements containing alkali sulfates," *Cem. Concr. Res.*, vol. 7, pp. 239–246, 1977.
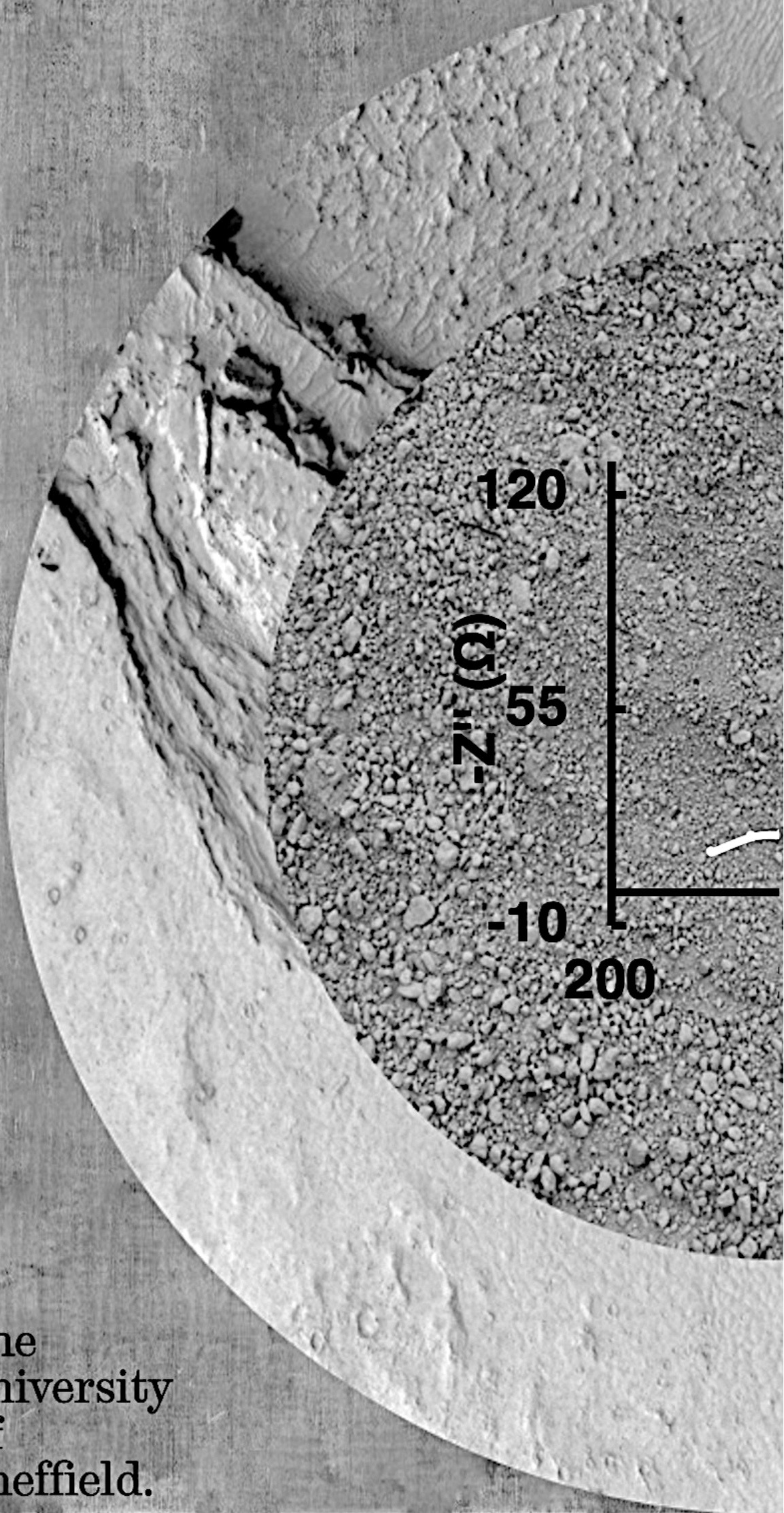
[375] R. F. Feldman and V. S. Ramachandran, "The influence of $CaSO_4.2H_2O$ upon the hydration character of $3CaO.Al_2O_3$," *Concr. Res.*, vol. 18, no. 57, pp. 185–196, 1966.

[376] X. Kang, G.-C. Kang, and L. Ge, "Modified time of setting test for fly ash paste and fly ash-soil mixtures," *J. Mater. Civ. Eng.*, vol. 25, no. 2, pp. 296–301, 2013.

[377] B. Dong, G. Li, J. Zhang, Y. Liu, F. Xing, and S. Hong, "Non-destructive tracing on hydration feature of slag blended cement with electrochemical method," *Constr. Build. Mater.*, vol. 149, pp. 467–473, 2017.

[378] J. Tao and X. Wei, "Effect of ground granulated blast-furnace slag on the hydration and properties of cement paste," *Adv. Cem. Res.*, pp. 251–260, 2018.

[379] B. Suryanto, W. J. McCarter, G. Starrs, and T. M. Chrisp, "Characterization of fly-ash using electrochemical impedance spectroscopy," *Procedia Eng.*, vol. 171, pp. 705–714, 2017.

[380] J. Zelić, D. Rušić, D. Veža, and R. Krstulović, "Role of silica fume in the kinetics and mechanisms during the early stage of cement hydration," *Cem. Concr. Res.*, vol. 30, no. 10, pp. 1655–1662, 2000.

[381] R. Yang and J. H. Sharp, "Hydration characteristics of Portland cement after heat curing: I, Degree of hydration of the anhydrous cement phases," *J. Am. Ceram. Soc.*, vol. 84, no. 5, pp. 1113–1119, 2001.

[382] S. Gauffinet-Garrault, *The rheology of cement during setting*, vol. 1. Woodhead Publishing Limited, 2012.

[383] L. E. Copeland and D. L. Kantro, "Chemistry of hydration of Portland cement: II. Kinetics of the hydration of Portland cement," in *International Symposium on Chemistry of Cement*, 1960, vol. 1, pp. 443–453.

[384] K. A. Snyder, X. Feng, B. D. Keen, and T. O. Mason, "Estimating the electrical conductivity of cement paste pore solutions from OH-, K+ and Na+ concentrations," *Cem. Concr. Res.*, vol. 33, no. 6, pp. 793–798, 2003.

[385] J. Wilson, "The electrical properties of concrete," University of Edinburgh, 1986.

[386] F. Rajabipour and J. Weiss, "Electrical conductivity of drying cement paste," *Mater. Struct.*, vol. 40, no. 10, pp. 1143–1160, 2007.

[387] H. Ma, D. Hou, J. Liu, and Z. Li, "Estimate the relative electrical conductivity of

C-S-H gel from experimental results," *Constr. Build. Mater.*, vol. 71, pp. 392–396, 2014.

[388] Q. Zhou and J. J. Beaudoin, "Effect of applied hydrostatic stress on the hydration of Portland cement and C$_3$S," *Adv. Cem. Res.*, vol. 15, no. 1, pp. 9–16, 2003.

[389] D. Jansen, S. T. Bergold, F. Goetz-Neunhoeffer, and J. Neubauer, "The hydration of alite: A time-resolved quantitative X-ray diffraction approach using the G-factor method compared with heat release," *J. Appl. Crystallogr.*, vol. 44, no. 5, pp. 895–901, 2011.

[390] V. S. Ramachandran, "Estimation of tricalcium silicate through polymorphic transformation," *J. Therm. Anal.*, vol. 3, pp. 181–190, 1971.

[391] I. G. Richardson, J. Skibsted, L. Black, and R. J. Kirkpatrick, "Characterisation of cement hydrate phases by TEM, NMR and Raman spectroscopy," *Adv. Cem. Res.*, vol. 22, no. 4, pp. 233–248, 2010.

[392] Z. Boz, F. Erdogdu, and M. Tutar, "Effects of mesh refinement, time step size and numerical scheme on the computational modeling of temperature evolution during natural-convection heating," *J. Food Eng.*, vol. 123, pp. 8–16, 2014.

[393] F. Liu, W. W. Hager, and A. V. Rao, "Adaptive mesh refinement method for optimal control using nonsmoothness detection and mesh size reduction," *J. Franklin Inst.*, vol. 352, no. 10, pp. 4081–4106, 2015.